ELECTRICALLY TUNABLE THERMAL CONDUCTIVITY AND EXHAUST HEAT RECOVERY APPLICATIONS OF THERMOELECTRIC MATERIALS

Albert Massaguer Colomer

Doctoral Thesis

Electrically Tunable Thermal Conductivity and Exhaust Heat Recovery Applications of Thermoelectric Materials

Albert **Massaguer Colomer**

2018

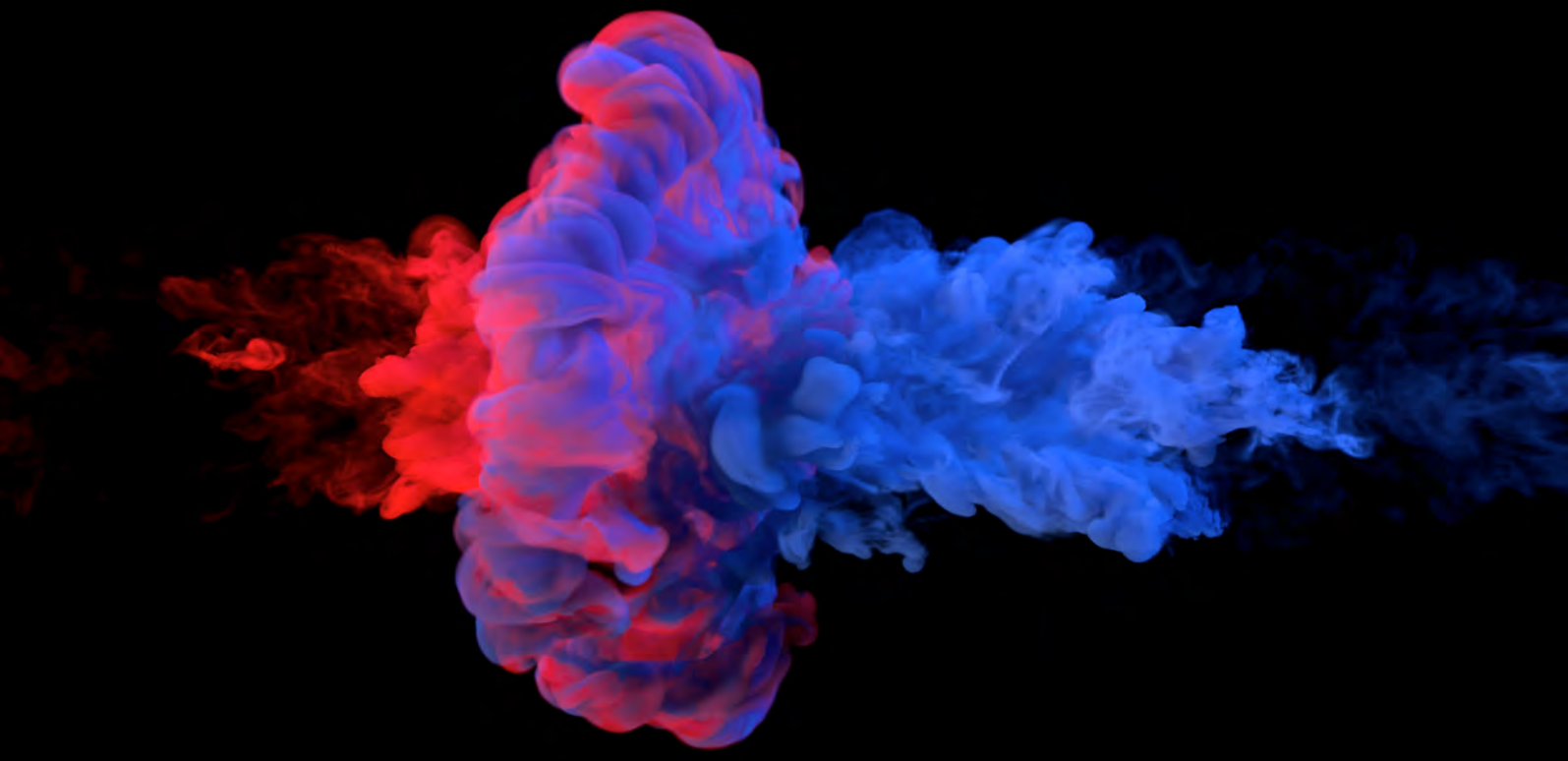

Universitat de Girona

Albert Massaguer Colomer

Universitat de Girona

DOCTORAL THESIS

Electrically Tunable Thermal Conductivity and Exhaust Heat Recovery Applications of Thermoelectric Materials

Albert Massaguer Colomer

2018

Doctoral Programme in Technology

Supervised by:

Dr. Toni Pujol Sagaró

Dr. Eduard Massaguer Colomer

This manuscript has been presented to opt for the **Doctoral Degree** from the **Universitat de Girona**

A la meva familia i amics. Als que hi són, i als que retrobarem.

"La Tarda molt intensa m'ha portat
aquest capvespre plàcid.
Reposo els ulls cansats
en l'ordre dels prestatges plens de llibres,
en l'ordre de la cambra.

Es fa fosc lentament, s'encenen llums,
i és més pausat el batec de la vida.

Estimo aquest silenci i aquesta hora
i més ara que em gronxa fins perdre'm
en el record de tu
que mai no m'abandona."

Miquel Martí i Pol, *Aquest silenci*

Acknowledgments

Les línies d'aquest epígraf són les darreres que escric i, ara que concloc, em semblen tan o més obligades que qualsevol dels capítols que vesteixen aquesta tesi. Per mi, les paraules que ara escric són rellevants ja que posen el punt i final a no només tres anys de feina, sinó a tota la meva etapa formativa. Així que em prenc la llibertat de dedicar-les als qui m'heu ajudat a arriba-hi, ara és l'hora.

Les jornades d'aquests últims anys han estat intenses. Tan intenses potser com les que descriu al seu poema el poeta Miquel Martí i Pol. D'una banda, i com és lògic, per la feina derivada de la investigació. Aquí vull fer un agraïment als companys del grup de recerca GREFEMA, en especial als meus directors de tesi, en Toni i l'Eduard. Professionals que amb una exquisida humilitat, van acceptar ser interpel·lats per un neòfit de la recerca com jo. El temps, el suport, els consells i l'autonomia que m'heu ofert m'han permès aconseguir-ho.

D'altra banda, a la intensitat dels dies també s'hi afegeixen preocupacions i maldecaps més quotidians, com els que tots carreguem fora de la feina, i que, com a conseqüència també de l'edat, sovint tenen relació amb els plans de futur. Això ho saben bé l'Eduard, el meu germà, i la Mercè, la meva parella, dos treballadors valents i incansables. Sense la vostra ajuda el que hem aconseguit no hauria estat possible. Sou un model per mi i un referent.

Tot i el treball viu, el poeta ja ho diu, quan arriba el final de la jornada és hora de reposar i posar en ordre les idees. La feina d'aquests darrers anys i que aquí es presenta és només en forma de nou coneixement. Sense voler menysprear la

feina feta, ni molt menys, vull remarcar que l'etapa educativa no només tracta de formar professionals competents, sinó també ciutadans ètics i compromesos. I en aquest sentit vull agrair als meus pares, en Ramon i l'Assumpció, que amb el seu immens esforç, paciència i estima, m'han educat, m'han donat l'oportunitat d'arribar fins aquí i, el més important, m'han fet com a persona. No només de professors aprèn l'ignorant. No crec que estigueu mai tan orgullosos de mi com jo de vosaltres.

Com no pot ser menys, vull agrair i recordar també als meus avis, la seva estima, els seus consells i el seu interès en el que he fet. Les àvies Anna i Margarita, que m'han cuidat i ensenyat de petit i també de més gran. Sempre recordaré les converses amb l'avi Jaume sobre els invents dels quals l'Eduard i jo li parlàvem, que tant li emplenaven el cap de preguntes i consells, i que al final han acabat servint per elaborar aquesta tesi.

No vull oblidar-me dels amics, els bons moments que passem junts són com els espais en blanc que hi ha entre aquestes paraules, poden semblar poc importants però sense ells no s'entendria res. Gràcies.

Vull agrair també l'ajuda econòmica rebuda per part de la Universitat de Girona a través de la beca doctoral, també a l'Associació/Col·legi d'Enginyers Industrials de Catalunya i la Fundació Caixa d'Enginyers per l'ajuda econòmica per a la realització d'aquesta tesi, i a la Fundación Repsol i el Centro de Tecnología Repsol per la seva col·laboració.

Finalment, no deixa d'estar el camí ple de dubtes i temors, però també ple de guanys, dels quals el més important sigui, crec jo, el descobriment que fem de la gent que ens envolta i de nosaltres mateixos. Sigui com sigui, i tal i com deia la veu de l'experiència del meu avi Josep, només hi ha una manera de fer una valoració apropiada d'una etapa, "s'ha de veure la fi". Així que, arribats al final d'aquest trajecte, deixo a les vostres mans fer-ne aquest judici.

Compendium of Publications

This Ph.D. thesis has been prepared as a compendium of papers, according to the regulations of the University of Girona (*Normativa d'ordenació dels ensenyaments universitaris de doctorat de la Universitat de Girona, aprovada pel Consell de Govern en la sessió 3/12 de 26 d'abril de 2012, i modificada pel Consell de Govern en la sessió 5/2013 de 25 de setembre de 2013*). This thesis includes two published papers and one submitted paper.

The complete references of the papers comprising this thesis, the impact factors, quartile, and category of the journals according to the Journal Citation Report are described below.

A Massaguer, E Massaguer, T Pujol, M Comamala, L Montoro, JR González. Electrically tunable thermal conductivity in thermoelectric materials: Active and passive control. *Applied Energy*, 154, 709-717, 2015. ISSN 0306-2619 (Impact factor 5.746; Journal 10 of 88; 1st quartile; Energy and Fuels)

http://dx.doi.org/10.1016/j.apenergy.2015.05.067

A Massaguer, E Massaguer, M Comamala, T Pujol, JR González, MD Cárdenas, D Carbonell, AJ Bueno. A method to assess the fuel economy of automotive thermoelectric generators. Submitted to *Applied Energy*. ISSN 0306-2619 (Impact factor 7.182; Journal 6 of 92; 1st quartile; Energy and Fuels)

A Massaguer, E Massaguer, M Comamala, T Pujol, L Montoro, MD Cárdenas, D Carbonell, AJ Bueno. Transient behavior under a normalized driving cycle of an automotive thermoelectric generator. *Applied Energy*, 206, 1282-1296, 2017. ISSN 0306-2619 (Impact factor 7.182; Journal 6 of 92; 1st quartile; Energy and Fuels)

http://dx.doi.org/10.1016/j.apenergy.2017.10.015

To whom it may concern,

Dr. Toni Pujol Sagaró, professor in the Department d'Enginyeria Mecànica i de la Construcció Industrial of Universitat de Girona.

and

Dr. Eduard Massaguer Colomer, chief executive officer of Nabla Thermoelectrics S.L.

DECLARE

That the thesis entitled *"Electrically Tunable Thermal Conductivity and Exhaust Heat Recovery Applications of Thermoelectric Materials"*, presented by Albert Massaguer Colomer to obtain a doctoral degree, has been completed under our supervision and meets the requirements to opt for the Doctoral Degree.

For all intents and purposes, we hereby sign this document.

Girona, November 2017

Dr. Toni Pujol Sagaró

Dr. Eduard Massaguer Colomer

Nomenclature

Abbreviation

ATEG	Automotive thermoelectric generator
AX	Axle ratio
BiTe	Bismuth Telluride
BPV	By-pass valves
SV	Swept volume (m^3)
FTPP	Full-throttle pedal position
IMEP	Indicated mean effective pressure (Pa)
IP	Indicated power (W)
LCV	Lower calorific value (kJ/kg)
MPP	Maximum power point
NEDC	New european driving cycle
PbTe	Lead Telluride
TE	Thermoelectric
TEC	Thermoelectric cooler
TEG	Thermoelectric generator
TEM	Thermoelectric module

TR	Transmission ratio
PCU	Power converter unit

Letters

a	Coefficient
b	Coefficient
B	Bore (mm)
C	Specific heat capacity (J/kgK)
$\boldsymbol{D}$	Electric flux density vector
BP	Backpressure (mbar)
F	Fuel economy (%)
φ	Electric scalar potential
h	Convective heat transfer coefficient (W/m^{2}K)
I	Electric current (A)
J	Current density (A/m^2)
$\dot{m}$	Mass flow rate (kg/h)
$\dot{v}$	Volumetric flow rate (m^3/s)
N	Frequency of rotation (rpm)
P	Power (W)
Q	Heat flux (W)
$\dot{q}$	Rate of heat flux
$\boldsymbol{q}$	Heat flux vector
R	Electric resistance (Ω)
s	Slope
S	Surface (mm^2)

ST	Stroke (mm)
T	Temperature (K)
t	Time (s)
th	Thickness (mm)
v	Velocity (m/s)
V	Electric voltage (V)
W	Weight (kg)
K	Thermal conductance (W/K)
z	Figure of merit

Greek symbols

α	Seebeck coefficient (V/K)
γ	Electrical resistivity (Ωm)
ε	Dielectric permittivity (F/m)
η	Efficiency (%)
κ	Thermal conductivity (W/mK)
μ	Thomson coefficient (V°C)
π	Peltier coefficient (V)
ρ	Material density (kg/m^3)
σ	Electrical conductivity (S/m)
τ	Torque (Nm)
ξ	Rolling resistance
ω	Rotational speed (rad/s)

Subscripts

amb	Ambient
c	Cold side
ce	Ceramic substrate
Cu	Copper
e	Electron
eff	Effective
el	Electrical
ex	Exhaust
h	Hot side
hs	Heat sink
l	Length
L	Load
n	n-type semiconductor
p	p-type semiconductor
ph	Phonon
pr	Constant pressure

List of Figures

List of Tables

Content

Resum

L'àmbit d'aplicació dels materials termoèlectrics és molt gran, des de sensors de temperatura, passant per refrigeradors portàtils, fins a generadors d'energia solar. En general, aquestes aplicacions es poden classificar segons la direcció de la conversió energètica. Mentre l'efecte Peltier s'utilitza en refrigeració en estat sòlid, l'efecte Seebeck és responsable de convertir les diferències de temperatura en tensió elèctrica en sistemes de recuperació d'energia.

Aquest treball se centra en dues àrees relacionades amb la termoelectricitat: (i) l'estudi de la capacitat de controlar la conductivitat tèrmica dels materials termoelèctrics i (ii) el desenvolupament, assaig i millora d'un generador termoelèctric per automoció (ATEG).

La primera part de la tesi proposa un nou enfocament sobre l'ús dels materials termoelèctrics, tractant-los com a aïllaments variables en sistemes tèrmics. Aquí, es demostra que la conductivitat tèrmica en materials termoelèctrics es pot controlar externament mitjançant paràmetres elèctrics com la càrrega elèctrica o la tensió en sistemes passius i actius, respectivament. El mode actiu és una bona solució quan es necessita un aïllament complet o un alt control de la conductivitat tèrmica. El mode passiu permet un increment de la conductivitat tèrmica d'$1+ZT$ vegades respecte a la conductivitat tèrmica inicial del semiconductor. Els resultats presenten un nou camp d'aplicació per als materials termoelèctrics.

La segona part d'aquesta investigació se centra en el desenvolupament de la recuperació de calor en tubs d'escapament. En primer lloc, l'autor descriu un

mètode per ajudar en el disseny d'ATEGs i predir l'estalvi de combustible. El procediment es divideix en dues parts principals. La primera consisteix a predir el rendiment de l'ATEG mitjançant una metodologia basada en elements/volums finits (FEM/FVM). Aquest estudi valida el model teòric basat en FEM/FVM que compara els seus valors de sortida amb els obtinguts experimentalment per un ATEG instal·lat en un sistema d'escapament d'un motor de gasolina. L'objectiu és determinar la viabilitat del mètode FEM/FVM per a la predicció del seu rendiment. La segona part proposa un mètode, basat en els resultats obtinguts en l'anàlisi FEM/FVM, per predir l'estalvi de combustible esperat gràcies a l'ATEG. Els resultats mostren la consistència de l'eina de simulació, que revela un ajust d'aproximadament el 97% entre la simulació i les dades experimentals. A més, el mètode aplicat a l'ATEG presentat ha pronosticat un valor màxim d'estalvi de combustible del 0.18%.

En segon lloc, l'autor dóna algunes recomanacions alhora de dissenyar ATEGs per tal d'obtenir un millor rendiment en condicions reals de conducció. Molts models i prototips que han estat desenvolupats i validats amb resultats molt prometedors han estat assajats només en condicions d'estat estacionari. Tanmateix, els vehicles lleugers operen sota càrregues molt variables, provocant una variació significativa del rendiment dels ATEGs. L'objectiu d'aquest estudi és provar i analitzar un ATEG sota diferents condicions de càrrega en estat estacionari i sota el cicle de conducció europeu NEDC. Les dades obtingudes mostren que tant la inèrcia tèrmica com la pèrdua de pressió tenen un paper clau en el disseny d'un ATEG per a aplicacions reals. Les variacions en la temperatura de l'escapament i el cabal màssic dels fums eviten l'assoliment l'estat tèrmic estacionari. En conseqüència, l'energia total generada durant el NEDC és inferior a l'esperada en estat estacionari. D'altra banda, l'excessiva pèrdua de càrrega en l'escapament redueix notablement el rendiment del motor. Els resultats demostren que la generació d'energia de l'ATEG es pot millorar significativament maximitzant la transferència de calor a través dels TEMs utilitzant una geometria aletejada per a l'absorvidor de calor, utilitzant materials termoelèctrics de temperatura més baixa i incloent un control de temperatura de la cara calenta.

Resumen

El ámbito de aplicación de los materiales termoeléctricos es muy grande, desde sensores de temperatura, pasando por refrigeradores portátiles, hasta generadores de energía solar. En general, estas aplicaciones se pueden clasificar según la dirección de la conversión energética. Mientras el efecto Peltier se utiliza en refrigeración en estado sólido, el efecto Seebeck es responsable de convertir las diferencias de temperatura en tensión eléctrica en sistemas de recuperación de energía.

Este trabajo se centra en dos áreas relacionadas con la termoelectricidad: (i) el estudio de la capacidad de controlar la conductividad térmica de los materiales termoeléctricos y (ii) el desarrollo, ensayo y mejora de un generador termoeléctrico para automoción (ATEG).

La primera parte de la tesis propone un nuevo enfoque sobre el uso de los materiales termoeléctricos, tratándolos como aislamientos variables en sistemas térmicos. Aquí, se demuestra que la conductividad térmica en materiales termoeléctricos se puede controlar externamente mediante parámetros eléctricos como la carga eléctrica o la tensión en sistemas pasivos y activos, respectivamente. El modo activo es una buena solución cuando se necesita un aislamiento completo o un alto control de la conductividad térmica. El modo pasivo permite un incremento de la conductividad térmica de $1+ZT$ veces respecto a la conductividad térmica inicial del semiconductor. Los resultados presentan un nuevo campo de aplicación para los materiales termoeléctricos. La segunda parte de esta investigación se centra en el desarrollo de la

recuperación de calor en tubos de escape. En primer lugar, el autor describe un método para ayudar en el diseño de ATEGs y predecir el ahorro de combustible. El procedimiento se divide en dos partes principales. La primera consiste en predecir el rendimiento del ATEG mediante una metodología basada en elementos/volúmenes finitos (FEM/FVM). Este estudio valida el modelo teórico basado en FEM/FVM que compara sus valores de salida con los obtenidos experimentalmente por un ATEG instalado en un sistema de escape de un motor de gasolina. El objetivo es determinar la viabilidad del método FEM/FVM para la predicción de su rendimiento. La segunda parte propone un método, basado en los resultados obtenidos en el análisis FEM/FVM, para predecir el ahorro de combustible esperado gracias al ATEG. Los resultados muestran la consistencia de la herramienta de simulación, que revela un ajuste de aproximadamente el 97% entre la simulación y los datos experimentales. Además, el método aplicado a la ATEG presentado pronosticó un valor máximo de ahorro de combustible del 0.18%.

En segundo lugar, el autor da algunas recomendaciones a la hora de diseñar ATEGs para obtener un mejor rendimiento en condiciones reales de conducción. Muchos modelos y prototipos que han sido desarrollados y validados con resultados muy prometedores han sido ensayados sólo en condiciones de estado estacionario. Sin embargo, los vehículos ligeros operan bajo cargas muy variables, provocando una variación significativa del rendimiento de los ATEGs. El objetivo de este estudio es probar y analizar un ATEG bajo diferentes condiciones de carga en estados estacionarios y bajo el ciclo de conducción europeo NEDC. Los datos obtenidos muestran que tanto la inercia térmica como la pérdida de presión tienen un papel clave en el diseño de un ATEG para aplicaciones reales. Las variaciones en la temperatura del escape y el caudal másico de los humos evitan el alcance del estado térmico estacionario. En consecuencia, la energía total generada durante el NEDC es inferior a la esperada en estado estacionario. Por otra parte, la excesiva pérdida de carga en el escape reduce notablemente el rendimiento del motor. Los resultados demuestran que la generación de energía de los ATEG se puede mejorar significativamente maximizando la transferencia de calor a través de los TEMs utilizando una

geometría aleteada para el absorbedor de calor, utilizando materiales termoeléctricos de temperatura más baja e incluyendo un control de temperatura de la cara caliente.

Abstract

Applications involving the use of thermoelectric materials can be found in many different areas ranging from thermocouple sensors and portable coolers, to solar power generators. Generally, they can be subdivided by the sense of the energy conversion. While the Peltier effect is used in solid-state refrigeration, the Seebeck effect is responsible for the conversion of temperature differences into electrical voltage in energy harvesting systems.

The current work is focused on two areas related to thermoelectricity: (i) the study of the capability of controlling the thermal conductivity of TEMs and (ii) the development, testing and improvement of an automotive thermoelectric generator (ATEG).

The first part of the thesis proposes a novel approach to the use of thermoelectric couples, treating them as variable insulators in thermal systems. Here, it is demonstrated that thermal conductivity in thermoelectric materials can be externally controlled by electrical parameters such as electrical load or DC voltage in passive and active systems, respectively. The active mode is a good solution when a complete insulation or a high control of thermal conductivity is needed. The passive mode permits a thermal conductivity increment of $1+ZT$ times with respect to semiconductor initial thermal conductivity. Results open new opportunities for the application of thermoelectric materials.

The second part of this investigation is focused on exhaust heat recovery development. In the first place, author describes a method to help ATEG design and to predict its performance in terms of fuel economy. The procedure is divided into two main parts. The first one consists in predicting the ATEG performance by using the finite element/volume model (FEM/FVM) methodology. The present study validates the theoretical FEM/FVM -based model comparing its output values with those obtained experimentally by an ATEG installed in an exhaust system of a gasoline engine. The goal is to determine the feasibility of FEM/FVM on predicting its performance. The second part proposes a method, based on results obtained in the FEM/FVM analysis, to predict the expected fuel economy of the ATEG. Results show the consistency of the simulation tool, revealing an agreement of about 97% between simulation and experimental data. In addition, the method applied to the ATEG developed in the present thesis, predicts a maximum fuel economy value of 0.18%.

In the second place, the work gives some ATEG design recommendations to obtain a better performance for real driving conditions. Many models and prototypes have been developed and validated with, a priori, very promising results. The majority of them have been tested under steady-state engine conditions. However, light-duty vehicles operate under wide variable loads, causing significant variation of the ATEG performance. The purpose of this study is to and to analyze an ATEG under different steady-state engine conditions and under the transient New European Driving Cycle (NEDC). Data obtained show that both thermal inertia and pressure drop play a key role in designing an ATEG for real applications. Variations on the exhaust gases temperature and mass flow rate prevent the achievement of the thermal steady state. Consequently, the total energy generated during the NEDC is lower than that expected from a steady-state analysis. On the other hand, excessive pressure loss on the exhaust considerably reduces the engine performance. Results show that the overall power generation of the ATEG can be significantly improved by maximizing the heat transfer through TEMs using a finned geometry, employing lower temperature thermoelectric materials and including a hot-side temperature control.

Chapter 1

Introduction

1.1 Introduction

Thermoelectrics (TE) refers to the direct conversion of an electrical current flow into a heat flow as well as of heat flow into an electrical current flow. The basic principle of thermoelectricity was recognized by Thomas Johann Seebeck in 1821 when he observed that a compass needle near two different interconnected metal wires was deflected when the temperatures at their junctions differ, with the degree of deflection being proportional to the temperature difference.

This phenomenon is due to an electrical field that is created by the temperature difference on the conductors. The Seebeck effect is defined as,

$$V = \alpha \Delta T \,, \tag{1.1}$$

where V is the electromotive force, ΔT is the temperature difference between the junctions, and α is the Seebeck coefficient.

In 1834, the French scientist Jean Peltier discovered that this effect can be reversed and used as a heat pump: if a current is applied to the interconnected conductors, a temperature difference is created at the junctions. Thermal energy is transported from one junction to the other. The so-called Peltier effect can be used either for heating or for cooling. The maximum possible yield when heat is thermoelectrically converted into electrical energy is physically determined by the efficiency of the Carnot cycle process. The Peltier effect can be defined as

$$\dot{q}_\pi = \pi I, \tag{1.2}$$

where $\dot{q}_\pi$ is the rate of heat absorbed or released, I is the applied electrical current and π is the Peltier coefficient.

William Thomson, in 1851, explained the discrepancies among experimental results and, also, the relationship between α and π, by postulating the existence of an additional reversible generation of heat when a temperature difference is applied to a current carrying conductor. This is known as Thomson heat and is proportional to the product of the current and the temperature gradient.

Thomson heat is reversible, i.e., heat is either absorbed or released when the direction of either the current or temperature gradient is reversed, but not concurrently. The Thomson heat can be defined as

$$\dot{q}_\mu = \mu I \Delta T, \tag{1.3}$$

where $\dot{q}_\mu$ is the rate of heat absorbed or released and μ is the Thompson coefficient.

Figure 1.1 illustrates a TE circuit (or couple) consisting of two dissimilar homogeneous materials A and B, their junctions are maintained at hot junction temperature T_h and cold junction temperature T_c ($T_h > T_c$), and the terminals of the circuit are connected to an external load R_L.

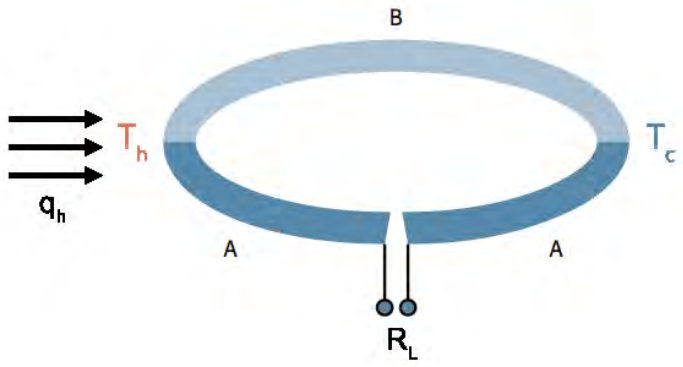

Figure 1.1 Thermoelectric circuit.

The thermal efficiency, η_t of the circuit shown in Figure 1.1 can be defined as

$$\eta_t = \frac{P}{q_h}, \tag{1.4}$$

where P is the electrical power delivered to the external load R_L and q_h is the heat input required to maintain the hot junction temperature at T_h. The electrical power P is defined by the Equation (1.5)

$$P = I^2 R_L, \tag{1.5}$$

where the current flowing through the circuit I can be calculated from the ratio of the electromotive force generated across the circuit with respect to the total resistance of the circuit,

$$I = \frac{\alpha \Delta T}{R_i + R_L}, \tag{1.6}$$

where R_i is the internal resistance of the materials A and B. The heat input to the hot junction is defined by,

$$q_h = K\Delta T + \alpha T_h I - \frac{1}{2} I^2 R_i \,, \tag{1.7}$$

where K, α, and R_i are the thermal conductance, Seebeck coefficient, and total electrical resistance, respectively, of the materials A and B. The terms $K\Delta T$ and $-\frac{1}{2}I^2R_i$ in Equation (1.7) are resulting from the two irreversible effects of heat transfer due to thermal conduction and Joule heating. While the term $\alpha T_h I$ is due to the reversible Peltier effect.

Using Equations (1.5)-(1.7), with $m = \frac{R_L}{R_i}$, the thermal efficiency defined in Equation (1.4) can be expressed as

$$\eta_t = \frac{m \frac{\Delta T}{T_h}}{\frac{1+m^2}{T_h}\frac{R_i K}{\alpha^2} + m + 1 - \frac{1}{2}\frac{\Delta T}{T_h}}. \tag{1.8}$$

For fixed temperatures T_h and T_c and load resistance R_L, the thermal efficiency can be maximized when the term $\frac{R_i K}{\alpha^2}$ in the denominator of Equation (1.8) is minimized. Also, α, R_i, and K are the thermoelectric properties. Therefore, we redefine this group of properties by calling it the thermoelectric figure of merit Z, being defined as

$$Z = \frac{\alpha^2}{R_i K}. \tag{1.9}$$

The higher the Z, the greater the thermal efficiency of the circuit. The figure of merit depends on both the TE materials and the geometry of the couple.

Modern thermoelectric modules (TEMs), presented in Figure 1.2, are solid-state systems consisting of a large number of alternate *p*- and *n*- type semiconductor thermoelements, which are connected electrically in series by metal

interconnectors and sandwiched between two electrically insulating and thermally conducting ceramic substrates. They can act as coolers, heaters, power generators or thermal energy sensors depending on the direction of current.

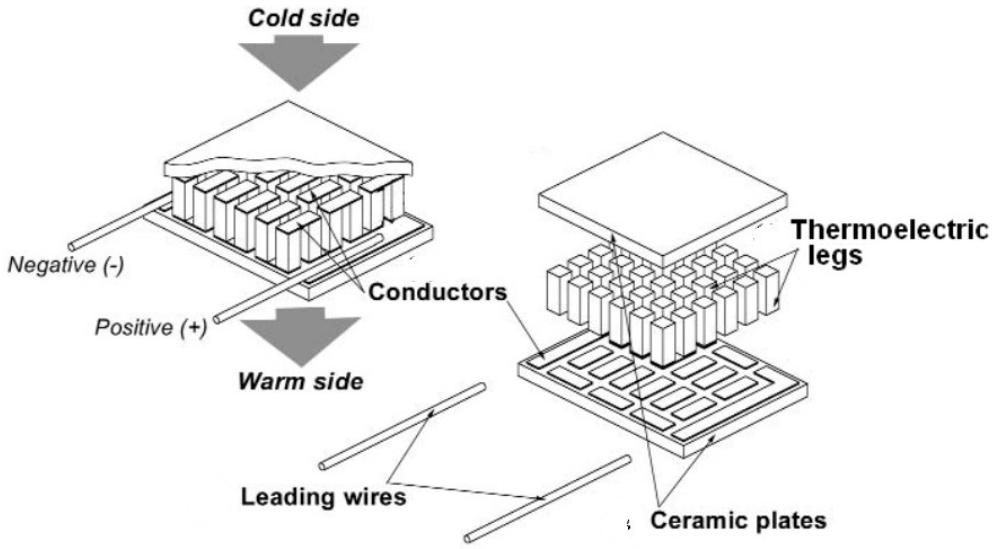

Figure 1.2 Constituents of a TE device [1].

As a consequence of this wide range of applications, and also due to the lack of moving parts nor working fluids, large range of operating temperatures, acoustically silent and its scalability, TE technology has been used in a wide variety of fields such as remote control and monitoring [2–7], aerospace [8,9], instrumentation [10–14], medicine [15,16], industrial [17–21] or vehicles [5,22–25].

By applying a power source of direct current (DC) to a TE couple, heat will be moved through the pair from one side to the other. Operation is shown in Figure 1.3. Therefore, one face will be cooled while simultaneously the opposite one will be heated. This phenomenon may be reversed by means of a change in the polarity (positive and negative) of the applied DC voltage. Consequently, TE couples may be used for both heating and cooling (TEC), thereby making it highly suitable for precise temperature control applications.

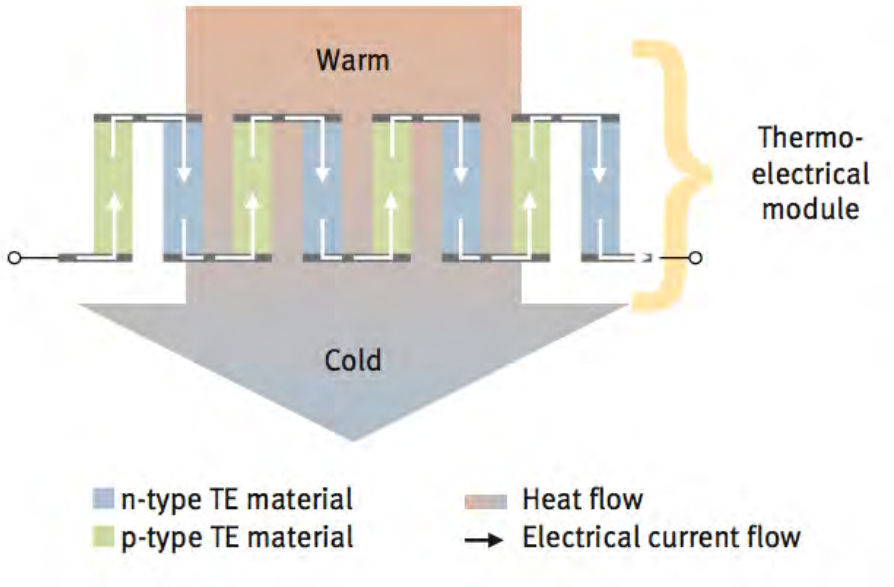

Figure 1.3 Design and operation of a TE device [26].

Thus, a TE device is an equipment capable to control the heat flux that passes through itself just by means of the applied voltage. This point of view suggested to the author of this thesis a new field of TE device-based applications, which puts forward as a different area from the traditional ones; treating them as controllable insulators.

Otherwise, when TE couples are subjected to a temperature difference, a flow of majority carriers inside the material occurs from the hot side to the cold one, resulting in a net generation of electrical current. This is the working mode configuration of a thermoelectric generator (TEG), as Figure 1.4 shows. When an electric load is applied across this circuit, useful amounts of power can be generated in response to the temperature difference applied.

This electric generation capability in addition to the global policies for reducing greenhouse gases emitted through the combustion of fossil fuels explain the enormous interest of this technology for waste heat recovery applications.

This thesis proposes advances in two different areas. The first one is a novel approach to the use of TE materials, considering them as controllable insulators in thermal systems. The second one focuses on the energy harvesting field applied to the automotive sector, giving new visions for fuel economy improvements and design recommendations.

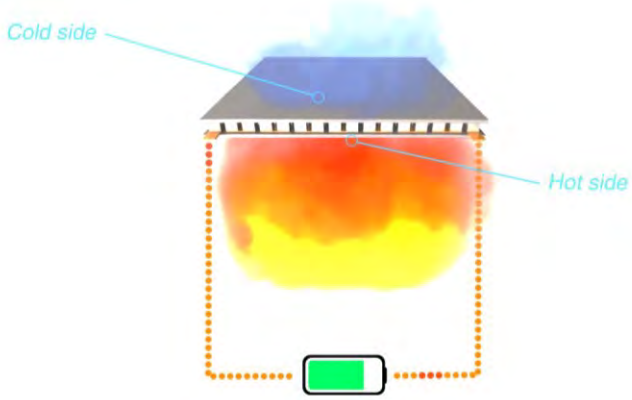

Figure 1.4 TE device working in generation mode.

1.2 Tunable thermal conductivity

Heat flow control promises major technological developments in thermal management. While materials with high and low thermal conductivities are available, materials with variable and reversible thermal conductivities are rare. The ability to accurately control the thermal conductivity of a material is fundamental in the development of on-chip heat management or energy conversion applications, and could be an important advance for the building sector.

Therefore, the purpose of this study is to conduct an exhaustive analysis of the behavior of the thermal conductivity of TE materials. We propose two configurations in order to control the thermal conductivity in TE materials. By considering that TE couples can work as thermoelectric coolers (TECs) or as thermoelectric generators (TEGs) two control modes can be established regarding the external control parameter (either active or passive control). Results demonstrate the capability of TEMs to act as an externally controlled insulator.

1.3 Exhaust energy recovery

The EU is leading the way in sustainable emissions' reductions [27]. Collectively the member states decided in 2008 to cut greenhouse gas emissions to at least 20% below 1990 levels by 2020. In doing so, targets have been set to meet 20% of the EU's energy needs from renewable sources and to move towards 20% energy efficiency improvement. Specifically, the EU car market regulations [28-29] include requirements for CO_2 emissions levels to be less than 95 gramsCO_2/km by 2020.

Internal combustion engines (ICE) are extensively used in our daily lives (either gasoline or diesel engines). Two-thirds of the thermal energy of combustion in vehicles is lost as waste heat, with 40% in the form of exhaust gases [23,30–36]. Only about 25% of the fuel energy is effectively used for vehicles operation. Therefore, recovery of a significant portion of the wasted energy in ICE by converting it into electricity would be highly advantageous [35,37–39]. An automotive thermoelectric generator (ATEG) is able to directly convert this waste heat into electrical energy. This electricity can be sent back to an auxiliary battery or a hybrid battery pack [40]. Hence, the alternator can be either reduced or even removed, which is expected to increase the efficiency of the vehicle and to improves the fuel economy from 8% to 19% [41]. This fuel consumption reduction would allow meeting the next car market regulations.

A significant number of studies, in cooperation with several automotive manufacturers, have been performed to improve vehicle performance by using ATEGs. Studies carried out focused on exhaust manifold, exhaust piping and catalytic converter packaging design for automotive tailpipe based on heat transfer analysis of the exhaust system.

One of the earliest studies on ATEGs exhaust heat recovery was constructed in 1963 by [42]. The original objective was to produce 500 W. However, the maximum output power obtained was 156.6 W with an efficiency of 2.20 % under their operating conditions. In 1988, Porsche [43] developed a prototype for testing a TE generator (TEG) by using the exhaust gas and water circulation

system of a vehicle. The TE material used was $FeSi_2$ and obtained an output power about 58 Watts when using 90 thermoelements. The authors suggested that the use of other materials with a higher dimensionless figure of merit could improve the power output. In 1994, Hi-Z technology [44-45] conducted several tests on an ATEG using eight diesel truck engines with a maximum output power of 1050 W at full power (300 hp). Ikoma et al. [24] developed an advanced ATEG that used TEMs based on SiGe material that generated 35.6 W. These authors claimed that the improvement on both heat transfer and TE materials are required to increase the overall performance of this technology. In 2002, Matsubara [46] developed a high efficiency thermoelectric generator that was assembled into a gasoline engine. He concluded that average *ZT*-values of 1.5 to 2 were needed to attain the goal of 10% overall efficiency. Researchers in Clarkson University [1] conducted a testing on a prototype of an automobile exhaust ATEG. The prototype was installed in a 1999 GMC Sierra pick-up truck. They concluded that the improvement in fuel efficiency was on the order of 1-2 %, depending on speed. In 2009 [47], researchers at BMW Company developed an ATEG prototype based on Bi_2Te_3 material. The vehicle involved was a BMW 530i. As a result, around 200 W of electrical power were achieved using 24 modules at 130 km/h. Finally, BMW claimed that the future enhancement of ATEG depended on how well the TE material could be improved. Kim et al. [48] fabricated an ATEG that employed the engine water coolant of passenger vehicles. Their experimental results revealed that the maximum electrical power was approximately 75 W in driving mode at constant 80 km/h.

The evolution of classical ATEGs to cylindrical shapes was studied by [49-50] in search for a high-power density device. Six-cylinder engines were used. The bench test was conducted using a Ford Lincoln and a BMW, and reported a maximum output electrical power of 125 W. The fuel improvement was predicted to range from 1% to 7%. In 2014, X. Liu et al. [51] constructed an ATEG and tested on road. The maximum output power was 600 W at an average temperature difference of 182°C while the system efficiency was 1.25%. Zhang et al. [52] developed a nanostructure bulk material to increase module performance. The fabricated module had a high-power density of 5.26 W/cm^2

with a 500 °C temperature difference. An ATEG system was built and tested using an automotive diesel engine. The system generated 1002.6 W of electrical power at an average temperature of 550 °C and mass flow rate of 480 g/s. In 2016, Kim et al. [53] investigated experimentally an ATEG for waste heat recovery. The maximum output power was about 119 W at 2000 RPM engine speed and 0.6 MPa. Other studies [54–56] also presented ATEG designs that were tested under steady state conditions.

However, all these investigations were only carried out under steady state engine conditions. It has been demonstrated that an ATEG designed only for steady states does not work properly for transient states, those that ATEG would face in a real driving situation. During real driving, exhaust temperature and gas flow rate substantially vary depending on engine operating conditions. This variability of energy flows, along with the thermal inertia of the ATEG, severely affects the power production [37,57–60]. Only [61–63] presented the transient behavior of ATEG designs although none of them gave any design recommendations of these devices.

1.4 Objectives

As it is said in Section 1.1, this thesis provides insight into two areas in the thermoelectricity field: heat flow control and energy harvesting.

The first objective of this thesis is to analyze the influence of the load resistance on the TE conductivity, and to investigate the possibility of using TE to obtain a controllable insulator. To do so, an exhaustive analysis of the thermal conductivity behavior in thermoelectric materials is conducted in order to discover the possibility of controlling the heat flow. Considering that TE couples can work as a thermoelectric cooler (TEC) or as a thermoelectric generator (TEG), two control modes can be established regarding the type of control of the external parameter: (i) active and (ii) passive.

The second goal is to develop an ATEG that should be capable of withstanding high exhaust gas temperatures and providing sufficient energy to reduce the

fuel consumption of the vehicle. The ATEG is tested using a gasoline engine under both steady-state and transient driving cycles, and data obtained are analyzed to address two main objectives: (i) to present a method to help ATEG designers predict the expected fuel economy, (ii) and to provide design recommendations in order to optimize the ATEG power generation during transient conditions.

1.5 Thesis organization

Backgrounds, objectives and organization of this thesis are included in chapter 1. Then, as this thesis has been prepared as a compendium of peer-reviewed journal publications, Chapters 2, 3 and 4 contains a transcription of the following published (i and iii) and submitted (ii) papers:

(i) "Electrically tunable thermal conductivity in thermoelectric materials: Active and passive control.".

(ii) "A method to assess the fuel economy of automotive thermoelectric generators";

(iii) "Transient behavior under a normalized driving cycle of an automotive thermoelectric generator".

All of them follow a single thematic unit related to the study of the field of thermoelectricity. The approach of this field is done from an applied point of view, trying not only to understand the phenomenon in depth, but to optimize it in each of its final applications. This thesis introduces itself into two branches of this field, such as the control of the heat flow and the recovery of energy in the automotive industry.

This first field, unpublished, represents a new area of study and it was conceived as a result of the experiments and simulations carried out in the field of heat recovery in this thesis. In them, it was seen that the load considerably affected the heat flow and reduced the expected energy recovered, so before studying more thoroughly the energy harvesting, it was necessary to study closely this phenomenon. This work resulted in article (i).

The second field deepens in the automotive waste heat recovery. Using the knowledge of previous studies, an ATEG was constructed and tested in a combustion engine. These tests allowed us to analyze the behavior of the ATEG both in transient and steady-state regimes. The first of them allowed to propose some new improvements, published in (iii), such as the introduction of a temperature control and the use of low temperature thermoelectric modules. The steady-state tests allowed to propose a numerical methodology, article (ii), to help in the designing of ATEGs. This methodology allows for predicting fuel savings without the need of building the equipment and conducting expensive tests.

Finally, results and discussions, and conclusions of this study are stated in Chapters 5 and 6.

Chapter 2

Electrically tunable thermal conductivity in thermoelectric materials: Active and passive control

This section is a transcription of the contents of the following paper (a copy of the published version can be found in Appendix A):

A Massaguer, E Massaguer, T Pujol, M Comamala, L Montoro, JR González. Electrically tunable thermal conductivity in thermoelectric materials: Active and passive control. *Applied Energy*, 154, 709-717, 2015. ISSN 0306-2619 (Impact factor 5,746; Journal 10 of 88; 1st quartile; Energy and Fuels)

http://dx.doi.org/10.1016/j.apenergy.2015.05.067

Abstract

Applications involving the use of thermoelectric materials can be found in many different areas ranging from thermocouple sensors, portable coolers, to solar power generators. Generally, they can be subdivided by the direction of energy conversion. While the Peltier effect is used in solid-state refrigeration, the Seebeck effect is responsible for the conversion of temperature gradients into electrical voltage in energy harvesting systems. However, this paper proposes a novel approach to the use of thermoelectric couples, treating them as variable insulators in thermal systems. Here, we demonstrate that thermal conductivity in thermoelectric materials can be externally controlled by electrical parameters such as electrical load or DC voltage in passive and active systems, respectively. Active mode is a good solution when a complete insulation or a high control of thermal conductivity is needed. Passive mode permits a thermal conductivity increment of $1 + ZT$ times with respect to semiconductor initial thermal conductivity. Results open new doors and new opportunities for thermoelectric materials.

2.1 Introduction

Thermoelectric (TE) modules are solid-state systems consisting of a number of alternate *p*- and *n*- type semiconductor thermoelements, which are connected electrically in series by metal interconnects and sandwiched between two electrically insulating and thermally conducting ceramic substrates. TE systems follow the laws of thermodynamics in the same manner as mechanical heat pumps, vapor compressors associated with conventional refrigerators, or other apparatus used to transfer energy [2]. They can act as coolers, heaters, power generators or thermal energy sensors depending on the direction of current. Due to the lack of moving parts or working fluids, TE technology has been used practically in almost all fields such as aerospace [8,9], instrumentation [10–14], medicine [15,16], industrial [17–21] or vehicles [5,22–25]. According to the working modes, these applications can be classified into three categories, which are coolers and heaters, power generators or thermal energy sensors.

By applying a voltage DC power source to a TE couple, heat will be moved through the pair from one side to the other. One face, therefore, will be cooled while the opposite face simultaneously is heated. This phenomenon may be reversed whereby a change in the polarity (positive and negative) of the applied DC voltage will cause heat to be moved in the opposite direction. Consequently, TE couples may be used for both heating and cooling thereby making it highly suitable for precise temperature control applications.

Otherwise, when TE couples are subjected to a temperature gradient, flow of majority carriers inside the material occurs from the hot to the cold side resulting in net generation of current. When an electric load is applied across this circuit, useful amounts of power can be generated in response to the temperature gradient applied. It is interesting to note the effect of heat transfer through TE couple with the applied load resistance; when electric load is the lowest the heat transfer is the highest due to the higher contribution of Joule and Peltier effect [64], and vice versa.

Taking into account these behaviors, it cannot be considered just the Fourier heat transport but also the Peltier, Thomson and Joule heat effects. These additional effects can be significantly greater or even opposite to Fourier's law and can be modified by the quantity and direction of current flow. Due to the capability of TE couples to tune the heat transfer flowing through them, another category can be added to the aforementioned applications list; externally controlled insulators.

Exploring the phenomenon at the nanoscale, transport can deviate strongly from the predictions of diffusion theory in macro and microscales [65,66]. With device or structure characteristic length scales becoming comparable to the mean free path and wavelength of heat carriers, classical laws are no longer valid and size effects become important [67–69]. Macroscopic heat conduction assumes that heat propagates at infinite speed, and it does not differentiate between the cause and effect relationship between heat flux and a temperature gradient.

In quantum mechanics, thermal conductivity k depends on the ability of sub-continuum energy carriers, which in solids are electrons and phonons, to travel to exchange this energy. k has contributions from both electrons and hole conductions k_e, and phonons k_{ph}, $k = k_e + k_{ph}$.

The ability to transfer heat by conduction is related to the capability of the electrons and phonons to travel and store/release thermal energy before losing it. When electrons are thermally excited, the mean free path increases, leading to a faster transmission of energy to cooler regions and a greater electronic thermal conductivity k_e. However, in semiconductors, k_e is generally smaller than in metals because there are few electrons available for conduction and they are continually interacting with the ionic lattice [70]. This interaction, due to the temperature gradient, causes energy to flow through the atomic lattice in the form of thermally generated lattice waves or phonons with a net energy flow from the hotter to the colder region. Then, primary heat carriers in

semiconductors are phonons, making the lattice thermal conductivity k_{ph} the main contributor to the thermal conductivity.

Heat flow control promises major technological developments in thermal management (e.g. transistors that control charge flow in electronics). Solid-state thermal switches and diodes [71] are particularly desirable for room-temperature cooling systems [72] or efficient building envelopes [73]. While materials with high and low thermal conductivities are available, materials with variable and reversible thermal conductivities are rare. The ability to precisely control the thermal conductivity of a material is fundamental in the development of on-chip heat management or energy conversion applications.

Thereafter, the purpose of this paper is to conduct an exhaustive analysis of thermal conductivity behavior in thermoelectric materials. We propose two configurations to obtain variable thermal conductivity in thermoelectric materials. Considering that TE couples can work as thermoelectric cooler (TEC) or as thermoelectric generator (TEG), two control modes can be established regarding the external parameter control: active and passive control. Results demonstrate the capability of thermoelectric modules (TEMs) to act as an externally controlled insulator.

As can be seen from Figure 2.1a and Figure 2.1c, active control occurs when the TE couple works as a thermoelectric heat pump hence heat transfer through it is controlled by input voltage magnitude and polarity [74]. The variation of heat flow is achieved by changing the electric current supplied to the thermoelectric module so an external power source is required [75].

Moreover, as can be shown from Figure 2.1b and Figure 2.1d, passive control occurs when the TE couple works as a generator hence load resistance controls heat transfer through itself [76]. Electrical power generated due to the Seebeck effect is fed back to the thermoelectric material via an electrical resistor to produce a self-powered Peltier effect so no external energy is required. This will result in an increase of heat flow through the thermoelectric material and consequently a decrease in temperature difference across it. The level of change

in heat flow or temperature difference can be controlled by the magnitude of the electrical resistance R_L. Geometrical values related to pellet surface S_{pn} and thickness th_{pn} are 2.3mm^2 and 2.54mm, respectively. Additionally, QTEC and QTEG represent the mean value of heat transfer across TEM.

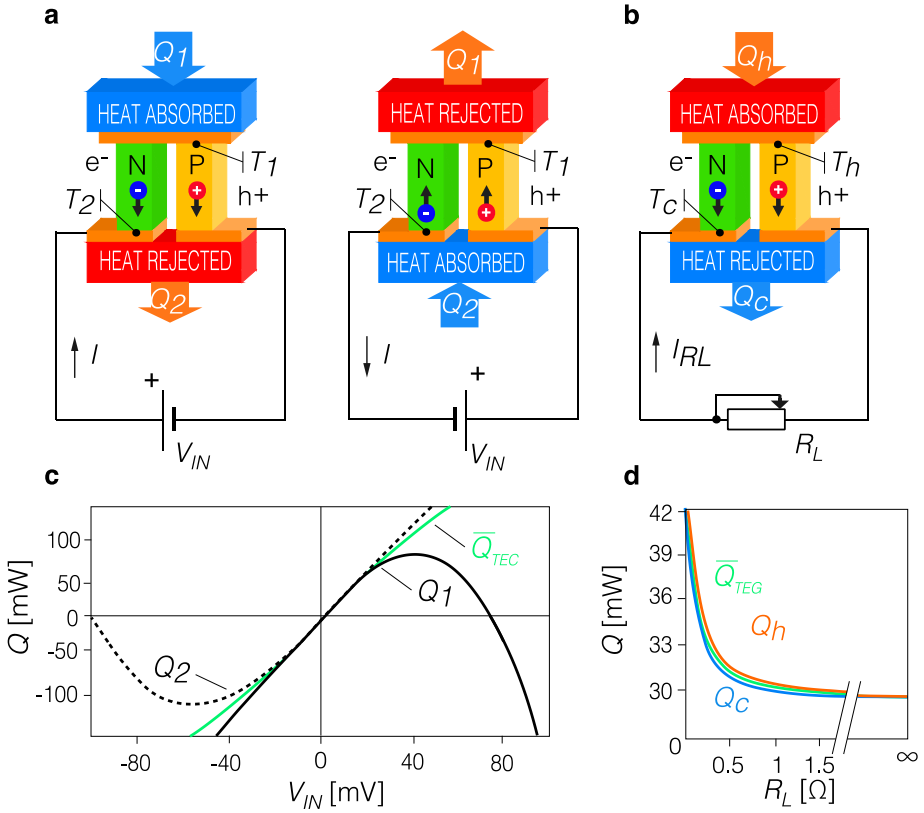

Figure 2.1 Proposed thermal conductivity control modes. (a) Schematic of the active control. (b) Schematic of the passive control. (c) Heat transfer of the active control when $T_1 = 20$ºC, $T_2 = 30$ºC. (d) Heat transfer of the passive control when $T_h = 150$ºC, $T_c = 125$ºC.

2.2 Methods

To carry out the following study, we have used various theoretical models [64,77–79] that allow us to simulate the electro-thermal behavior of a real TEM, working as a TEG or TEC. These models are based on the Equation (2.1), which can be used with the first law of thermodynamics, and determines the temperature distribution in a thermoelectric material [80]

$$\rho C_{pr}\frac{dT}{dt}=\frac{d}{dx}\left(k\frac{dT}{dx}\right)-\left(T\frac{d\alpha}{dT}\right)J_e\frac{dT}{dx}+\frac{J_e^2}{\sigma} \tag{2.1}$$

where ρ, C_{pr}, T, k, α, J_e and σ are the density, specific heat capacity at constant pressure, absolute temperature, thermal conductivity, Seebeck coefficient, coupled charge current flux and electrical conductivity, respectively.

However, due to the fact that nodal temperatures cannot be determined analytically without knowing the heat flux due to the thermoelectric effects, the models solve these nonlinearities using finite differences and Newton–Raphson methods, which calculate the temperature at different nodes separated in space by a discrete distance. In the transient state, the temperatures of these points are calculated at discrete periods of time and the temperatures for all the nodes are recalculated at the end of this time interval. Using the implicit finite difference method, the values of heat flux can be determined using the values of the temperatures of the time step before. The aforementioned models have been validated with experimental data at the same ranging temperatures used in this study. Simulations are carried out on a single thermoelectric pair. Figure 2.2 and Figure 2.3 show the heat transfer scheme of a TEG and a TEC, respectively, and model parameters can be checked at [25,77].

Equation (2.1) contains an extra term $\left(T\frac{d\alpha}{dT}\right)J_e\frac{dT}{dx}$ compared to the ordinary heat conduction equation. This is due to the Thomson effect, which suggests that distributed heating or cooling can occur even in the same solid because of the temperature dependence of Seebeck coefficient. However, as a result of that this study is focused on low-temperature system, the Thomson effect can be neglected [64].

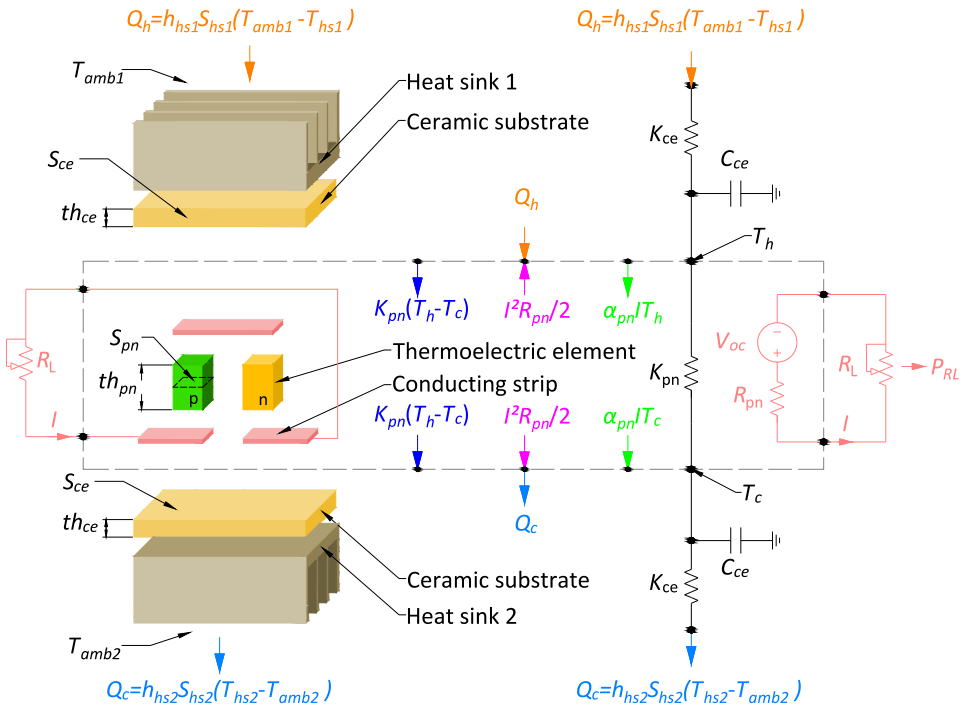

Figure 2.2 TEG model scheme. Scheme of the heat transfer through a TE couple, which is controlled by an external resistance R_L.

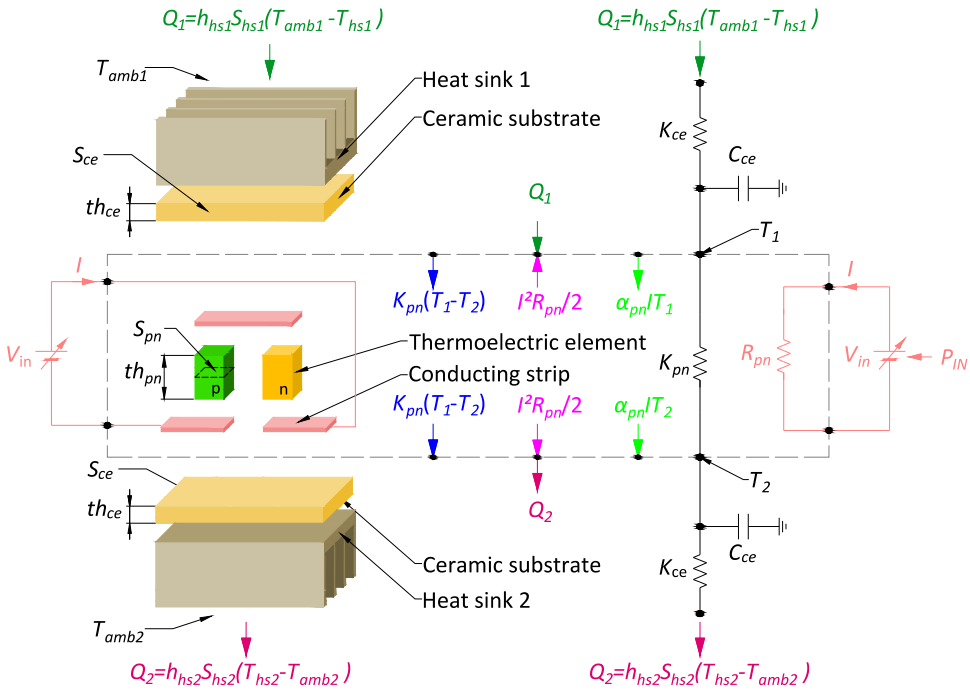

Figure 2.3 TEC model scheme. Scheme of the heat transfer through TE couple, which is controlled by external voltage V_{IN} magnitude and polarity.

Apart from this simplification, we made other common assumptions: (i) thermal conductivity, electrical resistivity, and specific heat capacity of non-thermoelectric materials are supposed constant within the operating temperature range, (ii) adiabatic boundary conditions are supposed on the outside surfaces of TE element, (iii) the heat leakage through solder layer and conducting strips are neglected and, finally, (iv) heat losses due to radiation and transverse convection through remaining area and lateral walls are also neglected.

On the other hand, temperature-dependent parameters of TEMs are considered in order to improve the accuracy of the models. The values of Seebeck coefficient α, electrical resistivity γ, and thermal conductivity k can be expressed mathematically by polynomial equations. These equations, which can be shown in Table 2.1, have been attached to the heat transfer ones. All coefficients are extracted from manufacturer's datasheet and can be calculated as a function of average temperature between hot and cold side of each TEM, $T = (T_1 + T_2)/2$. The rest of parameters used in the simulations are listed in Table 2.2.

Table 2.1 Thermoelectric parameters. In this table, each parameter is given as $a + bT + cT^2 + dT^3 + eT^4$, where a, b, c, d and e constants are tabulated.

	Parameter	***a***	***b***	***c***	***d***	***e***	***Units***
α_n	*n-type Seebeck coefficient*	-394.05	3.08	-1.26x10^{-2}	2.07x10^{-5}	-1.15x10^{-8}	μV/K
α_p	*p-type Seebeck coefficient*	143.29	-1.62	9.91x10^{-3}	-1.81x10^{-5}	1.01x10^{-8}	μV/K
k_n	*n-type thermal conductivity*	14.2	-0.10	3.14x10^{-4}	-4.23x10^{-7}	2.15x10^{-10}	W/mK
k_p	*p-type thermal conductivity*	-65.8	0.64	2.20x10^{-3}	3.26x10^{-6}	-1.74x10^{-9}	W/mK
γ_n	*n-type electrical resistivity*	-1.01x10^{-5}	5.63x10^{-8}	-9.78x10^{-11}	2.88x10^{-13}	-1.65x10^{-16}	Ωm
γ_p	*p-type electrical resistivity*	-6.26x10^{-5}	4.40x10^{-7}	-9.68x10^{-10}	1.12x10^{-12}	-5.40x10^{-16}	Ωm

Values taken from manufacturers specifications.

The root mean square errors (RMSE) for heat extracted, electrical power generated and temperature difference between inlet and outlet are 0.566 W, 3.9×10^{-3} W and 7.4×10^{-3} °C, respectively. Additionally, the normalized root mean square errors (NRMSE) are 0.67%, 0.5% and 0.894%, respectively.

Table 2.2 Simulation parameters.

Parameter		Value	Units	Source
th_n	n-type thickness	2.54×10^{-3}	m	[a]
th_p	p-type thickness	2.54×10^{-3}	m	[a]
S_n	n-type surface	2.3×10^{-6}	m^2	[a]
S_p	p-type surface	2.3×10^{-6}	m^2	[a]
ρ_n	n-type density	7700	kg/m^3	[b]
ρ_p	p-type density	7700	kg/m^3	[a]
C_n	n-type specific heat	200	J/kgK	[a]
C_p	p-type specific heat	200	J/kgK	[a]
S_{hs1}	Heat sink 1 surface	4.6×10^{-6}	m^2	[a]
S_{hs2}	Heat sink 2 surface	4.6×10^{-6}	m^2	[a]
h_{hs1}	Convection coefficient hs1	2000	W/m^2K	[b]
h_{hs2}	Convection coefficient hs2	2000	W/m^2K	[b]
th_{ce}	Ceramic substrate thickness	5×10^{-4}	m	[a]
S_{ce}	Ceramic substrate surface	4.6×10^{-6}	m^2	[a]
k_{ce}	Ceramic substrate thermal conductivity	36	W/mK	[a]
ρ_{ce}	Ceramic substrate density	3975	kg/m^3	[a]
C_{ce}	Ceramic substrate specific heat	765	J/kgK	[a]

[a] *Values taken from manufacturers specifications.* [b] *Calculated values.*

2.3 Active control

When a current I flows through a thermoelectric device, there is Peltier cooling at the source equal to $\alpha_{pn} I T_c$. This cooling effect is opposed by heat conduction at the rate $k_{pn} S_{pn} \Delta T / th_{pn}$. The cooling is also opposed to Joule heat within the thermoelements. It is easily shown that half of the Joule heating passes to the sink and half to the source, each half being equal to $I^2 R_{pn}/2$. The expressions for the heat transport in both sides of the TEM are the following.

$$Q_1 = \alpha_{pn} T_1 I - \frac{k_{pn} S_{pn}}{th_{pn}} \Delta T - \frac{1}{2} I^2 R_{pn} \tag{2.2}$$

$$Q_2 = \alpha_{pn} T_2 I - \frac{k_{pn} S_{pn}}{th_{pn}} \Delta T + \frac{1}{2} I^2 R_{pn} \tag{2.3}$$

where Q_1, Q_2, k_{pn}, α_{pn}, T_1, T_2, S_{pn}, th_{pn}, I and R_{pn} are heat transfers at sides 1 and 2, thermal conductivity, Seebeck coefficient, temperature at sides 1 and 2, total area, thickness, electrical current and internal resistance of the TE couple, respectively. ΔT is the temperature difference between side 1 and 2 $\Delta T = T_1 - T_2$.

Taking advantage of this effect, the heat transfer and consequently thermal conductivity in TECs can be controlled by adjusting the input voltage V. The analytical solution to the thermoelectric phenomena that governs the variation of thermal conductivity with V can be found applying the Fourier's law of conduction $k_{eff} = \bar{Q}_{TEC} th_{pn} / S_{pn} \Delta T$ to the entire system. Due to the fact that heat transfer is not equal on both sides of TEC, the equivalent heat transfer through TEC, $\bar{Q}_{TEC}$, is calculated as $\bar{Q}_{TEC} = (Q_1 + Q_2)/2$. Moreover, the current that flows through TE couple can be expressed as $I = (V - \alpha_{pn} \Delta T)/R_{pn}$. Finally, considering that TEC dimensions remain invariable during its operation, the function that describes the behavior of effective thermal conductivity k_{eff} can be written as:

$$k_{eff} = k_{pn}\left(\frac{ZTV}{\alpha_{pn}\Delta T} - ZT - 1\right) \tag{2.4}$$

where ZT is the figure-of-merit, expressed as $ZT = {\alpha_{pn}}^2 T/k_{pn}\rho_{pn}$ and $T = (T_h + T_c)/2$. Since changing the V polarity may reverse heat transfer direction, the electric current I values may be also positive or negative. However, when heat transfer is reversed, T_1 and T_2 also reverse hence k_{eff} always remains positive. Note that the evolution of k_{eff} does not depend on the geometric parameters.

In order to study the behavior of the Equation (2.4) as a function of external parameters, six temperature gradients $\Delta T_{amb} = T_{amb1} - T_{amb2}$ were established as boundary conditions for the dynamic simulation: -90ºC, -50ºC, -10ºC, 10ºC, 50ºC and 90ºC. A part from that, all simulations have been repeated at various input voltages to obtain the k_{eff} evolution. Input voltage ranges were selected in accordance with the maximum heat pumping capacity of both sides (i.e. A and D points) of the TEM at each ΔT_{amb}. The results of the simulation can be shown in Figure 2.4.

Four important points can be extracted from Figure 2.4:

- Point A corresponds to the maximum value of k_{eff} when heat transfer flows from 1 to 2 (A point). It is located where maximum cooling of Q_1 is achieved. From that point, $\bar{Q}_{TEC}$ and k_{eff} tend to decrease with voltage and the heat flow reverses again. A point can be obtained by deriving the Q_1 expression with respect input voltage $\frac{\partial Q_1}{\partial V} \rightarrow V = \alpha_{pn} T_2$. Including this equation into Equation (2.4) the maximum value of k_{eff} in cooling mode can be calculated as

$$k_{eff}^A = k_{pn}\left(\frac{ZTT_c}{\Delta T} - 1\right) \tag{2.5}$$

- The second point, B, corresponds to the minimum value of k_{eff}. That is the point where heat transfer becomes null and heat flow reverses, $k_{eff}^B = 0$ (i.e. where TEC becomes a perfect insulator). The heat flow

cancels when Seebeck effect $\alpha_{pn}\Delta T$ is counteracted by input voltage V. It is important to note that this point can be positive or negative depending on the stationary heat flow direction: while $T_1 < T_2$ the input voltage necessary to cancel heat flow is positive V^+, otherwise while $T_2 < T_1$ the voltage necessary is negative V^-.

$$V = \alpha_{pn}\Delta T\left(\frac{1}{ZT} + 1\right) \text{ when } k_{eff}^{B} = 0 \tag{2.6}$$

- Point C corresponds to the passive point where no voltage is applied, $V = 0$. It must be noted that when $V = 0$ the closed-circuit system is formed by a TE couple working as a TEG with its output short-circuited, $R_L = 0$. Consequently, k_{eff}^{C} can be expressed in the same way as equation (12) of the passive control. It is also interesting to note that k_{eff}^{C} is only temperature dependent, therefore, while $\overline{T}$ is maintained k_{eff}^{C} preserves, even when T_1 and T_2 are reversed.

$$k_{eff}^{C} = k_{pn}(1 + ZT) \tag{2.7}$$

- Finally, the point D corresponds to the maximum value of k_{eff} when heat transfer flows from side 2 to 1. That is when maximum cooling of Q_2 is achieved and it can be obtained by deriving the Q_2 expression with respect to input voltage $\frac{\partial Q_2}{\partial V} \rightarrow V = -\alpha_{pn}T_1$. From that point, the whole TEM tends to overheat as a consequence of the contribution of the electrical energy introduced to increase the Joule effect.

$$k_{eff}^{D} = k_{pn}\left(-\frac{ZTT_1}{\Delta T} - 1\right) \tag{2.8}$$

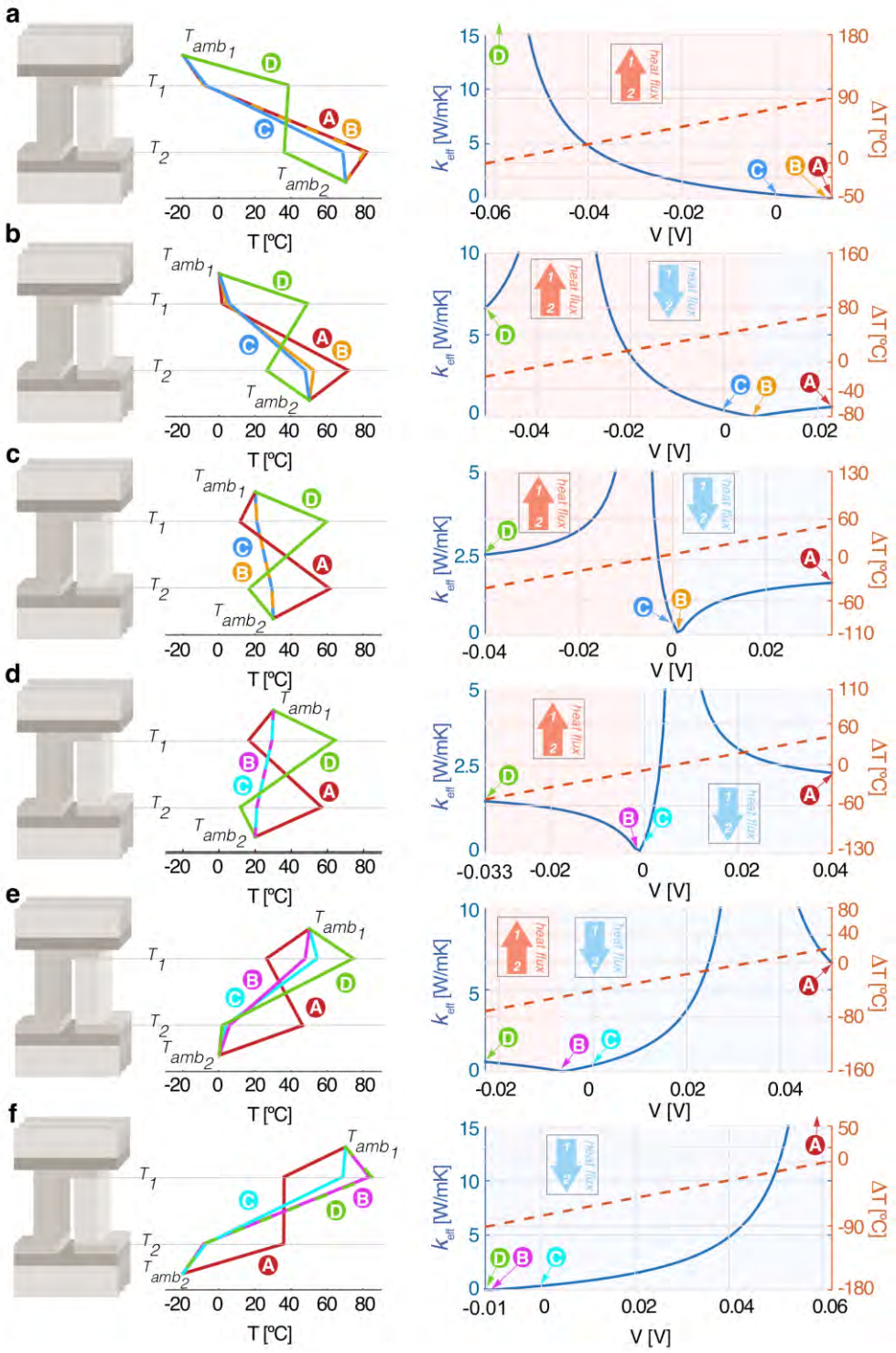

Figure 2.4 V dependence of k_{eff} under different thermal states. (a) k_{eff} as a function of V at $T_{amb1} = -20$°C and $T_{amb2} = 70$°C. (b) k_{eff} as a function of V at $T_{amb1} = 0$°C and $T_{amb2} = 50$°C. (c) k_{eff} as a function of V at $T_{amb1} = 20$°C and $T_{amb2} = 30$°C. (d) k_{eff} as a function of V at $T_{amb1} = 30$°C and $T_{amb2} = 20$°C. (e) k_{eff} as a function of V

at $T_{amb1} = 50$°C and $T_{amb2} = 0$°C. (f) k_{eff} as a function of V at $T_{amb1} = 70$°C and $T_{amb2} = -20$°C.

Figure 2.4 shows the behavior of Equation (2.4) under different temperatures and voltages. It can be observed that when temperature difference between faces is small, the heat transference can be easily controlled in terms of magnitude and direction. Therefore, the smaller the temperature differences between faces, the higher the control of k_{eff} (i.e. higher variation range) in both heat flow directions. As the temperature difference increase, k_{eff} can only be controlled when heat transfer flows in the same direction as it does the natural flow (i.e. the hottest ambient temperature to the coldest). This is on account of the thermocouple's limited heat pumping capacity, which, in this case, is exceeded when ΔT is higher than 90°C. Once heat-pumping capacity is surpassed, heat transfer cannot be reversed and B point cannot be achieved anymore. As ΔT_{amb} increase, k_{eff}^{A} and k_{eff}^{D} values tend to get closer to the $k_{eff} = 0$ value (i.e. B point). However, at the same time B point gets away from C point, hence major energy is required to maintain TEC working as a perfect insulator. Otherwise, the lower the ΔT_{amb} the lower the energy needed to do the same. It can also be shown that k_{eff} tends to infinite when $\Delta T = 0$ due to its situation on the Equation (2.4). The material properties used in the simulation are listed in Table 2.1 and Table 2.2.

2.4 Passive control

It is well known that thermoelectric materials produce electrical power from heat flow through a temperature gradient. As the heat flows from hot to cold, free charge carriers (electrons or holes) in the material are also driven to the cold end. By connecting an electron conducting (*n*-type) and hole conducting (*p*-type) material in series, a net voltage is produced that can be driven through a load. The resulting voltage V is proportional to the temperature difference ΔT via the Seebeck coefficient, α_{pn}, $V = \alpha_{pn}\Delta T$.

When electric load is the lowest, the heat transfer is the highest [64], and vice versa, because Peltier heat flows in the same direction as Fourier heat when TE couple is working as a generator. Consequently, high values of electric current I_{RL} will produce high contribution of Peltier and Joule terms of Equations (2.9) and (2.10). Contrarily, low values of I_{RL} will produce low Peltier and Joule effects causing a pure Fourier conduction.

$$Q_h = \frac{k_{pn}S_{pn}}{th_{pn}}\Delta T + \alpha_{pn}T_h I_{RL} - \frac{1}{2}{I_{RL}}^2 R_{pn} \tag{2.9}$$

$$Q_c = \frac{k_{pn}S_{pn}}{th_{pn}}\Delta T + \alpha_{pn}T_c I_{RL} + \frac{1}{2}{I_{RL}}^2 R_{pn} \tag{2.10}$$

where Q_h, Q_c, k_{pn}, α_{pn}, T_h, T_c, S_{pn}, th_{pn}, I_{RL} and R_{pn} are hot side heat transfer, cold side heat transfer, thermal conductivity, Seebeck coefficient, hot side temperature, cold side temperature, total area, thickness, electrical current and internal resistance of the TE couple, respectively.

Taking advantage of this effect, the heat transfer and consequently thermal conductivity in TEGs can be controlled by adjusting the load resistance. The analytical solution to the thermoelectric phenomena that governs the variation of thermal conductivity with load resistance R_L can be found applying the Fourier's law of conduction $k_{eff} = \bar{Q}_{TEG} th_{pn}/S_{pn}\Delta T$ to the entire system. Due to the fact that heat transfer is not equal on both sides of TEG, the equivalent heat transfer through TEG, $\bar{Q}_{TEG}$, is calculated as $\bar{Q}_{TEG} = (Q_h + Q_c)/2$. Moreover, considering that in a closed-circuit (i.e. when R_L is finite), the voltage generated across thermoelectric material due to the Seebeck effect will result in an electric current that circulates through the thermoelectric material and external resistor, the current I can be expressed as $I_{RL} = \alpha_{pn}\Delta T/(R_{pn} + R_L)$. Finally, taking into account that TEG dimensions remain invariable during its operation, the function that describes the behaviour of effective thermal conductivity k_{eff} with load resistance R_L can be written as:

$$k_{eff} = k_{pn} + \frac{{\alpha_{pn}}^2 \left(\frac{T_h + T_c}{2}\right) th_{pn}}{(R_{pn} + R_L) S_{pn}} \tag{2.11}$$

Note that in this case the k_{eff} evolution depends on the geometric parameters, th_{pn} and S_{pn}. It can be observed that Equation (2.11) has a maximum when $R_L = 0$ and a minimum when $R_L = \infty$.

$$k_{eff}^{R_L=0} = \lim_{R_L \to 0} \left[k_{pn} + \frac{{\alpha_{pn}}^2 \left(\frac{T_h + T_c}{2}\right) th_{pn}}{(R_{in} + R_L) S_{pn}} \right] = k_{pn}(1 + ZT) \tag{2.12}$$

$$k_{eff}^{R_L=\infty} = \lim_{R_L \to \infty} \left[k_{pn} + \frac{{\alpha_{pn}}^2 \left(\frac{T_h + T_c}{2}\right) th_{pn}}{(R_{in} + R_L) S_{pn}} \right] = k_{pn} \tag{2.13}$$

It can be observed that the absolute extent of variation of effective thermal conductivity in thermoelectric materials working as TEG is only dependent of its dimensionless figure-of-merit. Note that thermoelectric materials with higher values of ZT will permit higher variation ranges of k_{eff}. It must be remarked that a temperature gradient must exist between its faces in order to control this effect. However, it makes no sense to control it when temperatures on both sides are the same.

In order to validate these assumptions and analyze the effects of thermal, electrical and dimensional parameters of Equation (2.3), the simulations shown in Figure 2.2 have been carried out. The models used to simulate these behaviors are described in [64,79].

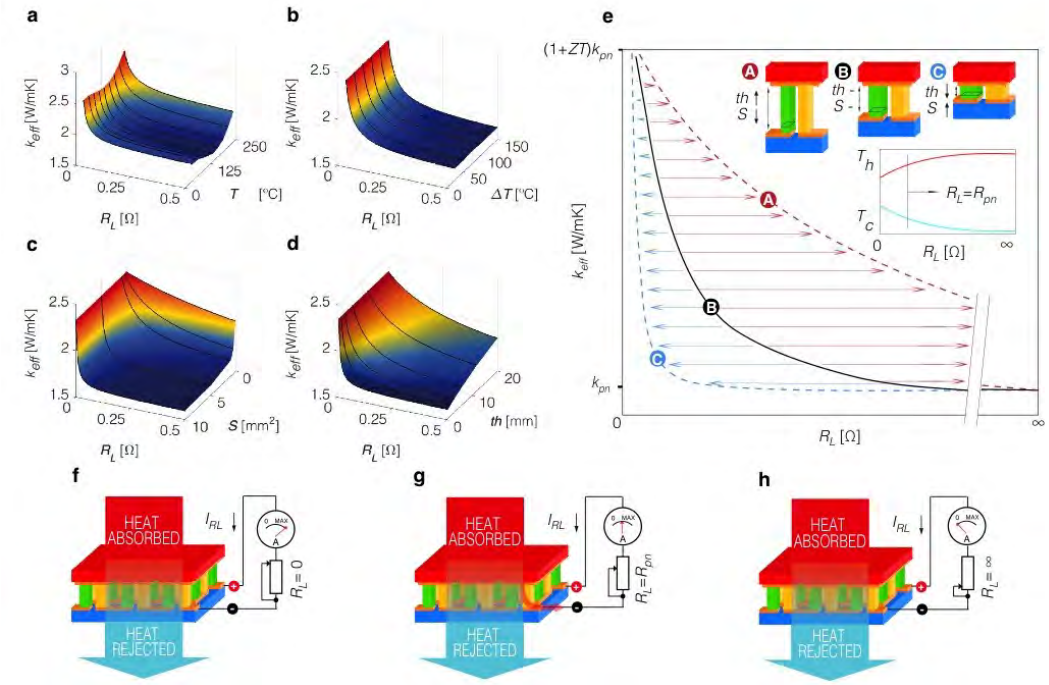

Figure 2.5 R_L dependence of k_{eff} under different thermal, electrical and dimensional states. (a) k_{eff} as a function of R_L at different average temperatures $T = (T_h + T_c)/2$. A constant $\Delta T = 25°C$ is considered. (b) R_L dependence of k_{eff} at different ΔT. A constant average temperature $T = 150°C$ is considered. (c) Pellet surface S_{pn} effects on R_L dependence of k_{eff}. (d) Pellet thickness th_{pn} effects on R_L dependence of k_{eff}. (e) A schematic diagram of th_{pn} and S_{pn} effects on the k_{eff} behaviour. The arrows show the direction and magnitude of the effect while T and ΔT are maintained. Also shown are the hot and cold side temperature evolutions with R_L. (f-h) Heat transfer profiles at different values of load resistance.

As can be shown from Figure 2.5a the highest values of Δk_{eff} are obtained when ZT values are also the highest. ZT presents a maximum point of 0.4692 when $T_h = 150°C$ and $T_c = 125°C$, hence maximum Δk_{eff} of 46.92% is obtained at this point ($k_{RL=0} = 2.33 W/mK$ and $k_{RL=\infty} = 1.58 W/mK$). These results corroborate the analytical hypothesis of Equation (2.11). Figure 2.5b demonstrates that ZT value preserved while T is maintained. However, the higher the ΔT the higher the power generated.

It is interesting to note that the evolution of the k_{eff} function can be tuned in order to easily achieve a highly precise control of it. Reducing the pellet area S_{pn},

Figure 2.5c, or increasing its thickness th_{pn}, Figure 2.5d, the curve stretches increasing the load resistance range. Otherwise, with a decrease of th_{pn} or an increase of S_{pn} the curve becomes steeper getting a high sensitivity thermal switch. Since the changes in ZT and Δk_{eff} are ascribed to T changes, they remain unchanged under dimensional changes. These behaviours are summarized and outlined in Figure 2.5e.

Finally, it can be observed that the variation range of k_{eff} is strongly dependent on ZT: the higher the ZT, the higher the thermal control. In this regard, looking for materials with high ZT is important in order to extend the use of TEMs as variable insulators. Recently, new promising alloys with enhanced figure of merit have been developed [81–86].

2.5 Conclusions

In summary, our theoretical analysis demonstrates that thermoelectric materials can be used as variable insulators for applications where the heat fluxes between two thermal bodies need to be altered conveniently. Two control modes can be established in order to control the effective thermal conductivity of the thermoelectric pair: active mode and passive mode.

Active mode, which can be controlled by external voltage, is a good solution when a complete insulation or a high control of thermal conductivity is needed. The smaller the temperature difference between faces the higher is the control of k_{eff} (i.e. higher values of k_{eff} can be obtained). However, as k_{eff} is strongly dependent of temperature gradient ΔT and ZT, thermocouple has a limited heat pumping capacity. For large values of ΔT the thermocouple is no capable to reverse the heat flux hence complete insulation is not achievable. The energy required to keep TEM working at this point increase with the ΔT. It is remarkable that the control of k_{eff} does not depend on the geometric parameters.

On the other hand, passive mode permits a k_{eff} increment of $1 + ZT$ times with respect to semiconductor thermal conductivity k_{pn}. In this mode, the extent of

k_{eff} variation is mainly dependent on the thermoelectric figure of merit ZT and on the pellet geometry. Unlike active mode, passive mode can be controlled by an external resistance, hence no external energy is required. However, the extent of k_{eff} variation is lower and a complete insulation cannot be attained.

Finally, it can be observed that in both cases, active and passive mode, the variation range of k_{eff} is strongly dependent on the figure of merit. Considering most common and commercial materials, such BiTe, the potential applications of TECs and TEGs are limited to material properties: the higher the zT, the higher the thermal control. In this regard, finding materials with high ZT is important in order to extend the use of TEMs as variable insulators.

The basic idea behind this tunable insulator is that certain instances it would be beneficial to selectively enable or impede heat flow within particular sections to selectively control heat flow. The application of this technology could be interesting for building sector, in spacecraft structures or in components of machinery. Instead of acting as a passive component, such as conventional building insulation, smart insulation is an adaptive component that can be selectively switched between low and high heat transfer states to take advantage of such instances where it would be beneficial to be able to turn off the insulation. Two example scenarios that would improve the energy efficiency in which little or no building insulation would be advantageous would be sunny winter days and cool summer evenings.

This study opens new doors and new opportunities for thermoelectric materials.

2.6 Acknowledgments

This work has been partially funded by the Generalitat de Catalunya under Grant No. 2014-SGR-36 and the MICINN-FEDER under Grants No. FIS-2012-31307. Authors would also like to thank Association of Industrial Engineers of Catalonia (AEIC) for they partial financial support.

Chapter 3

A method to assess the fuel economy of automotive thermoelectric generators

This section is a transcription of the contents of the following paper:

A Massaguer, E Massaguer, M Comamala, T. Pujol, JR González, MD Cárdenas, D Carbonell, AJ Bueno. A method to assess the fuel economy of automotive thermoelectric generators. Submitted to *Applied Energy*. ISSN 0306-2619 (Impact factor 7,182; Journal 6 of 92; 1st quartile; Energy and Fuels)

Abstract

For the widespread application of thermoelectric generators (TEG) it is of vital importance to have convenient simulation tools in order to test the behavioral consequences of a TEG device in almost real conditions. The simulation by numerical methods of the performance of automotive thermoelectric generators (ATEG) allows for time- and cost-saving assessment of material combinations and variations of crucial design parameters. However, even in the case of promising simulation results, it is complicated to guarantee the ATEG capacity for reducing the vehicle's fuel consumption. This work presents a method to assess the fuel economy of an ATEG design. The procedure is divided into two parts. The first one consists in predicting the ATEG performance by using a finite element model. This model is validated by comparing its output values with those obtained experimentally by an ATEG installed in the exhaust system of an internal combustion engine. The second part proposes a method, based on the results obtained in the FEM analysis, to estimate the expected fuel economy of the ATEG. Results show the consistency of the simulation tool, revealing an agreement of about 97% between simulation and experimental data. In addition, the method applied to the ATEG presented predicts a maximum fuel economy value of 0.18%.

3.1 Introduction

Thermoelectric (TE) devices are solid-state systems consisting of a number of

alternate *p*- and *n*- type semiconductor thermoelements, which are connected electrically in series by metal interconnectors and sandwiched between two electrically insulating and thermally conducting ceramic substrates. TE systems follow the laws of thermodynamics in the same manner as mechanical heat pumps, vapor compressors associated with conventional refrigerators, or other apparatus used to transfer energy [2]. Compared to the traditional power generation systems, thermoelectric generation (TEG) has its special characteristics such as simple structure, high reliability, operate without any noise or vibration and without waste generation [87–90]. Therefore, TEG is very suitable to be used in fields such as waste heat recovery or power generation for supplying electric energy to low or micro-power applications in electronic devices.

On the other hand, there are some obstacles to overcome in order to promote the use of TE technology, such as low thermoelectric conversion efficiency [91–93], low mechanical strength [94–97], need of efficient heat exchangers [22,98–101], current use of non-environmentally friendly materials [102], relatively high manufacturing cost [103–106], etc.

To deal with this sort of obstacles, the possibility of using numerical methods gains importance. The finite element/volume methods (FEM/FVM) have become essential solution techniques in many areas of engineering and physics. The FEM/FVM versatility lies in their abilities to model arbitrary shaped structures, to work with complex materials, and to apply various types of loading and boundary conditions. These methods can be easily adapted to different sets of constitutive equations, which make them particularly attractive for coupled physics simulations like that required in TEG. FEM/FVM programs help to predict the performance of TEG parameters and allow time- and cost-saving assessments of material combinations and variations of crucial design parameters.

Many researchers are focused on improving the physical properties of thermoelectric material and the manufacturing technique of thermoelectric

modules. However, the optimization of the thermal system design is equally important for improving the power generation of TEGs.

Recent works have yielded powerful numerical algorithms of one-dimensional models that identify TEG configurations with output power and thermal efficiency maximized for homogeneous, functionally graded and segmented thermoelectric materials. Hsiao et al. [30], Montecucco et al. [107,108], Rodríguez et al. [109], Massaguer et al. [64], Weng et al. [6] and Liang et al. [110] developed computational models to simulate the thermal and electrical behavior of thermoelectric generators. These models solved the system of nonlinear equations of thermoelectricity and heat transfer. Riffat and Ma [111] performed the geometry optimization of thermoelectric modules used as generators. Chen et al. [112] and Yu et al. [113,114] explored the influence of various design parameters on the system performance including the effect of having multiple layers of modules and the use of parallel-plate heat exchangers.

Other models [55,79,115], specifically developed for engine exhaust heat recovery, took into account the spatial-dependent heat flow rate that affected the power generation due to mismatch condition operations of thermoelectric modules. Zhang et al. [116] took also into account both heat and electricity losses at junctions as well as the space-dependent heat flow rate in the thermoelements.

Thus, there are several parameters involved in the mathematical model of a TEG. Many of them are difficult to determine, which often implies the acceptance of assumptions, leading to a lack of accuracy in the results. Generally, these models intend to propose thorough performance predictions as well as design recommendations. However, they show limited capabilities, or at least a low flexibility, for the implementation of additional effects such as geometry variations or non-uniform temperatures on the output power of the TEG system.

Otherwise, even though the simulation tools are capital in ATEG design aspects, it is also important to evaluate the ATEG performance in terms of vehicle's fuel

economy. There are many studies in this field that present a wide variety of advances in ATEG design, but only very few [117–121] of them address the problem from the fuel economy point of view.

The purpose of the current work is to present a method to assess the performance of an ATEG design. The procedure is divided into two main parts. The first one consists in predicting the ATEG performance by using a FEM/FVM-based methodology. The present study validates the theoretical FEM/FVM-based model comparing its output values with those obtained experimentally by an ATEG installed in the exhaust system of a gasoline engine. The goal is to determine the feasibility of the numerical model on predicting its performance. The second part proposes a method to, based on the results obtained in the FEM/FVM analyses, forecast the expected fuel economy when using the ATEG.

3.2 Experimental setup

3.2.1 System architecture

The ATEG presented in Figure 3.1 is designed for exhaust pipes of automobiles. The purpose of these kind of systems is to convert wasted energy into a useful one. In this case, wasted energy is turned into a source of electrical power, in order to feed many electrical parts of the vehicle, finally leading to savings in both fuel consumption and greenhouse gas emissions.

The working mode is based on the conversion of heat into electricity by using commercial thermoelectric modules (TEMs). These consists of an array of *n*- and *p*- type semiconductor pellets connected electrically in series and thermally in parallel between ceramic substrates.

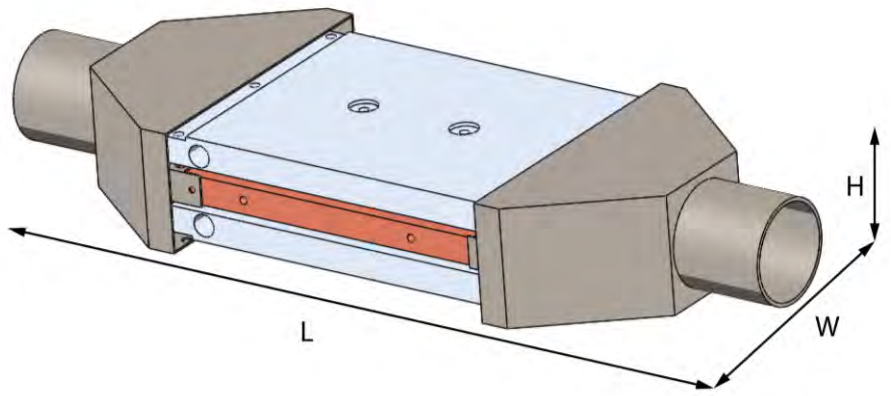

Figure 3.1 Waste heat recovery system prototype. Dimensions are 160x444x64 mm (WxLxH).

The objective of this ATEG is to get a high temperature gradient on both sides of the TEMs by using the energy contained in the exhaust fumes of a combustion engine. The gases flow internally through the device and transfer a portion of its heat through the TEMs to the cold plates. Then, the cooling circuit, that uses water as a coolant, takes the heat and dissipates it using a forced convection heat-exchanger. The more heat flows through the thermoelectric modules, the higher the power generated.

The size of the device is 160x444x64 mm (WxLxH) with a total weight of 7 kg. It is composed of 12 TEMs connected electrically in series but thermally in parallel. These modules are arranged on both surfaces of a copper heat exchanger (#2 in Figure 3.2), through which the exhaust gas flows, and two aluminum cold plates (#3 in Figure 3.2). ATEG is joined to the exhaust system using inlet and outlet parts (#1 in Figure 3.2) made of steel. Figure 3.2 shows the schematic diagram of the experimental ATEG.

The cooling system is composed of one pump and a forced-air heat exchanger. The pump drives the water through the cold plates (#3 in Figure 3.2) that are connected in parallel. The aluminum cold plates are heat exchangers with S-shaped flow paths within which the cooling fluid moves. Heat received from the ATEG is finally dissipated to the ambient air using a forced-air heat exchanger. In the present design, the room temperature in which the engine is installed is 20

°C. The cooling fluid used is water with a volumetric flow rate equal to 0.12 l/s measured at the exit of the volumetric pump.

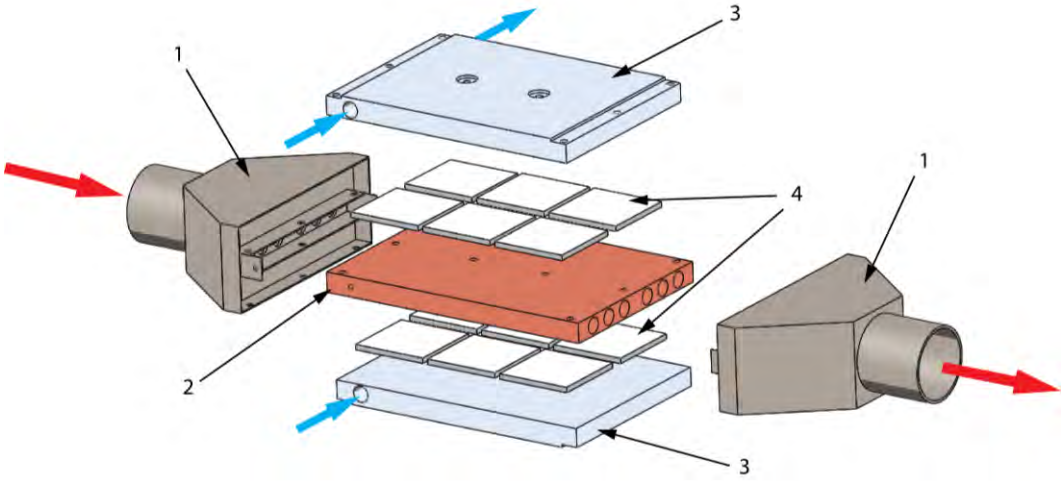

Figure 3.2 Exploded view of prototype. 1) Exhaust fumes inlet and outlet. 2) Heat exchanger. 3) Cold plates. 4) Thermoelectric modules. In red, exhaust gases. In blue, cooling system's water.

3.2.2 Series array configuration

All TEMs are interconnected forming an electrical array of twelve modules arranged in series. Figure 3.3 illustrates the series connection. Each TEM is represented by a voltage source $V_{1,\dots,12}$ and an internal resistance $R_{1,\dots,12}$.

Although there are several ways to interconnect TEMs, the way selected evaluates the model in a series configuration. Under ideal operating conditions, this configuration will make each TEM experience an equal temperature difference and consequently all TEMs will generate the same output voltage. In this case, the load resistance at the maximum power point would be $12R_1$ and the voltage $12V_1/2$ with R_1 the internal resistance of a TEM.

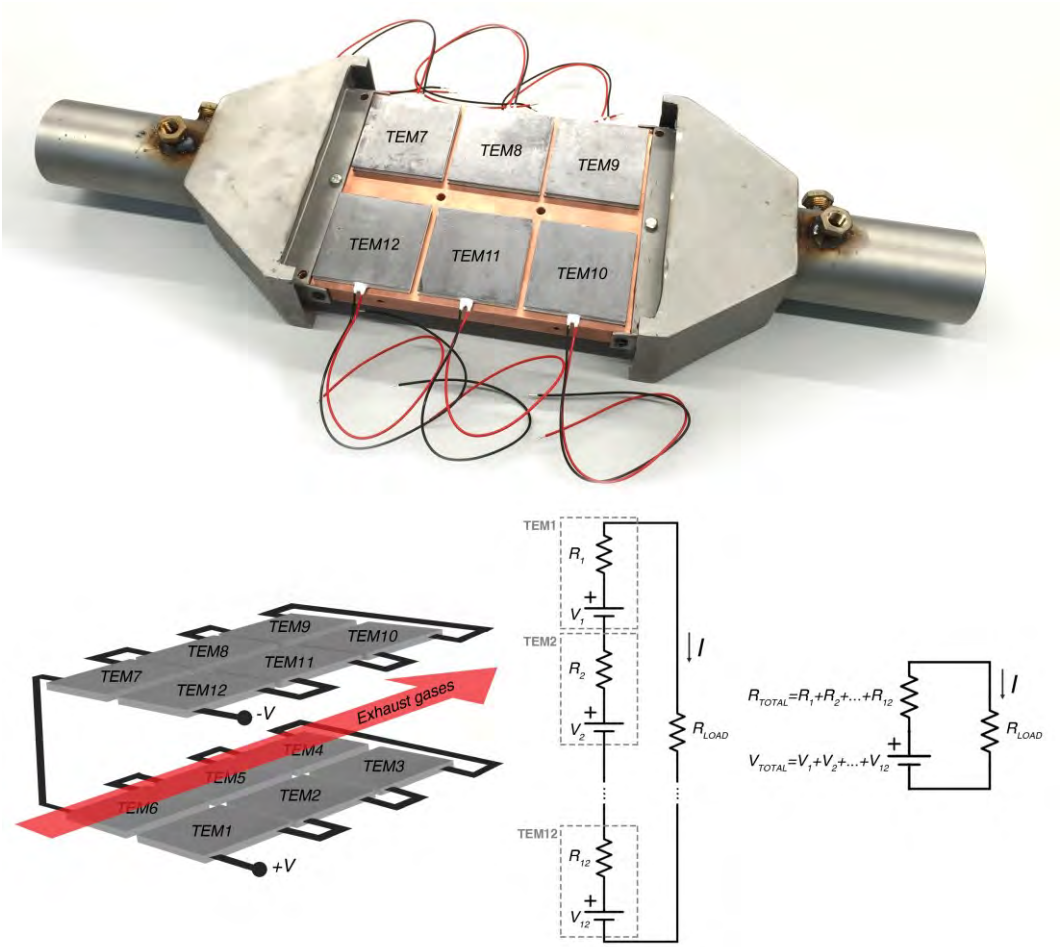

Figure 3.3 Electrical schematic of the array of TEMs electrically connected in series.

However, considering that TEMs are not connected thermally in parallel, this ideal operating condition is no longer valid in the present system. In a practical case, each TEM will experience a reduction of temperature difference along the direction of the exhaust gases. That is, TEMs #1, 6, 7 and 12 will experience the same temperature difference across their hot and cold faces $\Delta T_1 = \Delta T_6 = \Delta T_7 = \Delta T_{12}$, but, in comparison to TEMs #2, 5, 8 and 11, though with the same temperature difference $\Delta T_2 = \Delta T_5 = \Delta T_8 = \Delta T_{11}$, the latters will have a smaller value $\Delta T_1 = \Delta T_6 = \Delta T_7 = \Delta T_{12} > \Delta T_2 = \Delta T_5 = \Delta T_8 = \Delta T_{11}$. This is explained by the fact that exhaust gases temperature decreases along the exhaust pipe.

This situation creates an unbalanced system that leads to a complex condition with unequal voltages and internal resistances. Consequently, in order to obtain the maximum power point (MPP), a screening of different power points is carried

out by changing the external load resistance R_L of the electrical circuit performing a *VI* sweeping. Then, the MPP is located at the maximum of the power curve.

3.2.3 Experimental installation

To validate the ATEG model, experimental tests were performed on an engine test bench at the Repsol Technology Center. A 4-cylinder 4-stroke turbocharged, intercooled, gasoline direct injection engine, typical of those used in European cars, was employed as the experimental unit. Its specifications are listed in Table 3.1. The engine was coupled to an asynchronous machine model D2t MDA140, which also worked as starter during engine tests. The brake control system allowed measuring the engine speed, pedal accelerator position and effective torque. Additionally, a specific dyno controller set-up was adjusted in order to adapt its performance to dynamic test. The instantaneous gravimetric fuel consumption was determined using a Pierburg PLU 401/121 flow meter. In this study, the ATEG was installed downstream of the three-way catalyst (TWC).

Table 3.1 Main specifications of tested engine.

Parameter	**Value**
Maker	VW
Model	Golf 1.4 TSI ACT (engine family EA211)
Euro certification	Euro 6b
Max. rated power	103 kW (at 4500 – 6000 rpm)
Max. rated torque	250 Nm (at 1500 – 3500 rpm)
Cylinders	4, in line
Bore (mm)	74.5
Stroke (mm)	80
Swept volume (cm^3)	1395
Compression ratio	10:1
Tire diameter (m)	0.632
Axle ratio	3.65
Transmission ratio 1st	3.78:1
Transmission ratio 2nd	2.12:1
Transmission ratio 3rd	1.36:1
Transmission ratio 4th	1.03:1
Transmission ratio 5th	0.86:1
Transmission ratio 6th	0.73:1

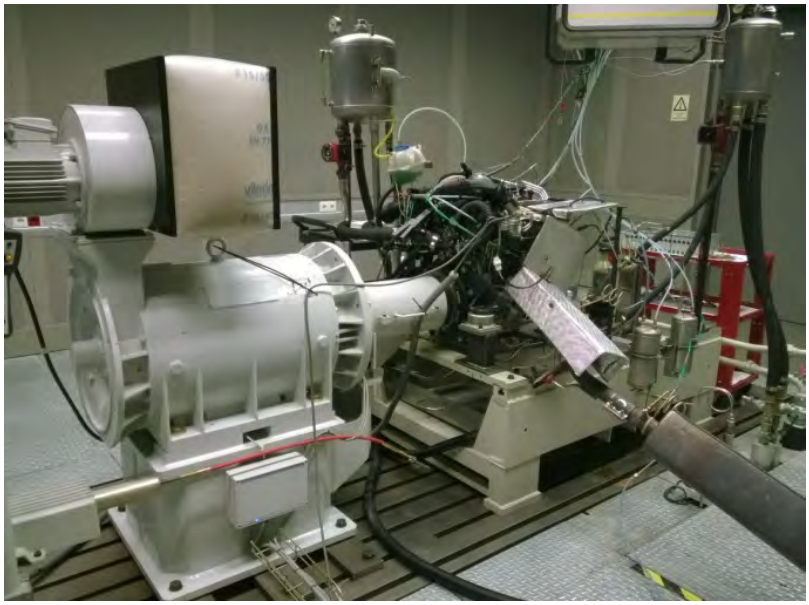

Figure 3.4 Engine test bench. Engine Lab (Repsol Technology Center).

In order to acquire the data from the system, a National Instruments Compact Rio (cRIO) unit was selected. Temperature, voltage and current modules were used. Other equipment such as flow meter and air flow bench were also used. The corresponding accuracy of each equipment is listed in Table 3.2.

Table 3.2 Equipment accuracy values.

Measurement	**Equipment**	**Accuracy**
Voltage V	cRIO with NI 9215	±0.20%
Current I	cRIO with NI 9227	±0.37%
Temperature	cRIO with NI 9217 (RTD)	±0.2ºC
	cRIO with NI 9211 (TC)	±1.5ºC
Water cooling flow meter	PCE-TDS 100H	±1%
Backpressure	Saenz air flowbench D-680	±5%
Mass flow rate	Saenz air flowbench D-680	±6%

3.2.4 Boundary conditions

The numerical model requires the definition of different boundary conditions in order to simulate the laboratory conditions. Table 3.3 shows laboratory data obtained at the test bench at different engine regimes from which some of the boundary conditions are defined in the simulations. The simulation of these thermal states is achieved by using the commercial multiphysics software ANSYS 17.1.

Table 3.3 Laboratory data obtained at different engine test modes.

Engine test modes (regimes)	***1***	***2***	***3***	***4***
Exhaust gases inlet temperature (°C)	407.9	569.4	690.8	709.3
Exhaust gases outlet temperature (°C)	264.9	415.0	557.1	569.9
Exhaust gases mass flow (g/s)	5.95	17.63	37.07	32.61
Coolant inlet temperature (°C)	38.4	48.5	65.7	74.7
Coolant outlet temperature (°C)	39.6	51.2	70.7	80.8
Coolant volumetric flow (l/s)	0.12	0.12	0.12	0.12
Hot side temperature (°C)	104.6	210.4	344.7	351.0
Cold side temperature (°C)	41.2	57.1	85.2	95.2
Electrical power generated (W)	5.52	37.68	111.27	106.76

Boundary conditions were taken in four different engine tests modes and they were collected under steady-state conditions. Regimes 1, 2, 3 and 4 correspond to an engine speed of 2000 rpm, 2000 rpm, 2000 rpm and 4000 rpm, and a full-throttle pedal position (FTPP) of 15%, 45%, 85% and 85%, respectively. FTPP, in percentage, represents the engine acceleration in terms of throttle pedal travel position.

The input temperature coming from the engine's exhaust gases and the coolant fluid vary in function of the engine regime. The coolant fluid used was water, and

its temperature variation at each mode was due to the higher heat flow passing through the device.

The cold side heat exchanger is modeled as a block of aluminum with an internal winding flow path. Heat is absorbed into the liquid and it is taken out of the plate. Heat is also removed to the ambient by natural convection. The convective heat transfer coefficient from aluminum to the ambient is set to 15 W/m^{2}K and the room temperature was 20°C.

3.3 Governing equations of thermoelectricity

The general heat flow and continuity equations of electric charge for the thermoelectric analysis can be expressed as Equations (3.1) and (3.2), respectively,

$$\rho C \frac{\partial T}{\partial t} + \nabla \boldsymbol{q} = \dot{q}\,, \tag{3.1}$$

$$\nabla\left(\boldsymbol{J} + \frac{\partial \boldsymbol{D}}{\partial t}\right) = 0\,, \tag{3.2}$$

where ρ, C, T, t, $\boldsymbol{q}$, $\dot{q}$, $\boldsymbol{J}$ and $\boldsymbol{D}$ are the density, specific heat capacity, absolute temperature, time, heat flux vector, heat generation rate per unit volume, electric current density vector and electric flux density vector, respectively.

Equations (3.1) and (3.2) are coupled by the set of thermoelectric constitutive equations and the constitutive equation for the dielectric medium. Considering this and the absence of time-varying magnetic fields, the coupled equations of thermoelectricity can be expressed as Equations (3.3) and (3.4),

$$\rho C \frac{\partial T}{\partial t} + \nabla([T\alpha]\boldsymbol{J}) - \nabla([\kappa]\nabla T) = \dot{q}, \tag{3.3}$$

$$\nabla\left([\varepsilon]\nabla\frac{\partial \varphi}{\partial t}\right) + \nabla([\sigma][\alpha]\nabla T) + \nabla([\sigma]\nabla\varphi) = 0\,, \tag{3.4}$$

where φ, κ, σ, α and ε are the electric scalar potential, thermal conductivity, electrical conductivity, Seebeck coefficient and dielectric permittivity, respectively. Square brackets mean matrices.

The system of thermoelectric finite element equations is obtained by applying the Galerkin FEM procedure to the previous coupled equations.

3.4 Finite element modeling

The thermoelectric analysis, which has been conducted with ANSYS Multiphysics software, accounts for the full set of thermoelectric relevant effects (Joule, Thomson, Peltier, and Seebeck) and it is carried out by means of a direct-coupled field solution. To improve the performance of calculations, the FEM model of the ATEG consists only of one half of the geometry, see Figure 3.9, exploiting the central symmetry plane.

When performing FEM simulations of complete TE modules several unknown properties related to the characteristics of the modules must be determined. These include the properties of the bulk material, e.g. Seebeck coefficient, thermal conductivity, and electrical resistivity, and their temperature dependences. These values rely on the choice of thermoelectric material, and also the thermal and electrical conductance at different material junctions inside the modules.

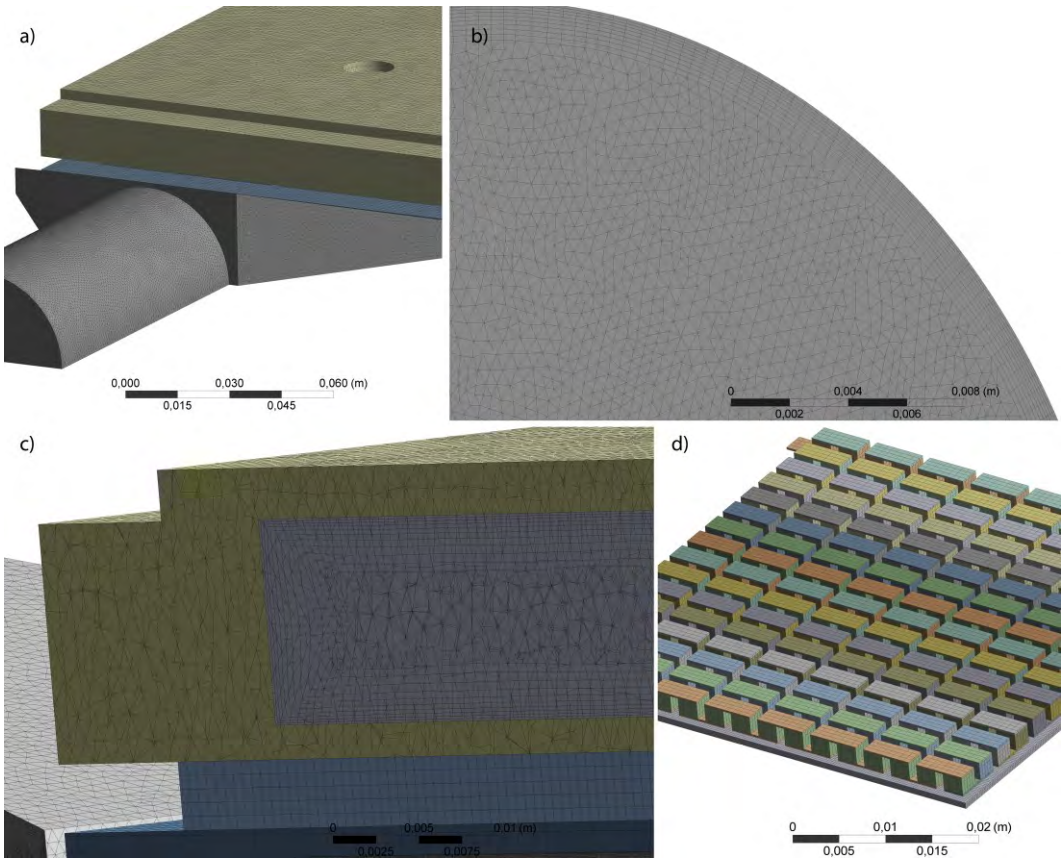

Figure 3.5 Details of FEM mesh: a) entire view, b) exhaust inlet pipe, c) cold plate and cooling circuit, d) TEM.

Figure 3.5 shows the geometry of some parts of the finite element model of the thermoelectric energy harvester designed. Material selections, meshing and boundary conditions for the model were set. The dimensions of the internal components of the TEM are listed in Figure 3.6 and Table 3.4, where *S* and *th* are the surface on the *xy* plane and thickness on *z*-axis direction of the element, respectively.

Table 3.4 TEM geometries.

Element	***S (mm²)***	***th (mm)***
Copper electrode	5.88x2.44	0.25
n-type leg	2.44x2.44	1.97
p-type leg	2.44x2.44	1.97
Ceramic plate	56x56	0.77

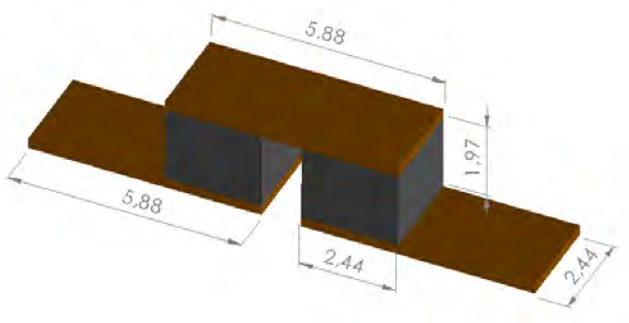

Figure 3.6 Single thermocouple geometry. Dimensions in millimeters.

The selection of thermoelectric materials strongly affects the performance of the thermoelectric device. This study uses a mixture of lead tin tellurium and bismuth tellurium as the material of thermoelectric module legs. The properties of this material such as the Seebeck coefficient, thermal conductivity and electrical resistivity (σ^{-1}) all depend on temperature. The physical properties of the thermoelectric modules used for this simulation have been calculated from the manufacturer's datasheet. TEMs used are TELBP1-12656-0.45 from Thermonamic Electronics Corp. Ltd. The equations describing the behavior of these properties follow,

$$\alpha_{pn} = a_1 + a_2 T_{avg} + a_3 {T_{avg}}^2 + a_4 {T_{avg}}^3 , \tag{3.5}$$

$$\kappa_{pn} = a_1 + a_2 T_{avg} + a_3 {T_{avg}}^2 + a_4 {T_{avg}}^3 , \tag{3.6}$$

$$\sigma_{pn}^{-1} = a_1 + a_2 T_{avg} + a_3 {T_{avg}}^2 , \tag{3.7}$$

where $T_{avg} = (T_h + T_c)/2$ is the mean temperature of the hot and cold junctions. Coefficients are presented in Table 3.5.

The physical properties of the remaining parts, presented in Figure 3.2, are included in Table 3.5.

Table 3.5 Material properties.

Material properties	***n-type element***				***p-type element***			
	a_1	a_2	a_3	a_4	a_1	a_2	a_3	a_4
α (V/K)	-1.60×10^{-5}	-2.06×10^{-6}	1.08×10^{-8}	-1.91×10^{-11}	-1.60×10^{-5}	2.06×10^{-6}	-1.08×10^{-8}	1.91×10^{-11}
κ(W/mK)	5.99×10^{-2}	8.69×10^{-3}	-9.74×10^{-6}	-1.14×10^{-8}	5.99×10^{-2}	8.69×10^{-3}	-9.74×10^{-6}	-1.14×10^{-8}
σ^{-1} (Ωm)	8.78×10^{-6}	4.87×10^{-9}	6.24×10^{-11}	-	8.78×10^{-6}	4.87×10^{-9}	6.24×10^{-11}	-
C(J/kgK)	200							
ρ (kg/m^3)	7700							

Parameter @ 300K	***Copper***	***Steel***	***Aluminum***	***Ceramic***
κ (W/mK)	394	43	237	25
σ^{-1} (Ωm)	3.20×10^{-8}	-	2.82×10^{-8}	1.00×10^{12}
C (J/kgK)	385	473	903	765
ρ (kg/m^3)	8933	7801	2702	3975
ε (mm)	0.0015	0.0024	0.01	-

Figure 3.7 and Figure 3.8 show the electrical and thermal resistances defined in this model for a couple of thermoelectric elements. Electrical resistances of copper, R_elCu, and thermoelectric elements, R_eln and R_elp, are internally calculated by the simulation software once the electrical resistivities of each material have been previously defined.

Table 3.7 presents the values of electrical resistivities of copper and *n*- and *p*-semiconductor materials. Electrical contact resistances between copper and thermoelectric materials, $R_elC1, \ldots, C4$, are also defined in Table 3.6.

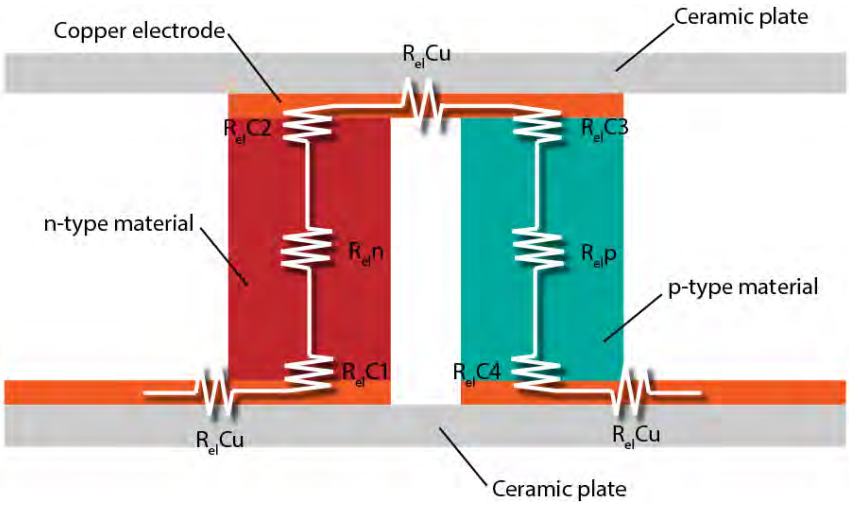

Figure 3.7 Electrical resistances for a thermoelectric uni-couple.

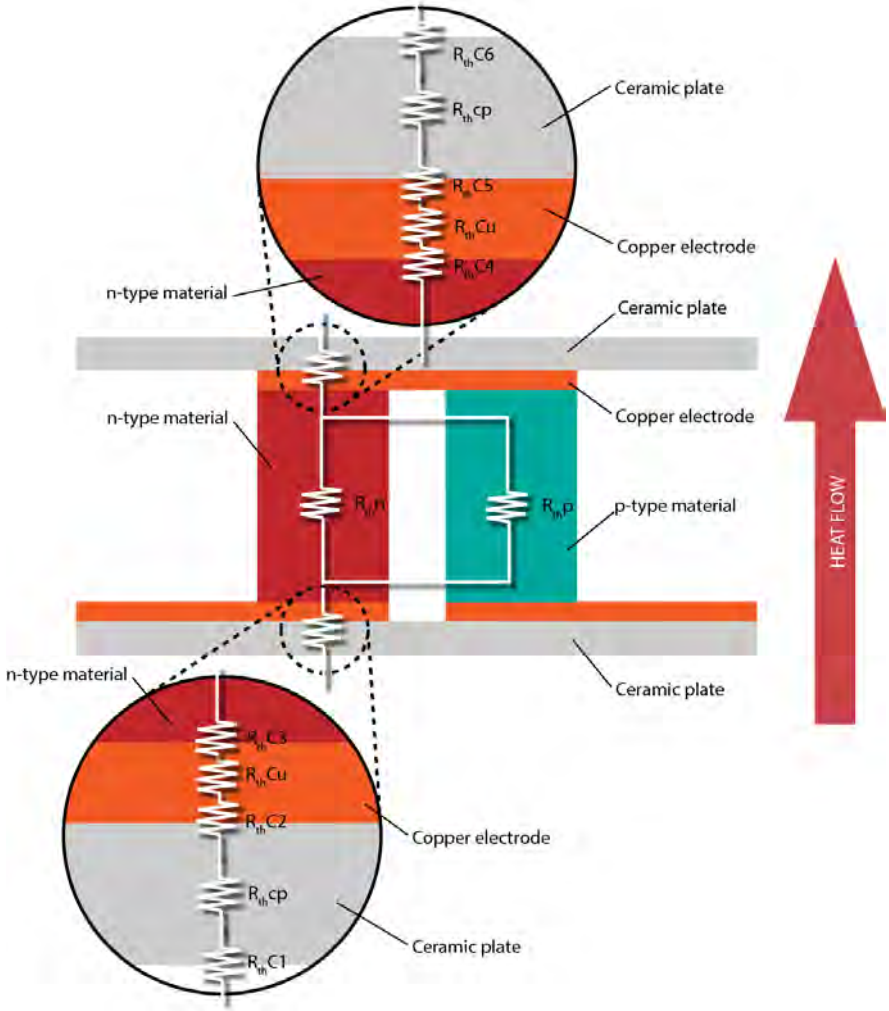

Figure 3.8 Thermal resistances for a thermoelectric uni-couple.

Table 3.6 Thermal and electrical properties.

Electrical properties	
Electrical resistivity	***Ωm***
${\sigma^{-1}}_{el}Cu$	3.2×10^{8}
${\sigma^{-1}}_{el}n$	temperature dependent*
${\sigma^{-1}}_{el}p$	temperature dependent*
Contact resistances	***Ωm²***
$R_{el}C1$	4.8×10^{-9}
$R_{el}C2$	4.8×10^{-9}
$R_{el}C3$	4.8×10^{-9}
$R_{el}C4$	4.8×10^{-9}

Thermal properties	
Thermal resistivity	***mK/W***
$R_{th}cp$	2.78×10^{-2}
$R_{th}Cu$	2.58×10^{-3}
$R_{th}n$	temperature dependent*
$R_{th}p$	temperature dependent*
Contact resistances	***W/m²K***
$R_{th}C1$	2×10^{3}
$R_{th}C2$	0
$R_{th}C3$	0
$R_{th}C4$	0
$R_{th}C5$	0
$R_{th}C6$	2×10^{3}

*See Table 3.5

The contact properties of the pellet-electrode and electrode-ceramic plate interfaces are implemented by contact elements, which are imposed on the boundary surfaces and assigned to user-specified thermal and electrical contact resistances.

As depicted in Figure 3.7, a thermoelectric uni-couple consists of both *n*- and *p*-type thermoelectric legs and electrodes that electrically connect these two legs in series. The TEM consists of many uni-couples that are connected in series. The

electric resistance is defined as follows,

$$R_{el} = \frac{l}{\sigma S} \tag{3.8}$$

where l is the length in the direction of the electrical current and S is the cross-sectional area of the element. Electrical resistances $R_{el}n$, $R_{el}p$ and $R_{el}Cu$ are not calculated because ANSYS software computes them internally using Equation (3.8) and the geometric dimensions.

Regarding the thermal behavior, the uni-couple structure contains the thermal resistances of each bulk material, i.e. the ceramic plate $R_{th}cp$, copper $R_{th}Cu$, the thermoelectric materials $R_{th}n$ and $R_{th}p$, and six thermal contact resistances $R_{th}C1, \dots, C6$, corresponding to each junction. Thermal resistance is the inverse of thermal conductivity, so it can be easily calculated as follows,

$$R_{th} = \frac{1}{\kappa}. \tag{3.9}$$

Högblom et al. [122] reported a method to determine the contact resistances in TEM. In that research, authors reported that neither thermal nor electrical contact resistances should be neglected when performing TEM simulations. At interfaces, thermal and electrical conductances depend on material properties, surface roughness, and applied contact pressure. Consequently, the thermal and electrical conductances of the different material interfaces inside the module can substantially vary. Ziolkowski et al. [123], Kim et al. [124], and Gupta et al. [125] reported electrical contact resistances in the range of 10^{-9} to 10^{-7} Ωm^2. Values of thermal contact conductances between 10^2 and 10^4 W/m^2K are reported in the literature [126]. In Ref. [123], authors have used simulations to study contact resistances within TEG and observed negligible thermal resistance between the pellets and the contact bridges. Besides, in Ref. [122], authors used almost identical TEMs to those used in the present study, same manufacturer and material. Therefore, contact resistances are defined as $R_{th}C1 = 5 \times 10^3 W/m^2K$, $R_{th}C6 = 10^4$ W/m^2K and $R_{el}C1 = R_{el}C2 = R_{el}C3 = R_{el}C4 = 4.8 \times$

10^{-9} Ωm^2. In addition, the clamping force applied to each TEM is 430 kg.

The model provides a mapped mesh with hexahedral elements (solid226), which has 20 nodes with up to five degrees of freedom per node. These elements represent the functional components such as bridges and pellets and, likewise, they form the filling media for the voids of construction. The mesh is refined in fluidic bodies, especially on the contact regions surrounded by solids. The sizes of the elements used in the fluid and solid regions are 0.5 mm and 1 mm, respectively. The total number of elements used in this model is 2,974,075. The turbulent model used in this paper is k-ε. A mesh sensitivity analysis for the thermoelectric power generation system was performed in order to check its mesh independency.

Once the model has been set, the performance of the thermoelectric device depends on the external load resistance, which yields the capture of the characteristic power parabola with respect to the electrical current. To solve this issue, as explained in chapter 3.2.2, the MPP is located at the maximum of the characteristic power parabola.

3.5 Results and discussion

As explained in chapter 3.2.4, the experiments were conducted under four different operating conditions; the measured data at these different engine test modes are summarized in Table 3.3. Simulations were performed at identical exhaust gases and coolant inlet temperatures and mass flow values.

The thermal analysis was conducted using ANSYS CFX. Figure 3.9 and Figure 3.10 show the evolution of each temperature over a longitudinal cross section of the symmetric half-model.

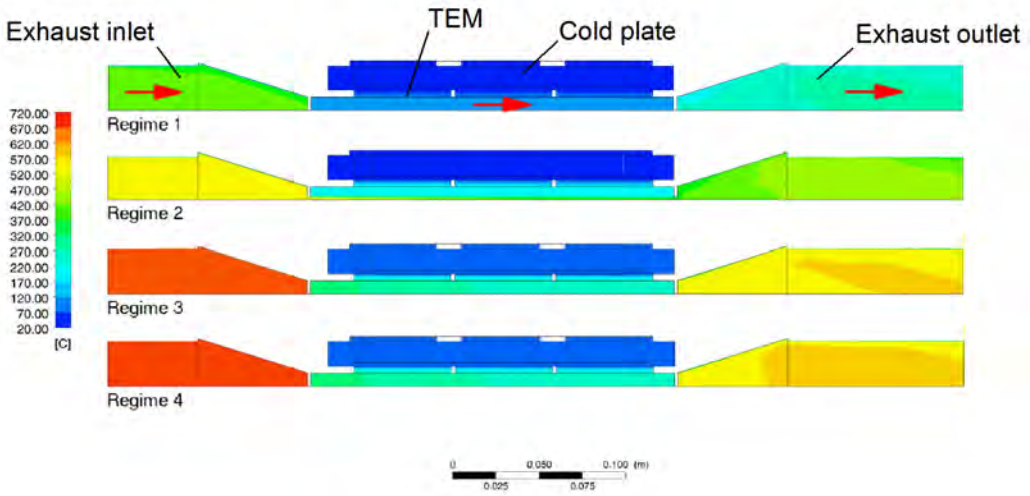

Figure 3.9 Simulated temperature contours over a longitudinal cross section of the ATEG. The symmetric half-model is represented. Exhaust gases flow from left to right.

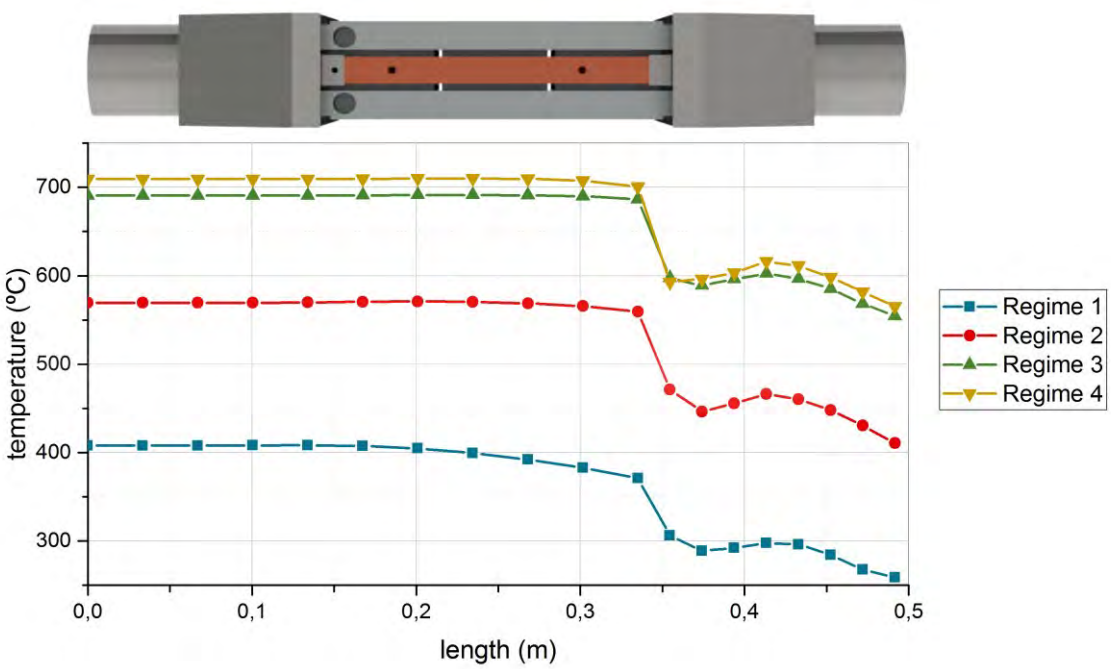

Figure 3.10 Temperature chart of exhaust gases flowing through ATEG.

As shown in Figure 3.9, temperatures of exhaust gases decrease when they flow through the ATEG. The heat contained in fumes dissipates through the TEMs to the cold plates to finally warm the cooling water. The goal is to maximize the heat flow passing through TEMs. Thus, it is necessary to extract the maximum

energy from fumes and transfer it to the cooling water. Since TEMs are the only union between hot and cold sources, it is ensured that the heat flow passes only through TEMs.

Focusing on the behavior of the exhaust gases, it can be assessed that the energy contained in the fumes is smaller in low regimes (see Regime 1 in Figure 3.10). Thus, the exhaust temperature decreases faster with length. This is explained because both temperature and exhaust gases flow rate are smaller than in the other working modes analyzed, and therefore there is less energy available.

In Figure 3.10, the temperature drop occurred at length 0.35 m is due to an air mixture issue. In Figure 3.11, the black line symbolizes the path used to build Figure 3.10. As seen, therein exhaust flow is forced to pass through six holes and, when the flow comes out at the end of the ATEG, due to its high velocity, it needs time to mix with the colder remaining exhaust gases contained in the outlet. This behavior produces six hot outlet channels responsible for the two temperature anomalies observed at 0.35 m and 0.42 m.

Another important parameter when developing an ATEG for combustion engines is the backpressure that the device offers to the exhaust line. The engine backpressure increases with the installation of an ATEG in a vehicle, resulting in a reduced engine volumetric efficiency and thus reducing the fuel conversion efficiency. This effect is explained by the obstruction caused to the exhaust fumes, or by the reduction in temperature of the exhaust gas or by a combination of both.

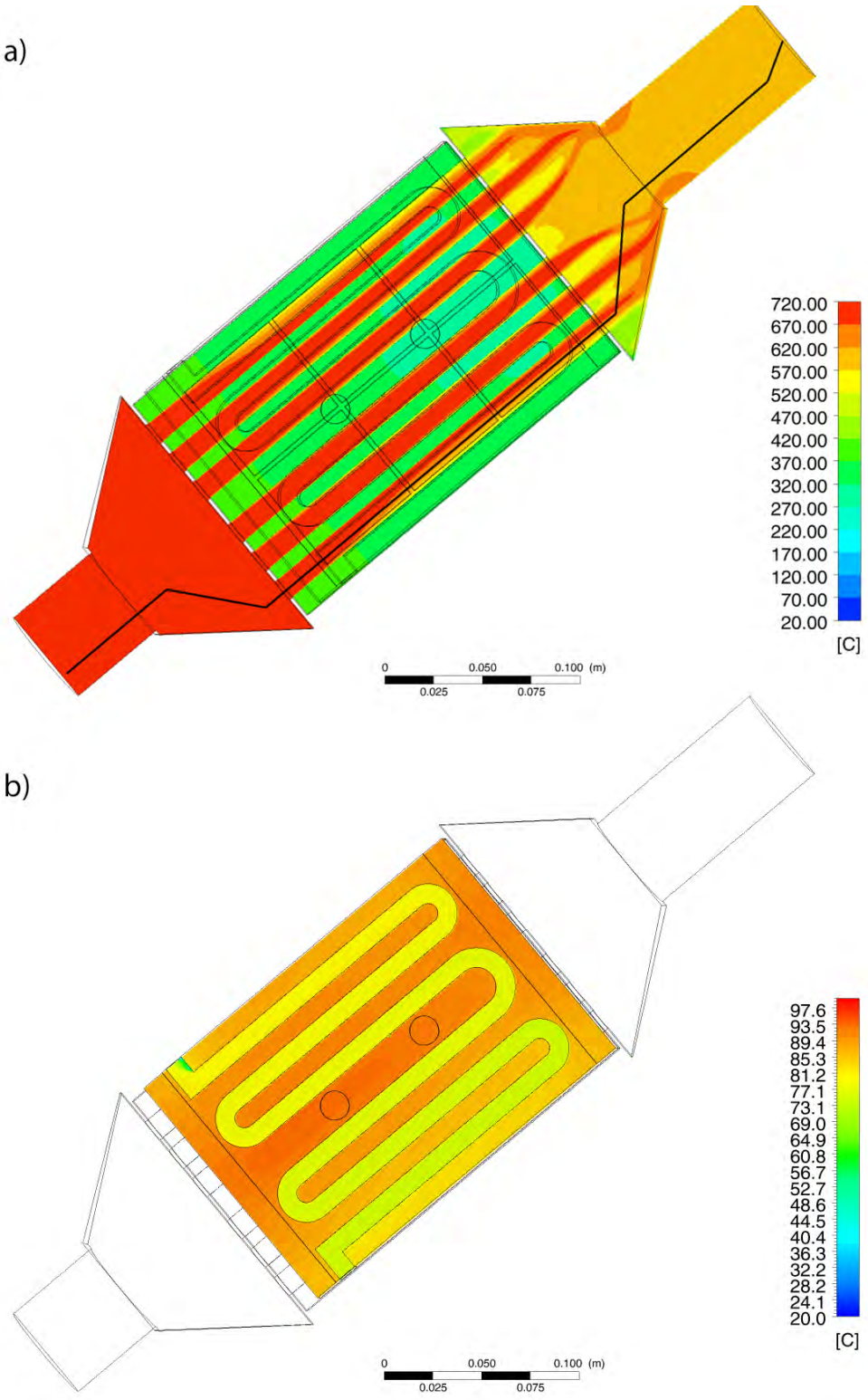

Figure 3.11 Temperature contour of ATEG under regime 4: a) exhaust gases, b) cooling circuit. The black line shows the path along which simulated data is represented in Figure 3.10.

Figure 3.12 shows the pressure drop that the ATEG here analyzed causes to the exhaust gases. As expected, the pressure drop increases in a quadratic form as a function of the mass flow rate, following the Darcy-Weisbach relationship. If we compare the experimental and simulated points, we can appreciate a good agreement for all flow rate regimes. Note that experimental data was taken in a different test, using a Saenz air flowbench D-680, in order to obtain more accurate data. The numerical comparison is presented in Table 3.7, and experimental points are calculated by using the curve fitting presented in Figure 3.12, where experimental data in the air flowbench have been corrected by density differences. In addition, *x-y* error bars for experimental points are included.

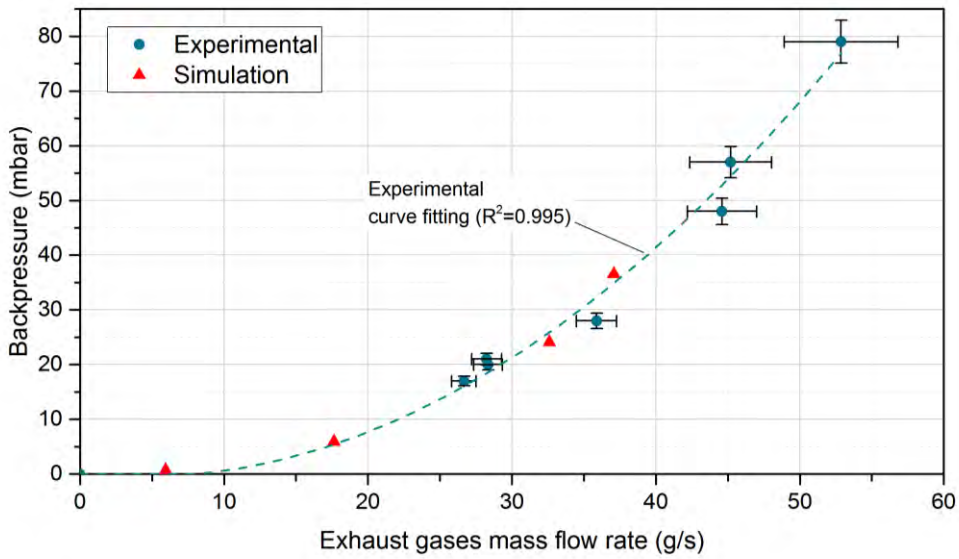

Figure 3.12 Correlation between experimental and simulated pressure drop caused by ATEG.

Regarding the electrical voltage generated by TEMs, Figure 3.13 shows the developed voltage within the module TEM12, given in volts, due to the temperature difference of 263°C between the hot and the cold side of the generator, referring to matched loading conditions of engine test mode 3. The results are presented graphically omitting the hot plate to reveal the inside structure of the module.

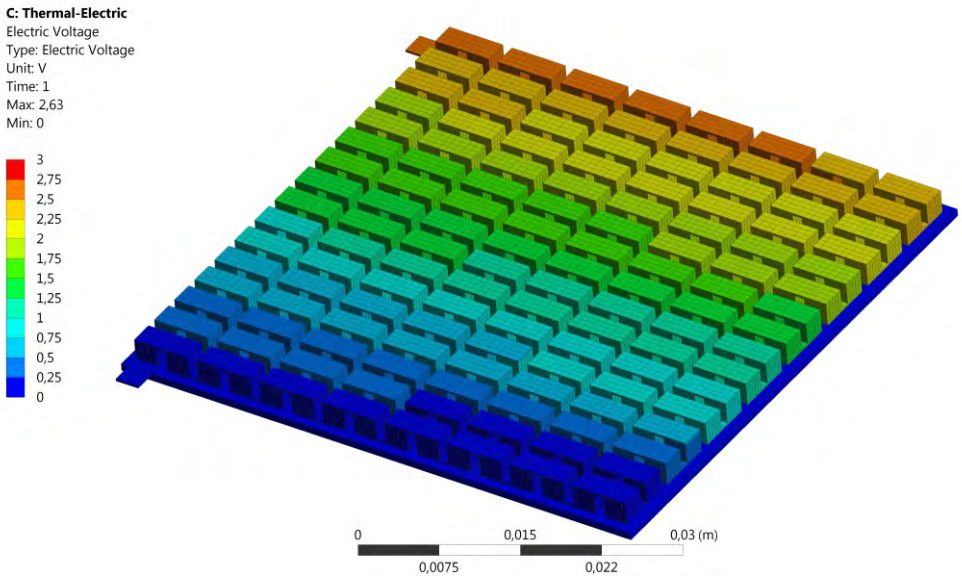

Figure 3.13 Voltage generated within TEM 12.

Finally, Table 3.7 shows a comparison between experimental and simulated results for the operating conditions provided in Table 3.3. Experimental values of backpressure are extracted from the curve fitting provided in Figure 3.12. Knowing the exhaust mass flow rate of each case we can extract the value of the backpressure.

Table 3.7 Experimental and simulated results comparison for the operating conditions.

Engine test mode	***1***				***2***				***3***				***4***				
	Exp.	***Sim.***	***Uncert.***	***Err. (%)***	***Exp.***	***Sim.***	***Uncert.***	***Err. (%)***	***Exp.***	***Sim.***	***Uncert.***	***Err. (%)***	***Exp.***	***Sim.***	***Uncert.***	***Err. (%)***	***mean error***
Electrical power generated (W)	5.52	5.69	±0.023	2.97	37.68	36.16	±0.158	-4.20	111.27	110.17	±0.467	-1.00	106.76	101.58	±0.448	-5.10	3.32
Hot side temperature TEM8 (ºC)	104.5	104.4	±1.5	-0.10	210.0	210.2	±1.5	0.10	344.7	347.1	±1.5	0.69	351.0	347.2	±1.5	-1.09	0.49
Cold side temperature TEM 8 (ºC)	41.0	41.3	±1.5	0.63	57.0	56.3	±1.5	-1.19	85.2	83.9	±1.5	-1.61	95.2	91.8	±1.5	-3.70	1.78
Exhaust gases outlet temp. (ºC)	264.9	262.7	±1.5	-0.83	414.9	416.1	±1.5	0.27	557.11	560.5	±1.5	0.60	569.9	570.5	±1.5	0.10	0.45
Coolant outlet temperature (ºC)	39. 6	39.4	±1.5	-0.38	51.2	48.6	±1.5	-5.42	70.72	71.8	±1.5	1.56	80.8	80.5	±1.5	-0.42	1.94
Output voltage (V)	7.18	6.60	±0.014	-8.79	18.49	17.64	±0.037	-4.82	31.78	31.54	±0.064	-0.76	31.26	30.32	±0.063	3.11	4.37
Output current (A)	0.78	0.86	±0.003	9.51	2.04	2.05	±0.008	0.49	3.50	3.49	±0.013	-0.20	3.42	3.35	±0.013	-2.07	3.07
Backpressure (mbar)	0.719	0.682	±0.036	-5.14	5.903	7.038	±0.295	-19.23	36.53	34.749	±1.827	4.88	24.12	26.378	±1.206	-9.36	9.66

As observed in Table 3.7, the main features of the ATEG are well achieved with the theoretical model. The maximum mean error between simulations and experimental data of the variables analyzed is 9.66% derived from the value of backpressure. This variation can be explained by some parameters related to fluid dynamics. The ATEG internal geometry has sharp edges, which, added to a high Reynolds number, can strongly affect the mass flow rate, appearing chaotic oscillations in the flow that may not be accurately resolved with the mesh used. In this paper, the mesh size was selected to fulfill the thermal behavior of the system and to properly simulate the thermoelectric effect. Then, we expect that a more refined mesh for the flow may improve the simulation of the backpressure effect.

3.6 ATEG performance assessment

The main objective of ATEG design is to develop a device capable to harvest the energy contained in exhaust fumes and transform it into electricity in order to charge the battery of the vehicle. The idea is that the collected energy could prevent the alternator to work, leading to a reduction in the vehicle's fuel consumption. However, due to many aspects like the engine type, the vehicle driving conditions or the ATEG design, this statement is not always fulfilled.

To estimate the achievable value of fuel economy of a specific ATEG design there are four factors that have to be addressed: the amount of power generated by the ATEG, the backpressure caused to the exhaust evacuation, the weight of the ATEG and the ATEG coolant pumping power. These factors are dependent on the ATEG design, and the net energy balance between them will determine the final ATEG feasibility.

In [128], the authors reported predictions of power and fuel savings produced by an ATEG placed in the exhaust line of a vehicle. The predictions were based on mathematical models of the four factors previously presented. Here, the influence of the coolant pumping power P_P of ATEG on fuel economy is not studied separately. The reason is because its power consumption is considered

constant, and this value will be substracted to the ATEG power generation P_G to obtain P_{Gnet}. Thus, the equations to calculate the fuel economy impacts are:

$$F_{e,G} = \frac{100\eta_{PCU}}{\eta_G IP} P_{Gnet} \tag{3.10}$$

$$F_{e,BP} = -\frac{10^4 \dot{v}_{ex}}{IP} BP \tag{3.11}$$

$$F_{e,W} = -\frac{100 g \xi v}{\eta_D IP} W \tag{3.12}$$

$$P_{G\,net} = P_G - P_P \tag{3.13}$$

where $F_{e,G}$, $F_{e,BP}$, and $F_{e,W}$ are the fuel economies due to ATEG power generation, back pressure and weight, respectively. In addition, η_{PCU}, η_G, IP, P_{Gnet}, $\dot{v}_{ex}$, BP, ξ, v, η_D, and W are the power converter unit (PCU) efficiency, alternator efficiency, engine indicated power, ATEG electrical power generation P_G minus coolant pumping power P_P, exhaust gases volumetric flow rate, backpressure, vehicle rolling resistance coefficient, vehicle velocity, transmission efficiency, and ATEG weight, respectively. The PCU is essentially a direct-current-to-direct-current converter functioning as a buck regulator, matching the generator's output voltage to 14.4 V potential of the battery and keeping the ATEG operating at its maximum power point.

The indicated power IP can be calculated using the following equation,

$$IP = \frac{\pi IMEP B^2 STN}{120} \tag{3.14}$$

where indicated mean effective pressure (IMEP) is calculated as,

$$IMEP = \frac{4\pi\tau}{SV} \tag{3.15}$$

where SV, B, ST, N, and τ are the swept volume, bore, stroke, frequency of rotation and torque, respectively. The parameters needed for the calculation of the previous equations are presented in Table 3.1. Equations (3.10), (3.11) and (3.12) are linear with

respect to P_{Gnet}, IP, BP, $\dot{v}_{ex}$, v and W, and the slope term s_{theo} is expected to coincide with the linear fitting slopes of the driving test

$$s_{1\,theo} = \frac{100\eta_{PCU}}{\eta_G} \tag{3.16}$$

$$s_{2\,theo} = -10^4 \tag{3.17}$$

$$s_{3\,theo} = -\frac{100g\xi}{\eta_D} \tag{3.18}$$

In order to shed light on the influence of each parameter on the fuel economy, a theoretical simulation using the GT-SUITE software is conducted (see Figure 3.14). A diesel mid-size vehicle is modeled using a fast running engine model (FRM). Although the engine is not the same as that tested experimentally, we chose it because the purpouse of this work is to investigate the behavior of the four parameters mentioned for any kind of engine, and it is expected to be a feasible model.

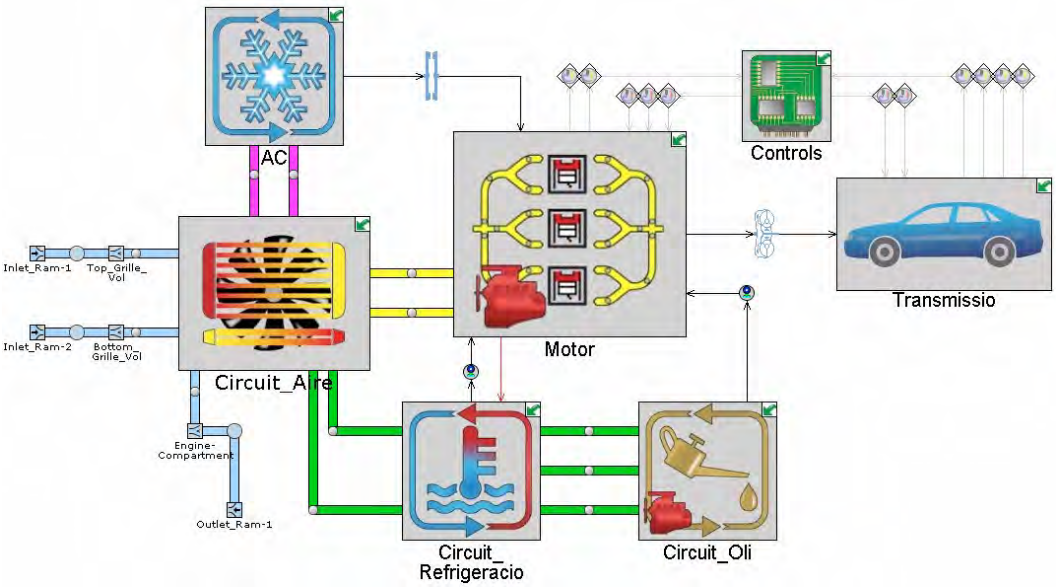

Figure 3.14 Vehicle model.

The engine is a four stroke cycle engine (Figure 3.15). The model includes vehicle drivetrain, engine, transmission, vehicle body, tires, axles, A/C refrigerant circuit, cabin and HVAC air circuit, as well as the underhood cooling module and compressor. All these components are geared directly to the engine crankshaft

so the power affects the fuel consumption. Vehicle is subjected to four steady state velocities: 50 km/h, 80 km/h, 100 km/h, and 120 km/h. The ambient temperature is 35ºC and the solar load applied is 1000W/m^2. Vehicle mass is 1850 kg.

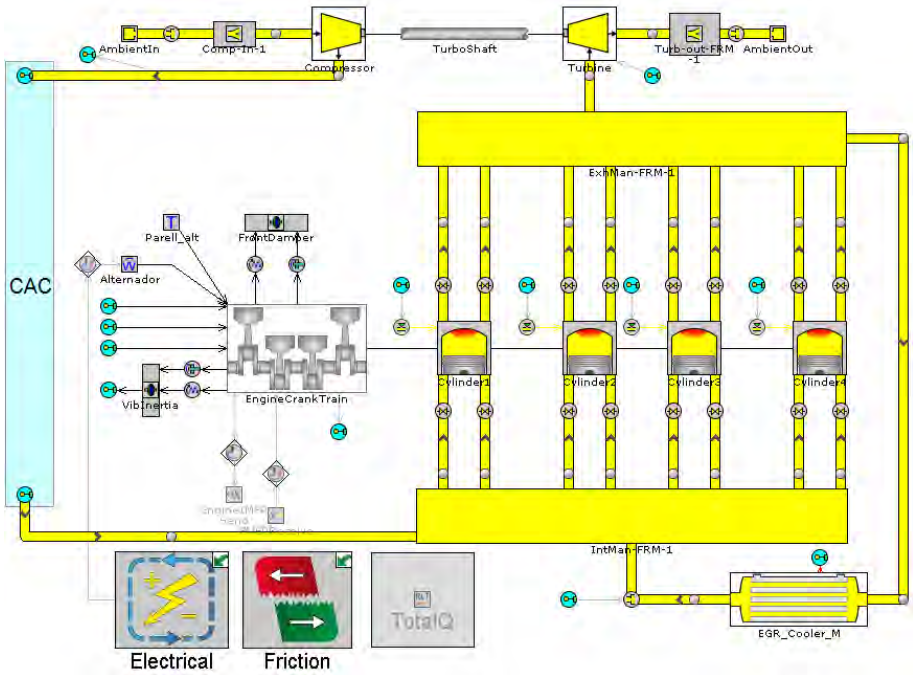

Figure 3.15. Engine model

To obtain the influence of power generation, backpressure, coolant pumping power and weight of ATEG, an isolated study of each parameter is conducted.

The goal of the ATEG power generation is to prevent the alternator to work. The alternator needs mechanical power to generate electricity, and this power is supplied from the engine shaft. To simulate the alternator influence on the fuel consumption, a variable torque, from 0 Nm to 10 Nm, is applied to the engine shaft of the model. Then, taking the value of the engine cyclic speed from each steady state test and the torque applied, the net ATEG electrical power generation can be calculated as follows,

$$P_{G\,net} = \frac{\eta_G \eta_{PCU} \tau \omega 2\pi}{60}, \tag{3.19}$$

where η_G, η_{PCU}, τ, and ω are the alternator efficiency, PCU efficiency, torque and engine speed, respectively. The alternator efficiency is 50%, typical of belt-driven units, and the PCU efficiency is 84%. The electrical output of the ATEG needs to be conditioned before connecting the ATEG output to the battery. The results of this test are shown in Figure 3.16.

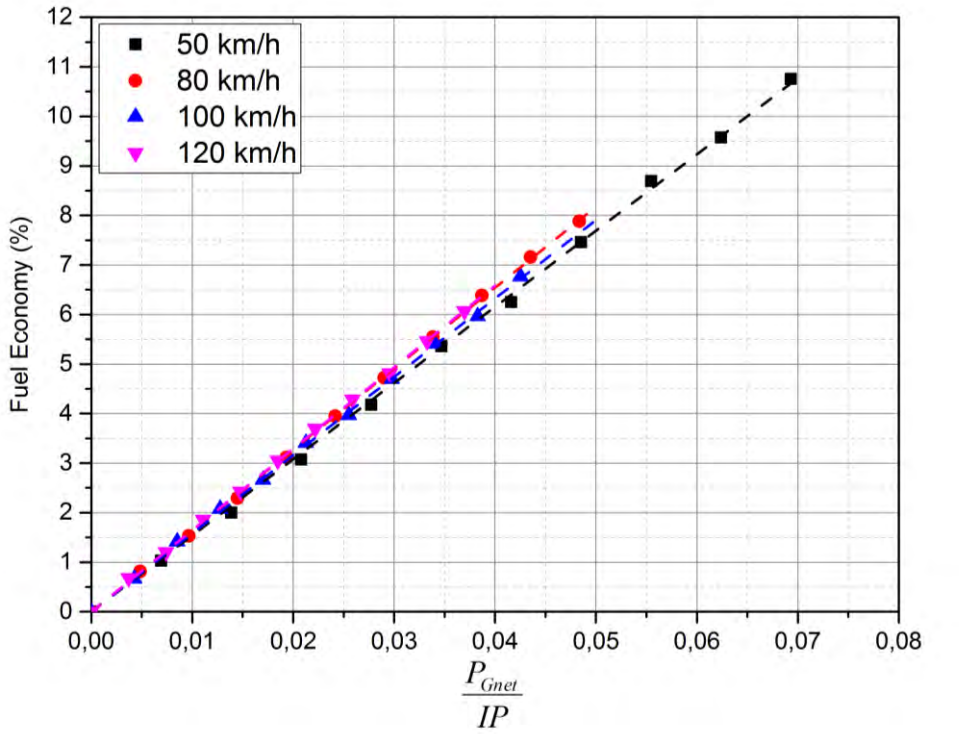

Figure 3.16 ATEG net power generation $P_{G\ net}$ influence on fuel economy for a mid-size vehicle. Slope corresponds to $s_{1\ sim}$.

In the same manner, the influence of backpressure is investigated by applying an extra pressure drop in the exhaust line. The position of this obstruction is placed after the turbine and as close as possible to the engine, to simulate the real position of the ATEG. Values of additional pressure drop from 22 mbar to 140 mbar are introduced. The results are shown in Figure 3.17.

Finally, and in order to assess the impact of weight on the fuel economy, masses from 25 kg to 100 kg are added to the total weight of the vehicle. The rolling resistance coefficient ξ and the transmission efficiency η_D values are 0.01 and 0.9, respectively. The results are shown in Figure 3.18.

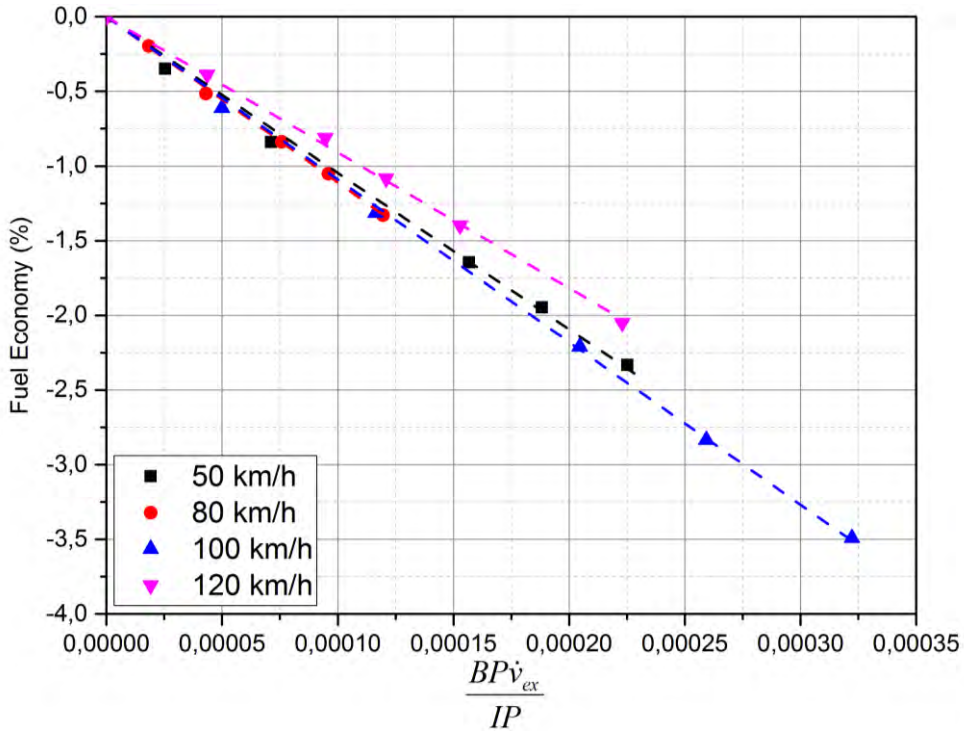

Figure 3.17 ATEG backpressure influence on fuel economy for a mid-size vehicle. Slope corresponds to $s_{2\ sim}$.

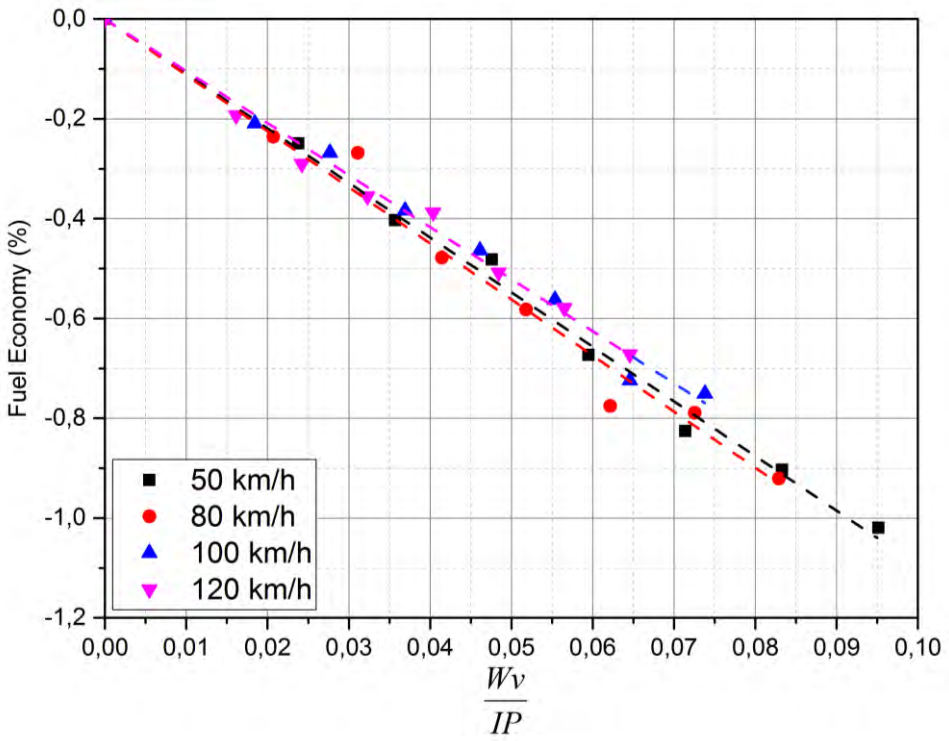

Figure 3.18 ATEG weight influence on fuel economy for a mid-size vehicle. Slope corresponds to $s_{3\ sim}$.

As previously mentioned, the influence of the increase in the coolant pumping power P_P of ATEG on fuel economy is not studied using the vehicle model. The reason is because its power consumption is considered constant.

Each test previously performed within GT-SUITE describes a relationship between predictor and response variables. All isolated studies show good agreements using a linear fitting for each steady state tests. Goodness of fittings r^2 are reported in Table 3.8.

Table 3.8 Theoretical and simulated results comparison for the operating conditions.

v (km/h)	**50**	**80**	**100**	**120**
IP(kW)	11.675	21.443	30.111	41.295
$s_{1\,theo}$ (%)	168	168	168	168
r^2	0.9992	0.9997	0.9995	0.9999
$s_{1\,sim}$ (%)	153.9	163.5	158.1	164.5
error (%)	8.39	2.68	5.89	2.08
$s_{2\,theo}$ (% W s/mbar m^3)	-10000	-10000	-10000	-10000
r^2	0.9961	0.9988	0.9986	0.9976
$s_{2\,sim}$ (% W s/mbar m^3)	-10466	-11098	-10896	-9085
error (%)	-4.66	-10.98	-8.96	9.15
$s_{3\,theo}$ (%/m/s)	-10.9	-10.9	-10.9	-10.9
r^2	0.9943	0.9813	0.9911	0.9892
$s_{3\,sim}$ (%/m/s)	-10.95	-11.241	-10.43	-10.43
error (%)	-0.43	-3.13	4.31	4.31

As seen in Table 3.8, the theoretical slopes s_{theo} have a good agreement with simulated ones s_{sim}. Then, combining Equations (3.10), (3.11) and (3.12) we can obtain the total fuel economy equation

$$F_e = F_{e,G} + F_{e,BP} + F_{e,W} = s_1 \frac{P_{Gnet}}{IP} + s_2 \frac{BP\dot{v}_{ex}}{IP} + s_3 \frac{Wv}{IP}, \tag{3.20}$$

The vehicle velocity v can be calculated as,

$$v = \frac{N\emptyset_T \pi}{60AXTR}, \tag{3.21}$$

where $\emptyset_T$, AX, and TR are the tire diameter, axle ratio, and transmission ratio corresponding to a Volkswagen Golf 1.4 TSI (vehicle that uses the engine experimentally tested), respectively.

The volumetric flow rate can be found as,

$$\dot{v}_{ex} = \frac{NSV\eta_v FTPP\rho_{in}}{120\rho_{out}}, \tag{3.22}$$

where $\eta_v, FTPP$, ρ_{in}, and ρ_{out} are the volumetric efficiency of the engine, throttle pedal position, and intake and exhaust gas densities, respectively.

In addition, using data provided in Figure 3.12 we can extract the relationship between BP and ${\dot{v}_{ex}}^2$as,

$$BP = K{\dot{v}_{ex}}^2, \tag{3.23}$$

where $K = 3.7 \times 10^4$.

Combining Equations (3.21) and (3.22), we can reformulate the velocity equation as

$$v = \frac{\emptyset_T \pi}{60AXTR} \frac{120\rho_{out}}{SV\eta_v FTPP\rho_{in}} \frac{\sqrt{BP}}{\sqrt{K}} = H\sqrt{BP}. \tag{3.24}$$

To simplify the model, we considered $\rho_{out}/\rho_{in} = 1.5$ and $FTPP = 0.75$. AX and TR are 3.65 and 0.86, respectively. The volumetric efficiency η_v is considered 0.85.

When the vehicle is traveling at a constant speed, the engine power necessary to move the entire mass can be calculated as $IP = Fv$. The force needed to move the vehicle must be equal to the sum of rolling F_r and drag F_d forces as

$$F = F_r + F_d = \xi g W_v + \frac{1}{2} d_c \rho_{air} S_d v^2, \tag{3.25}$$

where W_v, d_c and S_d are the weight, the drag coefficient and the drag surface of the vehicle. For a Volkswagen Golf 1.4 TSI, these values are 1170 kg, 0.36 and 2.05 m^2, respectively.

Then, combining Equations (3.20), (3.23), (3.24), and (3.25) we obtain the fuel economy equation in terms of P_{Gnet} and BP.

$$F_e = \frac{s_1 P_{Gnet}\sqrt{K} + s_2 BP\sqrt{BP} + s_3 HW\sqrt{K}\sqrt{BP}}{H\sqrt{K}\sqrt{BP}\left(\xi g W_v + \frac{1}{2} d_c \rho_{air} S_d H^2 BP\right)}, \tag{3.26}$$

Knowing the expression of fuel economy and stablishing $F_e = 0$, we can extract Equation (3.27) that shows the relationship between the power generation and the backpressure that fulfills the condition of achieving a positive fuel economy

$$P_{Gnet} > -\frac{s_2}{s_1}\frac{BP\sqrt{BP}}{\sqrt{K}} - \frac{s_3}{s_1} HW\sqrt{BP} = P_{cr}\,. \tag{3.27}$$

P_{cr} represents the critical power generation that delivers a null fuel economy. Therefore, it is necessary to know the relationship between pressure drop and power generation of the ATEG. This correspondence can be found by simulating or testing the ATEG under several engine conditions. In this study, the relationship is extracted from backpressure and power generation of the ATEG test, see Table 3.7. The correspondence is determined mathematically by Equation (3.28). Then, we can plot the feasible and unfeasible regions in terms of fuel economy balance Figure 3.19.

$$P_G = aBP^2 + bBP = -0.111BP^2 + 7.088BP \tag{3.28}$$

$$P_{G\,net} = P_G - P_P = aBP^2 + bBP - P_P \tag{3.29}$$

The critical points *CP* in Figure 3.19 represent the points where in between the ATEG is delivering a positive value of fuel economy. These points can be determined by solving the system of Equations (3.27) and (3.29). The minimum and maximum allowable backpressure values to prevent the ATEG from leaving the feasible region are BP_{CP1} and BP_{CP2}.

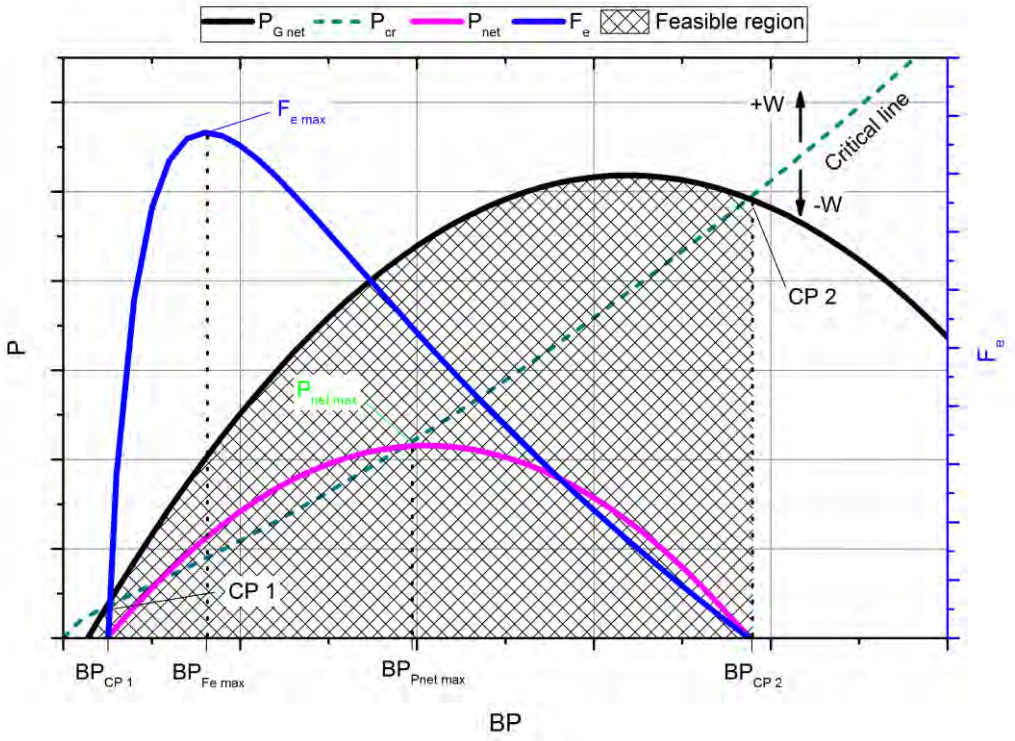

Figure 3.19 Theoretical regions of an ATEG design by means of the fuel economy balance.

The net power P_{net} varies depending on the ATEG net power generation P_{Gnet} and the engine backpressure. As seen in Figure 3.20, the difference between P_{cr} and $P_{G\,net}$ is not constant, leading to a maximum point when both are more distant. The maximum net power value $P_{net\,max}$ can be found when the following equation is maximum

$$P_{net} = P_{Gnet} - P_{cr} = aBP^2 + bBP - P_P - \left(-\frac{s_2}{s_1}\frac{BP\sqrt{BP}}{\sqrt{K}} - \frac{s_3}{s_1}HW\sqrt{BP}\right). \quad (3.30)$$

Finally, using Equation (3.26) we can calculate the expected net fuel economy of the ATEG presented in this study, installed in a mid-size vehicle and tested under four steady state velocities. Results are summarized in Table 3.9.

Table 3.9 Expected net fuel economy balance of the ATEG under four engine regimes.

	BP (mbar)	*P_G (W)*	*$P_{G\,net}$ (W)*	*P_{cr} (W)*	*P_{net} (W)*	*F_e (%)*
regime1	0.719	5.52	-3.98	4.51	-13.83	-0.972
regime2	5.903	37.68	28.18	16.82	13.64	0.160
regime3	36.53	111.27	101.77	99.11	26.89	0.003
regime4	24.12	106.76	97.26	61.68	38.58	0.076

As observed in Table 3.9, engine test modes 2, 3 and 4 generate a positive net fuel economy balance. This is explained by the good relationship between backpressure and electrical power generation of the ATEG. Otherwise, it can be observed that regime 1 lays on the unfeasible design region, see Figure 3.20. The reason is that the ATEG power generation in this regime is lower than the cooler pumping power, leading to a negative energy balance.

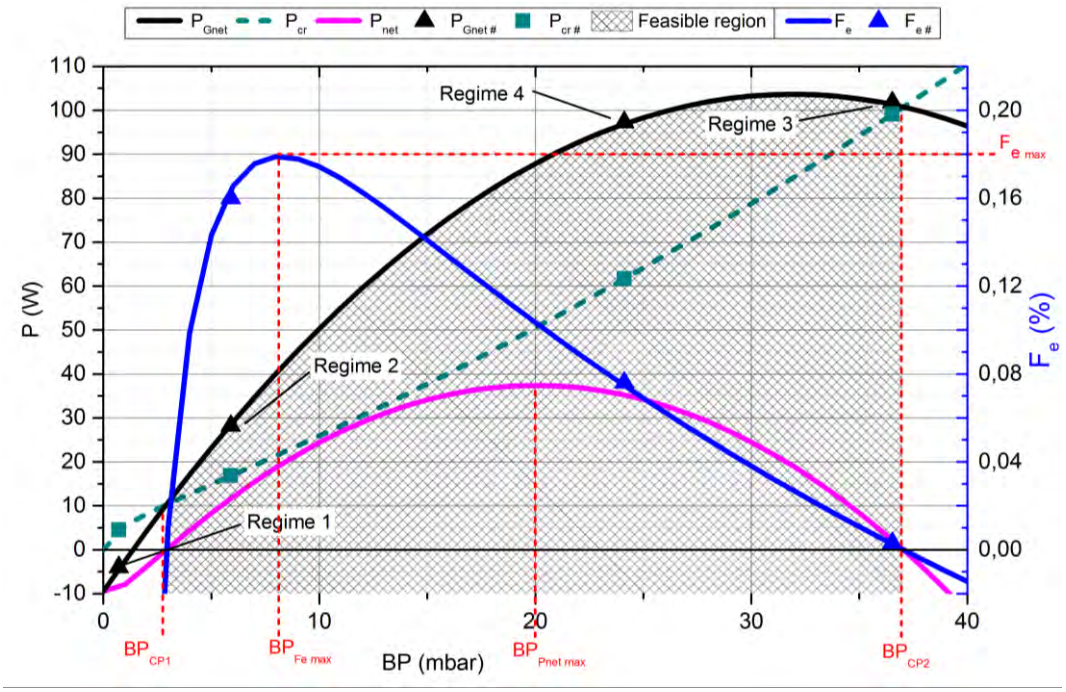

Figure 3.20 Feasible and unfeasible regions of the ATEG design analyzed in the present study by means of the fuel economy balance.

Table 3.10 Expected maximum net fuel economy balance and allowable backpressures of the ATEG here analyzed.

$F_{e\,max}$ (%)	0.179
$BP_{Fe\,max}$ (mbar)	8.19
$BP_{Pnet\,max}$ (mbar)	20.01
$BP_{CP\,1}$ (mbar)	2.92
$BP_{CP\,2}$ (mbar)	37.04

Then, the maximum fuel economy that our ATEG can supply is 0.179%. At this point, the engine backpressure supplied by the ATEG is 8.19 mbar. The maximum backpressure that ATEG can cause to the exhaust system is 37.04 mbar, coinciding with *CP2*. Beyond this point, the ATEG increases the vehicle fuel consumption due to an excessive pressure drop. On the other hand, a minimum net power generation of 10.25 W, coinciding with *CP1*, and a backpressure of 2.92 mbar is needed to guarantee a positive fuel economy value.

It is important to note that the backpressure at the maximum net power generation of ATEG, $BP_{Pnet\,max}$, does not coincide with the backpressure at the maximum fuel economy value $BP_{Fe\,max}$. This behavior is explained by the big influence of backpressure on the engine efficiency. Backpressure increases quadratically with exhaust gases volumetric flow. Then, for low regimes, with small backpressure values, engine is more capable to use the ATEG power generation to reduce the fuel economy, even when the power generation is smaller than in higher regimes. In ATEG design this is an important behavior, and it means that not only a maximum power generation needs to be reached, but also a small backpressure has to be supplied.

Finally, the ATEG designed and tested in this work fits the goal of generating a positive net fuel economy balance only for backpressures lower than 37 mbar. However, the internal design, with six holes where exhaust gases have to flow, causes too much backpressure. This means that, if this ATEG is used in real applications, there could be unfavorable engine regimes. A better design, with bigger internal exchange areas using, for example, fins instead of round holes would increase the heat flow to TEMs and reduce the pressure drop.

As observed in Figure 3.20, backpressure gains in importance for regimes with high gas flow rates, directing the ATEG performance to the unfeasible region.

3.7 Methodology for estimating in-vehicle ATEG performance

To properly analyze the expected performance of an ATEG during the development stage, a method is presented to help designers:

(i) Once the initial design is set, it is necessary to obtain the relationship between power generation and backpressure of the ATEG, see Equation (3.28). This equation can be obtained by either simulating (by means of the FEM/FVM methodology employed in the present work) or testing the ATEG under various engine regimes, preferably a representative amount of points of the most extreme real situations, varying the exhaust gases temperature and mass flow rate. The resulting equation might be similar to Equation (3.29), taking in consideration the coolant pumping power.

(ii) Using Equations (3.27) and (3.29), the operational limit of the ATEG designed can be determined by solving the system of equations. The maximum and minimum allowable values of backpressure to prevent ATEG from entering the unfeasible region can be found.

Thus, the range of backpressure values that maintains the ATEG in the feasible region is determined. Once this range is established, we can analyze whether or not this range fits the engine operational range. If not, the ATEG design must be reworked because it means that in some cases the ATEG could obstruct in excess the exhaust gases evacuation and cause undesirable fuel consumption increments. It is recommended to work on reducing the pressure drop rather than putting effort on incrementing the power generation because, as Equation (3.26) states, backpressure represents the main harmful parameter on fuel economy. In addition, obtaining a small backpressure allows ATEG to work on the region with higher fuel economy values, near $F_{e\,max}$.

(iii) To know the net balance fuel economy achievable by the ATEG design, the Equations (3.20) or (3.26) can be used.

Then, the backpressure that generates a maximum fuel economy value can be found deriving Equation (3.26). The maximum fuel economy value at this particular point can be calculated substituting the backpressure value into Equation (3.26).

(iv) It is important to design ATEGs to work as much time as possible close the maximum expected fuel economy point $F_{e\,max}$. This point is found at $BP_{Fe\,max}$, and it does not coincide with the maximum net power generation of ATEG $BP_{Pnet\,max}$. It is the duty of the designer to first determine this point, studying the engine characteristics and also its future operating conditions, because this decision will affect the final feasibility and the optimum performance of the ATEG.

3.8 Conclusions

This work describes a method to help in the ATEG design and to forecast its performance in terms of fuel economy.

Firstly, the study presents an implementation of an ATEG model using ANSYS 17.1 software, based on a 3D FEM and including hot-side convective heat transfer, and thermoelectric governing equations. The results obtained from simulations are compared with experimental tests. Good agreement is observed for each configuration over the entire temperature regimes investigated, which reveals the accuracy and reliability of the model. A maximum variation of 9.66 % in the backpressure was reported for all of the four-engine conditions analyzed.

On the other hand, the thermal contact resistances have a strong influence on power results, as already reported in the literature. This parameter is highly advisable to be correctly set because it strongly affects the final power generation and the heat flow through TEMs. The assumptions made in this work with data taken from literature are shown to be sufficient, and enable highly

accurate predictions of the ATEG performance.

Secondly, using TEGs with high efficiency, taking carefully into account its clamping force to reduce the thermal contact resistances and designing a good heat exchanger between exhaust gases and TEGs, like using fins, are capital points to obtain a feasible ATEG. Simulation tools are demonstrated to be useful in order to anticipate the design of these elements.

Thirdly, based on the results obtained by simulations, the ATEG performance assessment has been carried out giving insight of two key design parameters: power generation and backpressure value. The relationship between them define the feasibility of the design. In addition, this study presents an equation to predict the fuel economy provided by a given ATEG in terms of key design parameters, and it also gives insight about the optimal design point when the vehicle's fuel economy reaches its maximum value.

It can be concluded that the method presented in this paper enables the estimation of the ATEG performance accurately, gives detailed insight into how thermoelectric modules perform, and enables the prediction of module performances in terms of fuel economy.

In design stages, it is usually welcome the possibility to test the ATEG avoiding the need of constructing it. This work demonstrates the feasibility of using simulation tools to extract valuable information for fuel economy prediction.

Fourthly, the mathematical equations presented allow the designer to obtain valuable information about final performance of ATEG in real vehicle applications. Using these equations and analyzing the fuel economy of the ATEG presented in this paper installed in a midsize vehicle, we conclude that, even though the design is capable to reduce the fuel consumption up to 0.18%, there is a range of the engine operation that spreads to the unfeasible design region. Consequently, the ATEG can be prejudicial to the engine efficiency for certain driving conditions. To address this problem, designing a bigger internal exchange area, by using fins, will increase the heat flux through TEGs and will

reduce the pressure drop. The goal is to develop ATEGs with high power generation and small backpressure supply.

Finally, when designing ATEGs, it is important to know the overall working regimes of the vehicle in order to assure that the ATEG works always in the feasible region. Power generated by an ATEG should always be higher than the critical power generation presented in this study. Following this rule, we can guarantee the main objective of the ATEG: to reduce the fuel consumption of the vehicle.

3.9 Acknowledgments

This work has been partially funded by the University of Girona under Grant MPCUdG 2016-4. Authors would also like to thank Fundación Repsol for their collaboration, Association of Industrial Engineers of Catalonia (AEIC) for their partial financial support.

Chapter 4

Transient behavior under a normalized driving cycle of an automotive thermoelectric generator

This section is a transcription of the contents of the following paper (a copy of the published version can be found in Appendix B):

A Massaguer, E Massaguer, M Comamala, T. Pujol, L Montoro, MD Cárdenas, D Carbonell, AJ Bueno. Transient behavior under a normalized driving cycle of an automotive thermoelectric generator. *Applied Energy*, 206, 1282-1296, 2017. ISSN 0306-2619 (Impact factor 7,182; Journal 6 of 92; 1st quartile; Energy and Fuels)

http://dx.doi.org/10.1016/j.apenergy.2017.10.015

Abstract

Thermoelectric generators (TEGs) have become a promising technology for vehicle exhaust heat recovery. Many models and prototypes have been developed and validated with very promising results. The majority of them have been tested under steady-state engine conditions. However, light-duty vehicles operate under wide variable loads, causing significant variation of TEG performance. The purpose of this study is to test and analyze an automotive thermoelectric generator (ATEG) under different steady-state engine conditions and under the transient New European Driving Cycle (NEDC). Results show that both thermal inertia and pressure drop play a key role in designing an ATEG for real applications. Variations on exhaust temperature and mass flow rate prevent achievement of thermal steady state. Consequently, total energy generated during the NEDC is lower than that expected from a steady-state analysis. On the other hand, excessive pressure loss on the exhaust considerably minimizes engine performance.

Results show that the overall power generation of the ATEG can be significantly improved by maximizing the heat transfer through TEMs using a finned geometry, employing lower temperature thermoelectric materials and including a hot-side temperature control.

4.1 Introduction

Internal combustion engines waste through the tailpipe about the same amount of thermal power than that produced mechanically. It is estimated that this loss might be around 35-40 % of the fuel energy supplied, even when operating at top efficiency [23,30–36]. Therefore, recovery of a significant portion of this wasted energy by converting it into electricity would be highly advantageous [35,37–39]. Recovering the exhaust gas energy in a diesel passenger car under NEDC driving cycle can lead to potential fuel savings from 8% to 19% [41]. There are several feasible alternatives to recover energy from the exhaust. One of the most promising is using thermoelectric generators, due to their small weight and size, low maintenance costs, silent operation and high reliability [22,36,38,39]. This electric recovery will be especially useful in case of vehicles having a high degree of electrification, synergistically increasing the efficiency potential. Unfortunately, heat recovery systems have an important drawback, they increase fuel consumption due to back pressure in the exhaust [129–131].

A significant number of studies, in cooperation with several automotive manufacturers, have been performed to improve vehicle performance. Studies carried out focused on exhaust manifold, exhaust piping and catalytic converter packaging design for automotive tailpipe based on heat transfer analysis of the exhaust system. The most interesting results of these studies are detailed in Table 4.1, which summarizes the achievements reported in the literature.

Table 4.1 Summary of physical properties of ATEGs described in the literature.

Heat source	Max. ATEG power [W]		Temperatures [°C]			Cooling temperature [°C]	TE material	Exhaust flow rate [g/s]	Press. loss [mbar]	Ref
	Steady-state eng. cond.	Transient engine conditions	TE hot side	TE ΔT	Exhaust gases					
Cummins NTC350 14l 300HP Diesel truck engine	1068	-	-	175	-	-	BiTe	-	-	[45]
Toyota 2l	266	-	-	270	650	25	Skutterudites/ BiTe	-	-	[46]
Ruston 3YDA 3,6l	42,3	-	-	237	650	-	BiTe	-	-	[54]
Ford Lincoln BMW X6	700	450 (US06 Driving Cycle)	-	-	625	20	Skutterudites	45	-	[62] [61]
Combustor bench	35,6	-	-	396	595	25	SiGe	58	-	[24]
GMC Sierra 5.3l	177	-	283	-	550	88	BiTe	-	-	[1]
Chevy suburban	235	-	420	-	600	-	Skutterudites/ BiTe	-	-	[55]
Engine simulator	350	-	-	-	600	10	BiTe	-	-	[132]
Experimental rig	250	-	-	-	600	-	Silicide	-	<30	[56]
Light Duty Truck 2.3l diesel engine	500	150 (NEDC*) 200 (WLTP**)	-	-	450	-	BiTe	-	<30	[63]
Golf 1.4 TSI	111	30	344	260	557	65	BiTe+PbTe	37	36	Present work

* New European Driving Cycle (NEDC) ** Worldwide Harmonized Light vehicles Test Procedure (WLTP)

Various real engines and experimental exhaust simulators have been used in the literature to analyze the ATEGs performance. The aim of these investigations was not only to develop the most efficient ATEG but also to prove that ATEGs presented withstand the highest steady-state conditions of exhaust temperature and gas flow rate. The ATEGs power presented in Table 4.1 was obtained at maximum exhaust temperature and gas flow rate conditions. Most reported ATEG studies are carried out under steady state engine conditions, which are not representative of real driving conditions.

During real driving, exhaust temperature and gas flow rate vary depending on engine operating conditions. This variability of energy flows, along with thermal inertia of the ATEG, affects power production [37,57–60]. This effect can be observed in Table 4.1 for the few studies that tested ATEGs under transient conditions of a driving cycle such as NEDC, WLTP or US06. The results indicate a low energy recovery for transient driving conditions. The improvement of the thermal response of ATEG can significantly increase the recovered energy. Additionally, only few studies have been reported that consider the pressure drop and none of them studied its effect on engine performance.

Regarding thermoelectric materials used in the literature, Bismuth Telluride (BiTe) is the most popular thermoelectric material. However, its use is limited because its maximum operating temperature is relatively low. As BiTe is widely used and mass produced, their cost is more affordable compared to other thermoelectric materials. Other materials and techniques have been used to improve the power generation and efficiency of TEGs. Due to the high temperatures achieved on the exhaust line, the most promising and practical materials to be used for TEGs in exhaust heat recovery systems would be materials designed to withstand high temperatures. This means larger temperature gradients can be achieved with this material and thus more power and higher efficiency could be potentially achieved. Lead Telluride (PbTe) and calcium manganese have been used as materials in TEGs due to their ability to withstand higher temperatures [133,134]. Some TEGs have been manufactured with segmented materials. A material with larger zT at higher temperatures is

used on the hot side (e.g.: PbTe) and a material with a large zT at lower temperatures is used on the cold side (e.g.: BiTe). More power would be produced compared to a TEG made of high temperature rated material only. Other materials such as skutterudites and other manufacturing techniques such as quantum well structures have been investigated to improve TEG power generation efficiency but they are still very expensive and not commercially available [135,136].

ATEG presented in Figure 1 will be used in this study. It makes use of a hot side heat exchanger geometry that guarantees the TE material integrity under the highest exhaust temperature. This geometry was previously calculated using thermal simulations.

The main objectives of this study are (i) to test, compare, and analyze the performance of an ATEG under different steady-state conditions and under the New European Driving Cycle; (ii) to analyze the peak power generated and the total energy recovered on both experiments; (iii) to determine and analyze the effect of the backpressure on the global performance of the engine; and (iv) to present some ATEG design recommendations in order to optimize the power generation during transient conditions. Thermal model will be used to support the conclusions.

4.2 ATEG design

The ATEG presented in Figure 1 is designed to transform the energy contained in the exhaust gases of automobiles into profitable electric energy. The goal is to feed several electrical parts of the vehicle, preventing the alternator to work. This will lead to significant fuel and greenhouse gas emissions savings. It is estimated that this technology could drive to a reduction of about 5% in fuel consumption [39].

The size of the device is 160x500x60mm (WxLxH) with a total weight of about 7 kg. It consists of 12 thermoelectric modules (TEMs) electrically connected in

series but thermally connected in parallel. In this study, commercially available TEMs (TEG1-12611-6.0) are used as thermoelectric power generators in the ATEG. In Figure 2, the performance of electric power generated by a single TEM is plotted against hot side temperature T_h. The cold side temperature T_c was evaluated at 30°C, 50°C and 80°C.

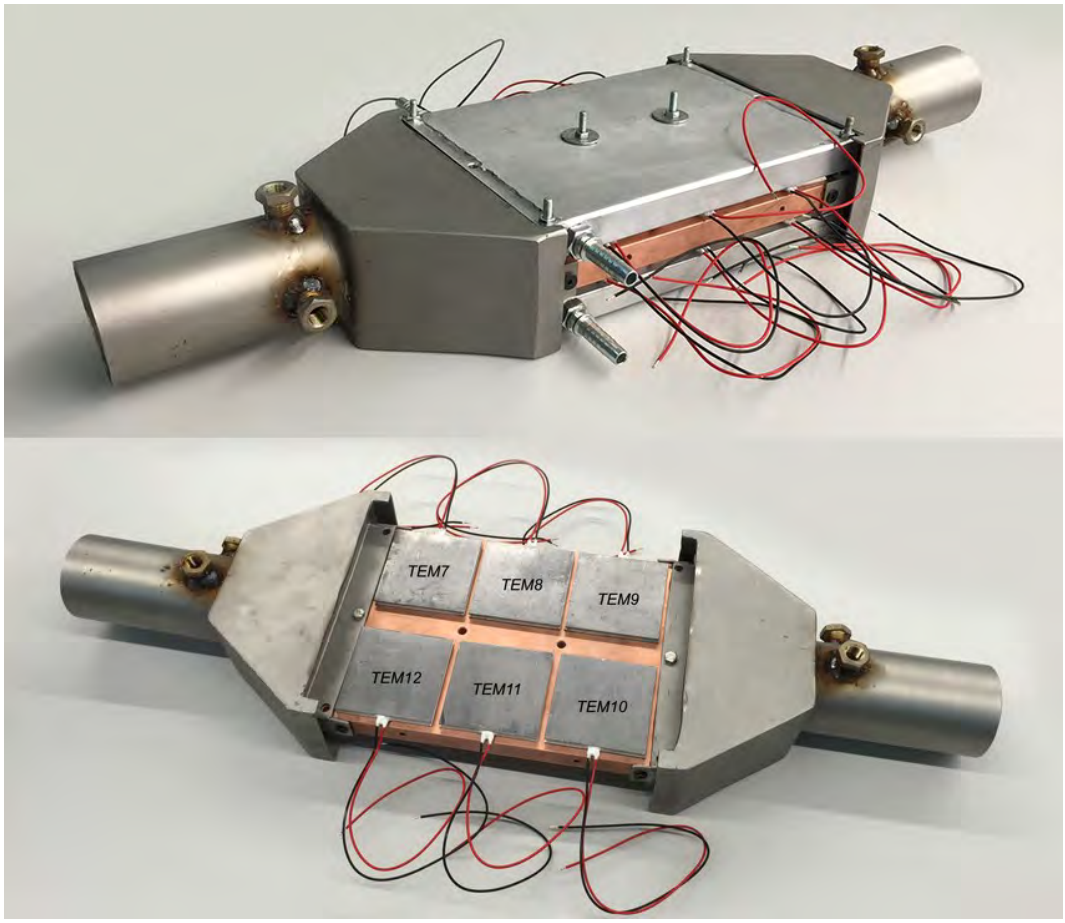

Figure 4.1 Waste heat recovery system prototype. Dimensions are 160x444x64mm (WxLxH).

TEMs used are constructed with PbTe and BiTe and stuck with high thermal conductivity graphite sheet on their both sides to provide low contact thermal resistance. The reason for choosing this kind of TEMs was its capability to withstand high temperatures.

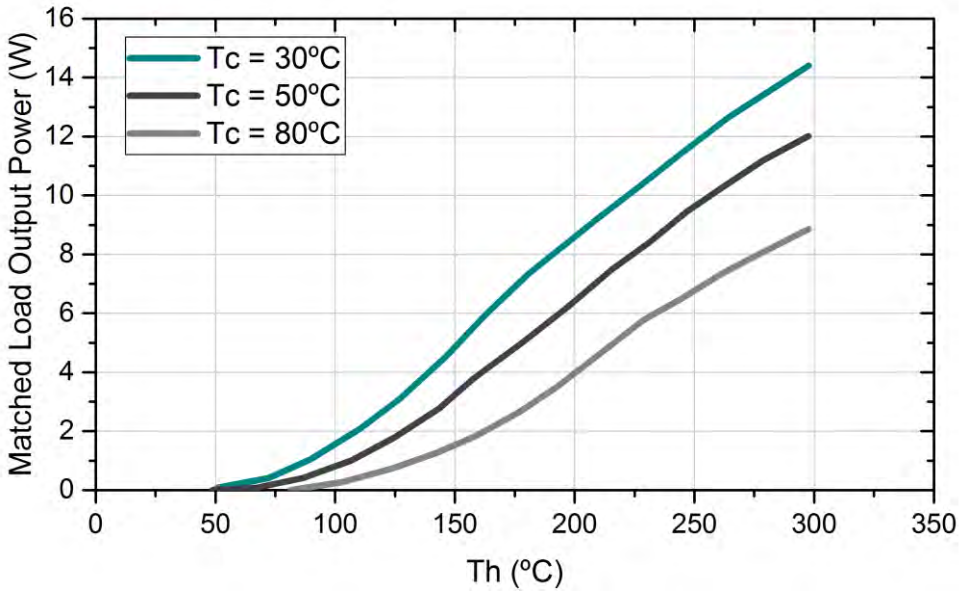

Figure 4.2 Performance of a single TEM (TEG1-12611-6.0) for the output power estimation of ATEG.

These modules are arranged between each surface of a copper heat exchanger (2), through which the exhaust gas is passed, and two aluminum cold plates (3). Figure 4.3 shows the schematic diagram of the experimental ATEG.

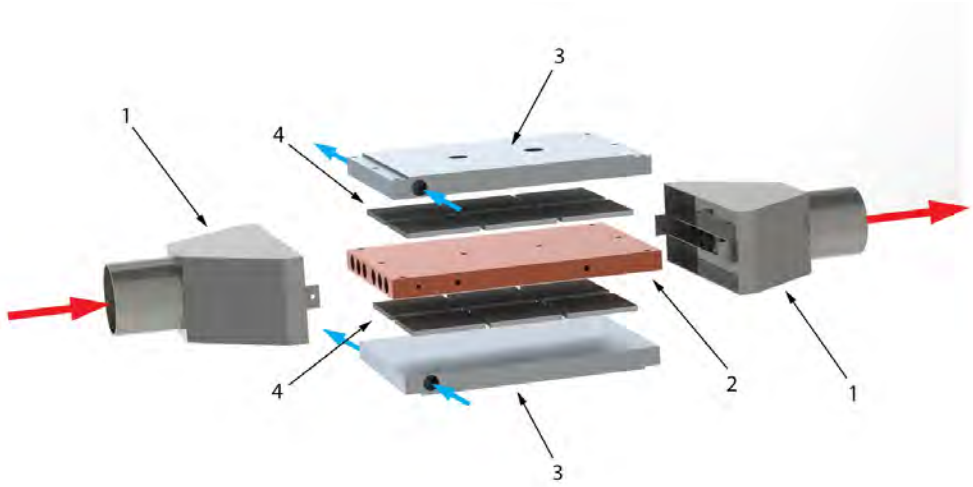

Figure 4.3 Assembly view of ATEG. 1) Exhaust fumes inlet and outlet. 2) Heat exchanger. 3) Cold plates. 4) Thermoelectric modules. In red, exhaust gases. In blue, water of cooling system.

Cooling system consists of a pump and a forced-air heat exchanger. Water is used as cooling fluid at a volumetric flow rate of 0.12 l/s. The pump moves the

water through the cold plates (3) connected in parallel. Water cooling method was chosen because it is proven to be more efficient than air cooling [137]. Water chiller used extract a maximum thermal power of 3kW.

The structure design, simulated using the commercial software ANSYS 17.1, was optimized to obtain an ATEG capable to withstand the highest measured temperatures of exhaust gases produced by a gasoline engine. Main specifications of the tested engine are explained in following sections and summarized in Table 4.2. The design of ATEG presented in this study is based on the worst steady state regime, in terms of high temperature and large exhaust gas flow.

The rated operating temperature of TEMs used is 350°C for short periods of time, and 310°C for extended operation. On the other hand, the maximum exhaust gases temperature measured at the same tailpipe position where ATEG is installed is about 720°C. This maximum temperature is achieved in steady-state condition with a mechanical load coupled to the engine. Therefore, to assure the integrity of the system, the ATEG was designed to synchronize the maximum working temperature of TEMs with the maximum exhaust gases temperature.

Figure 4 shows the simulation of the ATEG under four steady state conditions described in following sections. Boundary conditions for these four regimes were the exhaust gas inlet temperature and mass flow rate. They were extracted from four tests previously performed with a gasoline engine described in Table 4.2. Regimes 1, 2, 3 and 4 correspond to an engine speed of 2000 rpm, 2000 rpm, 2000 rpm, and 4000 rpm, and a full-throttle pedal position FTPP) of 15%, 45% 85%, and 85%. FTPP, in percentage, represents the engine acceleration in terms of throttle pedal travel position.

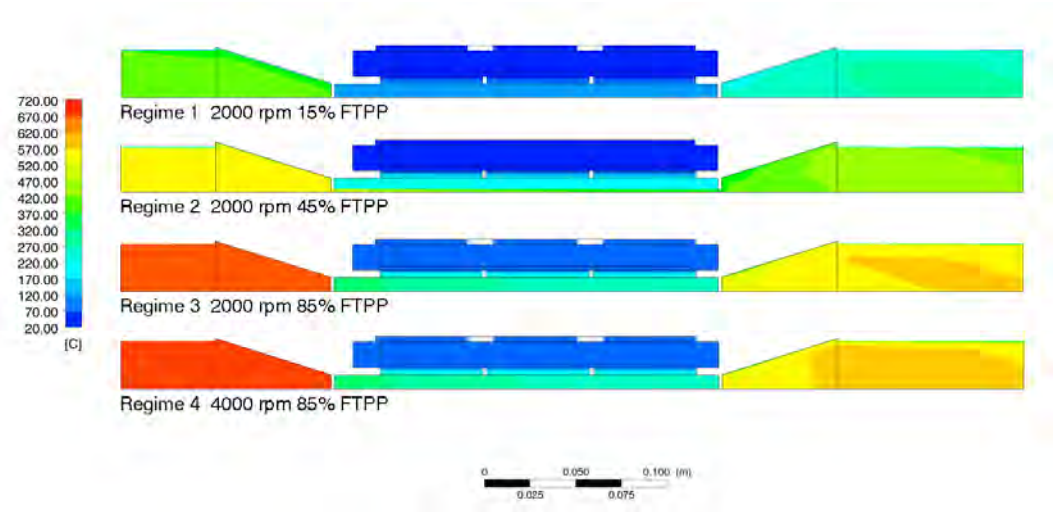

Figure 4.4 Temperature contour over a longitudinal cross section of ATEG. Here is represented only a symmetric half-model.

Regime 4 simulates the most extreme conditions, with a maximum exhaust gas temperature of 720°C and a cooling inlet temperature of 75°C. For this particular regime, TEMs hot and cold side temperatures are 347.2°C and 91.8°C, respectively. Simulation confirms the feasibility of the design, showing that hot side temperature does not exceed the maximum operating temperature.

Internally, exhaust gases are forced to flow through a copper heat exchanger containing six round holes. Figure 4.5 shows the temperature contour of the outlet side for the Regime 4.

With regard to the electrical part, all TEMs are interconnected forming an electrical array of twelve modules arranged in series. Figure 4.6 illustrates the series connection. Each TEM is represented by a voltage source $V_{1,\ldots,12}$ and an internal resistance $R_{1,\ldots,12}$ [64,79].

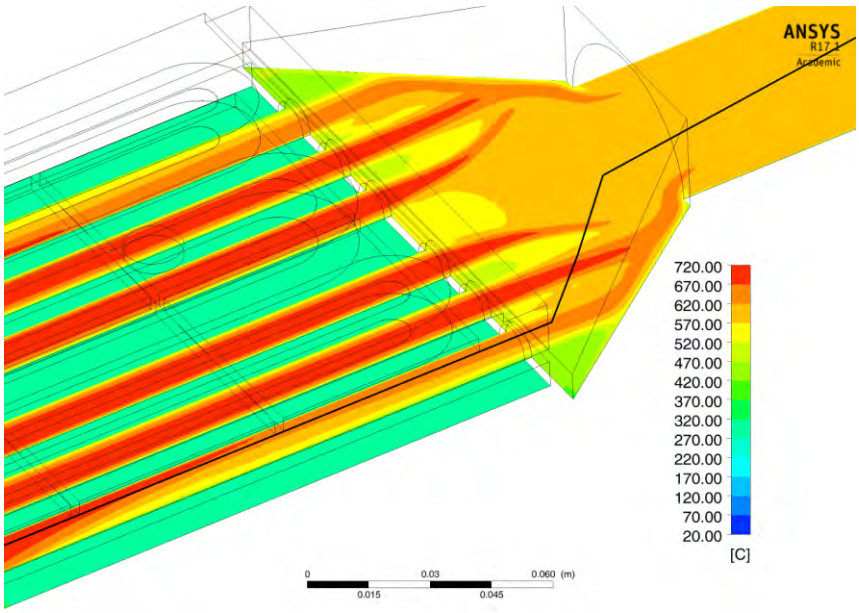

Figure 4.5 Temperature contour. Outlet. Regime 4.

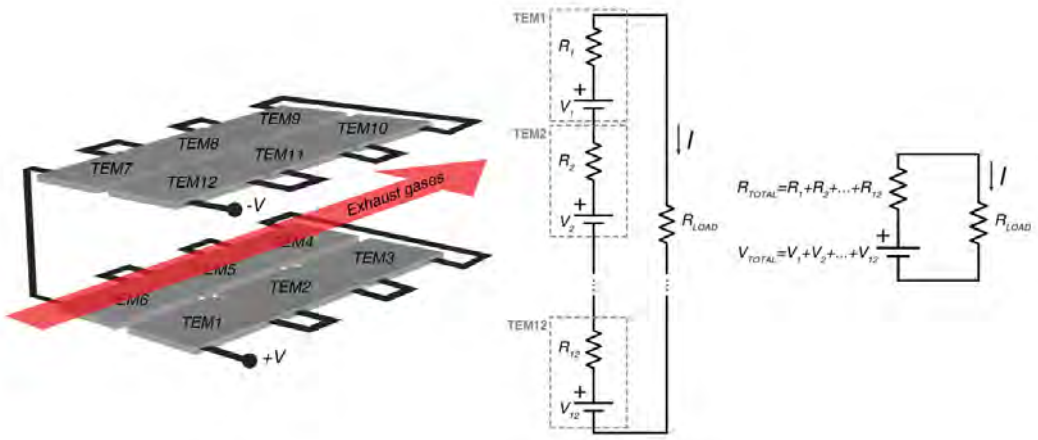

Figure 4.6 Electrical schematic of the array of TEMs electrically connected in series.

Although there are several ways to electrically interconnect TEMs, series configuration has been selected to allow assessment of the model.

4.3 Experimental setup

To assess the ATEG performance under steady state and transient conditions, experimental tests were accomplished on an engine test bench of Repsol Technology Center. A 4-cylinder 4-stroke turbocharged, intercooled, gasoline direct injection engine, typical of those used in European cars, was employed as

the experimental unit. Its specifications are listed in Table 1. The engine was coupled to an asynchronous machine model D2t MDA140, which also worked as starter during engine tests. The brake control system allowed measuring the engine speed, FTPP and effective torque. As said, FTPP, in percentage, represents the engine acceleration in terms of throttle pedal travel proportion. Additionally, a specific dyno controller set-up was adjusted in order to adapt its performance to dynamic test. The instantaneous gravimetric fuel consumption was determined using a Pierburg PLU 401/121 flow meter. In this study, the ATEG was installed downstream of the three-way catalyst (TWC).

Table 4.2 Main specifications of tested engine

Parameter	***Value***
Maker	VW
Model	Golf 1.4 TSI ACT (engine family EA211)
Euro certification	Euro 6b
Max. rated power	103 kW (at 4500 – 6000 rpm)
Max. rated torque	250 Nm (at 1500 – 3500 rpm)
Cylinders	4, in line
Bore (mm)	74.5
Stroke (mm)	80
Swept volume (cm^3)	1395
Compression ratio	10:1

As previously explained, the objective of this study is to test the aforementioned ATEG and obtain experimental data at various steady state and transient engine conditions. Steady-state engine modes were defined by setting constant engine speed and torque, which allow obtaining the desired exhaust temperature and mass flow rate. By setting different combinations of engine acceleration and

mechanical load the desired exhaust temperature and mass flow rate can be obtained.

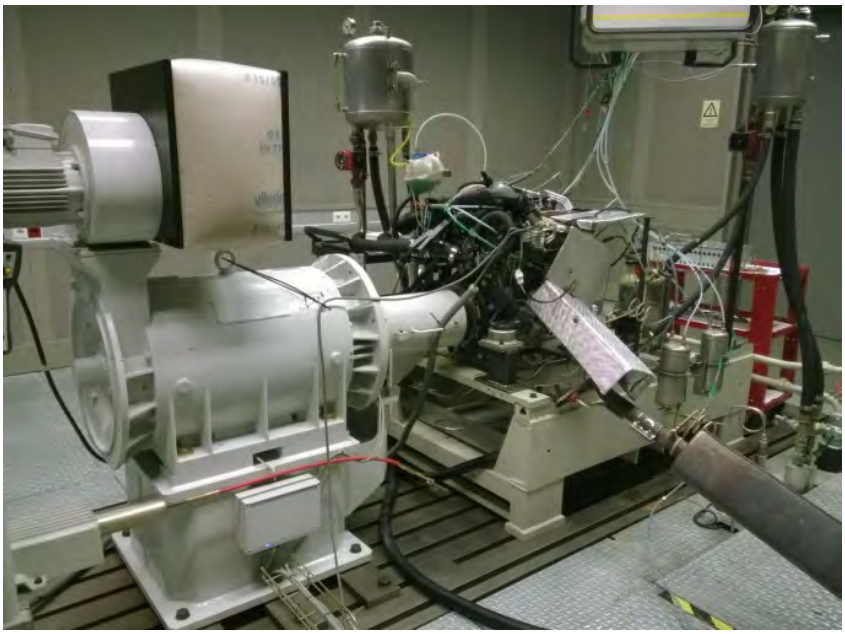

Figure 4.7 Engine test bench. Engine Lab of Repsol Technology Center.

On the other side, the transient engine tests allow observation of the behavior of the ATEG under more realistic working conditions. Then, the ATEG has been tested under a normalized driving cycle. A driving cycle is defined to standardize the evaluation of the vehicles' fuel economy and emissions, which is a speed profile as a function of time. It represents the traffic conditions and driving behavior in a specific area. A driving cycle consists of a mixture of driving modes including idle, cruise, and engine acceleration and deceleration conditions. Making use of a driving cycle permits comparing the results with other ATEGs.

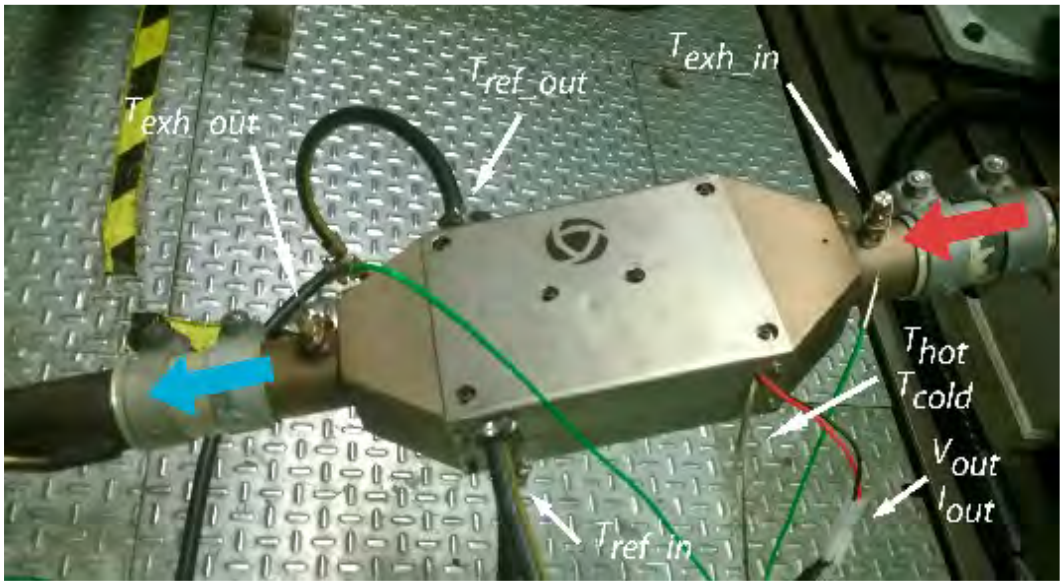

Figure 4.8 ATEG installed on the exhaust system of the engine cell.

Figure 4.8 shows the ATEG installed on the exhaust system. The acquired data is: exhaust gas inlet T_{exh_in} and outlet T_{exh_out} temperatures, water cooling inlet T_{ref_in} and outlet T_{ref_out} temperatures, hot T_{hot} and cold T_{cold} side temperatures and generated voltage V_{out} and current I_{out}. Additionally, parameters such as torque T, fuel consumption F, engine power P, and thermal efficiency η have also been obtained.

4.4 Results and discussion

4.4.1 Steady-state tests

Figure 4.9 and Figure 4.10 show the data obtained from the steady-state study. On the whole, four steady-state points were established: three common FTPP (15, 45 and 85 %) at 2000 rpm and the last mode at 4000 rpm and 85 % of FTPP. It can be observed that all electrical parameters such as V_{out}, I_{out} and P_{out} increase with the engine load. As detailed in Figure 4.10, as engine load increases, exhaust gas temperature and flow rate are higher and therefore more power is generated by the ATEG.

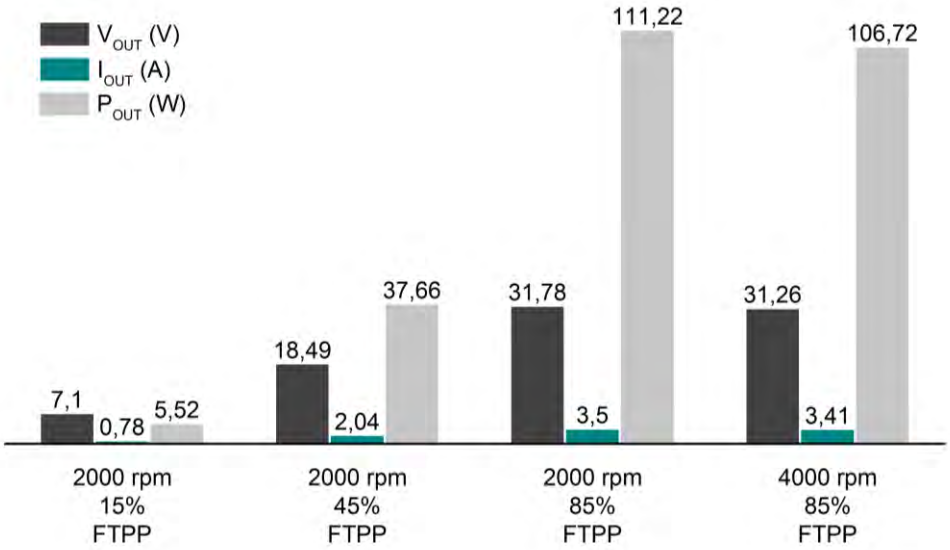

Figure 4.9 ATEG electrical outputs under different steady-state conditions.

Focusing on the last steady-state point (4000 rpm 85% FTPP), it can also be observed that, in spite of having the highest exhaust temperature, the electrical power production is lower than expected. That is because the higher temperature of the cooling system causes a ΔT decrease on TEGs, Figure 4.8. The exhaust temperature lost $T_{EXH\_IN} - T_{EXH\_OUT}$ through the ATEG remains almost constant throughout all the tests.

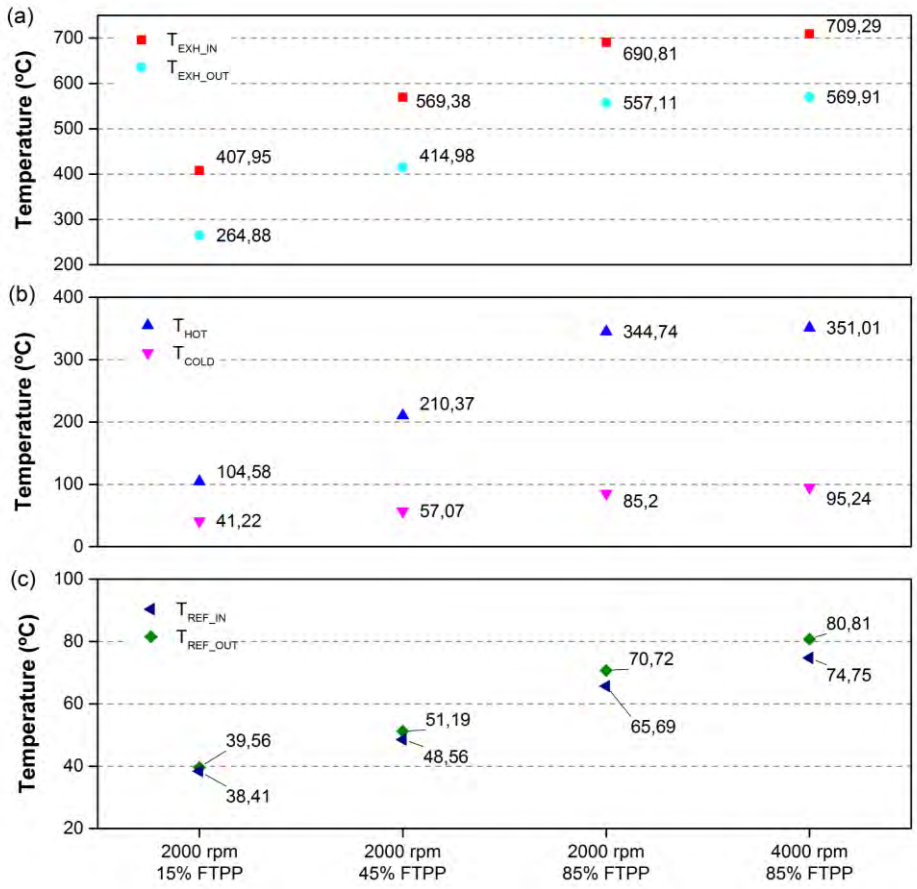

Figure 4.10 (a) ATEG inlet and outlet exhaust temperatures, (b) thermoelectric hot and cold side temperatures and (c) water cooling inlet and outlet temperatures.

Considering the data obtained from the experiments, the way vehicles are driven is a significant factor affecting ATEG performance for waste heat recovery. As vehicle speed and engine load increases, a better performance of ATEG is observed. It can be found that the higher the vehicle speed and engine load are, the better the performance of the ATEG is. That is because exhaust gas temperature and mass flow rate increase with the vehicle speed and engine load. Most of the ATEGs developed in the literature have been designed to withstand the maximum temperature of the exhaust gases. In this case, the ATEG was designed to withstand the maximum allowable temperature of TEGs, which was $T_{hot} = 350°C$ at $T_{exh\_in} = 700°C$. It should be noted that this working point is rarely achieved during normal driving conditions. It can be stated that the

majority of ATEGs will work below its maximum power point (MPP). This effect can be observed in more detail in the following chapter.

4.4.2 Transient tests

In order to study the thermal and electrical behaviors of the ATEG under transient conditions, the device has been tested under NEDC. NEDC is a combined cycle consisting of four Urban Driving Cycles (UDC) followed by an Extra Urban Driving Cycle (EUDC). During a NEDC driving cycle, the vehicle conditions change periodically, with idling, acceleration, cruise, and deceleration. At the EUDC stage, the vehicle speed increases up to 120 km/h, the exhaust temperature and mass flow rate increase as well, leading to improved performance of the TEG. Figure 4.11 shows the NEDC cycle.

The full test starts with four repetitions of the UDC cycle, also known as ECE. It was devised to represent city driving conditions, e.g. in Paris or in Rome. It is characterized by low vehicle speed, low engine load, and low exhaust gas temperature. EUDC segment has been added after the fourth UDC cycle to account for more aggressive high-speed driving modes. The maximum speed of the EUDC cycle is 120 km/h.

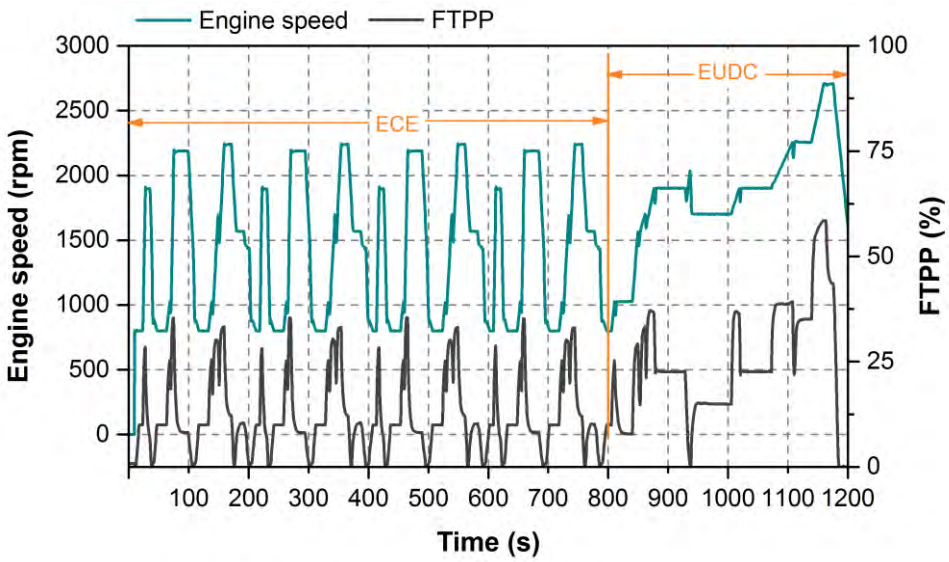

Figure 4.11 Engine speed and FTPP vs time of New European Driving Cycle.

Three NEDC tests were performed in total to evaluate the ATEG behavior: one cold-start NEDC test and two hot-start NEDC tests. The two hot-start tests were performed in the same way; therefore, only one test has been plotted. As can be seen in Figure 4.12, during the ECE cold start test, the exhaust temperatures are lower than those of the hot start test. It can also be observed that temperature difference of exhaust gases through the ATEG (ΔT) remain almost constant, maintained around 150°C over the test. In addition, the highest exhaust gases temperatures achieved are about 550°C. Considering that the ATEG is designed to withstand temperatures up to 720°C, TEMs will not be damaged due to excessive temperature.

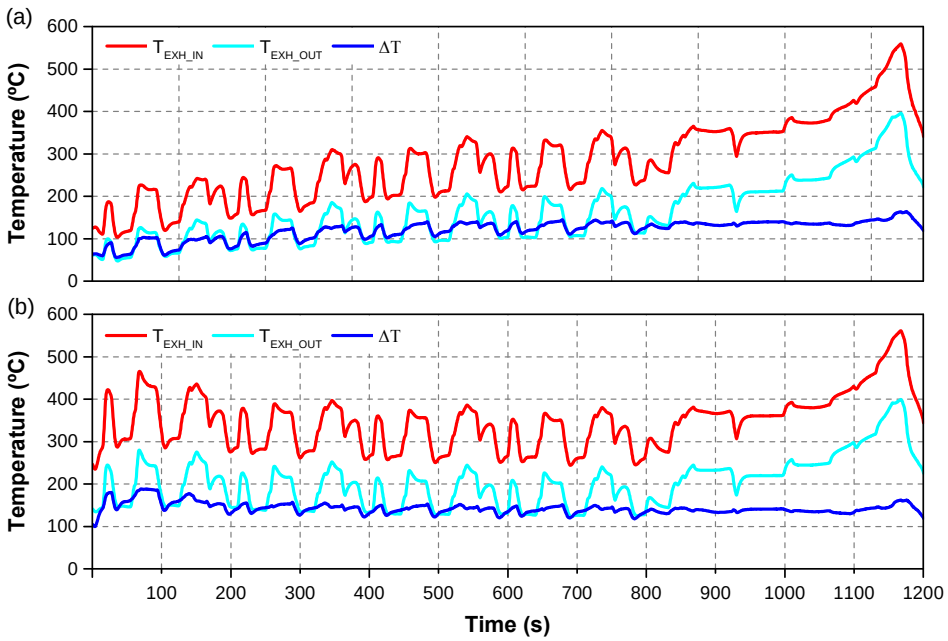

Figure 4.12 ATEG exhaust temperatures under a cold-start (a) and a hot-start (b) NEDC test.

Figure 4.13 shows the inlet and outlet cooling temperatures of the ATEG. Due to the fact that the ATEG cooling circuit is independent from the engine cooling system, temperatures T_{REF_IN} and T_{REF_OUT} are lower than the operating temperature of the engine, which was 80°C. These lower cooling temperatures allow the ATEG to achieve higher ΔT on TEGs, see Figure 4.14. Consequently, as

shown in Figure 4.15, voltage, current, and power generated was expected to be higher in this configuration than in an ATEG cooled by the engine cooling system.

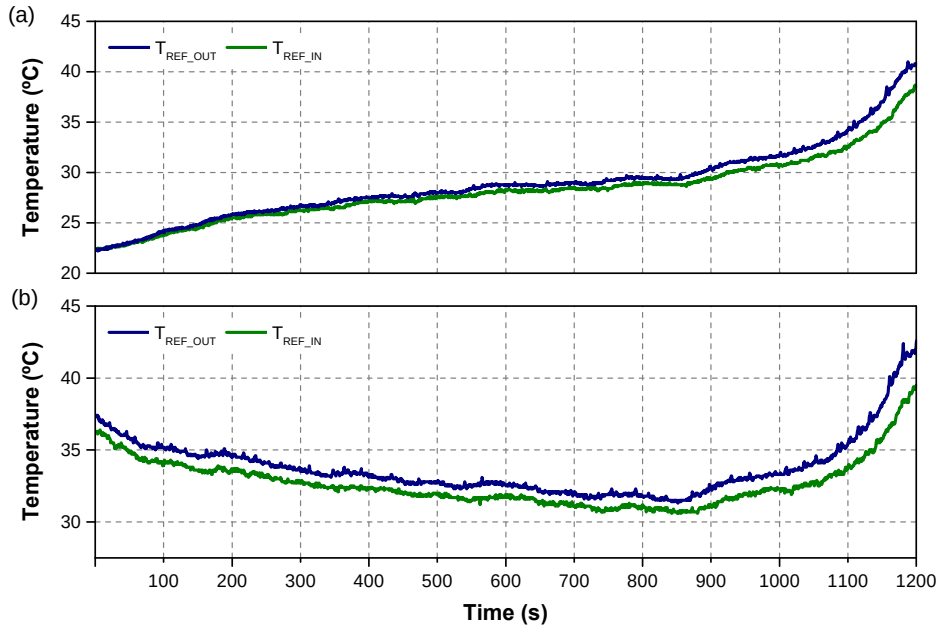

Figure 4.13 ATEG water cooling temperatures under a cold-start (a) and a hot-start (b) NEDC test.

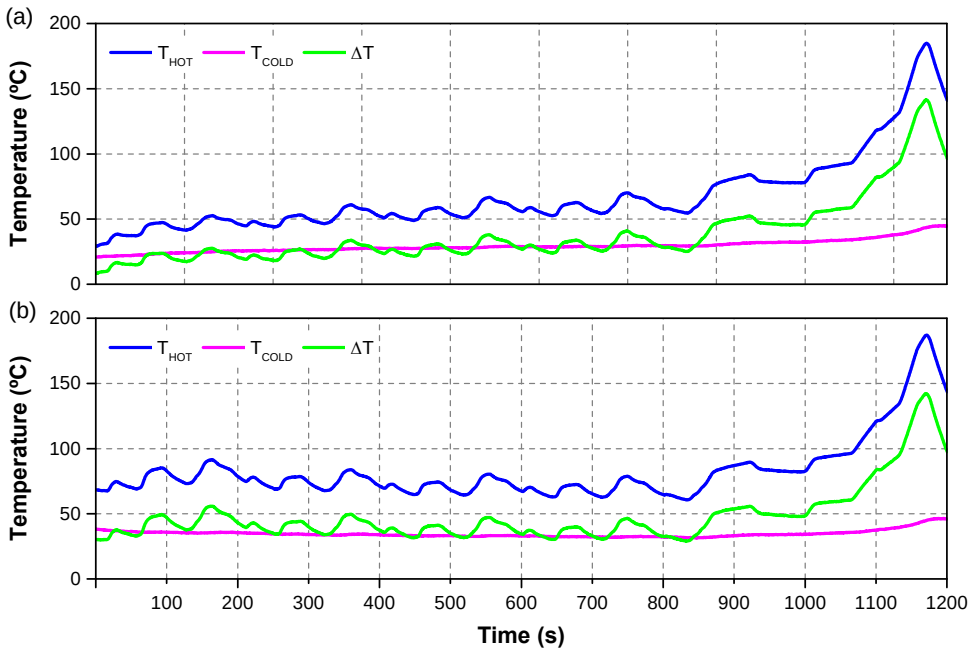

Figure 4.14 ATEG thermoelectric module temperatures under a cold-start (a) and a hot-start (b) NEDC test.

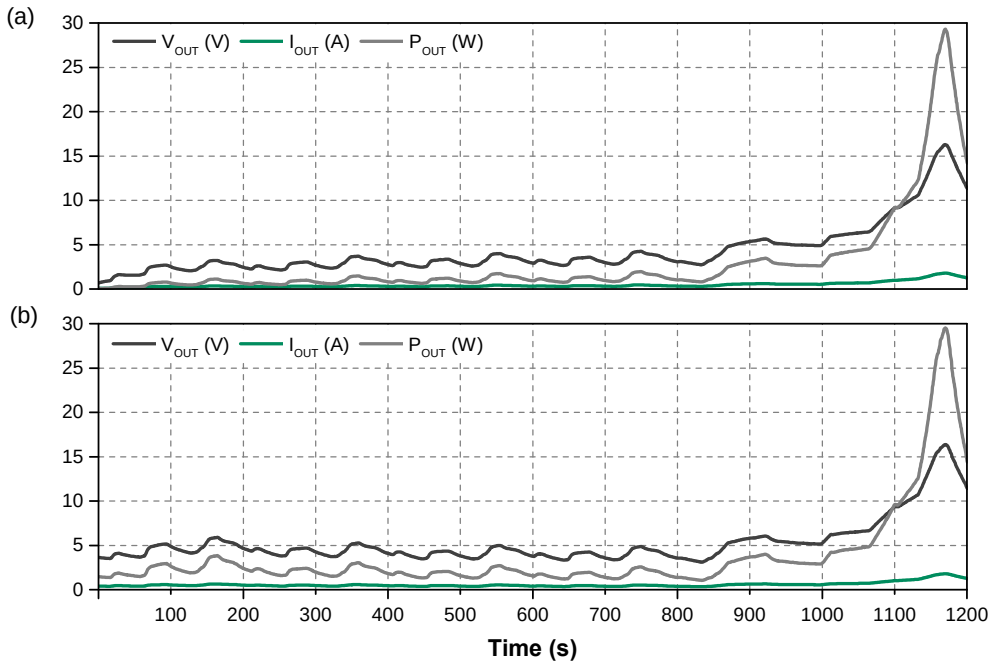

Figure 4.15 ATEG electrical outputs under a cold-start (a) and a hot-start (b) NEDC test.

However, even under these advantageous conditions, the electrical power generated during the NEDC driving cycle is very small. This is explained because ATEG is designed for steady-state situations, and when this design is applied to transient-state regimes, the thermal inertia detrimentally affects the result. In addition, the temperatures for which it has been designed greatly differ from those found in a driving cycle. It should be remarked that the ATEG presented is intended to generate the maximum power at 720ºC of exhaust gases temperature, and the average temperature of the whole test is 320ºC. These two aspects affect the final generation of ATEG.

4.4.3 Steady-state and transient tests comparison

Although it could be envisioned that both TEGs ΔT and power generated should be greater under a cold start due to the low cooling temperature, this thesis is not always fulfilled. The same occurs with exhaust temperature variations during ECE test. While ATEG has not reached a thermal steady-state point, most of the useful energy contained in exhaust gases contributes only to heating/cooling

the ATEG and not to producing electric power. The higher thermal inertia is the reason why ATEG under a NEDC produces less electric power than the same device under a steady-state engine condition at the same exhaust conditions, see Table 4.3.

Table 4.3 Power production comparison.

	Steady-state engine condition (2000 rpm 15% FTPP) (Regime 1)	NEDC (hot-start at 137s)	Steady-state engine condition (2000 rpm 45% FTPP) (Regime 2)	NEDC (hot-start at 1167s)
T_{exh_in} (°C)	408.0	407.8	569.4	561.4
T_{ref_in} (°C)	38.4	34.7	48.6	40.2
P (W)	5.5	2.07	37.7	29.0

Analyzing the EUDC part of the cycle, it can be observed that the engine is not capable of generating exhaust gases temperature close to the maximum expected, near 700°C. This fact is also responsible for why ATEG not generating the expected amount of electrical power under NEDC cycle. Therefore, an ATEG should be designed to work at its MPP preferably for lower temperatures.

On the other hand, the effect of the inclusion of ATEG on the engine performance has also been analyzed. In general, the engine performance was slightly reduced. As can be seen in Figure 4.16 and Figure 4.17, engine efficiency and power decrease when ATEG is attached to the exhaust system. The most significant reductions are observed on high acceleration regimes, when gas flow rate is maximum. These reductions can be explained by the additional pressure loss provided by the ATEG, which leads to an increase of the backpressure of the engine, see Figure 4.18. Higher FTPP accounts for higher exhaust gas flow rate and pressure loss. At 2000 rpm and 85 % FTPP, the mass flow rate is 37.07 g/s, corresponding to a maximum pressure drop of 36.53 mbar. Note that, in Figure

4.18, experimental data was taken in a different test, using a Saenz air flowbench D-680, in order to obtain more data points.

In Figure 4.16, $\eta_{WITHOUT\_ATEG}$ is the efficiency of the engine without the ATEG. Using exactly the same steady-state engine points, η_{WITH_ATEG} is presented, being the efficiency of the engine with the ATEG installed in the exhaust system. η_{WITH_ATEG} is calculated considering only the mechanical power generated by the engine. The energy generated by ATEG is not considered.

Efficiency is calculated considering the mechanical power generated by the engine and the average fuel mass consumed.

$$\eta_{WITHOUT\_ATEG} = \frac{P_{engine\_WITHOUT\_ATEG}}{\dot{m}_{fuel} LCV} 100 \tag{4.1}$$

$$\eta_{WITH\_ATEG} = \frac{P_{engine\_WITH\_ATEG}}{\dot{m}_{fuel} LCV} 100 \tag{4.2}$$

Where P, $\dot{m}_{fuel}$ and LCV are the power, fuel mass flow rate, and lower calorific value, respectively.

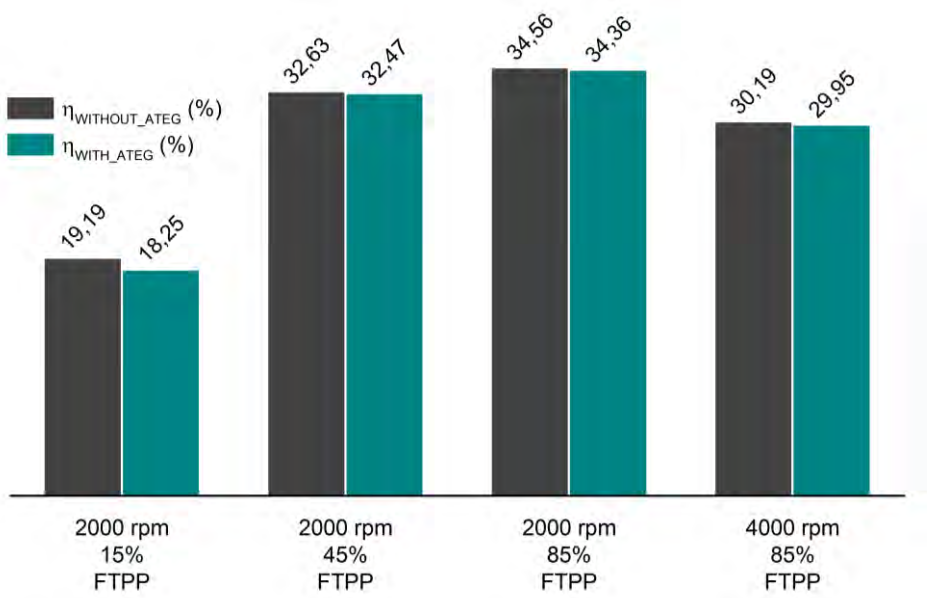

Figure 4.16 Engine efficiency with and without the inclusion of the ATEG during steady-state conditions.

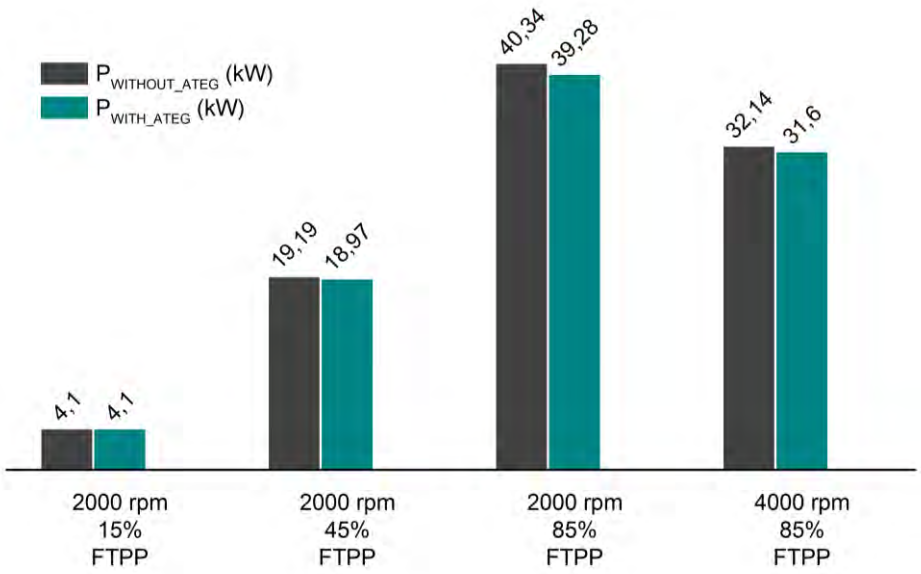

Figure 4.17 Engine power with and without the inclusion of the ATEG during steady-state conditions.

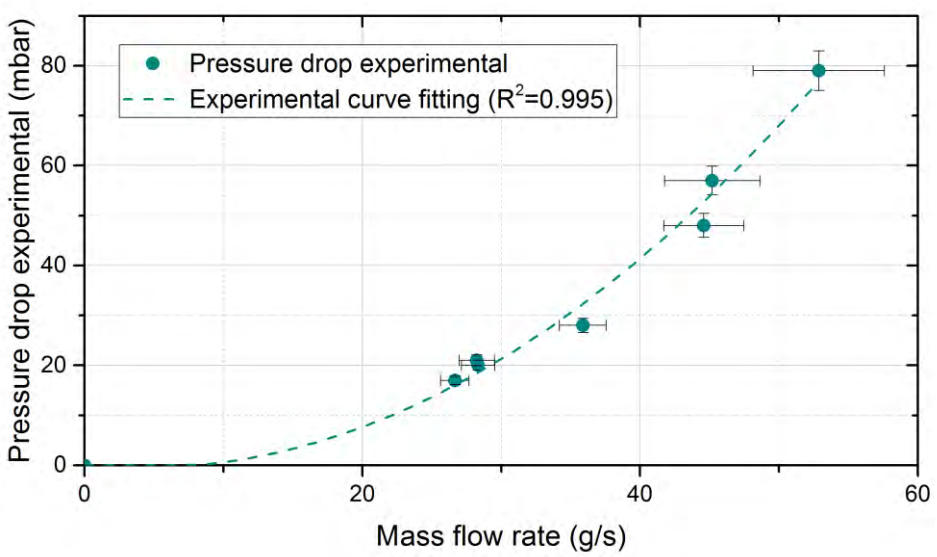

Figure 4.18 ATEG pressure drop as function of the exhaust mass flow rate.

Engine exhaust backpressure is defined as the exhaust gas pressure produced by the engine to overcome the hydraulic resistance of the exhaust system in order to discharge the gases into the atmosphere. At increased backpressure levels, the engine has to compress the exhaust gases to a higher pressure.

Consequently, additional mechanical work is needed and/or less energy is extracted by the exhaust turbine, which can affect the boost pressure of the intake manifold. This can lead to an increase of fuel consumption, see Figure 4.19, particulate matter (PM), CO emissions, and exhaust temperature. The increased exhaust temperature can result in an overheating of exhaust valves and the turbine. An increase in NOx emissions is also possible due to an increment of engine load.

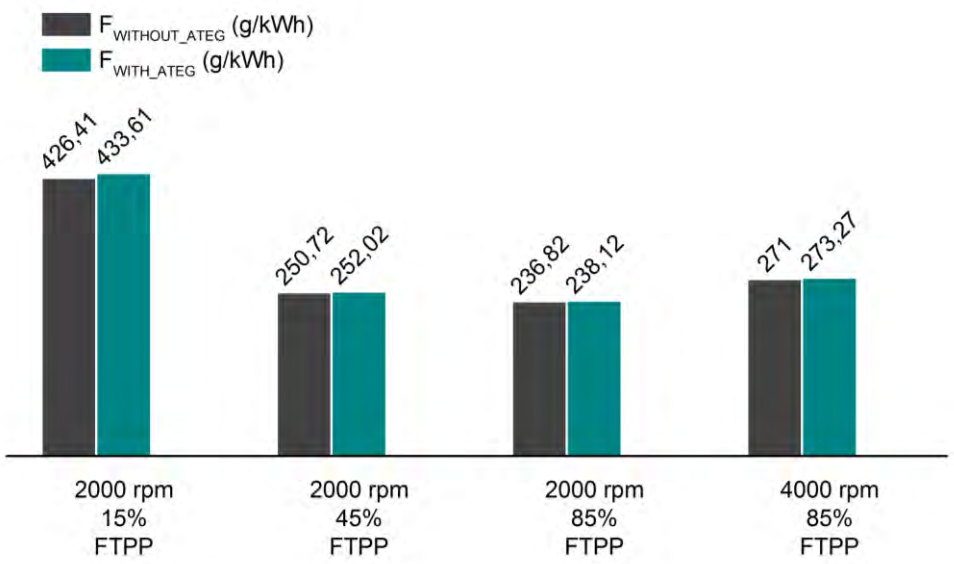

Figure 4.19 Engine specific consumption with and without the inclusion of the ATEG.

Figure 4.20 shows the exhaust gases temperatures collected during the three NEDC tests performed. The sampling time of tests was 0.5 s. The histogram presented shows the number of times (frequency) when temperature values fall into each given interval of 20°C. We can see that the most common temperatures appear in the range of 260°C to 380°C. Unfortunately, temperatures about 700°C, which are advantageous for the ATEG, rarely occur.

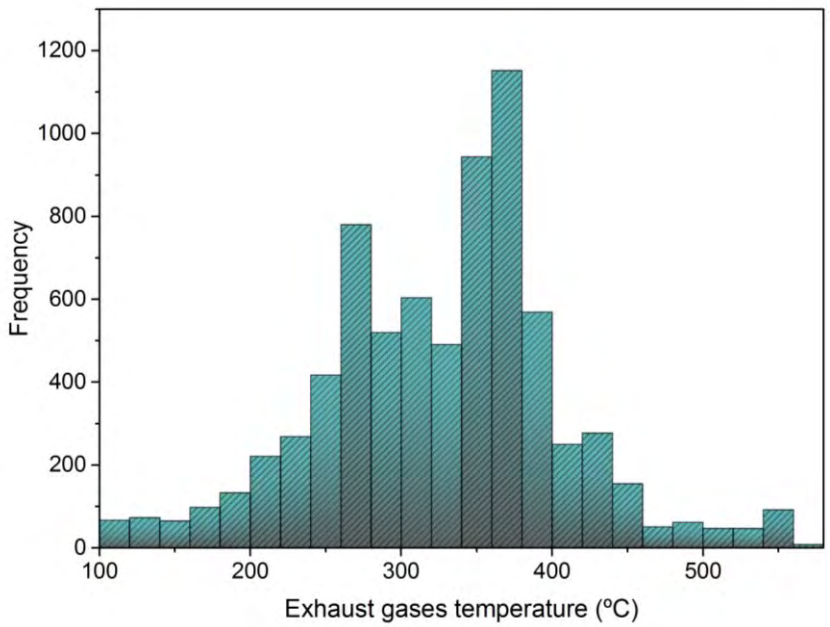

Figure 4.20 Exhaust temperatures histogram of 3 NEDC tests at 0.5 s sampling time.

In conclusion, an ATEG that generates around 4W during most of the cycle and about 30W during EUDC stage is obtained. These values differ from those which ATEG was designed for steady-state conditions.

Wang et al [5], show that the output power and efficiency increase significantly by changing the convection heat transfer coefficient of the high-temperature-side. Therefore, the electrical generation could be improved by using an internal geometry with larger exchange area, e.g. using fins. Thus, contact surface between the exhaust gases and the hot face would be enlarged. Consequently, the rate of heat transfer would increase by increasing convection. Therefore, an ATEG that would generate more power at lower temperature would be obtained. This is aligned with aim proposed in this study, to enhance the ATEG performance by reducing the optimal working temperature to fit the most common exhaust temperatures. However, when the engine would reach a high regime, such as 4000 rpm and 85% FTTP where temperatures of 700ºC are generated, TEMs would be damaged due to excessive temperature.

4.5 ATEG design enhancement

It has been demonstrated that an ATEG designed only for steady states does not work properly for transient states, which are those which ATEG would face in a real driving situation. In general, the following dichotomy exists: either an ATEG is designed to generate very little power in transient states to withstand higher temperatures, or to generate the maximum power in transient states but with the possibility of damaging TEMs due to higher exhaust temperatures.

As previously indicated, to improve the performance for real driving conditions, it is necessary to take advantage of lower temperatures, because they occur more often in a NEDC cycle.

Until now, high temperature materials like PbTe, SiGe or MgSi have been used to withstand the exhaust gases temperatures. BiTe has also been used but in a controlled environment, monitoring the exhaust temperature. Only Boretti et al [15] proposed a methodology using a by-pass of exhaust gases to lower the temperatures over a Rankine waste heat recovery system.

The best option would be to use lower temperature materials that would produce larger amounts of power at lower temperatures and, besides, that would maximize the time when ATEG would be operating in a NEDC. Figure 4.21 compares the power production of a PbTe and BiTe TEMs at various temperature gradients. BiTe TEM selected is a commercial module H-288-14-06-L2 with the same size as PbTe TEM.

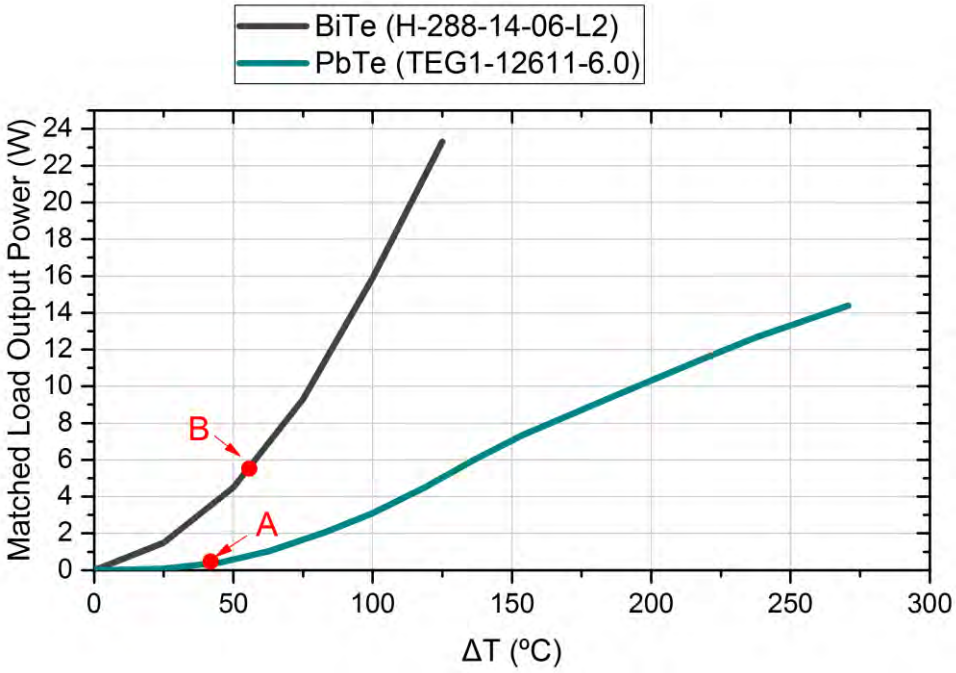

Figure 4.21 Performance of TEMs TEG1-12611-6.0 and H-288-14-06-L2 vs temperature gradient.

During hot-start ECE cycle, the mean hot and cold side TEM temperatures are 76.7°C and 35.2°C respectively. The mean temperature gradient is 41.5°C, point A in Figure 21. The mean power production during the same period is 2.26 W. In Figure 21, using the gradient of 41.5°C, the expected power production using PbTe is 0.21 W for each TEM, see point A. This leads to a total power output of the ATEG of 2.52 W. The divergence between expected and measured output power may be due to contact resistance.

Thus, going back to the simulation and changing the material of TEMs to BiTe, the expected overall output power of ATEG is shown, in dark grey, in Figure 4.22.

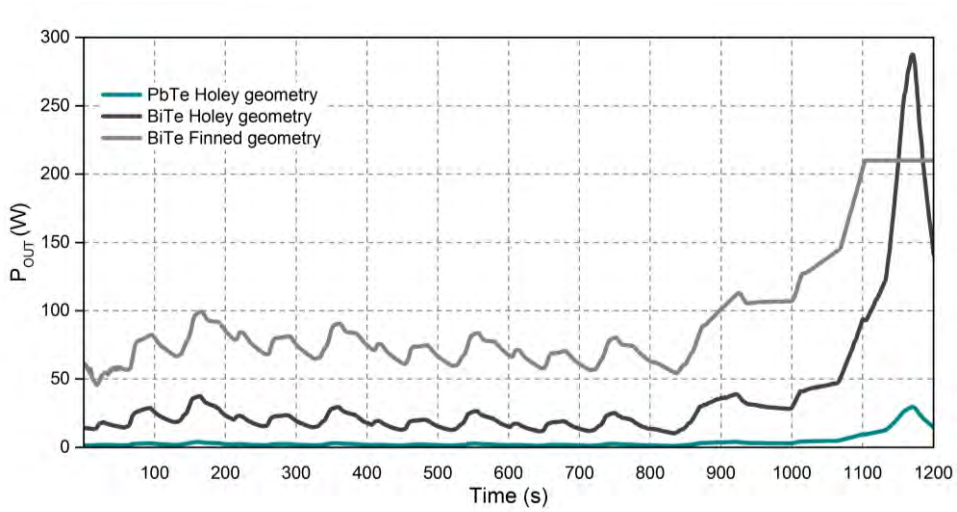

Figure 4.22 Output power of ATEGs presented under a NEDC driving cycle.

As an be observed, the expected power generation of ATEG using BiTe TEMs is higher compared to PbTe TEMs. This is because BiTe TEMs generate more power at lower temperature gradients, see Figure 4.21. Analyzing the temperatures of BiTe TEMs during NEDC cycle, the manufacturer's maximum hot-side temperature is never reached. This does not mean that at a given time, in real driving conditions, TEMs could reach higher temperatures. It is important to notice that exhaust gases could easily reach 700°C, and the maximum temperature reached during NEDC cycle is about 550°C. Therefore, the integrity of the system is not totally guaranteed.

As previously stated, the design could be further improved using an internal geometry with fins. The objective is to capture as much energy as possible from exhaust gases by increasing convection. Figure 4.23 shows, in green, the thermal resistance of the initial design, a copper heat exchanger with six passing-through holes. To improve the rate of heat transfer, a new finned geometry is proposed. The design was based on previously published conclusions [98,99,138–142].

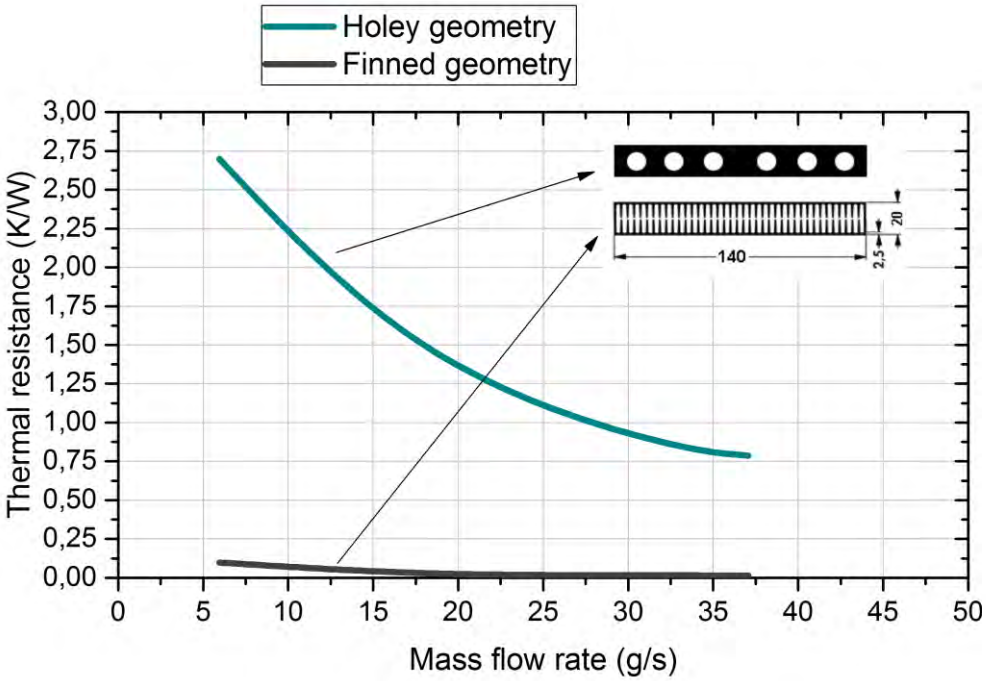

Figure 4.23 Thermal resistance of holey and finned heat exchangers.

The new geometry consists of two aluminum finned heat exchangers joined together as shown in Figure 4.23. External size of finned geometry is the same as the holey one. To prevent an excessive backpressure, internal cross-section area is maintained. As expected, thermal resistance of finned geometry is considerably smaller than holey geometry. Therefore, TEMs temperatures of hot and cold sides would reach faster higher values. Then, the ATEG would generate more power during the NEDC cycle. During hot-start ECE cycle, the mean hot and cold side TEM temperatures are 131.9 °C and 74.8°C respectively. The mean temperature gradient is 57.1°C. In Figure 4.21, using the gradient of 57.1°C, the expected power production using BiTe is 5.8 W for each TEM, see point B. This leads to a total power output of the ATEG of 69.6 W. The results shown in Figure 4.22 confirm these predictions.

As seen in Figure 4.24, TEMs are exposed to temperatures over 200°C. Manufacturer's recommended hot-side temperature of H-288-14-06-L2 is 150°C for continuous duty and 200°C for intermittent duty. This means that it is necessary to control the hot side temperature. As mentioned previously, this can be solved by using a system to by-pass the exhaust gases, see Figure 4.25.

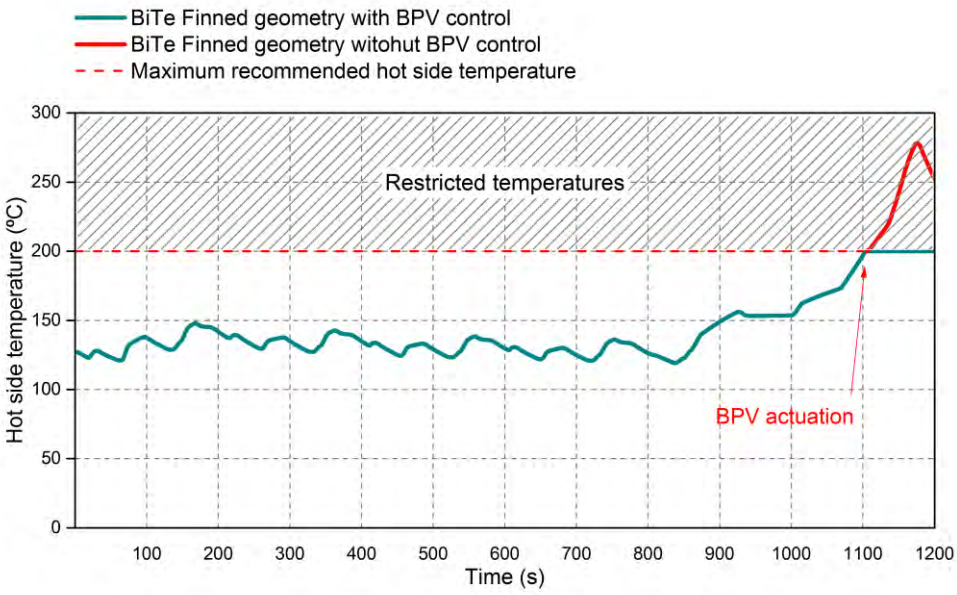

Figure 4.24 Hot side temperature of ATEG with BiTe finned geometry during NEDC duty cycle.

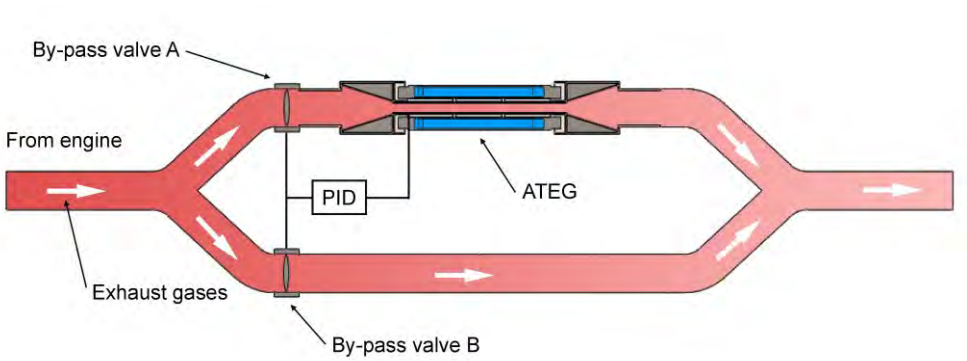

Figure 4.25 By-pass valves regulation scheme for the exhaust systems.

By-pass valves (BPV) control the amount of exhaust gases that flow through ATEG. Then, temperature of TEMs can be controlled using a PID control that regulates the aperture of the valves and a temperature sensor on TEMs hot side. When TEMs hot side temperatures remained below manufacturer's recommended temperature, BPV B would be closed and BPV A would be opened. Consequently, all exhaust gases would flow only through ATEG. When TEMs hot side temperatures exceeded manufacturer's recommended temperature, BPV A would stay closed and BPV B would be totally opened. Thus, exhaust gases flow only through the by-pass pipe and ATEG can be refrigerated.

While BPV A would be closed, ATEG temperature will decrease, so it is important to introduce a PID control to manage the opening and closing of PBVs to fix the TEMs hot side temperature at its maximum recommended value.

Consequently, introducing a system to control and fix TEMs hot side temperature prevents ATEG from damage, as seen in the straight red line region of Figure 4.24. Temperatures above red dashed line are blocked using the system previously mentioned. This explains the continuous power production beyond 1100 s in Figure 4.22.

Finally, to properly analyze the performance of an ATEG and with the aim of comparing the performance of various designs, it is useful, and more appropriate than using the power generation, to calculate the overall energy generated during a driving cycle. The following table shows the total energy generated by the three designs proposed.

Table 4.4 Energy generated by the three ATEG designs presented

Design	***Energy (Wh)***
PbTe + Holey geometry	1.35
BiTe + Holey geometry	13.14
BiTe + Finned geometry	32.70

4.6 Conclusions

In this study, an automotive thermoelectric generator ATEG based on vehicle waste heat recovery has been developed. The ATEG system behavior has been investigated under constant and dynamic driving conditions. It has been found that vehicle speed and load are significant factors affecting the ATEG performance for waste heat recovery, and that higher vehicle speed and load account for higher temperature of the exhaust gases and the better ATEG performance. In steady-state conditions, the maximum power output is 5.52 W at 2000 rpm at 15 % FTPP, and it reaches 111.22 W at 2000 rpm at 85 % FTPP.

Transient tests have demonstrated that the way in which the vehicle is driven is also a significant factor affecting the ATEG performance.

Most of ATEGs described in the literature have been designed to withstand the maximum temperature of the exhaust gases. However, during normal driving conditions this working point is rarely achieved. Additionally, the high thermal inertia of the ATEG presented prevents thermoelectric materials from achieving its MPP when it is subjected to transient conditions, such as those present in a NEDC driving cycle. Consequently, the results suggest that the majority of ATEGs will produce significantly less energy than expected from steady-state analysis. Highly frequent change of driving conditions may have a negative effect on the ATEG performance. Only vehicles that work in a very constant regime such as heavy-duty vehicles, combustion engines of range extender vehicles (electric series hybrid architecture) or stationary combustion engines for marine or cogeneration applications will take advantage of this kind of energy harvesters [143].

In addition, exhaust gases temperatures achieved under a NEDC test are concentrated on the range of 260ºC to 380ºC for a mid-size vehicle engine. Then, the design of ATEGs should be focused on this range in order to maximize the electrical power generation. The goal is to obtain the highest temperature gradient of TEGs at lower exhaust gases temperatures and protect TEGs from higher temperature situations that may occur.

Two modifications of the initial design were proposed and evaluated according to these premises. Results show that maximizing the heat transfer through TEMs using a finned geometry, employing lower temperature thermoelectric materials and including a hot-side temperature control, significantly improve the overall power generation of the ATEG. Following these considerations and for this particular study, energy generation during a NEDC duty cycle has been increased about 24 times its initial value.

Finally, the additional pressure drop provided by the ATEG has an adverse effect on the engine performance: engine efficiency, power, and torque are reduced

and specific fuel consumption is increased. In order to introduce thermoelectric waste heat recovery into vehicles, it will be mandatory to previously reduce this effect. Besides, it is also necessary to determine which is the minimum amount of electrical power recovered that makes a significant improvement on the vehicle performance. In some cases, these adverse effects can be overcome by the advantages provided by the ATEG.

4.7 Acknowledgments

This work has been partially funded by the Generalitat de Catalunya under Grant No. 2009.SGR-374 and the MINECO Grant No. FIS2012-31307. Authors would also like to thank Fundación Repsol for their collaboration, Association of Industrial Engineers of Catalonia (AEIC) for their partial financial support and the University of Girona under Grant MPCUdG 2016-4.

Chapter 5

Results and discussion

The current work has focused on two areas related to thermoelectricity: (i) the study of the capacity of controlling the thermal conductivity of TE and (ii) the development, testing and improvement of ATEG for real driving conditions.

The first part of the thesis proves that thermoelectric materials can be used as variable insulators for applications where the heat fluxes between two thermal bodies need to be properly altered. In order to meet the objectives of this part, which are described in Chapter 1, a thermoelectric model, explained in Chapter 2, was used. From the simulations, two control modes can be established in order to control the effective thermal conductivity of the thermoelectric pair: active mode and passive mode.

Active mode, which can be controlled by external voltage, is a good solution when a complete insulation or a high control of thermal conductivity is needed. The smaller the temperature difference between faces the higher the control of k_{eff} (i.e. higher values of k_{eff} can be obtained). However, as k_{eff} is strongly dependent on temperature gradient ΔT and ZT, the thermocouple has a limited heat pumping capacity. For large values of ΔT the thermocouple is no capable to reverse the heat flux and, hence, complete insulation is not achievable. The energy required to keep the TEM working at this point increases with ΔT. It is remarkable that the control of k_{eff} does not depend on geometrical parameters.

On the other hand, the passive mode permits a k_{eff} increment of $1 + ZT$ times with respect to the semiconductor thermal conductivity k_{pn}. In this mode, the extent of the k_{eff} variation is mainly dependent on the thermoelectric figure of merit ZT and on the pellet geometry. Unlike the active mode, the passive mode can be controlled by an external resistance, hence no external energy is required. However, the extent of the k_{eff} variation is lower and complete insulation cannot be attained.

Finally, it can be observed that in both cases, active and passive modes, the variation range of k_{eff} is strongly dependent on the figure of merit. By considering the most common (and commercial) TE materials, such as BiTe, the potential applications of TECs and TEGs are limited: the higher the ZT, the higher

the thermal control. In this regard, finding materials with high ZT is important in order to extend the use of TEMs as variable insulators.

The basic purpose behind this tunable insulator is that under certain circumstances it would be beneficial to selectively enable or impede the heat flow within particular sections to selectively control it. The application of this technology can be of interest, for example, in the building sector, in spacecraft structures or in components of machinery. Instead of acting as a passive component, such as conventional building insulators, the smart insulation is an adaptive component that can be selectively switched between low and high heat transfer states to take advantage of such instances where it would be beneficial to be able to turn off the insulation. Two example scenarios that would improve the energy efficiency in which little or no building insulation would be advantageous would be sunny winter days and cool summer evenings. This study opens new doors and new opportunities for thermoelectric materials.

The second part of the thesis has focused on exhaust heat recovery development. In order to meet the objectives of this part, which are explained in Chapter 1, an ATEG, described in Chapters 3 and 4, was constructed and tested. The present work describes a method to help ATEG designers to predict ATEGs performance in terms of fuel economy and it provides some design recommendations to obtain a better performance during transient behavior.

Firstly, the study presents an implementation of an ATEG model using ANSYS 17.1 software, based on a 3D FEM/FVM and including hot-side convective heat transfer, and thermoelectric governing equations. The results obtained from simulations are compared with experimental tests. Good agreement is shown for each configuration and over the entire temperature regimes investigated, which reveals the accuracy and reliability of the model. A maximum variation of 9.66 % with respect to measured backpressure data was reported for all four-engine conditions analyzed.

The present study confirms that the thermal contact resistances have a strong influence on power results, as already reported in the literature. It is highly advisable to correctly set this parameter because it strongly affects both the final

power generation and the heat flow through the TEM. However, the assumptions made in this work, with data taken from literature, were shown to be sufficient and they enabled highly accurate predictions of the ATEG performance.

Secondly, capital points to obtain a feasible ATEG are 1) using TEGs with high efficiency, 2) taking carefully into account the clamping force to reduce the thermal contact resistances, and 3) designing a good heat exchanger between exhaust gases and TEGs, are. Simulation tools like ANSYS are shown to be useful in order to determine the influence of these parameters.

Thirdly, based on the results obtained by the simulations, the ATEG performance assessment has been carried out giving insight of two key design parameters, power generation and backpressure. The relationship between them defines the feasibility of the design. In addition, this study presents an equation to predict the fuel economy provided by a given ATEG in terms of key design parameters, and it also gives insight about the optimal design point when fuel economy reaches its maximum value.

It can be concluded that the method presented in this paper enables ATEG performance estimation to be determined accurately, gives detailed insight into how thermoelectric modules perform in general, and enables prediction of ATEG performance in terms of fuel economy.

Besides, analyzing the fuel economy that ATEG presented in this paper could generate to a midsize vehicle, we conclude that, even though the design is capable to reduce fuel consumption up to 0.18%, there is a range of the engine operation that spreads into the unfeasible design region. Consequently, ATEG can be prejudicial to the engine efficiency for certain driving conditions. To address this problem, designing a bigger internal exchange area, i.e. using fins, would increase the heat flux through TEGs and reduce the pressure drop. The goal is to develop ATEGs with high power generation and small backpressure supply.

When designing ATEGs, it is important to know the overall working regimes of the vehicle in order to assure that the ATEG works always in the feasible region. The power generated by the ATEG should always be higher than the critical power generation presented in the present study. Following this rule, we can guarantee the fulfillment of the main objective of the ATEG: to reduce the fuel consumption of the vehicle.

We noted that the working regimes used to test ATEGs are usually steady state points, mainly due to its simplicity for laboratory set up. The inconvenience of using this testing method is that steady state regimes are not representative of real driving conditions. During real driving, exhaust temperatures and gas flow rates vary depending on engine operating conditions. This variability of the energy flow, along with the thermal inertia of the ATEG, affects the power production.

In order to investigate the performance affectation of this variability, the ATEG designed in the present work has been tested under both constant and dynamic driving conditions. It has been found that vehicle speed and load are significant factors affecting the ATEG performance for an efficient waste heat recovery, and that higher vehicle speeds and loads account for higher temperature of the exhaust gases, which leads to a better ATEG performance. In steady-state conditions, the maximum output power is 5.52 W at 2000 rpm at 15 % FTPP, and it reaches 111.22 W at 2000 rpm at 85 % FTPP. As expected, transient tests have shown that the way in which the vehicle is driven is also a significant factor affecting the ATEG performance.

Most of ATEGs described in the literature have been designed to withstand the maximum temperature of the exhaust gases. However, during normal driving conditions this working point is rarely achieved. Additionally, the high thermal inertia of ATEGs prevents that thermoelectric materials achieve their MPP when it is subjected to transient conditions, such as those present in a NEDC driving cycle. Consequently, the results suggest that the majority of ATEGs will produce significantly less energy than that expected from steady-state analyses. In addition, highly frequent changes of driving conditions may have a negative

effect on the ATEG performance. Only vehicles that work in a very constant regime such as heavy-duty vehicles, combustion engines of range extender vehicles (electric series hybrid architecture) or stationary combustion engines for marine or cogeneration applications will take advantage of this kind of energy harvesters [143].

In addition, exhaust gases temperatures achieved under a NEDC test are concentrated on the range of 260ºC to 380ºC for a mid-size vehicle engine. Then, the design of ATEGs should be focused on this range in order to maximize the electrical power generation. The goal is to obtain the highest temperature difference of TEGs at lower exhaust gases temperatures and to protect TEGs from higher temperature situations that may occur.

Two modifications of the initial design were proposed and evaluated according to these premises. Results show that maximizing the heat transfer through TEMs using a finned geometry, employing lower temperature thermoelectric materials and including a hot-side temperature control, significantly improve the overall power generation of the ATEG. Following these considerations and for this particular study, energy generation during a NEDC duty cycle has been increased about 24 times its initial value.

Finally, we note that the additional pressure drop provided by the installation of the ATEG in the exhaust line has an adverse effect on the engine performance: engine efficiency, power, and torque are reduced and specific fuel consumption is increased. In order to introduce thermoelectric waste heat recovery into vehicles, it will be mandatory to previously reduce or balance this effect. Besides, it is also necessary to determine which is the minimum amount of electrical power recovered that makes a significant improvement on the vehicle performance. In some cases, these adverse effects can be overcome by the advantages provided by the ATEG.

Chapter 6

Conclusions

The present thesis deals with the automotive waste heat recovery. The work focuses on the use of thermoelectric materials in order to reduce the vehicle's fuel consumption.

From the preliminary tests it was seen that thermal conductivity of TEMs have an important influence on the ATEG performance depending on the load applied. The first objective of this thesis was to analyze the influence of the load resistance on the TE thermal conductivity. The main conclusions of this work are found below.

- A mathematical model has been developed in order to simulate the electrical load influence on the thermal conductivity.
- The mathematical model, including TEG and TEC behaviors, has been proposed and validated following previous developments and other studies available in the literature.
- Thermal conductivity varies up to $1 + ZT$ times with respect to semiconductor thermal conductivity according to the load value. This behavior, called passive mode, is mainly dependent on the thermoelectric figure of merit ZT and on the pellet geometry.
- Under cooling mode, thermal conductivity is also dependent of the external voltage applied. This behavior, called active mode, is strongly dependent of temperature gradient ΔT and ZT. However, this mode it is not dependent on the geometric parameters.
- TEMs can be used as variable insulators for applications where the heat fluxes between two thermal bodies need to be altered conveniently.

The second goal was to develop an ATEG capable of withstanding high exhaust gas temperatures and providing enough energy to reduce the fuel consumption of the vehicle. The ATEG was tested using a gasoline engine under both steady-state and transient driving cycles. Conclusions are presented below.

- An ATEG prototype has been constructed and tested under steady-state and transient driving cycles.
- FEM has been developed to predict ATEG performance. Model reveals a good agreement with experimental tests.

- The thermal contact resistances have a strong influence on power results, as already reported in the literature. This parameter is highly advisable to be correctly set because it strongly affects the final power generation and the heat flow through TEMs. The assumptions made in this work with data taken from literature are shown to be sufficient, and enable highly accurate predictions of the ATEG performance.
- The relationship between ATEG power generation and backpressure define the feasibility of the design. This work presents an equation to predict the fuel economy provided by a given ATEG in terms of key design parameters, and it also gives insight about the optimal design point when the vehicle's fuel economy reaches its maximum value.
- ATEG presented in this paper is capable to reduce a mid-size vehicle's fuel consumption up to 0.18%.
- It is highly recommendable to design ATEGs with big internal exchange area maintaining enough cross sectional area. This will increase the heat flux through TEGs and will reduce the pressure drop.
- Transient results show that maximizing the heat transfer through TEMs using a finned geometry, employing lower temperature thermoelectric materials and including a hot-side temperature control, significantly improve the overall power generation of the ATEG. Following these considerations and for this particular study, energy generation during a NEDC duty cycle has been increased about 24 times its initial value.

Appendixes

Appendix A

Published paper: Electrically tunable thermal conductivity in thermoelectric materials: Active and passive control

---

Applied Energy 154 (2015) 709–717

Contents lists available at ScienceDirect

Applied Energy

journal homepage: www.elsevier.com/locate/apenergy

Electrically tunable thermal conductivity in thermoelectric materials: Active and passive control

Albert Massaguer Colomer*, Eduard Massaguer, Toni Pujol, Martí Comamala, Lino Montoro, J.R. González

Department of Mechanical Engineering and Industrial Construction, University of Girona, C. de Maria Aurèlia Capmany, 61, 17071 Girona, Spain

HIGHLIGHTS

- TE couples can be used as externally controlled insulators.
- Two control modes can be established: active and passive control.
- Active mode is a good option when a complete insulation is needed.
- Passive mode permits a thermal conductivity increment of $1 + ZT$ times.

GRAPHICAL ABSTRACT

This paper proposes a novel approach to the use of thermoelectric couples, treating them as variable insulators in thermal systems. Thermal conductivity in thermoelectric materials can be externally controlled by electrical parameters such as electrical load or DC voltage in passive and active systems, respectively.

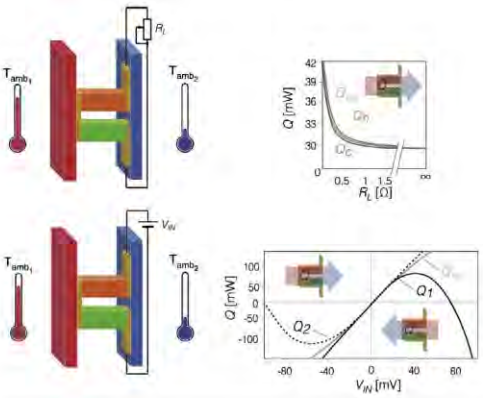

ARTICLE INFO

Article history:
Received 7 April 2015
Received in revised form 12 May 2015
Accepted 20 May 2015

Keywords:
Thermoelectricity
Thermal conductivity
Active control
Passive control
Insulator
Tunable

ABSTRACT

Applications involving the use of thermoelectric materials can be found in many different areas ranging from thermocouple sensors, portable coolers, to solar power generators. Generally, they can be subdivided by the direction of energy conversion. While the Peltier effect is used in solid-state refrigeration, the Seebeck effect is responsible for the conversion of temperature gradients into electrical voltage in energy harvesting systems. However, this paper proposes a novel approach to the use of thermoelectric couples, treating them as variable insulators in thermal systems. Here, we demonstrate that thermal conductivity in thermoelectric materials can be externally controlled by electrical parameters such as electrical load or DC voltage in passive and active systems, respectively. Active mode is a good solution when a complete insulation or a high control of thermal conductivity is needed. Passive mode permits a thermal conductivity increment of $1 + ZT$ times with respect to semiconductor initial thermal conductivity. Results open new doors and new opportunities for thermoelectric materials.

* Tel.: +34 972 418 489; fax: +34 972 418 098.
E-mail address: albert.massaguer@udg.edu (A. Massaguer Colomer).

http://dx.doi.org/10.1016/j.apenergy.2015.05.067
0306-2619/

1. Introduction

Thermoelectric (TE) devices are solid-state systems consisting of a number of alternate p- and n- type semiconductor thermoelements, which are connected electrically in series by metal interconnects and sandwiched between two electrically insulating and thermally conducting ceramic substrates. TE systems follow the laws of thermodynamics in the same manner as mechanical heat pumps, vapour compressors associated with conventional refrigerators, or other apparatus used to transfer energy [1]. They can act as coolers, heaters, power generators or thermal energy sensors depending on the direction of current. Due to the lack of moving parts or working fluids, TE technology has been used practically in almost all fields such as aerospace [2,3], instrumentation [4–8], medicine [9,10], industrial [11–15] or vehicles [16–20]. According to the working modes, these applications can be classified into three categories, which are coolers and heaters, power generators or thermal energy sensors.

By applying a voltage DC power source to a TE couple, heat will be moved through the pair from one side to the other. One face, therefore, will be cooled while the opposite face simultaneously is heated. This phenomenon may be reversed whereby a change in the polarity (positive and negative) of the applied DC voltage will cause heat to be moved in the opposite direction. Consequently, TE couples may be used for both heating and cooling thereby making it highly suitable for precise temperature control applications.

Otherwise, when TE couples are subjected to a temperature gradient, flow of majority carriers inside the material occurs from the hot to the cold side resulting in net generation of current. When an electric load is applied across this circuit, useful amounts of power can be generated in response to the temperature gradient applied. It is interesting to note the effect of heat transfer through TE couple with the applied load resistance; when electric load is the lowest the heat transfer is the highest due to the higher contribution of Joule and Peltier effect [21], and vice versa.

Taking into account these behaviours, it cannot be considered just the Fourier heat transport but also the Peltier, Thomson and Joule heat effects. These additional effects can be significantly greater or even opposite to Fourier's law and can be modified by the quantity and direction of current flow. Due to the capability of TE couples to tune the heat transfer flowing through them, another category can be added to the aforementioned applications list; externally controlled insulators.

Exploring the phenomenon at the nanoscale, transport can deviate strongly from the predictions of diffusion theory in macro and microscales [22,23]. With device or structure characteristic length scales becoming comparable to the mean free path and wavelength of heat carriers, classical laws are no longer valid and size effects become important [24–26]. Macroscopic heat conduction assumes that heat propagates at infinite speed, and it does not differentiate between the cause and effect relationship between heat flux and a temperature gradient.

In quantum mechanics, thermal conductivity k depends on the ability of sub-continuum energy carriers, which in solids are electrons and phonons, to travel to exchange this energy. k has contributions from both electrons and hole conductions k_e, and phonons k_p, $k = k_e + k_p$.

The ability to transfer heat by conduction is related to the capability of the electrons and phonons to travel and store/release thermal energy before losing it. When electrons are thermally excited, the mean free path increases, leading to a faster transmission of energy to cooler regions and a greater electronic thermal conductivity k_e. However, in semiconductors, k_e is generally smaller than in metals because there are few electrons available for conduction and they are continually interacting with the ionic lattice [27]. This interaction, due to the temperature gradient, causes energy to flow through the atomic lattice in the form of thermally generated lattice waves or phonons with a net energy flow from the hotter to the colder region. Then, primary heat carriers in semiconductors are phonons, making the lattice thermal conductivity k_p the main contributor to the thermal conductivity.

Heat flow control promises major technological developments in thermal management (e.g. transistors that control charge flow in electronics). Solid-state thermal switches and diodes [28] are particularly desirable for room-temperature cooling systems [29] or efficient building envelopes [30]. While materials with high and low thermal conductivities are available, materials with variable and reversible thermal conductivities are rare. The ability to precisely control the thermal conductivity of a material is fundamental in the development of on-chip heat management or energy conversion applications.

Thereafter, the purpose of this paper is to conduct an exhaustive analysis of thermal conductivity behaviour in thermoelectric materials. We propose two configurations to obtain variable thermal conductivity in thermoelectric materials. Considering that TE couples can work as thermoelectric cooler (TEC) or as thermoelectric generator (TEG), two control modes can be established regarding the external parameter control: active and passive control. Results demonstrate the capability of thermoelectric modules (TEMs) to act as an externally controlled insulator.

As can be seen from Fig. 1a and c, active control occurs when the TE couple works as a thermoelectric heat pump hence heat transfer through it is controlled by input voltage magnitude and polarity [31]. The variation of heat flow is achieved by changing the electric current supplied to the thermoelectric module so an external power source is required [32].

Moreover, as can be shown from Fig. 1b and d, passive control occurs when the TE couple works as a generator hence load resistance controls heat transfer through itself [33]. Electrical power generated due to the Seebeck effect is fed back to the thermoelectric material via an electrical resistor to produce a self-powered Peltier effect so no external energy is required. This will result in an increase of heat flow through the thermoelectric material and consequently a decrease in temperature difference across it. The level of change in heat flow or temperature difference can be controlled by the magnitude of the electrical resistance R_L. Geometrical values related to pellet surface S_{pn} and thickness th_{pn} are 2.3 mm^2 and 2.54 mm, respectively. Additionally, Q_{TEC} and Q_{TEG} represent the mean value of heat transfer across TEM.

2. Methods

To carry out the following study, we have used various theoretical models [21,34–36] that allow us to simulate the electro-thermal behaviour of a real TEM, working as a TEG or TEC. These models are based on the Eq. (1), which can be used with the first law of thermodynamics, and determines the temperature distribution in a thermoelectric material [37].

$$C_p \frac{dT}{dt} = \frac{d}{dx}\left(k\frac{dT}{dx}\right) - \left(T\frac{d\alpha}{dT}\right)J_e\frac{dT}{dx} + \frac{J_e^2}{\sigma} \tag{1}$$

where C_p, T, k, α, J_e and σ are the specific heat per unit volume at constant pressure, absolute temperature, thermal conductivity, Seebeck coefficient, coupled charge current flux and electrical conductivity, respectively.

However, due to the fact that nodal temperatures cannot be determined analytically without knowing the heat flux due to the thermoelectric effects, the models solve these nonlinearities using finite differences and Newton–Raphson methods, which

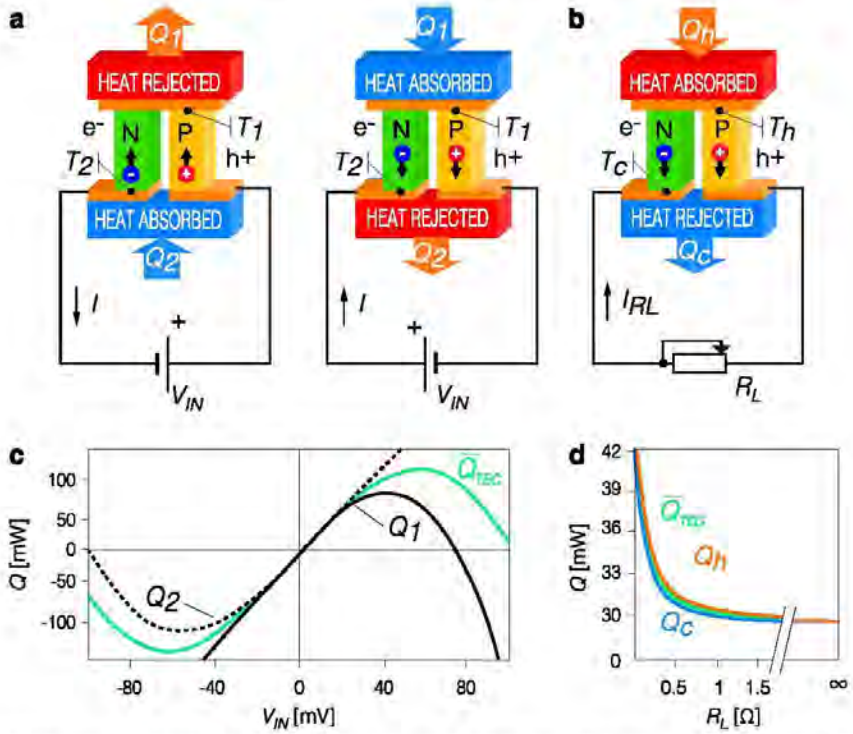

Fig. 1. Proposed thermal conductivity control modes. (a) Schematic of the active control. (b) Schematic of the passive control. (c) Heat transfer of the active control when $T_1 = 20$ °C, $T_2 = 30$ °C. (d) Heat transfer of the passive control when $T_h = 150$ °C, $T_c = 125$ °C.

calculate the temperature at different nodes separated in space by a discrete distance. In the transient state, the temperatures of these points are calculated at discrete periods of time and the temperatures for all the nodes are recalculated at the end of this time interval. Using the implicit finite difference method, the values of heat flux can be determined using the values of the temperatures of the time step before. The aforementioned models have been validated with experimental data at the same ranging temperatures used in this study. Simulations are carried out on a single thermoelectric pair. Figs. 2 and 3 show the heat transfer scheme of a TEG and a TEC, respectively, and model parameters can be checked at [20,34].

Eq. (1) contains an extra term $(T\frac{d\alpha}{dT})J_e\frac{dT}{dx}$ compared to the ordinary heat conduction equation. This is due to the Thomson effect, which suggests that distributed heating or cooling can occur even in the same solid because of the temperature dependence of Seebeck coefficient. However, as a result of that this study is focused on low-temperature system, the Thomson effect can be neglected [21].

Apart from this simplification, we made other common assumptions: (i) thermal conductivity, electrical resistivity, and specific heat capacity of non-thermoelectric materials are supposed constant within the operating temperature range, (ii) adiabatic boundary conditions are supposed on the outside surfaces of TE element, (iii) the heat leakage through solder layer and conducting strips are neglected and, finally, (iv) heat losses due to radiation and transverse convection through remaining area and lateral walls are also neglected.

On the other hand, temperature-dependent parameters of TEMs are considered in order to improve the accuracy of the models. The values of Seebeck coefficient α, electrical resistivity γ, and thermal conductivity k can be expressed mathematically by polynomial equations. These equations, which can be shown in Table 1, have been attached to the heat transfer ones. All coefficients are extracted from manufacturer's datasheet and can be calculated as a function of average temperature between hot and cold side of each TEM, $T = (T_1 + T_2)/2$. The rest of parameters used in the simulations are listed in Table 2.

The root mean square errors RMSE for heat extracted, electrical power generated and temperature difference between inlet and outlet are 0.566 W, 3.9×10^{-3} W and 7.4×10^{-3} °C, respectively. Additionally, the normalized root mean square errors NRMSE are 0.67%, 0.5% and 0.894%, respectively.

3. Active control

When a current I flows through a thermoelectric device, there is Peltier cooling at the source equal to $\alpha_{pn}IT_c$. This cooling effect is opposed by heat conduction at the rate $k_{pn}A_{pn}\Delta T/e_{pn}$. The cooling is also opposed to Joule heat within the thermoelements. It is easily shown that half of the Joule heating passes to the sink and half to the source, each half being equal to $I^2R_{pn}/2$. The expressions for the heat transport in both sides of the TEM are the following.

$$Q_1 = \alpha_{pn}T_1 I - \frac{k_{pn}S_{pn}}{th_{pn}}\Delta T - \frac{1}{2}I^2R_{pn} \quad (2)$$

$$Q_2 = \alpha_{pn}T_2 I - \frac{k_{pn}S_{pn}}{th_{pn}}\Delta T + \frac{1}{2}I^2R_{pn} \quad (3)$$

where Q_1, Q_2, k_{pn}, α_{pn}, T_1, T_2, S_{pn}, th_{pn}, I and R_{pn} are heat transfers at sides 1 and 2, thermal conductivity, Seebeck coefficient, temperature at sides 1 and 2, total area, thickness, electrical current and

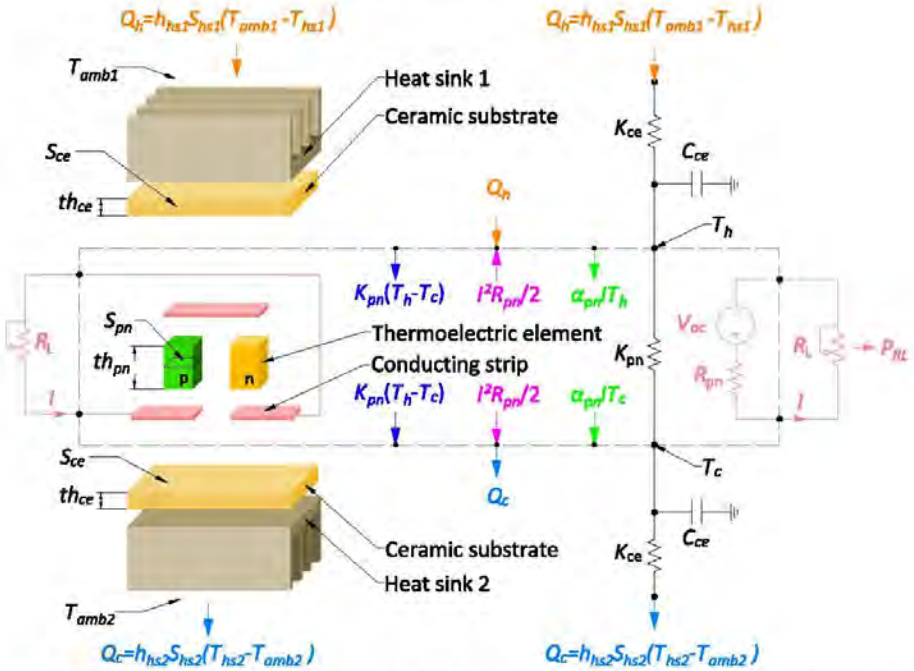

Fig. 2. TEG model scheme. Scheme of the heat transfer through a TE couple, which is controlled by an external resistance R_L.

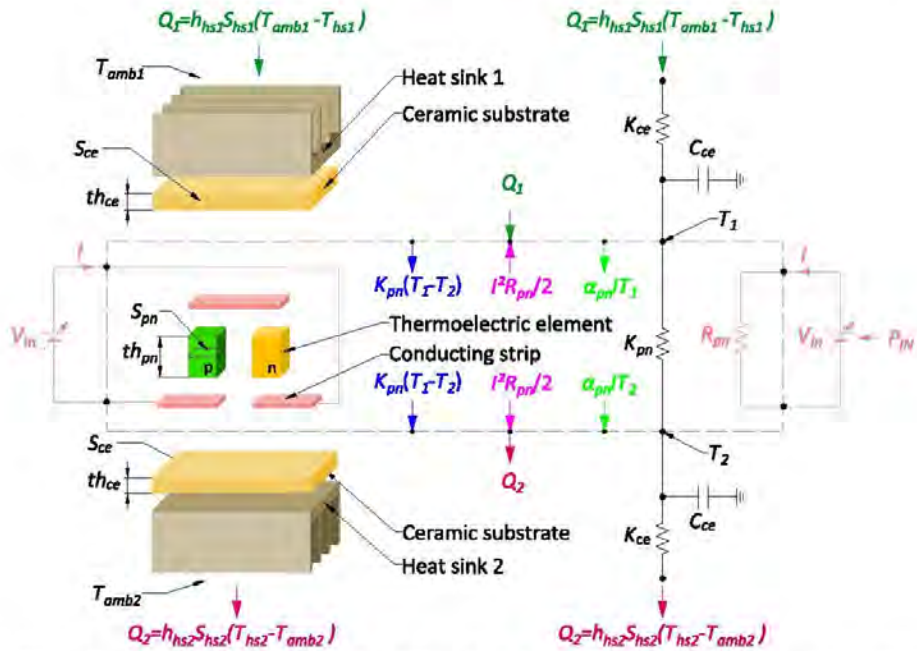

Fig. 3. TEC model scheme. Scheme of the heat transfer through TE couple, which is controlled by external voltage V_{IN} magnitude and polarity.

internal resistance of the TE couple, respectively. ΔT is the temperature difference between side 1 and 2 $\Delta T = T_1 - T_2$.

Taking advantage of this effect, the heat transfer and consequently thermal conductivity in TECs can be controlled by adjusting the input voltage V. The analytical solution to the thermoelectric phenomena that governs the variation of thermal conductivity with V can be found applying the Fourier's law of conduction $k_{eff} = Q_{TEC} th_{pn}/S_{pn}\Delta T$ to the entire system. Due to the

Table 1
Thermoelectric parameters. In this table each parameter is given as $a + bT + cT^2 + dT^3 + eT^4$, where a, b, c, d and e constants are tabulated.

	Parameter	a[a]	b[a]	c[a]	d[a]	e[a]	Units
α_n	n-type Seebeck coefficient	−394.05	3.08	-1.26×10^{-2}	2.07×10^{-5}	-1.15×10^{-8}	μV/K
α_p	p-type Seebeck coefficient	143.29	−1.62	9.91×10^{-3}	-1.81×10^{-5}	1.01×10^{-8}	μV/K
k_n	n-type thermal conductivity	14.2	−0.10	3.14×10^{-4}	-4.23×10^{-7}	2.15×10^{-10}	W/mK
k_p	p-type thermal conductivity	−65.8	0.64	-2.20×10^{-3}	3.26×10^{-6}	-1.74×10^{-9}	W/mK
γ_n	n-type electrical resistivity	-1.01×10^{-5}	5.63×10^{-8}	-9.78×10^{-11}	2.88×10^{-13}	-1.65×10^{-16}	Ωm
γ_p	p-type electrical resistivity	-6.26×10^{-5}	4.40×10^{-7}	-9.68×10^{-10}	1.12×10^{-12}	-5.40×10^{-16}	Ωm

[a] Values taken from manufacturers specifications.

Table 2
Simulation parameters.

Parameter		Values	Units	Source
th_n	n-type thickness	2.54×10^{-3}	m	[a]
th_p	p-type thickness	2.54×10^{-3}	m	[a]
S_n	n-type surface	2.3×10^{-6}	m^2	[a]
S_p	p-type surface	2.3×10^{-6}	m^2	[a]
ρ_n	n-type density	7700	kg/m^3	[b]
ρ_p	p-type density	7700	kg/m^3	[a]
C_n	n-type specific heat	200	J/kgK	[a]
C_p	p-type specific heat	200	J/kgK	[a]
S_{hs1}	Heat sink 1 surface	4.6×10^{-6}	m^2	[a]
S_{hs2}	Heat sink 2 surface	4.6×10^{-6}	m^2	[a]
h_{hs1}	Convection coefficient hs1	2000	W/m^2K	[b]
h_{hs2}	Convection coefficient hs2	2000	W/m^2K	[b]
th_{ce}	Ceramic substrate thickness	5×10^{-4}	m	[a]
S_{ce}	Ceramic substrate surface	4.6×10^{-6}	m^2	[a]
k_{ce}	Ceramic substrate thermal conductivity	36	W/mK	[a]
ρ_{ce}	Ceramic substrate density	3975	kg/m^3	[a]
C_{ce}	Ceramic substrate specific heat	765	J/kgK	[a]

[a] Values taken from manufacturers specifications.
[b] Calculated values.

fact that heat transfer is not equal on both sides of TEC, the equivalent heat transfer through TEC, Q_{TEC}, is calculated as $Q_{TEC} = (Q_1 + Q_2)/2$. Moreover, the current that flows through TE couple can be expressed as $I = (V - \alpha_{pn}\Delta T)/R_{pn}$. Finally, considering that TEC dimensions remain invariable during its operation, the function that describes the behaviour of effective thermal conductivity k_{eff} can be written as:

$$k_{eff} = k_{pn}\left(\frac{ZTV}{\alpha_{pn}\Delta T} - ZT - 1\right) \tag{4}$$

Since changing the V polarity may reverse heat transfer direction, the electric current I values may be also positive or negative. However, when heat transfer is reversed, T_1 and T_2 also reverse hence k_{eff} always remains positive. Note that the evolution of k_{eff} does not depend on the geometric parameters.

In order to study the behaviour of the Eq. (4) as a function of external parameters, six temperature gradients $\Delta T_{amb} = T_{amb1} - T_{amb2}$ were established as boundary conditions for the dynamic simulation: −90 °C, −50 °C, −10 °C, 10 °C, 50 °C and 90 °C. A part from that, all simulations has been repeated at various input voltages to obtain the k_{eff} evolution. Input voltage ranges were selected in accordance with the maximum heat pumping capacity of both sides (i.e. A and D points) of the TEM at each ΔT_{amb}. The results of the simulation can be shown in Fig. 4.

Four important points can be extracted from Fig. 4:

- Point A corresponds to the maximum value of k_{eff} when heat transfer flows from 1 to 2 (A point). It is located where maximum cooling of Q_1 is achieved. From that point, Q_{TEC} and k_{eff} tend to decrease with voltage and the heat flow reverses again. A point can be obtained by deriving the Q_1 expression with respect input voltage $\frac{\partial Q_1}{\partial V} \rightarrow V = \alpha_{pn}T_2$. Including this equation into Eq. (4) the maximum value of k_{eff} in cooling mode can be calculated as

$$k_{eff}^A = k_{pn}\left(\frac{ZT_c}{\Delta T} - 1\right) \tag{5}$$

- The second point, B, corresponds to the minimum value of k_{eff}. That is the point where heat transfer becomes null and heat flow reverses, $k_{eff}^B = 0$ (i.e. where TEC becomes a perfect insulator). The heat flow cancels when Seebeck effect $\alpha_{pn}\Delta T$ is counteracted by input voltage V. It is important to note that this point can be positive or negative depending on the stationary heat flow direction: while $T_1 < T_2$ the input voltage necessary to cancel heat flow is positive V^+, otherwise while $T_2 < T_1$ the voltage necessary is negative V^-.

$$V = \alpha_{pn}\Delta T\left(\frac{1}{ZT} + 1\right) \text{ when } k_{eff}^B = 0 \tag{6}$$

- Point C corresponds to the passive point where no voltage is applied, $V = 0$. It must be noted that when $V = 0$ the closed-circuit system is formed by a TE couple working as a TEG with its output short-circuited, $R_L = 0$. Consequently, k_{eff}^C can be expressed in the same way as Eq. (12) of the passive control. It is also interesting to note that k_{eff}^C is only temperature dependent, therefore, while $\overline{T}$ is maintained k_{eff}^C preserves, even when T_1 and T_2 are reversed.

$$k_{eff}^C = k_{pn}(1 + ZT) \tag{7}$$

- Finally, the point D corresponds to the maximum value of k_{eff} when heat transfer flows from side 2 to 1. That is when maximum cooling of Q_2 is achieved and it can be obtained by deriving the Q_2 expression with respect to input voltage $\frac{\partial Q_2}{\partial V} \rightarrow V = -\alpha_{pn}T_1$. From that point, the whole TEM tends to overheat as a consequence of the contribution of the electrical energy introduced to increase the Joule effect.

$$k_{eff}^D = k_{pn}\left(-\frac{ZT_1}{\Delta T} - 1\right) \tag{8}$$

Fig. 4 shows the behaviour of Eq. (4) under different temperatures and voltages. It can be observed that when temperature difference between faces is small, the heat transference can be easily controlled in terms of magnitude and direction. Therefore, the smaller the temperature differences between faces, the higher the control of k_{eff} (i.e. higher variation range) in both heat flow directions. As the temperature difference increase, k_{eff} can only be controlled when heat transfer flows in the same direction as it does the natural flow (i.e. the hottest ambient temperature to the coldest). This is on account of the thermocouple's limited heat pumping capacity, which, in this case, is exceeded when ΔT is

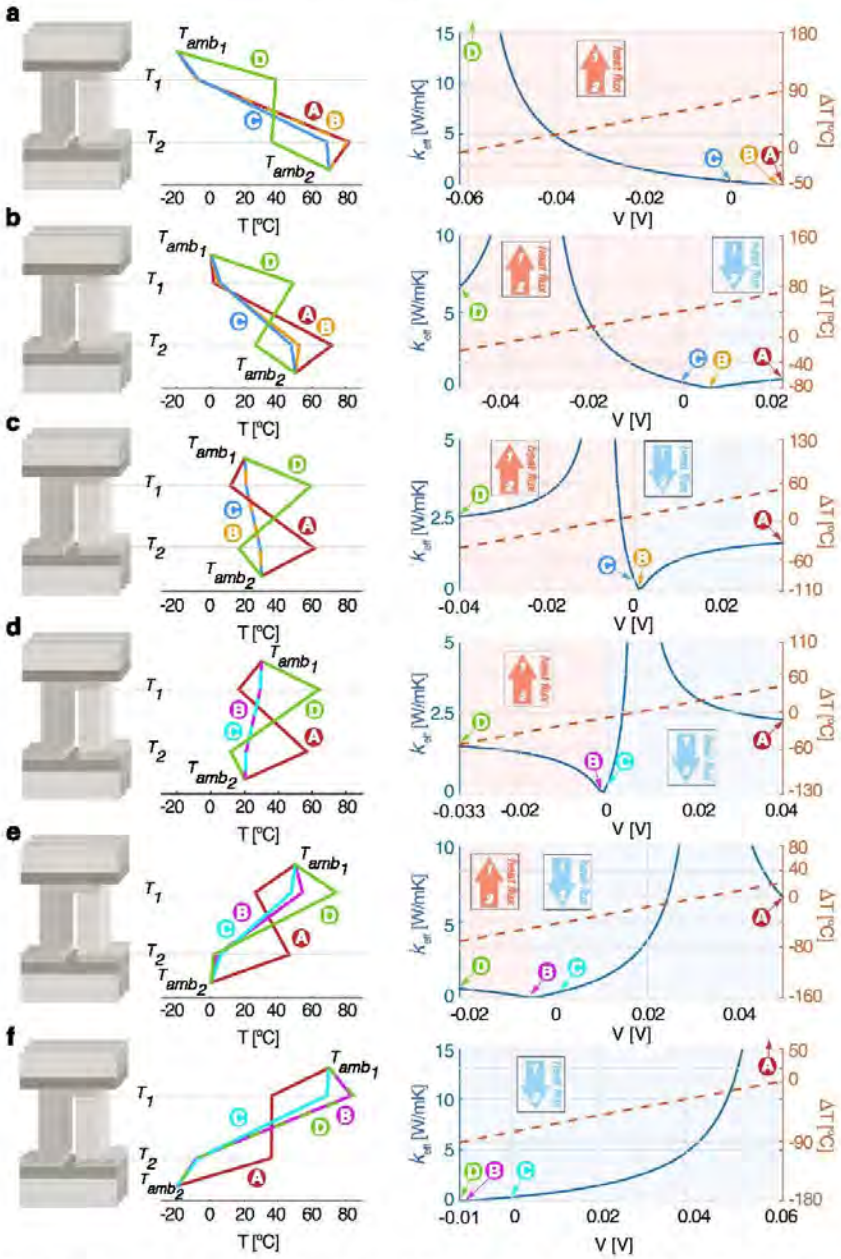

Fig. 4. V dependence of k_{eff} under different thermal states. (a) k_{eff} as a function of V at $T_{amb1} = -20$ °C and $T_{amb2} = 70$ °C. (b) k_{eff} as a function of V at $T_{amb1} = 0$ °C and $T_{amb2} = 50$ °C. (c) k_{eff} as a function of V at $T_{amb1} = 20$ °C and $T_{amb2} = 30$ °C. (d) k_{eff} as a function of V at $T_{amb1} = 30$ °C and $T_{amb2} = 20$ °C. (e) k_{eff} as a function of V at $T_{amb1} = 50$ °C and $T_{amb2} = 0$ °C. (f) k_{eff} as a function of V at $T_{amb1} = 70$ °C and $T_{amb2} = -20$ °C.

higher than 90 °C. Once heat-pumping capacity is surpassed, heat transfer cannot be reversed and B point cannot be achieved anymore. As ΔT_{amb} increase, k_{eff}^{A} and k_{eff}^{D} values tend to get closer to the $k_{eff} = 0$ value (i.e. B point). However, at the same time B point gets away from C point, hence major energy is required to maintain TEC working as a perfect insulator. Otherwise, the lower the ΔT_{amb} the lower the energy needed to do the same. It can also be shown that k_{eff} tends to infinite when $\Delta T = 0$ due to its situation on the Eq. (4). The material properties used in the simulation are listed in Table 1 and 2.

4. Passive control

It is well known that thermoelectric materials produce electrical power from heat flow through a temperature gradient. As the heat flows from hot to cold, free charge carriers (electrons or holes)

in the material are also driven to the cold end. By connecting an electron conducting (n-type) and hole conducting (p-type) material in series, a net voltage is produced that can be driven through a load. The resulting voltage V is proportional to the temperature difference ΔT via the Seebeck coefficient, α_{pn}, $V = \alpha_{pn}\Delta T$.

When electric load is the lowest, the heat transfer is the highest [21], and vice versa, because Peltier heat flows in the same direction as Fourier heat when TE couple is working as a generator. Consequently, high values of electric current I_{RL} will produce high contribution of Peltier and Joule terms of Eqs. (9) and (10). Contrarily, low values of I_{RL} will produce low Peltier and Joule effects causing a pure Fourier conduction.

$$Q_h = \frac{k_{pn}S_{pn}}{th_{pn}}\Delta T + \alpha_{pn}T_h I_{RL} - \frac{1}{2}I_{RL}^2 R_{pn} \tag{9}$$

$$Q_c = \frac{k_{pn}S_{pn}}{th_{pn}}\Delta T + \alpha_{pn}T_c I_{RL} + \frac{1}{2}I_{RL}^2 R_{pn} \tag{10}$$

where Q_h, Q_c, k_{pn}, α_{pn}, T_h, T_c, S_{pn}, th_{pn}, I_{RL} and R_{pn} are hot side heat transfer, cold side heat transfer, thermal conductivity, Seebeck coefficient, hot side temperature, cold side temperature, total area, thickness, electrical current and internal resistance of the TE couple, respectively.

Taking advantage of this effect, the heat transfer and consequently thermal conductivity in TEGs can be controlled by adjusting the load resistance. The analytical solution to the thermoelectric phenomena that governs the variation of thermal conductivity with load resistance R_L can be found applying the Fourier's law of conduction $k_{eff} = \overline{Q}_{TEG} th_{pn}/S_{pn}\Delta T$ to the entire system. Due to the fact that heat transfer is not equal on both sides of TEG, the equivalent heat transfer through TEG, $\overline{Q}_{TEG}$, is calculated as $\overline{Q}_{TEG} = (Q_h + Q_c)/2$. Moreover, considering that in a closed-circuit (i.e. when R_L is finite), the voltage generated across thermoelectric material due to the Seebeck effect will result in an electric current that circulates through the thermoelectric material and external resistor, the current I can be expressed as $I_{RL} = \alpha_{pn}\Delta T/(R_{pn} + R_L)$. Finally, taking into account that TEG dimensions remain invariable during its operation, the function that describes the behaviour of effective thermal conductivity k_{eff} with load resistance R_L can be written as:

$$k_{eff} = k_{pn} + \frac{\alpha_{pn}^2\left(\frac{T_h+T_c}{2}\right)th_{pn}}{(R_{pn}+R_L)S_{pn}} \tag{11}$$

Note that in this case the k_{eff} evolution depends on the geometric parameters, th_{pn} and S_{pn}. It can be observed that Eq. (3) has a maximum when $R_L = 0$ and a minimum when $R_L = \infty$,

$$k_{eff}^{R_L=0} = \lim_{R_L\to 0}\left[k_{pn} + \frac{\alpha_{pn}^2\left(\frac{T_h+T_c}{2}\right)th_{pn}}{(R_{in}+R_L)S_{pn}}\right] = k_{pn}(1+ZT) \tag{12}$$

$$k_{eff}^{R_L=\infty} = \lim_{R_L\to\infty}\left[k_{pn} + \frac{\alpha_{pn}^2\left(\frac{T_h+T_c}{2}\right)th_{pn}}{(R_{in}+R_L)S_{pn}}\right] = k_{pn} \tag{13}$$

where ZT is the figure-of-merit, expressed as $ZT = \alpha_{pn}^2 T/k_{pn}\rho_{pn}$ and $T = (T_h + T_c)/2$. It can be observed that the absolute extent of variation of effective thermal conductivity in thermoelectric materials

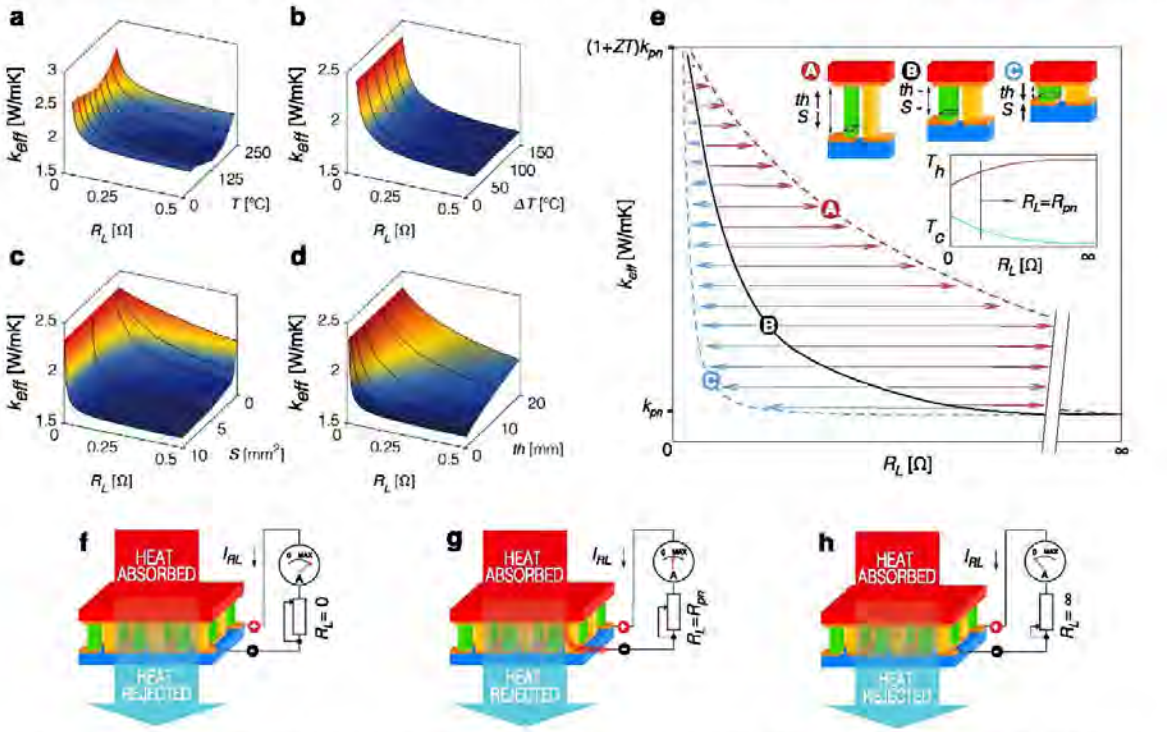

Fig. 5. R_L dependence of k_{eff} under different thermal, electrical and dimensional states. (a) k_{eff} as a function of R_L at different average temperatures $T = (T_h + T_c)/2$. A constant $\Delta T = 25$ °C is considered. (b) R_L dependence of k_{eff} at different ΔT. A constant average temperature $T = 150$ °C is considered. (c) Pellet surface S_{pn} effects on R_L dependence of k_{eff}. (d) Pellet thickness th_{pn} effects on R_L dependence of k_{eff}. (e) A schematic diagram of th_{pn} and S_{pn} effects on the k_{eff} behaviour. The arrows show the direction and magnitude of the effect while T and ΔT are maintained. Also shown are the hot and cold side temperature evolutions with R_L. (f)–(h) Heat transfer profiles at different values of load resistance.

working as TEG is only dependent of its dimensionless figure-of-merit. Note that thermoelectric materials with higher values of ZT will permit higher variation ranges of k_{eff}. It must be remarked that a temperature gradient must exist between its faces in order to control this effect. However, it makes no sense to control it when temperatures on both sides are the same.

In order to validate these assumptions and analyse the effects of thermal, electrical and dimensional parameters of Eq. (3), the simulations shown in Fig. 2 have been carried out. The models used to simulate these behaviours are described in [21,36].

As can be shown from Fig. 5a the highest values of Δk_{eff} are obtained when ZT values are also the highest. ZT presents a maximum point of 0.4692 when $T_h = 150$ °C and $T_c = 125$ °C, hence maximum Δk_{eff} of 46.92% is obtained at this point ($k_{RL=0} = 2.33$ W/mK and $k_{RL=\infty} = 1.58$ W/mK). These results corroborate the analytical hypothesis of Eq. (11). Fig. 5b demonstrates that ZT value preserved while T is maintained. However, the higher the ΔT the higher the power generated.

It is interesting to note that the evolution of the k_{eff} function can be tuned in order to easily achieve a highly precise control of it. Reducing the pellet area S_{pn}, Fig. 5c, or increasing its thickness th_{pn}, Fig. 5d, the curve stretches increasing the load resistance range. Otherwise, with a decrease of th_{pn} or an increase of S_{pn} the curve becomes steeper getting a high sensitivity thermal switch. Since the changes in ZT and Δk_{eff} are ascribed to T changes, they remain unchanged under dimensional changes. These behaviours are summarized and outlined in Fig. 5e.

Finally, it can be observed that the variation range of k_{eff} is strongly dependent on ZT: the higher the ZT, the higher the thermal control. In this regard, looking for materials with high ZT is important in order to extend the use of thermoelectric devices as variable insulators. Recently, new promising alloys with enhanced figure of merit have been developed [38–43].

5. Conclusions

In summary, our theoretical analysis demonstrates that thermoelectric materials can be used as variable insulators for applications where the heat fluxes between two thermal bodies need to be altered conveniently. Two control modes can be established in order to control the effective thermal conductivity of the thermoelectric pair: active mode and passive mode.

Active mode, which can be controlled by external voltage, is a good solution when a complete insulation or a high control of thermal conductivity is needed. The smaller the temperature difference between faces the higher is the control of k_{eff} (i.e. higher values of k_{eff} can be obtained). However, as k_{eff} is strongly dependent of temperature gradient ΔT and ZT, thermocouple has a limited heat pumping capacity. For large values of ΔT the thermocouple is no capable to reverse the heat flux hence complete insulation is not achievable. The energy required to keep TEM working at this point increase with the ΔT. It is remarkable that the control of k_{eff} does not depend on the geometric parameters.

On the other hand, passive mode permits a k_{eff} increment of $1 + ZT$ times with respect to semiconductor thermal conductivity k_{pn}. In this mode the extent of k_{eff} variation is mainly dependent on the thermoelectric figure of merit ZT and on the pellet geometry. Unlike active mode, passive mode can be controlled by an external resistance, hence no external energy is required. However, the extent of k_{eff} variation is lower and a complete insulation cannot be attained.

Finally, it can be observed that in both cases, active and passive mode, the variation range of k_{eff} is strongly dependent on the figure of merit. Considering most common and commercial materials, such BiTe, the potential applications of TECs and TEGs are limited to material properties: the higher the ZT, the higher the thermal control. In this regard, finding materials with high ZT is important in order to extend the use of thermoelectric devices as variable insulators.

The basic idea behind this tunable insulator is that certain instances it would be beneficial to selectively enable or impede heat flow within particular sections to selectively control heat flow. The application of this technology could be interesting for building sector, in spacecraft structures or in components of machinery. Instead of acting as a passive component, such as conventional building insulation, smart insulation is an adaptive component that can be selectively switched between low and high heat transfer states to take advantage of such instances where it would be beneficial to be able to turn off the insulation. Two example scenarios that would improve the energy efficiency in which little or no building insulation would be advantageous would be sunny winter days and cool summer evenings.

This study open new doors and new opportunities for thermoelectric materials.

Acknowledgments

This work has been partially funded by the Generalitat de Catalunya under Grant No. 2014-SGR-36 and the MICINN-FEDER under Grants No. FIS-2012-31307. Authors would also like to thank Association of Industrial Engineers of Catalonia (AEIC) for they partial financial support.

References

[1] Riffat SB, Ma X. Thermoelectrics: a review of present and potential applications. Appl Therm Eng 2003;23:913–35.
[2] Stivers G. Radioisotope thermoelectric space power supplies. IEEE Trans Aerosp 1964;2.
[3] Pedersen ES. Nuclear-thermoelectric space power system. IEEE Trans Aerosp Navig Electron Tech 1963.
[4] Xiao H, Qiu K, Gou X, Ou Q. A flameless catalytic combustion-based thermoelectric generator for powering electronic instruments on gas pipelines. Appl Energy 2013;112:1161–5.
[5] Leonov V, Torfs T, Fiorini P, Van Hoof C. Thermoelectric converters of human warmth for self-powered wireless sensor nodes. IEEE Sens J 2007;7:650–6.
[6] Shin W, Matsumiya M, Izu N, Murayama N. Hydrogen-selective thermoelectric gas sensor. Sensor Actuator, B Chem 2003;93:304–8.
[7] Samson D, Kluge M, Becker T, Schmid U. Wireless sensor node powered by aircraft specific thermoelectric energy harvesting. Sensor Actuator, A Phys 2011;172:240–4.
[8] Kopparthy VL, Tangutoori SM, Nestorova GG, Guilbeau EJ. Thermoelectric microfluidic sensor for bio-chemical applications. Sensor Actuators B Chem 2012;166–167:608–15.
[9] Field RL. Photovoltaic/thermoelectric refrigerator for medicine storage for developing countries. Sol Energy 1980;25:445–7.
[10] Nestorova GG, Guilbeau EJ. Thermoelectric method for sequencing DNA. Lab Chip 2011;11:1761–9.
[11] Goudarzi A, Mozaffari A, Samadian P, Rezania A, Rosendahl LA. Intelligent design of waste heat recovery systems using thermoelectric generators and optimization tools. Meccanica 2014;49:1211–23.
[12] Meng F, Chen L, Sun F, Yang B. Thermoelectric power generation driven by blast furnace slag flushing water. Energy 2014;66:965–72.
[13] Kristiansen NR, Snyder GJ, Nielsen HK, Rosendahl L. Waste heat recovery from a marine waste incinerator using a thermoelectric generator. J Electron Mater 2012;41:1024–9.
[14] Zheng XF, Yan YY, Simpson K. A potential candidate for the sustainable and reliable domestic energy generation–thermoelectric cogeneration system. Appl Therm Eng 2013;53:305–11.
[15] Codecasa MP, Fanciulli C, Gaddi R, Gomez-Paz F, Passaretti F. Update on the design and development of a TEG cogenerator device integrated into self-standing gas heaters. J Electron Mater 2013;42:2243–8.
[16] Wang Y, Dai C, Wang S. Theoretical analysis of a thermoelectric generator using exhaust gas of vehicles as heat source. Appl Energy 2013;112:1171–80.
[17] Love ND, Szybist JP, Sluder CS. Effect of heat exchanger material and fouling on thermoelectric exhaust heat recovery. Appl Energy 2012;89:322–8.
[18] Saqr KM, Mansour MK, Musa MN. Thermal design of automobile exhaust based thermoelectric generators: objectives and challenges. Int J Automot Technol 2008;9:155–60.
[19] Ikoma K, et al. Thermoelectric module and generator for gasoline engine vehicles. In: Seventeenth int conf thermoelectr proc ICT98 (Cat. No. 98TH8365) 464–467; 1998 http://dx.doi.org/10.1109/ICT.1998.740419.

Appendix A. Published paper: Electrically tunable thermal conductivity in thermoelectric materials: Active and passive control

[20] Zheng XF, Liu CX, Yan YY, Wang Q. A review of thermoelectrics research – recent developments and potentials for sustainable and renewable energy applications. Renew Sustain Energy Rev 2014;32:486–503.
[21] Massaguer E, Massaguer A, Montoro L, Gonzalez JR. Development and validation of a new TRNSYS type for the simulation of thermoelectric generators. Appl Energy 2014;134:65–74.
[22] Chen G. Nonlocal and nonequilibrium heat conduction in the vicinity of nanoparticles. J Heat Transfer 1996;118:539.
[23] Mahan GD, Sofo JO. The best thermoelectric. Proc Natl Acad Sci U.S.A. 1996;93:7436–9.
[24] Chen G. Nanoscale energy transport and conversion. Heat Mass Transf 2005;531.
[25] Chen G, Borca-Tasciuc D, Yang RG. Encycl Nanosci Nanotechnol 2004;7:429–59.
[26] Cahill DG et al. Nanoscale thermal transport. J Appl Phys 2003;93:793–818.
[27] Turney JE, Landry ES, McGaughey aJH, Amon CH. Predicting phonon properties and thermal conductivity from anharmonic lattice dynamics calculations and molecular dynamics simulations. Phys Rev B – Condens Matter Mater Phys 2009;79:1–12.
[28] Li N et al. Colloquium: phononics: manipulating heat flow with electronic analogs and beyond. Rev Mod Phys 2012;84:1045–66.
[29] Chang CW, Okawa D, Majumdar A, Zettl A. Solid-state thermal rectifier. Science 2006;314:1121–4.
[30] Taylor B, Imbabi M. The application of dynamic insulation in buildings. Renew Energy 1998;15:377–82.
[31] Székely V, Nagy A, Török S, Hajas G, Rencz M. Realization of an electronically controlled thermal resistance. Microelectronics J 2000;31:811–4.
[32] Székely V, Török S, Kollár E. Improvements of the variable thermal resistance. In: Collect Pap Present 13th Int Work Therm Investig ICs Syst THERMINIC 180–183; 2007 http://dx.doi.org/10.1109/THERMINIC.2007.4451773.
[33] Min G, Yatim NM. Variable thermal resistor based on self-powered Peltier effect. J Phys D Appl Phys 2008;41:222001.
[34] Cheng CH, Huang SY, Cheng TC. A three-dimensional theoretical model for predicting transient thermal behavior of thermoelectric coolers. Int J Heat Mass Transf 2010;53:2001–11.
[35] Cheng CH, Huang SY. Development of a non-uniform-current model for predicting transient thermal behavior of thermoelectric coolers. Appl Energy 2012;100:326–35.
[36] Massaguer E, Massaguer A, Montoro L, Gonzalez JR. Modeling analysis of longitudinal thermoelectric energy harvester in low temperature waste heat recovery applications. Appl Energy 2015;140:184–95.
[37] Domenicali Ca. Irreversible thermodynamics of thermoelectricity. Rev Mod Phys 1954;26:237–75.
[38] Kraèmer D et al. High thermoelectric conversion efficiency of MgAgSb-based material with hot-pressed contacts. Energy Environ Sci 2015;00:1–10.
[39] Zhang Q et al. Enhancement of thermoelectric figure-of-merit by resonant states of aluminium doping in lead selenide. Energy Environ Sci 2012;5:5246.
[40] Pei Y, LaLonde A, Iwanaga S, Snyder GJ. High thermoelectric figure of merit in heavy hole dominated PbTe. Energy Environ Sci 2011;4:2085.
[41] Biswas K et al. High thermoelectric figure of merit in nanostructured p-type PbTe–MTe (M = Ca, Ba). Energy Environ Sci 2011;4:4675.
[42] Li J et al. A high thermoelectric figure of merit ZT > 1 in Ba heavily doped BiCuSeO oxyselenides. Energy Environ Sci 2012;5:8543.
[43] Fu C, Zhu T, Liu Y, Xie H, Zhao X. Band engineering of high performance p-type FeNbSb based half-Heusler thermoelectric materials for figure of merit zT > 1. Energy Environ Sci 2015;8:216–20.

Appendix B

Published paper: Transient behavior under a normalized driving cycle of an automotive thermoelectric generator

---

Applied Energy 206 (2017) 1282–1296

Contents lists available at ScienceDirect

Applied Energy

journal homepage: www.elsevier.com/locate/apenergy

Transient behavior under a normalized driving cycle of an automotive thermoelectric generator

A. Massaguer[a,*], E. Massaguer[b], M. Comamala[a], T. Pujol[a], L. Montoro[a], M.D. Cardenas[c], D. Carbonell[c], A.J. Bueno[c]

[a] Department of Mechanical Engineering and Industrial Construction, University of Girona, C. Universitat de Girona, 4, 17003 Girona, Spain
[b] Nabla Thermoelectrics, C. de la Llibertat, 71, 17820 Banyoles, Spain
[c] Energy for Transportation Department, Repsol Technology Centre, Agustin de Betancourt s/n, 28935 Mostoles, Spain

HIGHLIGHTS

- An ATEG is tested under NEDC transient driving cycle.
- Backpressure strongly affects the engine efficiency.
- Thermal inertia prevent TEMs from achieving its maximum power point.
- ATEGs need to be designed for the most common temperatures found in a driving cycle.
- Performance can be enhanced by using lower temperature TEMs and a temperature control.

ARTICLE INFO

Keywords:
Thermoelectric generator
TEG
Longitudinal thermoelectric energy harvester
LTEH
Automotive engine exhaust waste heat recovery
ATEG

ABSTRACT

Thermoelectric generators (TEGs) have become a promising technology for vehicle exhaust heat recovery. Many models and prototypes have been developed and validated with very promising results. The majority of them have been tested under steady-state engine conditions. However, light-duty vehicles operate under wide variable loads, causing significant variation of TEG performance. The purpose of this study is to test and analyze an automotive thermoelectric generator (ATEG) under different steady-state engine conditions and under the transient New European Driving Cycle (NEDC). Results show that both thermal inertia and pressure drop play a key role in designing an ATEG for real applications. Variations on exhaust temperature and mass flow rate prevent achievement of thermal steady state. Consequently, total energy generated during the NEDC is lower than that expected from a steady-state analysis. On the other hand, excessive pressure loss on the exhaust considerably minimizes engine performance.

Results show that the overall power generation of the ATEG can be significantly improved by maximizing the heat transfer through TEMs using a finned geometry, employing lower temperature thermoelectric materials and including a hot-side temperature control.

1. Introduction

Internal combustion engines waste through the tailpipe about the same amount of thermal power than that produced mechanically. It is estimated that this loss might be around 35–40% of the fuel energy supplied, even when operating at top efficiency [1–8]. Therefore, recovery of a significant portion of this wasted energy by converting it into electricity would be highly advantageous [7,9–11]. Recovering the exhaust gas energy in a diesel passenger car under NEDC driving cycle can lead to potential fuel savings from 8% to 19% [12]. There are several feasible alternatives to recover energy from the exhaust. One of the most promising is using thermoelectric generators, due to their small weight and size, low maintenance costs, silent operation and high reliability [8,10,11,13]. This electric recovery will be especially useful in case of vehicles having a high degree of electrification, synergistically increasing the efficiency potential. Unfortunately, heat recovery systems have an important drawback, they increase fuel consumption due to back pressure in the exhaust [14–16].

A significant number of studies, in cooperation with several automotive manufacturers, have been performed to improve vehicle

* Corresponding author.
E-mail address: albert.massaguer@udg.edu (A. Massaguer).

http://dx.doi.org/10.1016/j.apenergy.2017.10.015
Received 17 March 2017; Received in revised form 12 September 2017; Accepted 5 October 2017
Available online 12 October 2017

Table 1
Summary of physical properties of ATEGs described in the literature.

Heat source	Max. ATEG power [W]		Temperatures [°C]			Cooling temperature [°C]	TE material	Exhaust flow rate [g/s]	Pressure loss [mbar]	Ref
	Steady-state eng. cond.	Transient engine conditions	TE hot side	TE ΔT	Exhaust gases					
Cummins NTC350 14l 300HP Diesel truck engine	1068	-	-	175	-	-	BiTe	-	-	[17]
Toyota 2l	266	-	-	270	650	25	Skutterudites/BiTe	-	-	[18]
Ruston 3YDA 3, 6l	42.3	-	-	237	650	-	BiTe	-	-	[19]
Ford Lincoln BMW X6	700	450 (US06 Driving Cycle)	-	-	625	20	Skutterudites	45	-	[20] [21]
Combustor bench	35.6	-	-	396	595	25	SiGe	58	-	[22]
GMC Sierra 5.3l	177	-	283	-	550	88	BiTe	-	-	[23]
Chevy suburban	235	-	420	-	600	-	Skutterudites/BiTe	-	-	[24]
Engine simulator	350	-	-	-	600	10	BiTe	-	-	[25]
Experimental rig	250	-	-	-	600	-	Silicide	-	< 30	[26]
Light Duty Truck 2.3l diesel engine	500	150 (NEDC *) 200 (WLTP **)	-	-	450	-	BiTe	-	< 30	[27]
Golf 1.4 TSI	111	30	344	260	557	65	BiTe + PbTe	37	36	***

* New European Driving Cycle (NEDC).
** Worldwide Harmonized Light vehicles Test Procedure (WLTP).
*** Present work.

performance. Studies carried out focused on exhaust manifold, exhaust piping and catalytic converter packaging design for automotive tailpipe based on heat transfer analysis of the exhaust system. The most interesting results of these studies are detailed in Table 1, which summarizes the achievements reported in the literature.

Various real engines and experimental exhaust simulators have been used in the literature to analyze the ATEGs performance. The aim of these investigations was not only to develop the most efficient ATEG but also to prove that ATEGs presented withstand the highest steady-state conditions of exhaust temperature and gas flow rate. The ATEGs power presented in Table 1 was obtained at maximum exhaust temperature and gas flow rate conditions. Most reported ATEG studies are carried out under steady state engine conditions, which are not representative of real driving conditions.

During real driving, exhaust temperature and gas flow rate vary depending on engine operating conditions. This variability of energy flows, along with thermal inertia of the ATEG, affects power production [9,28–31]. This effect can be observed in Table 1 for the few studies that tested ATEGs under transient conditions of a driving cycle such as NEDC, WLTP or US06. The results indicate a low energy recovery for transient driving conditions. The improvement of the thermal response of ATEG can significantly increase the recovered energy. Additionally, only few studies have been reported that consider the pressure drop and none of them studied its effect on engine performance.

Regarding thermoelectric materials used in the literature, Bismuth Telluride (BiTe) is the most popular thermoelectric material. However, its use is limited because its maximum operating temperature is relatively low. As BiTe is widely used and mass produced, their cost is more affordable compared to other thermoelectric materials. Other materials and techniques have been used to improve the power generation and efficiency of TEGs. Due to the high temperatures achieved on the exhaust line, the most promising and practical materials to be used for TEGs in exhaust heat recovery systems would be materials designed to withstand high temperatures. This means larger temperature gradients can be achieved with this material and thus more power and higher efficiency could be potentially achieved. Lead Telluride (PbTe) and calcium manganese have been used as materials in TEGs due to their ability to withstand higher temperatures [32,33]. Some TEGs have been manufactured with segmented materials. A material with larger zT at higher temperatures is used on the hot side (e.g.: PbTe) and a material with a large zT at lower temperatures is used on the cold side (e.g.: BiTe). More power would be produced compared to a TEG made of high temperature rated material only. Other materials such as skutterudites and other manufacturing techniques such as quantum well structures have been investigated to improve TEG power generation efficiency but they are still very expensive and not commercially available [34,35].

ATEG presented in Fig. 1 will be used in this study. It makes use of a hot side heat exchanger geometry that guarantees the TE material integrity under the highest exhaust temperature. This geometry was previously calculated using thermal simulations.

The main objectives of this study are (i) to test, compare, and analyze the performance of an ATEG under different steady-state conditions and under the New European Driving Cycle; (ii) to analyze the peak power generated and the total energy recovered on both experiments; (iii) to determine and analyze the effect of the backpressure on the global performance of the engine; and (iv) to present some ATEG design recommendations in order to optimize the power generation during transient conditions. Thermal model will be used to support the conclusions.

2. ATEG design

The ATEG presented in Fig. 1 is designed to transform the energy contained in the exhaust gases of automobiles into profitable electric energy. The goal is to feed several electrical parts of the vehicle, preventing the alternator to work. This will lead to significant fuel and greenhouse gas emissions savings. It is estimated that this technology could drive to a reduction of about 5% in fuel consumption [11].

The size of the device is 160 × 500 × 60 mm (W × L × H) with a total weight of about 7 kg. It consists of 12 thermoelectric modules (TEMs) electrically connected in series but thermally connected in parallel. In this study, commercially available TEMs (TEG1-12611-6.0) are used as thermoelectric power generators in the ATEG. In Fig. 2, the performance of electric power generated by a single TEM is plotted against hot side temperature (T_h). The cold side temperature (T_c) was evaluated at 30 °C, 50 °C and 80 °C.

TEMs used are constructed with PbTe and BiTe and stuck with high thermal conductivity graphite sheet on their both sides to provide low contact thermal resistance. The reason for choosing this kind of TEMs was its capability to withstand high temperatures.

These modules are arranged between each surface of a copper heat exchanger (2), through which the exhaust gas is passed, and two aluminum cold plates (3). Fig. 3 shows the schematic diagram of the experimental ATEG.

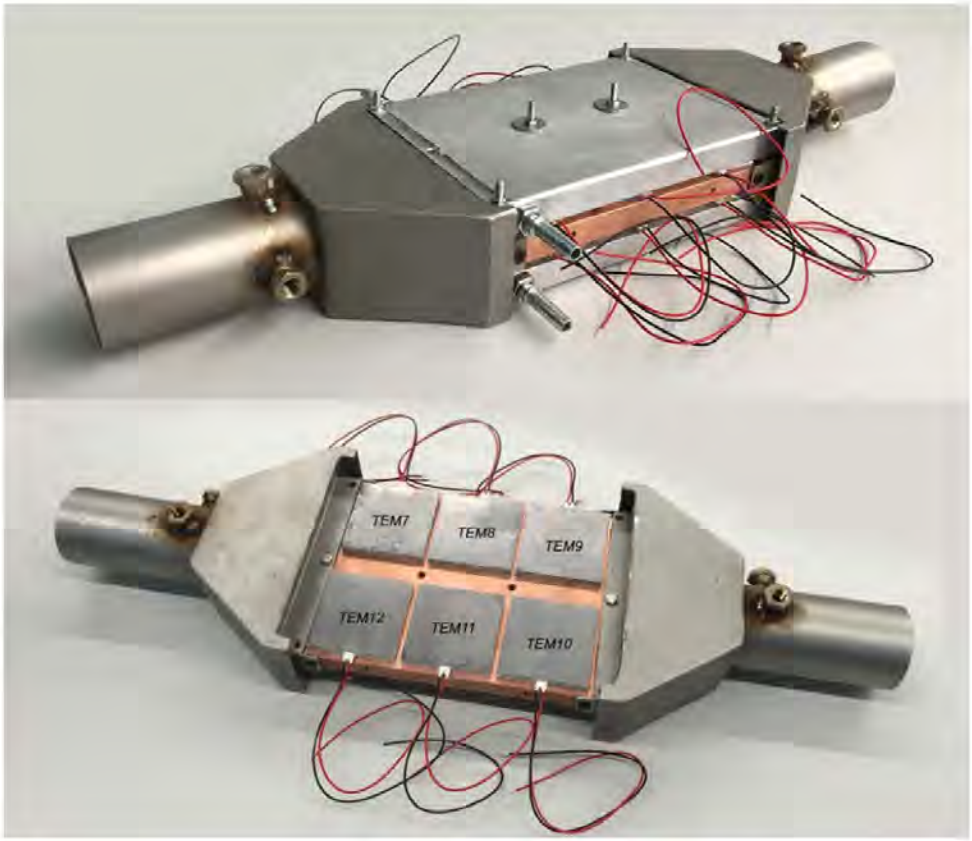

Fig. 1. Waste heat recovery system prototype. Dimensions are 160 × 444 × 64 mm (W × L × H).

Cooling system consists of a pump and a forced-air heat exchanger. Water is used as cooling fluid at a volumetric flow rate of 0.12 L/s. The pump moves the water through the cold plates (3) connected in parallel. Water cooling method was chosen because it is proven to be more efficient than air cooling [36]. Water chiller used extract a maximum thermal power of 3 kW.

The structure design, simulated using the commercial software ANSYS 17.1, was optimized to obtain an ATEG capable to withstand the highest measured temperatures of exhaust gases produced by a gasoline engine. Main specifications of the tested engine are explained in following sections and summarized in Table 2. The design of ATEG presented in this study is based on the worst steady state regime, in terms of high temperature and large exhaust gas flow.

The rated operating temperature of TEMs used is 350 °C for short periods of time, and 310 °C for extended operation. On the other hand, the maximum exhaust gases temperature measured at the same tailpipe

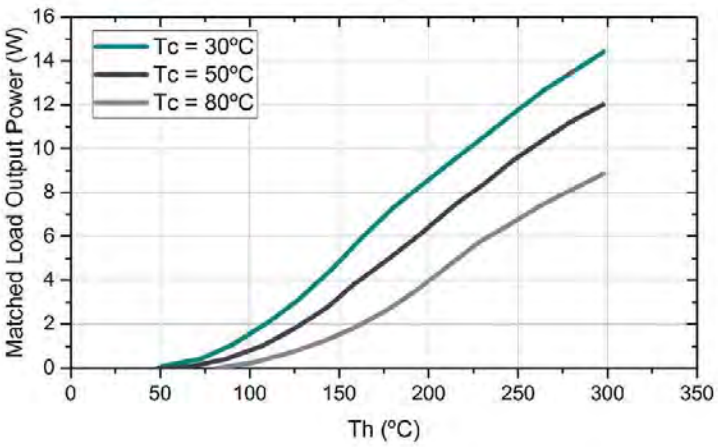

Fig. 2. Performance of a single TEM (TEG1-12611-6.0) for the output power estimation of ATEG.

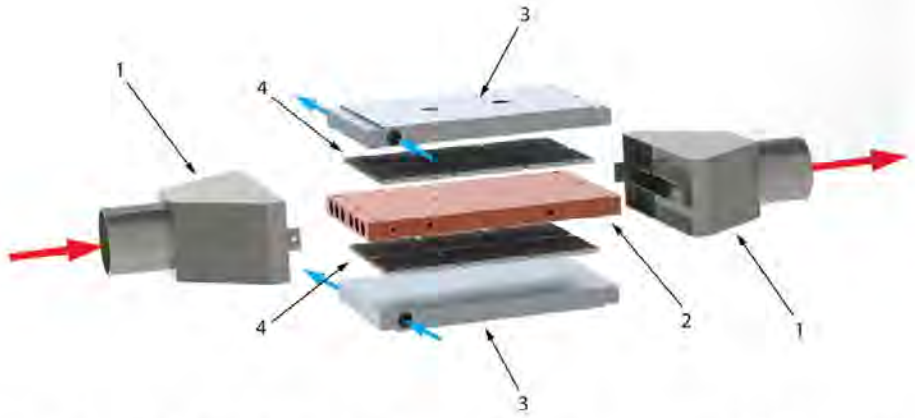

Fig. 3. Assembly view of ATEG. (1) Exhaust fumes inlet and outlet. (2) Heat exchanger. (3) Cold plates. (4) Thermoelectric modules. In red, exhaust gases. In blue, water of cooling system. (For interpretation of the references to colour in this figure legend, the reader is referred to the web version of this article.)

Table 2
Main specifications of tested engine.

Parameter	Value
Maker	VW
Model	Golf 1.4 TSI ACT (engine family EA211)
Euro certification	Euro 6b
Max. rated power	103 kW (at 4500–6000 rpm)
Max. rated torque	250 Nm (at 1500–3500 rpm)
Cylinders	4, in line
Bore (mm)	74.5
Stroke (mm)	80
Swept volume (cm^3)	1395
Compression ratio	10:1

position where ATEG is installed is about 720 °C. This maximum temperature is achieved in steady-state condition with a mechanical load coupled to the engine. Therefore, to assure the integrity of the system, the ATEG was designed to synchronize the maximum working temperature of TEMs with the maximum exhaust gases temperature.

Fig. 4 shows the simulation of the ATEG under four steady state conditions described in following sections. Boundary conditions for these four regimes were the exhaust gas inlet temperature and mass flow rate. They were extracted from four tests previously performed with a gasoline engine described in Table 2. Regimes 1, 2, 3 and 4 correspond to an engine speed of 2000 rpm, 2000 rpm, 2000 rpm, and 4000 rpm, and a full-throttle pedal position FTPP) of 15%, 45% 85%, and 85%. FTPP, in percentage, represents the engine acceleration in terms of throttle pedal travel position.

Regime 4 simulates the most extreme conditions, with a maximum exhaust gas temperature of 720 °C and a cooling inlet temperature of 75 °C. For this particular regime, TEMs hot and cold side temperatures are 347.2 °C and 91.8 °C, respectively. Simulation confirms the feasibility of the design, showing that hot side temperature does not exceed the maximum operating temperature.

Internally, exhaust gases are forced to flow through a copper heat exchanger containing six round holes. Fig. 5 shows the temperature contour of the outlet side for the Regime 4.

With regard to the electrical part, all TEMs are interconnected forming an electrical array of twelve modules arranged in series. Fig. 6 illustrates the series connection. Each TEM is represented by a voltage

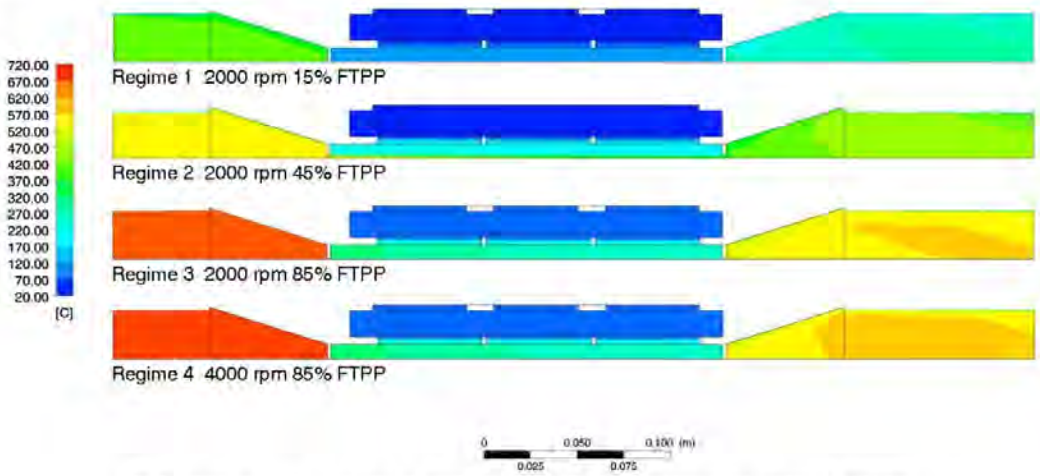

Fig. 4. Temperature contour over a longitudinal cross section of ATEG. Here is represented only a symmetric half-model.

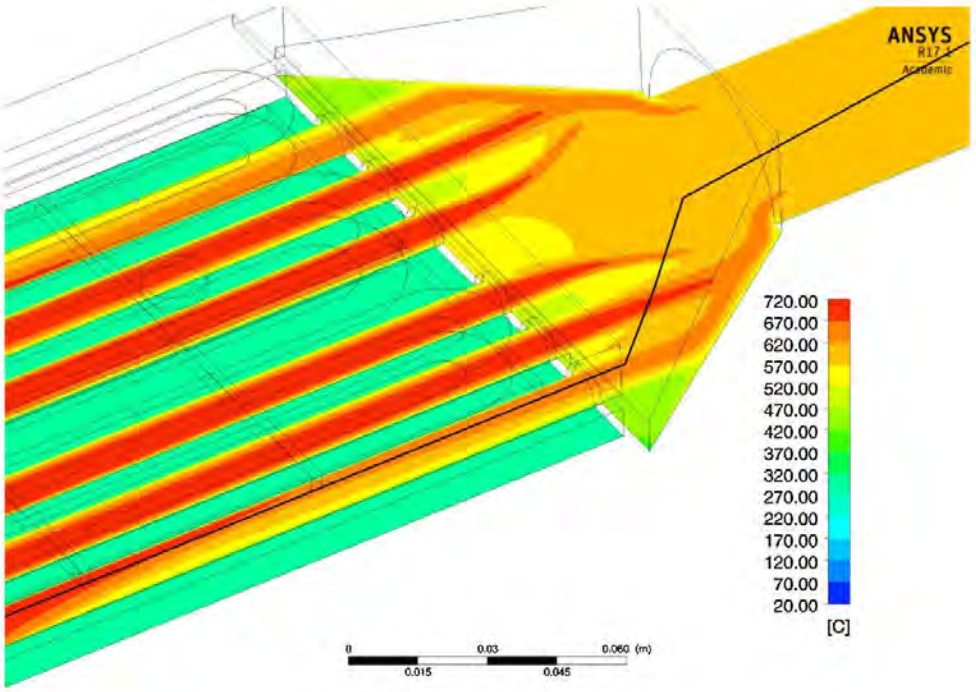

Fig. 5. Temperature contour. Outlet. Regime 4.

source $V_{1,...,12}$ and an internal resistance $R_{1,...,12}$ [37,38].

Although there are several ways to electrically interconnect TEMs, series configuration has been selected to allow assessment of the model.

3. Experimental setup

To assess the ATEG performance under steady state and transient conditions, experimental tests were accomplished on an engine test bench of Repsol Technology Center. Fig. 7 shows the experimetal setup. A 4-cylinder 4-stroke turbocharged, intercooled, gasoline direct injection engine, typical of those used in European cars, was employed as the experimental unit. Its specifications are listed in Table 1. The engine was coupled to an asynchronous machine model D2t MDA140, which also worked as starter during engine tests. The brake control system allowed measuring the engine speed, FTPP and effective torque. As said, FTPP, in percentage, represents the engine acceleration in terms of throttle pedal travel proportion. Additionally, a specific dyno controller set-up was adjusted in order to adapt its performance to dynamic test. The instantaneous gravimetric fuel consumption was determined using a Pierburg PLU 401/121 flow meter. In this study the ATEG was installed downstream of the three-way catalyst (TWC).

As previously explained, the objective of this study is to test the aforementioned ATEG and obtain experimental data at various steady state and transient engine conditions. Steady-state engine modes were defined by setting constant engine speed and torque, which allow obtaining the desired exhaust temperature and mass flow rate. By setting

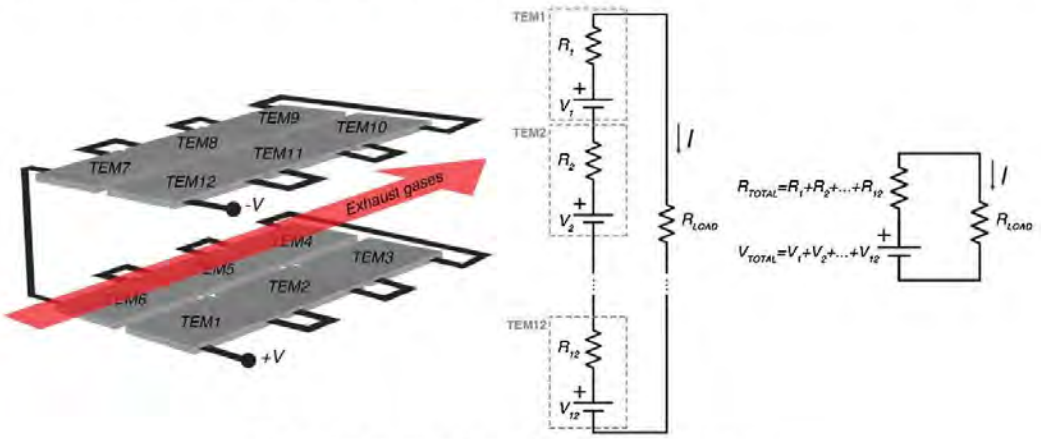

Fig. 6. Electrical schematic of the array of TEMs electrically connected in series.

Fig. 7. Engine test bench. Engine Lab of Repsol Technology Center.

different combinations of engine acceleration and mechanical load the desired exhaust temperature and mass flow rate can be obtained.

On the other side, the transient engine tests allow observation of the behavior of the ATEG under more realistic working conditions. Then, the ATEG has been tested under a normalized driving cycle. A driving cycle is defined to standardize the evaluation of the vehicles' fuel economy and emissions, which is a speed profile as a function of time. It represents the traffic conditions and driving behavior in a specific area. A driving cycle consists of a mixture of driving modes including idle, cruise, and engine acceleration and deceleration conditions. Making use of a driving cycle permits comparing the results with other ATEGs.

Fig. 8 shows the ATEG installed on the exhaust system. The acquired data is: exhaust gas inlet ($T_{exh,in}$) and outlet (T_{exhout}) temperatures, water cooling inlet ($T_{ref,in}$) and outlet ($T_{ref,out}$) temperatures, hot (T_{hot}) and cold (T_{cold}) side temperatures and generated voltage (V_{out}) and current (I_{out}). Additionally, parameters such as torque (T), fuel consumption (F), engine power (P), and thermal efficiency (η) have also been obtained.

4. Results and discussion

4.1. Steady-state tests

Figs. 9 and 10 show the data obtained from the steady-state study. On the whole, four steady-state points were established: three common FTPP (15, 45 and 85%) at 2000 rpm and the last mode at 4000 rpm and 85% of FTPP. It can be observed that all electrical parameters such as V_{out}, I_{out} and P_{out} increase with the engine load. As detailed in Fig. 10, as engine load increases, exhaust gas temperature and flow rate are higher and therefore more power is generated by the ATEG.

Focusing on the last steady-state point (4000 rpm 85% FTPP), it can also be observed that, in spite of having the highest exhaust temperature, the electrical power production is lower than expected. That is because the higher temperature of the cooling system causes a ΔT decrease on TEGs, Fig. 8. The exhaust temperature lost ($T_{EXHIN}-T_{EXHOUT}$) through the ATEG remains almost constant throughout all the tests.

Considering the data obtained from the experiments, the way vehicles are driven is a significant factor affecting ATEG performance for waste heat recovery. As vehicle speed and engine load increases, a better performance of ATEG is observed. It can be found that the higher the vehicle speed and engine load are, the better the performance of the ATEG is. That is because exhaust gas temperature and mass flow rate increase with the vehicle speed and engine load. Most of the ATEGs developed in the literature have been designed to withstand the maximum temperature of the exhaust gases. In this case, the ATEG was designed to withstand the maximum allowable temperature of TEGs, which was T_{hot} = 350 °C at $T_{exh,in}$ = 700 °C. It should be noted that this working point is rarely achieved during normal driving conditions. It can be stated that the majority of ATEGs will work below its maximum power point (MPP). This effect can be observed in more detail in the following chapter.

4.2. Transient tests

In order to study the thermal and electrical behaviors of the ATEG under transient conditions, the device has been tested under NEDC. NEDC is a combined cycle consisting of four Urban Driving Cycles (UDC) followed by an Extra Urban Driving Cycle (EUDC). During a NEDC driving cycle, the vehicle conditions change periodically, with idling, acceleration, cruise, and deceleration. At the EUDC stage, the vehicle speed increases up to 120 km/h, the exhaust temperature and mass flow rate increase as well, leading to improved performance of the TEG. Fig. 11 shows the NEDC cycle.

The full test starts with four repetitions of the UDC cycle, also known as ECE. It was devised to represent city driving conditions, e.g. in Paris or in Rome. It is characterized by low vehicle speed, low engine load, and low exhaust gas temperature. EUDC segment has been added after the fourth UDC cycle to account for more aggressive high-speed driving modes. The maximum speed of the EUDC cycle is 120 km/h.

Three NEDC tests were performed in total to evaluate the ATEG behavior: one cold-start NEDC test and two hot-start NEDC tests. The two hot-start tests were performed in the same way; therefore only one test has been plotted. As can be seen in Fig. 12, during the ECE cold start test, the exhaust temperatures are lower than those of the hot start test. It can also be observed that temperature difference of exhaust gases through the ATEG (ΔT) remain almost constant, maintained

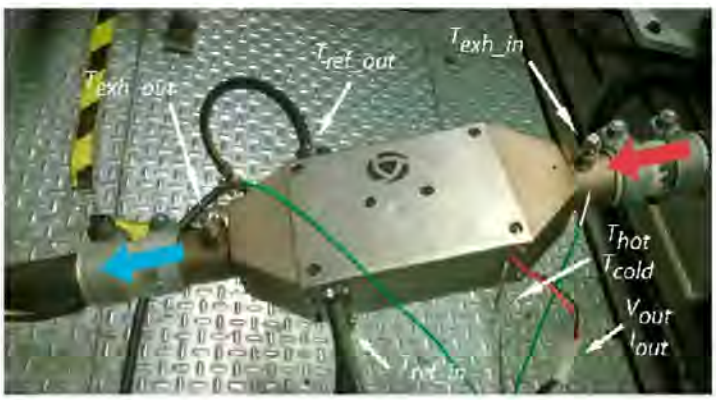

Fig. 8. ATEG installed on the exhaust system of the engine cell.

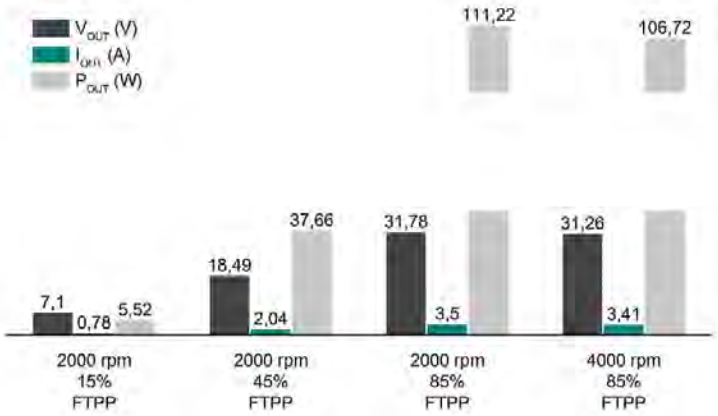

Fig. 9. ATEG electrical outputs under different steady-state conditions.

around 150 °C over the test. In addition, the highest exhaust gases temperatures achieved are about 550 °C. Considering that the ATEG is designed to withstand temperatures up to 720 °C, TEMs will not be damaged due to excessive temperature.

Fig. 13 shows the inlet and outlet cooling temperatures of the ATEG. Due to the fact that the ATEG cooling circuit is independent from the engine cooling system, temperatures $T_{REF,IN}$ and $T_{REF,OUT}$ are lower than the operating temperature of the engine, which was 80 °C. These lower cooling temperatures allow the ATEG to achieve higher ΔT on TEGs, see Fig. 14. Consequently, as shown in Fig. 15, voltage, current, and power generated was expected to be higher in this configuration than in an ATEG cooled by the engine cooling system.

However, even under these advantageous conditions, the electrical power generated during the NEDC driving cycle is very small. This is explained because ATEG is designed for steady-state situations, and when this design is applied to transient-state regimes, the thermal inertia detrimentally affects the result. In addition, the temperatures for which it has been designed greatly differ from those found in a driving cycle. It should be remarked that the ATEG presented is intended to generate the maximum power at 720 °C of exhaust gases temperature, and the average temperature of the whole test is 320 °C. These two aspects affect the final generation of ATEG.

4.3. Steady-state and transient tests comparison

Although it could be envisioned that both TEGs ΔT and power

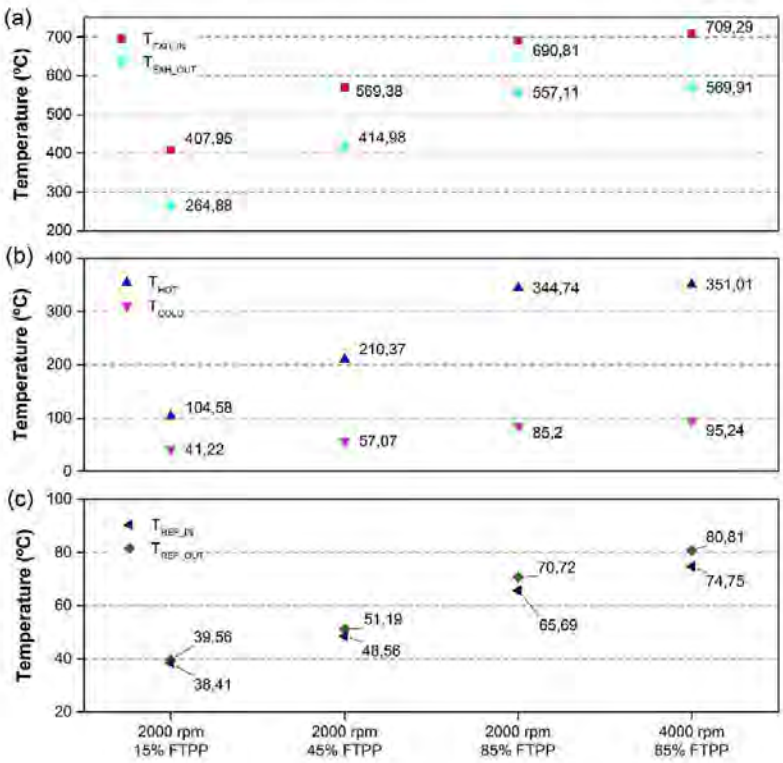

Fig. 10. ATEG inlet and outlet exhaust temperatures (a), thermoelectric hot and cold side temperatures (b) and water cooling inlet and outlet temperatures (c).

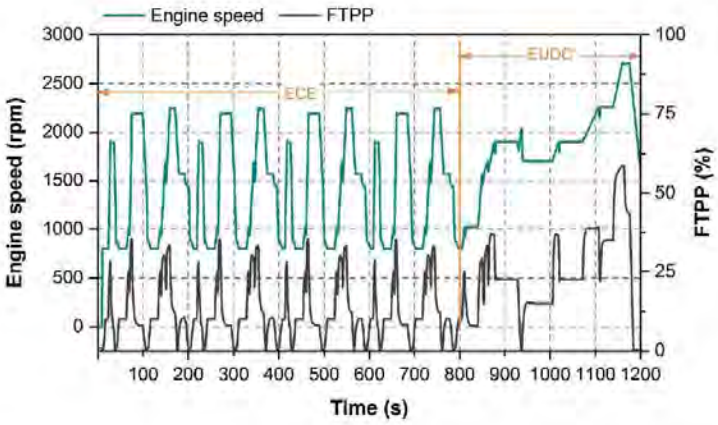

Fig. 11. Engine speed and FTPP vs time of New European Driving Cycle.

generated should be greater under a cold start due to the low cooling temperature, this thesis is not always fulfilled. The same occurs with exhaust temperature variations during ECE test. While ATEG has not reached a thermal steady-state point, most of the useful energy contained in exhaust gases contributes only to heating/cooling the ATEG and not to producing electric power. The higher thermal inertia is the reason why ATEG under a NEDC produces less electric power than the same device under a steady-state engine condition at the same exhaust conditions, see Table 3.

Analyzing the EUDC part of the cycle, it can be observed that the engine is not capable of generating exhaust gases temperature close to the maximum expected, near 700 °C. This fact is also responsible for why ATEG not generating the expected amount of electrical power under NEDC cycle. Therefore, an ATEG should be designed to work at its MPP preferably for lower temperatures.

On the other hand, the effect of the inclusion of ATEG on the engine performance has also been analyzed. In general, the engine performance was slightly reduced. As can be seen in Figs. 16 and 17, engine efficiency and power decrease when ATEG is attached to the exhaust system. The most significant reductions are observed on high acceleration regimes, when gas flow rate is maximum. These reductions can be explained by the additional pressure loss provided by the ATEG, which leads to an increase of the backpressure of the engine, see Fig. 18. Higher FTPP accounts for higher exhaust gas flow rate and pressure loss. At 2000 rpm and 85% FTPP, the mass flow rate is 37.07 g/s, corresponding to a maximum pressure drop of 36.53 mbar. Note that, in Fig. 18, experimental data was taken in a different test, using a Saenz air flowbench D-680, in order to obtain more data points.

In Fig. 16, $\eta_{WITHOUT\,ATEG}$ is the efficiency of the engine without the ATEG. Using exactly the same steady-state engine points, $\eta_{WITH\,ATEG}$ is presented, being the efficiency of the engine with the ATEG installed in the exhaust system. $\eta_{WITH\,ATEG}$ is calculated considering only the mechanical power generated by the engine. The energy generated by ATEG is not considered.

Efficiency is calculated considering the mechanical power generated by the engine and the average fuel mass consumed.

$$\eta_{WITHOUT\,ATEG} = \frac{P_{engine\,WITHOUT\,ATEG}}{\dot{m}_{fuel} LCV} 100 \quad (1)$$

$$\eta_{WITH\,ATEG} = \frac{P_{engine\,WITH\,ATEG}}{\dot{m}_{fuel} LCV} 100 \quad (2)$$

where P, $\dot{m}_{fuel}$ and LCV are the power, fuel mass flux, and lower calorific value, respectively.

Engine exhaust backpressure is defined as the exhaust gas pressure produced by the engine to overcome the hydraulic resistance of the

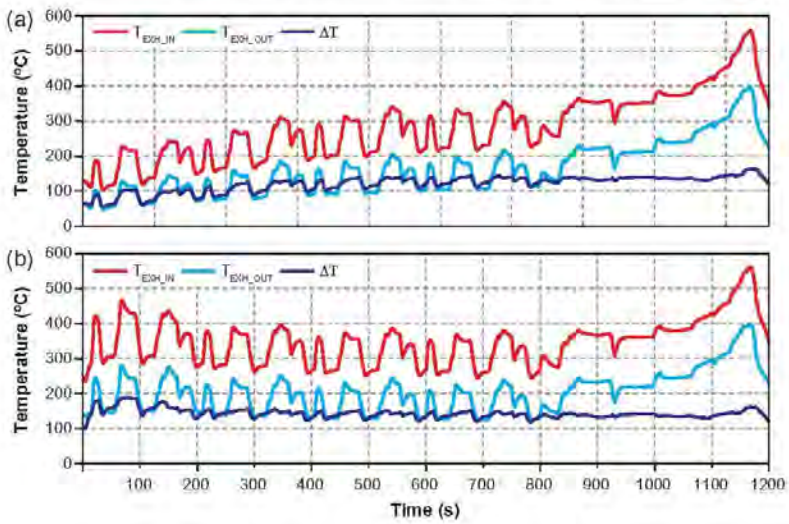

Fig. 12. ATEG exhaust temperatures under a cold-start (a) and a hot-start (b) NEDC test.

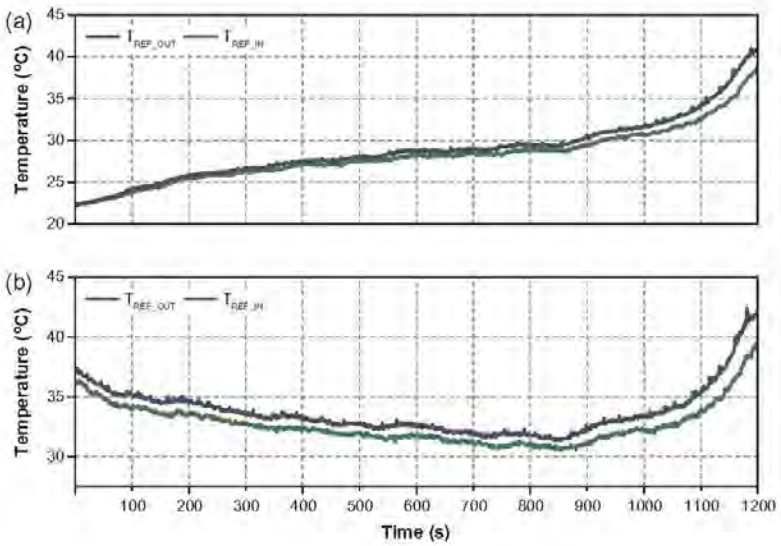

Fig. 13. ATEG water cooling temperatures under a cold-start (a) and a hot-start (b) NEDC test.

exhaust system in order to discharge the gases into the atmosphere. At increased backpressure levels, the engine has to compress the exhaust gases to a higher pressure. Consequently, additional mechanical work is needed and/or less energy is extracted by the exhaust turbine, which can affect the boost pressure of the intake manifold. This can lead to an increase of fuel consumption, see Fig. 19, particulate matter (PM), CO emissions, and exhaust temperature. The increased exhaust temperature can result in an overheating of exhaust valves and the turbine. An increase in NOx emissions is also possible due to an increment of engine load.

Fig. 20 shows the exhaust gases temperatures collected during the three NEDC tests performed. The sampling time of tests was 0.5 s. The histogram presented shows the number of times (frequency) when temperature values fall into each given interval of 20 °C. We can see that the most common temperatures appear in the range of 260–380 °C. Unfortunately, temperatures about 700 °C, which are advantageous for the ATEG, rarely occur.

In conclusion, an ATEG that generates around 4 W during most of the cycle and about 30 W during EUDC stage is obtained. These values differ from those which ATEG was designed for steady-state conditions.

Wang et al. [39] show that the output power and efficiency increase significantly by changing the convection heat transfer coefficient of the high-temperature-side. Therefore, the electrical generation could be improved by using an internal geometry with larger exchange area, e.g. using fins. Thus, contact surface between the exhaust gases and the hot face would be enlarged. Consequently, the rate of heat transfer would increase by increasing convection. Therefore, an ATEG that would generate more power at lower temperature would be obtained. This is aligned with aim proposed in this study, to enhance the ATEG performance by reducing the optimal working temperature to fit the most common exhaust temperatures. However, when the engine would reach a high regime, such as 4000 rpm and 85% FTTP where temperatures of

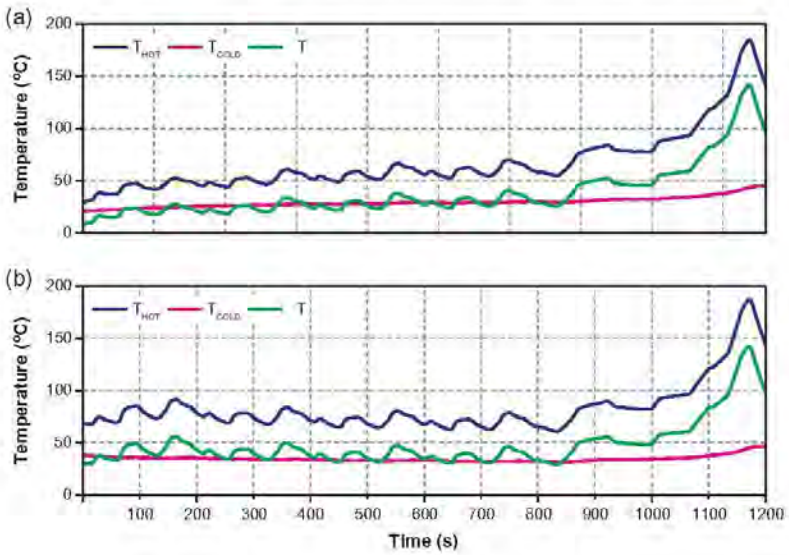

Fig. 14. ATEG thermoelectric module temperatures under a cold-start (a) and a hot-start (b) NEDC test.

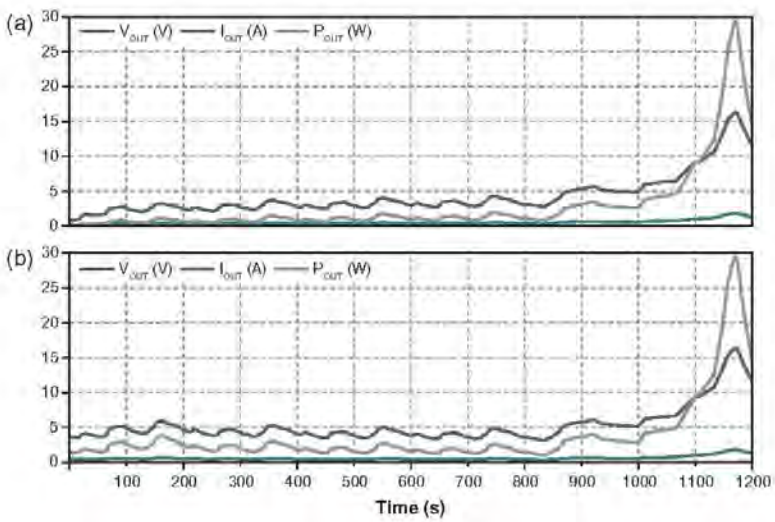

Fig. 15. ATEG electrical outputs under a cold start (a) and a hot-start (b) NEDC test.

Table 3
Power production comparison.

	Steady state engine condition (2000 rpm 15% acc.) (Regime 1)	NEDC (hot-start at 137s)	Steady-state engine condition (2000 rpm 45% acc.)(Regime 2)	NEDC (hot-start at 1167s)
T_{exhin} (°C)	408.0	407.8	569.4	561.4
T_{refin} (°C)	38.4	34.7	48.6	40.2
P (W)	5.5	2.07	37.7	29.0

700 °C are generated, TEMs would be damaged due to excessive temperature.

5. ATEG design enhancement

It has been demonstrated that an ATEG designed only for steady states does not work properly for transient states, which are those which ATEG would face in a real driving situation. In general, the following dichotomy exists: either an ATEG is designed to generate very little power in transient states to withstand higher temperatures, or to generate the maximum power in transient states but with the possibility of damaging TEMs due to higher exhaust temperatures.

As previously indicated, to improve the performance for real driving conditions, it is necessary to take advantage of lower temperatures, because they occur more often in a NEDC cycle.

Until now, high temperature materials like PbTe, SiGe or MgSi have been used to withstand the exhaust gases temperatures. BiTe has also been used but in a controlled environment, monitoring the exhaust temperature. Only Boretti et al. [15] proposed a methodology using a by-pass of exhaust gases to lower the temperatures over a Rankine waste heat recovery system.

The best option would be to use lower temperature materials that would produce larger amounts of power at lower temperatures and, besides, that would maximize the time when ATEG would be operating in a NEDC. Fig. 21 compares the power production of a PbTe and BiTe TEMs at various temperature gradients. BiTe TEM selected is a commercial module H-288-14-06-L2 with the same size as PbTe TEM.

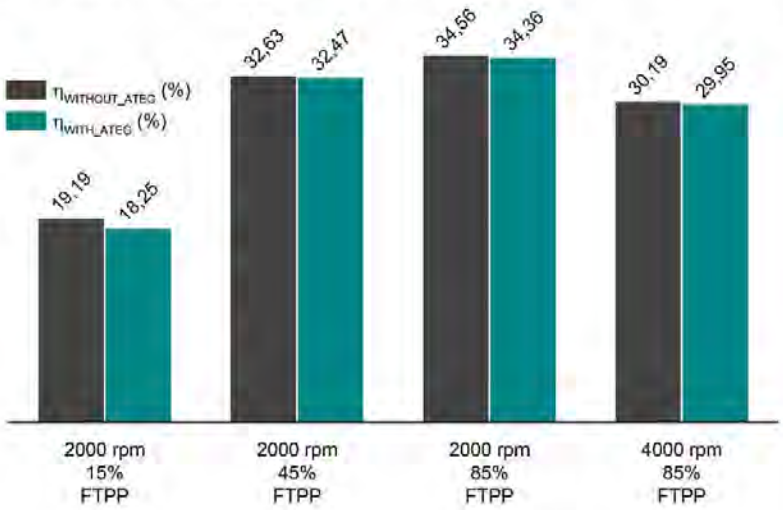

Fig. 16. Engine efficiency with and without the inclusion of the ATEG during steady-state conditions.

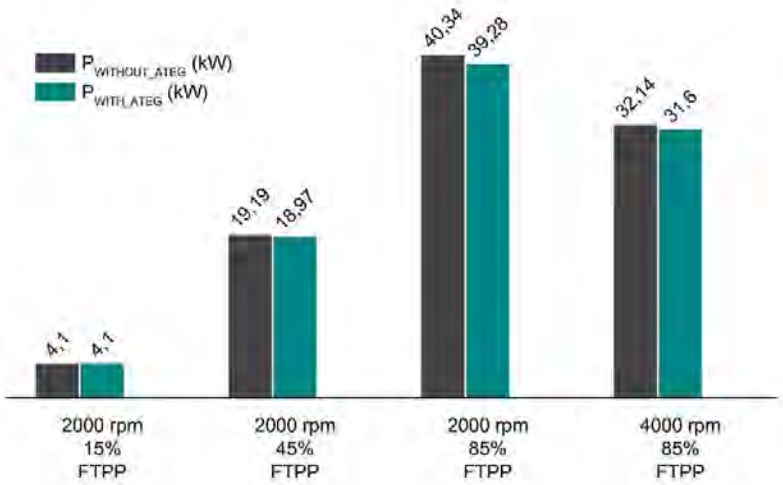

Fig. 17. Engine power with and without the inclusion of the ATEG during steady state conditions.

During hot-start ECE cycle, the mean hot and cold side TEM temperatures are 76.7 °C and 35.2 °C respectively. The mean temperature gradient is 41.5 °C, point A in Fig. 21. The mean power production during the same period is 2.26 W. In Fig. 21, using the gradient of 41.5 °C, the expected power production using PbTe is 0.21 W for each TEM, see point A. This leads to a total power output of the ATEG of 2.52 W. The divergence between expected and measured output power may be due to contact resistance.

Thus, going back to the simulation and changing the material of TEMs to BiTe, the expected overall output power of ATEG is shown, in dark grey, in Fig. 22.

As an be observed, the expected power generation of ATEG using BiTe TEMs is higher compared to PbTe TEMs. This is because BiTe TEMs generate more power at lower temperature gradients, see Fig. 21. Analyzing the temperatures of BiTe TEMs during NEDC cycle, the manufacturer's maximum hot-side temperature is never reached. This does not mean that at a given time, in real driving conditions, TEMs could reach higher temperatures. It is important to notice that exhaust gases could easily reach 700 °C, and the maximum temperature reached during NEDC cycle is about 550 °C. Therefore, the integrity of the system is not totally guaranteed.

As previously stated, the design could be further improved using an internal geometry with fins. The objective is to capture as much energy as possible from exhaust gases by increasing convection. Fig. 23 shows, in green, the thermal resistance of the initial design, a copper heat exchanger with six passing-through holes. To improve the rate of heat transfer, a new finned geometry is proposed. The design was based on previously published conclusions [40–46].

The new geometry consists of two aluminum finned heat exchangers joined together as shown in Fig. 23. External size of finned geometry is the same as the holey one. To prevent an excessive backpressure, internal cross-section area is maintained. As expected, thermal resistance of finned geometry is considerably smaller than holey geometry. Therefore, TEMs temperatures of hot and cold sides would reach faster higher values. Then, the ATEG would generate more power during the NEDC cycle. During hot-start ECE cycle, the mean hot and cold side TEM temperatures are 131.9 °C and 74.8 °C respectively. The mean temperature gradient is 57.1 °C. In Fig. 21, using the gradient of 57.1 °C, the expected power production using BiTe is 5.8 W for each TEM, see point B. This leads to a total power output of the ATEG of 69.6 W. The results shown in Fig. 22 confirm these predictions.

As seen in Fig. 24, TEMs are exposed to temperatures over 200 °C. Manufacturer's recommended hot-side temperature of H-288-14-06-L2 is 150 °C for continuous duty and 200 °C for intermittent duty. This means that it is necessary to control the hot side temperature. As mentioned previously, this can be solved by using a system to by-pass the exhaust gases, see Fig. 25.

By-pass valves (BPV) control the amount of exhaust gases that flow through ATEG. Then, temperature of TEMs can be controlled using a PID control that regulates the aperture of the valves and a temperature

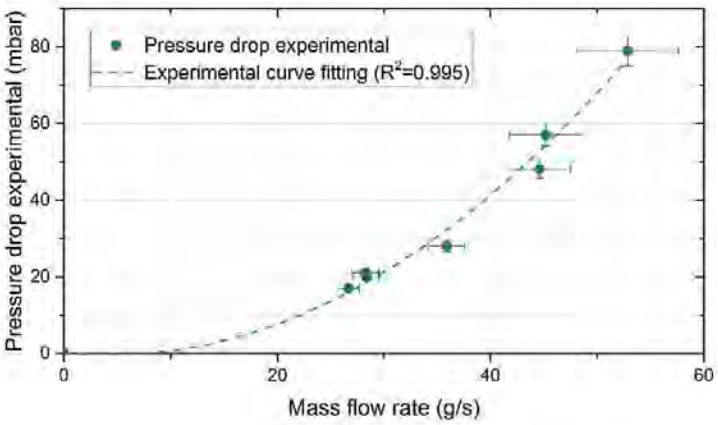

Fig. 18. ATEG pressure drop as function of the exhaust mass flow rate.

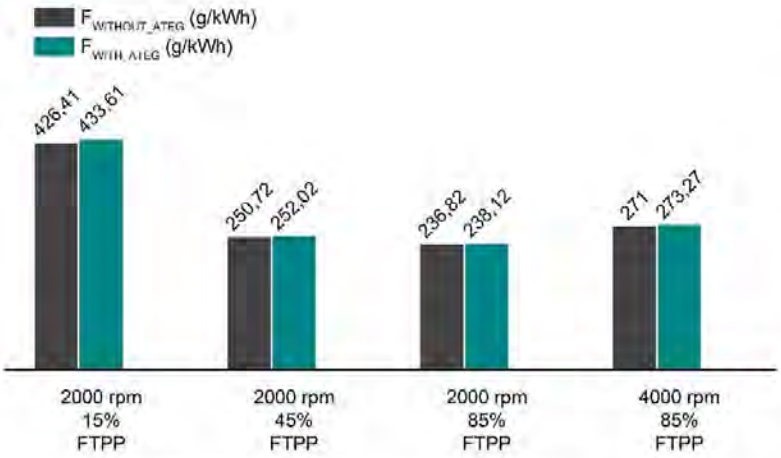

Fig. 19. Engine specific consumption with and without the inclusion of the ATEG.

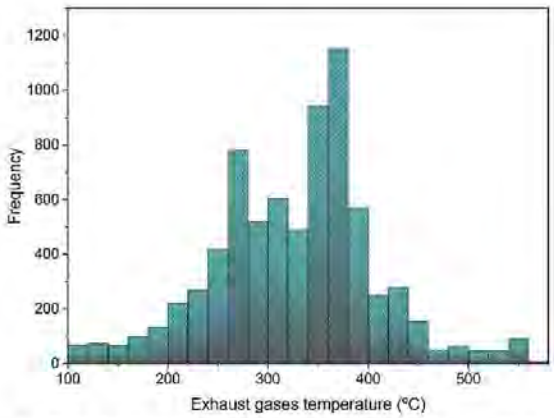

Fig. 20. Exhaust temperatures histogram of 3 NEDC tests at 0.5 s sampling time.

sensor on TEMs hot side. When TEMs hot side temperatures remained below manufacturer's recommended temperature, BPV B would be closed and BPV A would be opened. Consequently, all exhaust gases would flow only through ATEG. When TEMs hot side temperatures exceeded manufacturer's recommended temperature, BPV A would stay closed and BPV B would be totally opened. Thus, exhaust gases flow only through the by-pass pipe and ATEG can be refrigerated. While BPV A would be closed, ATEG temperature will decrease, so it is important to introduce a PID control to manage the opening and closing of PBVs to fix the TEMs hot side temperature at its maximum recommended value.

Consequently, introducing a system to control and fix TEMs hot side temperature prevents ATEG from damage, as seen in the straight red line region of Fig. 24. Temperatures above red dashed line are blocked using the system previously mentioned. This explains the continuous power production beyond 1100 s in Fig. 22.

Finally, to properly analyze the performance of an ATEG and with the aim of comparing the performance of various designs, it is useful, and more appropriate than using the power generation, to calculate the overall energy generated during a driving cycle. Table 4 shows the total energy generated by the three designs proposed.

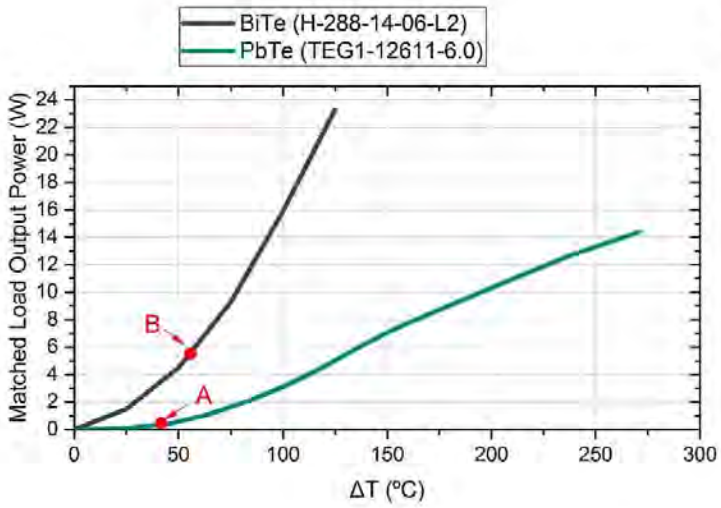

Fig. 21. Performance of TEMs TEG1-12611-6.0 and H-288-14-06-L2 vs temperature gradient.

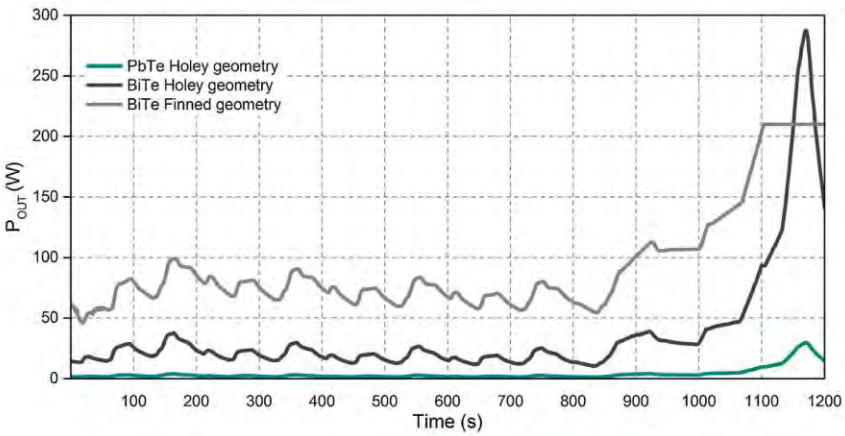

Fig. 22. Output power of ATEGs presented under a NEDC driving cycle.

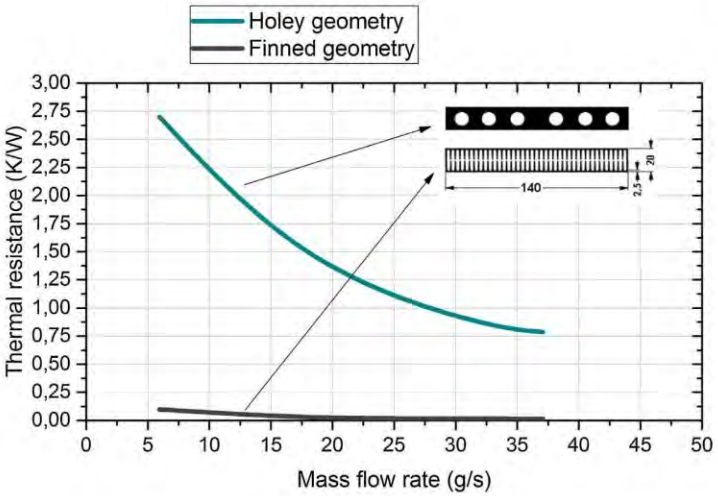

Fig. 23. Thermal resistance of holey and finned heat exchangers.

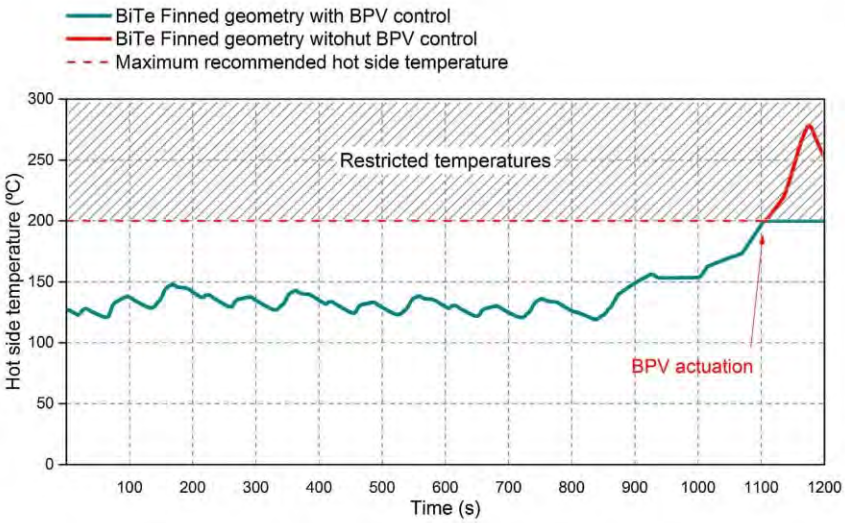

Fig. 24. Hot side temperature of ATEG with BiTe finned geometry during NEDC duty cycle.

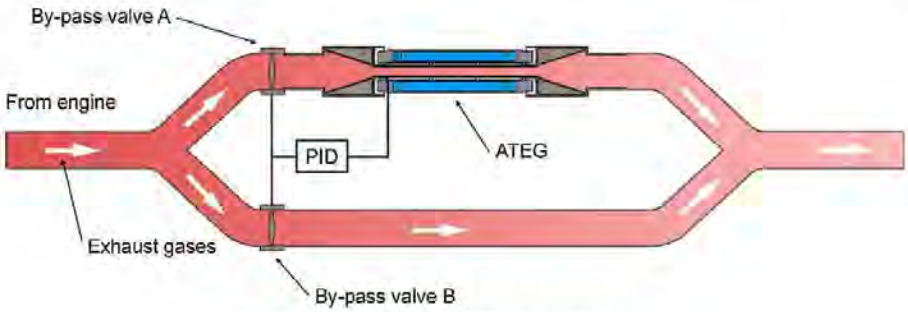

Fig. 25. By-pass valves regulation scheme for the exhaust systems.

Table 4
Energy generated by the three ATEG designs presented.

Design	Energy (Wh)
PbTe + Holey geometry	1.35
BiTe + Holey geometry	13.14
BiTe + Finned geometry	32.70

6. Conclusions

In this study, an automotive thermoelectric generator ATEG based on vehicle waste heat recovery has been developed. The ATEG system behavior has been investigated under constant and dynamic driving conditions. It has been found that vehicle speed and load are a significant factors affecting the ATEG performance for waste heat recovery, and that higher vehicle speed and load account for higher temperature of the exhaust gases and the better ATEG performance. In steady-state conditions, the maximum power output is 5.52 W at 2000 rpm at 15% FTPP, and it reaches 111.22 W at 2000 rpm at 85% FTPP. Transient tests have demonstrated that the way in which the vehicle is driven is also a significant factor affecting the ATEG performance.

Most of ATEGs described in the literature have been designed to withstand the maximum temperature of the exhaust gases. However, during normal driving conditions this working point is rarely achieved. Additionally, the high thermal inertia of the ATEG presented prevents thermoelectric materials from achieving its MPP when it is subjected to transient conditions, such as those present in a NEDC driving cycle. Consequently, the results suggest that the majority of ATEGs will produce significantly less energy that expected from steady-state analysis. Highly frequent change of driving conditions may have a negative effect on the ATEG performance. Only vehicles that work in a very constant regime such as heavy-duty vehicles, combustion engines of range extender vehicles (electric series hybrid architecture) or stationary combustion engines for marine or cogeneration applications will take advantage of this kind of energy harvesters [47].

In addition, exhaust gases temperatures achieved under a NEDC test are concentrated on the range of 260–380 °C for a mid size vehicle engine. Then, the design of ATEGs should be focused on this range in order to maximize the electrical power generation. The goal is to obtain the highest temperature gradient of TEGs at lower exhaust gases temperatures and protect TEGs from higher temperature situations that may occur.

Two modifications of the initial design were proposed and evaluated according to these premises. Results show that maximizing the heat transfer through TEMs using a finned geometry, employing lower temperature thermoelectric materials and including a hot-side temperature control, significantly improve the overall power generation of the ATEG. Following these considerations and for this particular study, energy generation during a NEDC duty cycle has been increased about 24 times its initial value.

Finally, the additional pressure drop provided by the ATEG has an adverse effect on the engine performance: engine efficiency, power, and torque are reduced and specific fuel consumption is increased. In order to introduce thermoelectric waste heat recovery into vehicles, it will be mandatory to previously reduce this effect. Besides, it is also necessary to determine which is the minimum amount of electrical power recovered that makes a significant improvement on the vehicle performance. In some cases, this adverse effects can be overcome by the advantages provided by the ATEG.

Acknowledgments

This work has been partially funded by the Generalitat de Catalunya under Grant No. 2009.SGR-374 and the MINECO Grant No. FIS2012-31307. Authors would also like to thank Fundación Repsol for their collaboration, Association of Industrial Engineers of Catalonia (AEIC) for their partial financial support and the University of Girona under Grant MPCUdG 2016-4.

References

[1] Hsiao YY, Chang WC, Chen SL. A mathematic model of thermoelectric module with applications on waste heat recovery from automobile engine. Energy 2010;35:1447–54. http://dx.doi.org/10.1016/j.energy.2009.11.030.
[2] Su C, Tong N, Xu Y, Chen S, Liu X. Effect of the sequence of the thermoelectric generator and the three-way catalytic converter on exhaust gas conversion efficiency. J Electron Mater 2013;42:1877–81. http://dx.doi.org/10.1007/s11664-012-2454-2.
[3] Saqr KM, Mansour MK, Musa MN. Thermal design of automobile exhaust based thermoelectric generators: objectives and challenges. Int J Automot Technol 2008;9:155–60. http://dx.doi.org/10.1007/s12239-008-0020-y.
[4] Wang T, Zhang Y, Peng Z, Shu G. A review of researches on thermal exhaust heat recovery with Rankine cycle. Renew Sustain Energy Rev 2011;15:2862–71. http://dx.doi.org/10.1016/j.rser.2011.03.015.
[5] Al-Najem N, Diab J. Energy-exergy analysis of a diesel engine. Heat Recover Syst CHP 1992;12:525–9.
[6] Heidrich P, Krisch T. Assessment of waste heat recovery options in passenger car applications by various rankine cycles. Heat Transf Eng 2015;36:1321–31. http://dx.doi.org/10.1080/01457632.2015.995027.
[7] Peng Z, Wang T, He Y, Yang X, Lu L. Analysis of environmental and economic benefits of integrated Exhaust Energy Recovery (EER) for vehicles. Appl Energy 2013;105:238–43. http://dx.doi.org/10.1016/j.apenergy.2013.01.004.
[8] Rahman A, Razzak F, Afroz R, AKM M, Hawlader M. Power generation from waste of IC engines. Renew Sustain Energy Rev 2015;51:382–95. http://dx.doi.org/10.1016/j.rser.2015.05.077.
[9] Shabashevich A, Richards N, Hwang J, Erickson PA. Analysis of powertrain design on effective waste heat recovery from conventional and hybrid electric vehicles. Appl Energy 2015;157:754–61. http://dx.doi.org/10.1016/j.apenergy.2015.02.067.
[10] Saidur R, Rezaei M, Muzammil WK, Hassan MH, Paria S, Hasanuzzaman M. Technologies to recover exhaust heat from internal combustion engines. Renew Sustain Energy Rev 2012;16:5649–59. http://dx.doi.org/10.1016/j.rser.2012.05.018.
[11] Karvonen M, Kapoor R, Uusitalo A, Ojanen V. Technology competition in the internal combustion engine waste heat recovery: a patent landscape analysis. J Clean Prod 2016;112:3735–43. http://dx.doi.org/10.1016/j.jclepro.2015.06.031.
[12] Agudelo AF, García-Contreras R, Agudelo JR, Armas O. Potential for exhaust gas energy recovery in a diesel passenger car under European driving cycle. Appl

Appendix B. Published paper: Transient behavior under a normalized driving cycle of an automotive thermoelectric generator

Energy 2016;174:201–12. http://dx.doi.org/10.1016/j.apenergy.2016.04.092.
[13] Love ND, Szybist JP, Sluder CS. Effect of heat exchanger material and fouling on thermoelectric exhaust heat recovery. Appl Energy 2012;89:322–8. http://dx.doi.org/10.1016/j.apenergy.2011.07.042.
[14] D(Battista D, Mauriello M, Cipollone R. Waste heat recovery of an ORC-based power unit in a turbocharged diesel engine propelling a light duty vehicle. Appl Energy 2015;152:109–20. http://dx.doi.org/10.1016/j.apenergy.2015.04.088.
[15] Boretti AA. Transient operation of internal combustion engines with Rankine waste heat recovery systems. Appl Therm Eng 2012;48:18–23. http://dx.doi.org/10.1016/j.applthermaleng.2012.04.043.
[16] Grelet V, Reiche T, Lemort V, Nadri M, Dufour P. Transient performance evaluation of waste heat recovery rankine cycle based system for heavy duty trucks. Appl Energy 2016;165:878–92. http://dx.doi.org/10.1016/j.apenergy.2015.11.004.
[17] Bass JC, Elsner NB, Leavitt FA. Performance of the 1 kW thermoelectric generator for diesel engines. AIP AIP conf proc1994. p. 295–8. http://dx.doi.org/10.1063/1.46818.
[18] Matsubara K. Development of a high efficient thermoelectric stack for a waste exhaust heat recovery of vehicles. Twenty-first int conf Thermoelectr Proc ICT '02., IEEE 2002. p. 418–23. http://dx.doi.org/10.1109/ICT.2002.1190350.
[19] Haidar JG, Ghojel JI. Waste heat recovery from the exhaust of low-power diesel engine using thermoelectric generators. Proc ICT2001. 20 int conf thermoelectr (Cat. No.01TH8589), IEEE 2001. p. 413–8. http://dx.doi.org/10.1109/ICT.2001.979919.
[20] Crane DT, Lagrandeur J. Thermoelectric waste heat recovery program for passenger vehicles. 2012 Vehicle technologies program annual merit review. Present Slide p. 1–23 [n.d.].
[21] Crane D, Lagrandeur J, Jovovic V, Ranalli M, Adldinger M, Poliquin E, et al. TEG on-vehicle performance and model validation and what it means for further teg development. J. Electron. Mater. 2013;42:1582–91. http://dx.doi.org/10.1007/s11664-012-2327-8.
[22] Ikoma K, Munekiyo M, Furuya K, Kobayashi M, Izumi T, Shinohara K. Thermoelectric module and generator for gasoline engine vehicles. In: Seventeenth int conf thermoelectr. Proc ICT98 (Cat. No.98TH8365); 1998. p. 464–7. 10.1109/ICT.1998.740419.
[23] Thacher EF, Helenbrook BT, Karri MA, Richter CJ. Testing of an automobile exhaust thermoelectric generator in a light truck. Proc Inst Mech Eng D J Automob Eng 2007;221:95–107. http://dx.doi.org/10.1243/09544070JAUTO51.
[24] Kumar S, Heister SD, Xu X, Salvador JR, Meisner GP. Thermoelectric generators for automotive waste heat recovery systems Part II: Parametric evaluation and topological studies. J Electron Mater 2013;42:944–55. http://dx.doi.org/10.1007/s11664-013-2472-8.
[25] Kim S, Won B, Rhi S, Kim S, Yoo J, Jang J. Thermoelectric power generation system for future hybrid vehicles using hot exhaust gas. J Electron Mater 2011;40:778–83. http://dx.doi.org/10.1007/s11664-011-1569-1.
[26] Aixala L. RENOTER Project Introduction – Volvo Group Thermoelectr. Appl Work; 2011.
[27] Magnetto D, Brignone M, Ziggiotti A. HeatReCar Thermoelectric Waste Heat Recovery In Light Duty Trucks optimal use of energy consortium and main objectives. Present Slide; 2010.
[28] Pandiyarajan V, Chinnappandian M, Raghavan V, Velraj R. Second law analysis of a diesel engine waste heat recovery with a combined sensible and latent heat storage system. Energy Policy 2011;39:6011–20. http://dx.doi.org/10.1016/j.enpol.2011.06.065.
[29] Yu S, Du Q, Diao H, Shu G, Jiao K. Start-up modes of thermoelectric generator based on vehicle exhaust waste heat recovery. Appl Energy 2015;138:276–90. http://dx.doi.org/10.1016/j.apenergy.2014.10.062.
[30] Yu S, Du Q, Diao H, Shu G, Jiao K. Effect of vehicle driving conditions on the performance of thermoelectric generator. Energy Convers Manage 2015;96:363–76. http://dx.doi.org/10.1016/j.enconman.2015.03.002.
[31] He W, Wang S, Zhang X, Li Y, Lu C. Optimization design method of thermoelectric generator based on exhaust gas parameters for recovery of engine waste heat. Energy 2015;91:1–9. http://dx.doi.org/10.1016/j.energy.2015.08.022.
[32] Dughaish ZH. Lead telluride as a thermoelectric material for thermoelectric power generation. Phys B Condens Matter 2002;322:205–23. http://dx.doi.org/10.1016/S0921-4526(02)01187-0.
[33] LeBlanc S. Thermoelectric generators: Linking material properties and systems engineering for waste heat recovery applications. Sustain Mater Technol 2014;1–2:26–35. http://dx.doi.org/10.1016/j.susmat.2014.11.002.
[34] Salzgeber K, Prenninger P, Grytsiv A, Rogl P, Bauer E. Skutterudites: thermoelectric materials for automotive applications? J Electron Mater 2009;39:2074–8. http://dx.doi.org/10.1007/s11664-009-1005-y.
[35] Champier D. Thermoelectric generators: a review of applications. Energy Convers Manage 2017;140:167–81. http://dx.doi.org/10.1016/j.enconman.2017.02.070.
[36] He W, Wang S, Lu C, Zhang X, Li Y. Influence of different cooling methods on thermoelectric performance of an engine exhaust gas waste heat recovery system. Appl Energy 2016;162:1251–8. http://dx.doi.org/10.1016/j.apenergy.2015.03.036.
[37] Massaguer E, Massaguer A, Montoro L, Gonzalez JR. Modeling analysis of longitudinal thermoelectric energy harvester in low temperature waste heat recovery applications. Appl Energy 2015;140:184–95. http://dx.doi.org/10.1016/j.apenergy.2014.12.005.
[38] Massaguer E, Massaguer A, Montoro L, Gonzalez JR. Development and validation of a new TRNSYS type for the simulation of thermoelectric generators. Appl Energy 2014;134:65–74. http://dx.doi.org/10.1016/j.apenergy.2014.08.010.
[39] Wang Y, Dai C, Wang S. Theoretical analysis of a thermoelectric generator using exhaust gas of vehicles as heat source. Appl Energy 2013;112:1171–80. http://dx.doi.org/10.1016/j.apenergy.2013.01.018.
[40] Pandiyarajan V, Chinna Pandian M, Malan E, Velraj R, Seeniraj RV. Experimental investigation on heat recovery from diesel engine exhaust using finned shell and tube heat exchanger and thermal storage system. Appl Energy 2011;88:77–87. http://dx.doi.org/10.1016/j.apenergy.2010.07.023.
[41] Peru E, de Jager B, Willems F, Steinbuch M. Two-phase plate-fin heat exchanger modeling for waste heat recovery systems in diesel engines. Appl Energy 2014;133:183–96. http://dx.doi.org/10.1016/j.apenergy.2014.07.073.
[42] Niu Z, Diao H, Yu S, Jiao K, Du Q, Shu G. Investigation and design optimization of exhaust-based thermoelectric generator system for internal combustion engine. Energy Convers Manage 2014;85:85–101. http://dx.doi.org/10.1016/j.enconman.2014.05.061.
[43] Wang T, Luan W, Wang W, Tu S-T. Waste heat recovery through plate heat exchanger based thermoelectric generator system. Appl Energy 2014;136:860–5. http://dx.doi.org/10.1016/j.apenergy.2014.07.082.
[44] He W, Wang S, Li Y, Zhao Y. Structural size optimization on an exhaust exchanger based on the fluid heat transfer and flow resistance characteristics applied to an automotive thermoelectric generator. Energy Convers Manage 2016;129:240–9. http://dx.doi.org/10.1016/j.enconman.2016.10.032.
[45] Ma T, Lu X, Pandit J, Ekkad SV, Huxtable ST, Deshpande S, et al. Numerical study on thermoelectric–hydraulic performance of a thermoelectric power generator with a plate-fin heat exchanger with longitudinal vortex generators. Appl Energy 2016. http://dx.doi.org/10.1016/j.apenergy.2016.01.078.
[46] He W, Wang S, Yue L. High net power output analysis with changes in exhaust temperature in a thermoelectric generator system. Appl Energy 2017;196:259–67. http://dx.doi.org/10.1016/j.apenergy.2016.12.078.
[47] Patyk A. Thermoelectric generators for efficiency improvement of power generation by motor generators – environmental and economic perspectives. Appl Energy 2013;102:1448–57. http://dx.doi.org/10.1016/j.apenergy.2012.09.007.

Bibliography

[1] E.F. Thacher, B.T. Helenbrook, M.A. Karri, C.J. Richter, Testing of an automobile exhaust thermoelectric generator in a light truck, Proc. Inst. Mech. Eng. Part D J. Automob. Eng. 221 (2007) 95–107. doi:10.1243/09544070JAUTO51.

[2] S.B. Riffat, X. Ma, Thermoelectrics: A review of present and potential applications, Appl. Therm. Eng. 23 (2003) 913–935. doi:10.1016/S1359-4311(03)00012-7.

[3] S.A. Omer, D.G. Infield, Design and thermal analysis of a two stage solar concentrator for combined heat and thermoelectric power generation, Energy Convers. Manag. 41 (2000) 737–756. doi:http://dx.doi.org/10.1016/S0196-8904(99)00134-X.

[4] S. Risse, H. Zellbeck, Close-Coupled Exhaust Gas Energy Recovery In A Gasoline Engine, MTZ Worldw. 74 (2013) 54–61. doi:10.1007/s38313-013-0010-y.

[5] Y. Wang, C. Dai, S. Wang, Theoretical analysis of a thermoelectric generator using exhaust gas of vehicles as heat source, Appl. Energy. 112 (2013) 1171–1180. doi:10.1016/j.apenergy.2013.01.018.

[6] C.-C. Weng, M.-J. Huang, A simulation study of automotive waste heat recovery using a thermoelectric power generator, Int. J. Therm. Sci. 71

(2013) 302–309. doi:10.1016/j.ijthermalsci.2013.04.008.

[7] D. Champier, J.P. Bédécarrats, T. Kousksou, M. Rivaletto, F. Strub, P. Pignolet, Study of a TE (thermoelectric) generator incorporated in a multifunction wood stove, Energy. 36 (2011) 1518–1526. doi:http://dx.doi.org/10.1016/j.energy.2011.01.012.

[8] G. Stivers, Radioisotope Thermoelectric Space Power Supplies, IEEE Trans. Aerosp. 2 (1964). doi:10.1109/TA.1964.4319650.

[9] E.S. Pedersen, Nuclear-Thermoelectric Space Power System, IEEE Trans. Aerosp. Navig. Electron. Technical_ (1963). doi:10.1109/TANE.1963.4502266.

[10] H. Xiao, K. Qiu, X. Gou, Q. Ou, A flameless catalytic combustion-based thermoelectric generator for powering electronic instruments on gas pipelines, Appl. Energy. 112 (2013) 1161–1165. doi:10.1016/j.apenergy.2013.01.078.

[11] V. Leonov, T. Torfs, P. Fiorini, C. Van Hoof, Thermoelectric converters of human warmth for self-powered wireless sensor nodes, IEEE Sens. J. 7 (2007) 650–656. doi:10.1109/JSEN.2007.894917.

[12] W. Shin, M. Matsumiya, N. Izu, N. Murayama, Hydrogen-selective thermoelectric gas sensor, Sensors Actuators, B Chem. 93 (2003) 304–308. doi:10.1016/S0925-4005(03)00225-9.

[13] D. Samson, M. Kluge, T. Becker, U. Schmid, Wireless sensor node powered by aircraft specific thermoelectric energy harvesting, in: Sensors Actuators, A Phys., 2011: pp. 240–244. doi:10.1016/j.sna.2010.12.020.

[14] V.L. Kopparthy, S.M. Tangutooru, G.G. Nestorova, E.J. Guilbeau, Thermoelectric microfluidic sensor for bio-chemical applications, Sensors Actuators, B Chem. 166–167 (2012) 608–615. doi:10.1016/j.snb.2012.03.021.

[15] R.L. Field, Photovoltaic/Thermoelectric refrigerator for medicine storage for developing countries, Sol. Energy. 25 (1980) 445–447.

doi:10.1016/0038-092X(80)90452-1.

[16] G.G. Nestorova, E.J. Guilbeau, Thermoelectric method for sequencing DNA., Lab Chip. 11 (2011) 1761–1769. doi:10.1039/c0lc00733a.

[17] a. Goudarzi, a. Mozaffari, P. Samadian, a. Rezania, L. a. Rosendahl, Intelligent design of waste heat recovery systems using thermoelectric generators and optimization tools, Meccanica. 49 (2014) 1211–1223. doi:10.1007/s11012-014-9878-0.

[18] F. Meng, L. Chen, F. Sun, B. Yang, Thermoelectric power generation driven by blast furnace slag flushing water, Energy. 66 (2014) 965–972. doi:10.1016/j.energy.2014.02.018.

[19] N.R. Kristiansen, G.J. Snyder, H.K. Nielsen, L. Rosendahl, Waste Heat Recovery from a Marine Waste Incinerator Using a Thermoelectric Generator, J. Electron. Mater. 41 (2012) 1024–1029. doi:10.1007/s11664-012-2009-6.

[20] X.F. Zheng, Y.Y. Yan, K. Simpson, A potential candidate for the sustainable and reliable domestic energy generation–Thermoelectric cogeneration system, Appl. Therm. Eng. 53 (2013) 305–311. doi:10.1016/j.applthermaleng.2012.03.020.

[21] M.P. Codecasa, C. Fanciulli, R. Gaddi, F. Gomez-Paz, F. Passaretti, Update on the Design and Development of a TEG Cogenerator Device Integrated into Self-Standing Gas Heaters, J. Electron. Mater. 42 (2013) 2243–2248. doi:10.1007/s11664-013-2598-8.

[22] N.D. Love, J.P. Szybist, C.S. Sluder, Effect of heat exchanger material and fouling on thermoelectric exhaust heat recovery, Appl. Energy. 89 (2012) 322–328. doi:10.1016/j.apenergy.2011.07.042.

[23] K.M. Saqr, M.K. Mansour, M.N. Musa, Thermal design of automobile exhaust based thermoelectric generators: Objectives and challenges, Int. J. Automot. Technol. 9 (2008) 155–160. doi:10.1007/s12239-008-0020-y.

[24] K. Ikoma, M. Munekiyo, K. Furuya, M. Kobayashi, T. Izumi, K. Shinohara,

Thermoelectric module and generator for gasoline engine vehicles, Seventeenth Int. Conf. Thermoelectr. Proc. ICT98 (Cat. No.98TH8365). (1998) 464–467. doi:10.1109/ICT.1998.740419.

[25] X.F. Zheng, C.X. Liu, Y.Y. Yan, Q. Wang, A review of thermoelectrics research - Recent developments and potentials for sustainable and renewable energy applications, Renew. Sustain. Energy Rev. 32 (2014) 486–503. doi:10.1016/j.rser.2013.12.053.

[26] Bine Information Service, Thermoelectrics: power from waste heat, Themeninfo I. (2016). http://www.bine.info/en/publications/themeninfos/publikation/thermoelektrik-strom-aus-abwaerme/.

[27] European Parliament, Council of the European Union, Regulation (EC) no. 443/2009, Off. J. Eur. Union. 140 (2009) 1–15. doi:10.1524/zkri.2009.1105.

[28] EU Commission, COMMISSION REGULATION (EU) No 582/2011 of 25 May 2011 - Heavy Duty, Off. J. Eur. Union. L 167 (2011) 1.

[29] European Parliament, Council of the European Union, REGULATION (EC) No 715/2007 OF THE EUROPEAN PARLIAMENT AND OF THE COUNCIL of 20 June 2007 on type approval of motor vehicles with respect to emissions from light passenger and commercial vehicles (Euro 5 and Euro 6) and on access to vehicle repair and mai, Off. J. Eur. Union. L171 (2007) 1–16. doi:OJEU 29.6.2007 L171.

[30] Y.Y.Y. Hsiao, W.C.C. Chang, S.L.L. Chen, A mathematic model of thermoelectric module with applications on waste heat recovery from automobile engine, Energy. 35 (2010) 1447–1454. doi:10.1016/j.energy.2009.11.030.

[31] C. Su, N. Tong, Y. Xu, S. Chen, X. Liu, Effect of the sequence of the thermoelectric generator and the three-way catalytic converter on exhaust gas conversion efficiency, J. Electron. Mater. 42 (2013) 1877–1881. doi:10.1007/s11664-012-2454-2.

[32] T. Wang, Y. Zhang, Z. Peng, G. Shu, A review of researches on thermal exhaust heat recovery with Rankine cycle, Renew. Sustain. Energy Rev. 15 (2011) 2862–2871. doi:10.1016/j.rser.2011.03.015.

[33] N. Al-Najem, J. Diab, Energy-exergy analysis of a diesel engine., Heat Recover. Syst. CHP. 12 (1992) 525–529.

[34] P. Heidrich, T. Krisch, Assessment of Waste Heat Recovery Options in Passenger Car Applications by Various Rankine Cycles, Heat Transf. Eng. 36 (2015) 1321–1331. doi:10.1080/01457632.2015.995027.

[35] Z. Peng, T. Wang, Y. He, X. Yang, L. Lu, Analysis of environmental and economic benefits of integrated Exhaust Energy Recovery (EER) for vehicles, Appl. Energy. 105 (2013) 238–243. doi:10.1016/j.apenergy.2013.01.004.

[36] A. Rahman, F. Razzak, R. Afroz, M. AKM, M. Hawlader, Power generation from waste of IC engines, Renew. Sustain. Energy Rev. 51 (2015) 382–395. doi:10.1016/j.rser.2015.05.077.

[37] A. Shabashevich, N. Richards, J. Hwang, P.A. Erickson, Analysis of powertrain design on effective waste heat recovery from conventional and hybrid electric vehicles, Appl. Energy. 157 (2015) 754–761. doi:10.1016/j.apenergy.2015.02.067.

[38] R. Saidur, M. Rezaei, W.K. Muzammil, M.H. Hassan, S. Paria, M. Hasanuzzaman, Technologies to recover exhaust heat from internal combustion engines, Renew. Sustain. Energy Rev. 16 (2012) 5649–5659. doi:10.1016/j.rser.2012.05.018.

[39] M. Karvonen, R. Kapoor, A. Uusitalo, V. Ojanen, Technology competition in the internal combustion engine waste heat recovery: a patent landscape analysis, J. Clean. Prod. 112 (2016) 3735–3743. doi:10.1016/j.jclepro.2015.06.031.

[40] D.T. Crane, G.S. Jackson, Optimization of cross flow heat exchangers for thermoelectric waste heat recovery, Energy Convers. Manag. 45 (2004)

1565–1582. doi:10.1016/j.enconman.2003.09.003.

[41] A.F. Agudelo, R. García-Contreras, J.R. Agudelo, O. Armas, Potential for exhaust gas energy recovery in a diesel passenger car under European driving cycle, Appl. Energy. 174 (2016) 201–212. doi:10.1016/j.apenergy.2016.04.092.

[42] A.B. Neild, Portable Thermoelectric Generators, 1963. doi:10.4271/630019.

[43] K.V. Birkholz, E. Grob, U. Stohrer, Conversion of waste exhaust heat in automobiles using FeSi2 thermoelements, in: Proc. 7th Int. Conf. Thermoelectr. Energy Convers., 1988: pp. 124–128.

[44] J.C. Bass, A.S. Kushch, N.B. Elsner, Thermoelectric Generator (TEG) for Heavy Diesel Trucks, Proc. Tenth Int. Conf. Thermoelectr. (2001) 1–6.

[45] J.C. Bass, N.B. Elsner, F.A. Leavitt, Performance of the 1 kW thermoelectric generator for diesel engines, AIP Conf. Proc. 316 (1994) 295–298. doi:10.1063/1.46818.

[46] K. Matsubara, Development of a high efficient thermoelectric stack for a waste exhaust heat recovery of vehicles, in: Twenty-First Int. Conf. Thermoelectr. Proc. ICT '02., IEEE, 2002: pp. 418–423. doi:10.1109/ICT.2002.1190350.

[47] and J.D. Eder A., Liebi J., Thermoelektrik Eine Chance fur die Automobilindustrie, 2009.

[48] S. Kim, S. Park, S. Kim, S.H. Rhi, A thermoelectric generator using engine coolant for light-duty internal combustion Engine-Powered Vehicles, J. Electron. Mater. 40 (2011) 812–816. doi:10.1007/s11664-011-1580-6.

[49] D.T. Crane, J.W. Lagrandeur, Progress report on BSST-led US Department of Energy Automotive Waste Heat Recovery Program, J. Electron. Mater. 39 (2010) 2142–2148. doi:10.1007/s11664-009-0991-0.

[50] D.T. Crane, J.W. Lagrandeur, F. Harris, L.E. Bell, Performance results of a high-power-density thermoelectric generator: Beyond the couple, J.

Electron. Mater. 38 (2009) 1375–1381. doi:10.1007/s11664-009-0674-x.

[51] X. Liu, Y.D. Deng, Z. Li, C.Q. Su, Performance analysis of a waste heat recovery thermoelectric generation system for automotive application, Energy Convers. Manag. 90 (2015) 121–127. doi:10.1016/j.enconman.2014.11.015.

[52] Y. Zhang, M. Cleary, X. Wang, N. Kempf, L. Schoensee, J. Yang, G. Joshi, L. Meda, High-temperature and high-power-density nanostructured thermoelectric generator for automotive waste heat recovery, Energy Convers. Manag. 105 (2015) 946–950. doi:10.1016/j.enconman.2015.08.051.

[53] T.Y. Kim, A.A. Negash, G. Cho, Waste heat recovery of a diesel engine using a thermoelectric generator equipped with customized thermoelectric modules, Energy Convers. Manag. 124 (2016) 280–286. doi:10.1016/j.enconman.2016.07.013.

[54] J.G. Haidar, J.I. Ghojel, Waste heat recovery from the exhaust of low-power diesel engine using thermoelectric generators, in: Proc. ICT2001. 20 Int. Conf. Thermoelectr. (Cat. No.01TH8589), IEEE, 2001: pp. 413–418. doi:10.1109/ICT.2001.979919.

[55] S. Kumar, S.D. Heister, X. Xu, J.R. Salvador, G.P. Meisner, Thermoelectric Generators for Automotive Waste Heat Recovery Systems Part II: Parametric Evaluation and Topological Studies, J. Electron. Mater. 42 (2013) 944–955. doi:10.1007/s11664-013-2472-8.

[56] L. Aixala, RENOTER Project Introduction - Volvo Group, Thermoelectr. Appl. Work. (2011).

[57] V. Pandiyarajan, M. Chinnappandian, V. Raghavan, R. Velraj, Second law analysis of a diesel engine waste heat recovery with a combined sensible and latent heat storage system, Energy Policy. 39 (2011) 6011–6020. doi:10.1016/j.enpol.2011.06.065.

[58] S. Yu, Q. Du, H. Diao, G. Shu, K. Jiao, Start-up modes of thermoelectric

generator based on vehicle exhaust waste heat recovery, Appl. Energy. 138 (2015) 276–290. doi:10.1016/j.apenergy.2014.10.062.

[59] S. Yu, Q. Du, H. Diao, G. Shu, K. Jiao, Effect of vehicle driving conditions on the performance of thermoelectric generator, Energy Convers. Manag. 96 (2015) 363–376. doi:10.1016/j.enconman.2015.03.002.

[60] W. He, S. Wang, X. Zhang, Y. Li, C. Lu, Optimization design method of thermoelectric generator based on exhaust gas parameters for recovery of engine waste heat, Energy. 91 (2015) 1–9. doi:10.1016/j.energy.2015.08.022.

[61] D. Crane, J. Lagrandeur, V. Jovovic, M. Ranalli, M. Adldinger, E. Poliquin, J. Dean, D. Kossakovski, B. Mazar, C. Maranville, TEG on-vehicle performance and model validation and what it means for further teg development, J. Electron. Mater. 42 (2013) 1582–1591. doi:10.1007/s11664-012-2327-8.

[62] D.T. Crane, J. Lagrandeur, Thermoelectric Waste Heat Recovery Program for Passenger Vehicles. 2012 Vehicle Technologies Program Annual Merit Review, Present. Slide. (n.d.) 1–23.

[63] D. Magnetto, M. Brignone, A. Ziggiotti, HeatReCar Thermoelectric Waste Heat Recovery in Light Duty Trucks optimal use of energy Consortium and main objectives, Present. Slide. (2010).

[64] E. Massaguer, A. Massaguer, L. Montoro, J.R. Gonzalez, Development and validation of a new TRNSYS type for the simulation of thermoelectric generators, Appl. Energy. 134 (2014) 65–74. doi:10.1016/j.apenergy.2014.08.010.

[65] G. Chen, Nonlocal and Nonequilibrium Heat Conduction in the Vicinity of Nanoparticles, J. Heat Transfer. 118 (1996) 539. doi:10.1115/1.2822665.

[66] G.D. Mahan, J.O. Sofo, The best thermoelectric., Proc. Natl. Acad. Sci. U. S. A. 93 (1996) 7436–7439. doi:10.1073/pnas.93.15.7436.

[67] G. Chen, Nanoscale Energy Transport and Conversion, 2005.

[68] G. Chen, D. Borca-Tasciuc, R.G. Yang, Nanoscale Heat Transfer, in: Encycl. Nanosci. Nanotechnol., 2004: pp. 429–459. doi:10.1051/jp4:2005125116.

[69] D.G. Cahill, W.K. Ford, K.E. Goodson, G.D. Mahan, A. Majumdar, H.J. Maris, R. Merlin, S.R. Phillpot, Nanoscale thermal transport, J. Appl. Phys. 93 (2003) 793–818. doi:10.1063/1.1524305.

[70] J.E. Turney, E.S. Landry, A.J.H. Mcgaughey, C.H. Amon, Predicting phonon properties and thermal conductivity from anharmonic lattice dynamics calculations and molecular dynamics simulations, (2009) 1–12. doi:10.1103/PhysRevB.79.064301.

[71] N. Li, J. Ren, L. Wang, G. Zhang, P. Hänggi, B. Li, Colloquium: Phononics: Manipulating heat flow with electronic analogs and beyond, Rev. Mod. Phys. 84 (2012) 1045–1066. doi:10.1103/RevModPhys.84.1045.

[72] C.W. Chang, D. Okawa, A. Majumdar, A. Zettl, Solid-state thermal rectifier., Science. 314 (2006) 1121–1124. doi:10.1126/science.1132898.

[73] B. Taylor, M. Imbabi, The application of dynamic insulation in buildings, Renew. Energy. 15 (1998) 377–382. doi:10.1016/S0960-1481(98)00190-6.

[74] V. Székely, A. Nagy, S. Török, G. Hajas, M. Rencz, Realization of an electronically controlled thermal resistance, Microelectronics J. 31 (2000) 811–814. doi:10.1016/S0026-2692(00)00063-X.

[75] V. Székely, S. Török, E. Kollár, Improvements of the variable thermal resistance, in: Collect. Pap. Present. 13th Int. Work. Therm. Investig. ICs Syst. THERMINIC, 2007: pp. 180–183. doi:10.1109/THERMINIC.2007.4451773.

[76] G. Min, N.M. Yatim, Variable thermal resistor based on self-powered Peltier effect, J. Phys. D. Appl. Phys. 41 (2008) 222001. doi:10.1088/0022-3727/41/22/222001.

[77] C.H. Cheng, S.Y. Huang, T.C. Cheng, A three-dimensional theoretical model for predicting transient thermal behavior of thermoelectric coolers, Int. J. Heat Mass Transf. 53 (2010) 2001–2011.

doi:10.1016/j.ijheatmasstransfer.2009.12.056.

[78] C.H. Cheng, S.Y. Huang, Development of a non-uniform-current model for predicting transient thermal behavior of thermoelectric coolers, Appl. Energy. 100 (2012) 326–335. doi:10.1016/j.apenergy.2012.05.063.

[79] E. Massaguer, A. Massaguer, L. Montoro, J.R. Gonzalez, Modeling analysis of longitudinal thermoelectric energy harvester in low temperature waste heat recovery applications, Appl. Energy. 140 (2015) 184–195. doi:10.1016/j.apenergy.2014.12.005.

[80] C. a. Domenicali, Irreversible thermodynamics of thermoelectricity, Rev. Mod. Phys. 26 (1954) 237–275. doi:10.1103/RevModPhys.26.237.

[81] D. Kraemer, J. Sui, K. McEnaney, H. Zhao, Q. Jie, Z.F. Ren, G. Chen, High thermoelectric conversion efficiency of MgAgSb-based material with hot-pressed contacts, Energy Environ. Sci. 0 (2015) 1–10. doi:10.1039/C4EE02813A.

[82] E. Environ, Q. Zhang, H. Wang, W. Liu, H. Wang, B. Yu, Q. Zhang, Z. Tian, G. Ni, S. Lee, K. Esfarjani, Z. Ren, Environmental Science Enhancement of thermoelectric figure-of-merit by resonant states of aluminium doping in lead selenide, (2012) 5246–5251. doi:10.1039/c1ee02465e.

[83] Y. Pei, A. LaLonde, S. Iwanaga, G.J. Snyder, High thermoelectric figure of merit in heavy hole dominated PbTe, Energy Environ. Sci. 4 (2011) 2085. doi:10.1039/c0ee00456a.

[84] K. Biswas, J. He, G. Wang, S.-H. Lo, C. Uher, V.P. Dravid, M.G. Kanatzidis, High thermoelectric figure of merit in nanostructured p-type PbTe–MTe (M = Ca, Ba), Energy Environ. Sci. 4 (2011) 4675. doi:10.1039/c1ee02297k.

[85] J. Li, J. Sui, Y. Pei, C. Barreteau, D. Berardan, N. Dragoe, W. Cai, J. He, L.-D. Zhao, A high thermoelectric figure of merit ZT > 1 in Ba heavily doped BiCuSeO oxyselenides, Energy Environ. Sci. 5 (2012) 8543. doi:10.1039/c2ee22622g.

[86] C. Fu, T. Zhu, Y. Liu, H. Xie, X. Zhao, Band engineering of high performance

p-type FeNbSb based half-Heusler thermoelectric materials for figure of merit zT > 1, Energy Environ. Sci. 8 (2015) 216–220. doi:10.1039/C4EE03042G.

[87] D.V. Singh, E. Pedersen, A review of waste heat recovery technologies for maritime applications, Energy Convers. Manag. 111 (2016) 315–328. doi:10.1016/j.enconman.2015.12.073.

[88] B. Orr, A. Akbarzadeh, M. Mochizuki, R. Singh, A review of car waste heat recovery systems utilising thermoelectric generators and heat pipes, Appl. Therm. Eng. (2015). doi:10.1016/j.applthermaleng.2015.10.081.

[89] C.T. Hsu, G.Y. Huang, H.S. Chu, B. Yu, D.J. Yao, Experiments and simulations on low-temperature waste heat harvesting system by thermoelectric power generators, Appl. Energy. 88 (2011) 1291–1297. doi:10.1016/j.apenergy.2010.10.005.

[90] A. Massaguer Colomer, E. Massaguer, T. Pujol, M. Comamala, L. Montoro, J.R. González, Electrically tunable thermal conductivity in thermoelectric materials: Active and passive control, Appl. Energy. 154 (2015) 709–717. doi:10.1016/j.apenergy.2015.05.067.

[91] J. Sharp, Reference Module in Materials Science and Materials Engineering, Elsevier, 2016. doi:10.1016/B978-0-12-803581-8.01093-6.

[92] A. Sellitto, V.A. Cimmelli, D. Jou, Influence of electron and phonon temperature on the efficiency of thermoelectric conversion, Int. J. Heat Mass Transf. 80 (2015) 344–352. doi:10.1016/j.ijheatmasstransfer.2014.09.032.

[93] G. Zhang, K. Jiao, Z. Niu, H. Diao, Q. Du, H. Tian, G. Shu, Power and efficiency factors for comprehensive evaluation of thermoelectric generator materials, Int. J. Heat Mass Transf. 93 (2016) 1034–1037. doi:10.1016/j.ijheatmasstransfer.2015.10.051.

[94] X. Jia, Y. Gao, Estimation of thermoelectric and mechanical performances of segmented thermoelectric generators under optimal operating

conditions, Appl. Therm. Eng. 73 (2014) 335–342. doi:10.1016/j.applthermaleng.2014.07.069.

[95] A.B. Zhang, B.L. Wang, Explicit solutions of an elliptic hole or a crack problem in thermoelectric materials, Eng. Fract. Mech. 151 (2016) 11–21. doi:10.1016/j.engfracmech.2015.11.013.

[96] G. Zhang, Y.-W. Zhang, Strain effects on thermoelectric properties of two-dimensional materials, Mech. Mater. 91 (2015) 382–398. doi:10.1016/j.mechmat.2015.03.009.

[97] B.L. Wang, Y.B. Guo, C.W. Zhang, Cracking and thermal shock resistance of a Bi2Te3 based thermoelectric material, Eng. Fract. Mech. 152 (2016) 1–9. doi:10.1016/j.engfracmech.2015.12.005.

[98] T. Ma, X. Lu, J. Pandit, S. V. Ekkad, S.T. Huxtable, S. Deshpande, Q. wang Wang, Numerical study on thermoelectric–hydraulic performance of a thermoelectric power generator with a plate-fin heat exchanger with longitudinal vortex generators, Appl. Energy. 185 (2016) 1343–1354. doi:10.1016/j.apenergy.2016.01.078.

[99] T. Wang, W. Luan, W. Wang, S.-T. Tu, Waste heat recovery through plate heat exchanger based thermoelectric generator system, Appl. Energy. 136 (2014) 860–865. doi:10.1016/j.apenergy.2014.07.083.

[100] C. Lu, S. Wang, C. Chen, Y. Li, Effects of heat enhancement for exhaust heat exchanger on the performance of thermoelectric generator, Appl. Therm. Eng. 89 (2015) 270–279. doi:10.1016/j.applthermaleng.2015.05.086.

[101] S. Bai, H. Lu, T. Wu, X. Yin, X. Shi, L. Chen, Numerical and experimental analysis for exhaust heat exchangers in automobile thermoelectric generators, Case Stud. Therm. Eng. 4 (2014) 99–112. doi:10.1016/j.csite.2014.07.003.

[102] Y. Kishita, Y. Ohishi, M. Uwasu, M. Kuroda, H. Takeda, K. Hara, Evaluating the life cycle CO2 emissions and costs of thermoelectric generators for passenger automobiles: a scenario analysis, J. Clean. Prod. (2016).

doi:10.1016/j.jclepro.2016.02.121.

[103] C. Dames, Cost optimization of thermoelectric materials for power generation: The case for ZT at (almost) any cost, Scr. Mater. 111 (2016) 16–22. doi:10.1016/j.scriptamat.2015.06.018.

[104] A. Schönecker, B. Kraaijveld, A.E. van Til, A.J. Böttger, P. Brinks, M. Huijben, M. den Heijer, Cost Efficient Manufacturing of Silicide Thermoelectric Materials and Modules using RGS Technique, Mater. Today Proc. 2 (2015) 538–547. doi:10.1016/j.matpr.2015.05.074.

[105] S. LeBlanc, S.K. Yee, M.L. Scullin, C. Dames, K.E. Goodson, Material and manufacturing cost considerations for thermoelectrics, Renew. Sustain. Energy Rev. 32 (2014) 313–327. doi:10.1016/j.rser.2013.12.030.

[106] H. Kim, W. Kim, A way of achieving a low $/W and a decent power output from a thermoelectric device, Appl. Energy. 139 (2015) 205–211. doi:10.1016/j.apenergy.2014.11.040.

[107] A. Montecucco, A.R. Knox, Accurate simulation of thermoelectric power generating systems, Appl. Energy. 118 (2014) 166–172. doi:10.1016/j.apenergy.2013.12.028.

[108] A. Montecucco, J. Siviter, A.R. Knox, The effect of temperature mismatch on thermoelectric generators electrically connected in series and parallel, Appl. Energy. 123 (2014) 47–54. doi:10.1016/j.apenergy.2014.02.030.

[109] A. Rodríguez, J.G. Vián, D. Astrain, A. Martínez, Study of thermoelectric systems applied to electric power generation, Energy Convers. Manag. 50 (2009) 1236–1243. doi:10.1016/j.enconman.2009.01.036.

[110] G. Liang, J. Zhou, X. Huang, Analytical model of parallel thermoelectric generator, Appl. Energy. 88 (2011) 5193–5199. doi:10.1016/j.apenergy.2011.07.041.

[111] S.B. Riffat, X. Ma, Optimum selection (design) of thermoelectric modules for large capacity heat pump applications, Int. J. Energy Res. 28 (2004) 1231–1242. doi:10.1002/er.1025.

[112] L. Chen, J. Li, F. Sun, C. Wu, Performance optimization of a two-stage semiconductor thermoelectric-generator, Appl. Energy. 82 (2005) 300–312. doi:10.1016/j.apenergy.2004.12.003.

[113] J. Yu, H. Zhao, A numerical model for thermoelectric generator with the parallel-plate heat exchanger, J. Power Sources. 172 (2007) 428–434. doi:10.1016/j.jpowsour.2007.07.045.

[114] X. Niu, J. Yu, S. Wang, Experimental study on low-temperature waste heat thermoelectric generator, J. Power Sources. 188 (2009) 621–626. doi:10.1016/j.jpowsour.2008.12.067.

[115] Z.B. Tang, Y.D. Deng, C.Q. Su, W.W. Shuai, C.J. Xie, A research on thermoelectric generator's electrical performance under temperature mismatch conditions for automotive waste heat recovery system, Case Stud. Therm. Eng. 5 (2015) 143–150. doi:10.1016/j.csite.2015.03.006.

[116] T. Zhang, New thinking on modeling of thermoelectric devices, Appl. Energy. 168 (2016) 65–74. doi:10.1016/j.apenergy.2016.01.057.

[117] M. et al. Mori, M., Yamagami, T., Oda, N., Hattori, Current Possibilities of Thermoelectric Technology Relative to Fuel Economy, SAE Tech. Pap. (2009) 11. doi:10.4271/2009-01-0170.

[118] P. He, Y. Li, L. Zhao, STUDY ON EXHAUST SYSTEM PARAMETERS FOR FUEL ECONOMY IMPROVEMENT OF SMALL GASOLINE, (n.d.).

[119] N.A. Khripach, B.A. Papkin, V.S. Korotkov, A.S. Nekrasov, Effect of a Thermoelectric Generator on the Fuel Economy of a Vehicle Operating in a Real-world Environment, 12 (2015) 375–386.

[120] R. Vijayagopal, N. Shidore, M. Reynolds, C. Folkerts, A. Rousseau, Fuel displacement potential of a Thermoelectric Generator in a conventional vehicle, World Electr. Veh. J. 6 (2013) 663–668. doi:10.1109/EVS.2013.6914719.

[121] A. Massaguer, E. Massaguer, M. Comamala, T. Pujol, L. Montoro, M.D. Cardenas, D. Carbonell, A.J. Bueno, Transient behavior under a normalized

driving cycle of an automotive thermoelectric generator, Appl. Energy. 206 (2017) 1282–1296. doi:10.1016/j.apenergy.2017.10.015.

[122] O. Högblom, R. Andersson, Analysis of thermoelectric generator performance by use of simulations and experiments, J. Electron. Mater. 43 (2014) 2247–2254. doi:10.1007/s11664-014-3020-x.

[123] P. Ziolkowski, P. Poinas, J. Leszczynski, G. Karpinski, Estimation of Thermoelectric Generator Performance by Finite Element Modeling, 39 (2010) 1934–1943. doi:10.1007/s11664-009-1048-0.

[124] Y. Kim, G. Yoon, S.H. Park, Direct Contact Resistance Evaluation of Thermoelectric Legs, Exp. Mech. 56 (2016) 861–869. doi:10.1007/s11340-016-0131-8.

[125] R.P. Gupta, R. McCarty, J. Sharp, Practical Contact Resistance Measurement Method for Bulk Bi2Te3-Based Thermoelectric Devices, J. Electron. Mater. 43 (2013) 1608–1612. doi:10.1007/s11664-013-2806-6.

[126] N. Espinosa, M. Lazard, L. Aixala, H. Scherrer, Modeling a thermoelectric generator applied to diesel automotive heat recovery, J. Electron. Mater. 39 (2010) 1446–1455. doi:10.1007/s11664-010-1305-2.

[127] M. Mori, T. Yamagami, O. Nobuyuki, H. Makoto, H. Tomohide, S. Mitsumasa, Heat Recovery Technology of Automobile Using Thermoelectric Element and Its Effect on Fuel Economy, Honda R&D Tech. Rev. 21 (2009).

[128] M. a. Karri, E.F. Thacher, B.T. Helenbrook, Exhaust energy conversion by thermoelectric generator: Two case studies, Energy Convers. Manag. 52 (2011) 1596–1611. doi:10.1016/j.enconman.2010.10.013.

[129] D. Di Battista, M. Mauriello, R. Cipollone, Waste heat recovery of an ORC-based power unit in a turbocharged diesel engine propelling a light duty vehicle, Appl. Energy. 152 (2015) 109–120. doi:10.1016/j.apenergy.2015.04.088.

[130] A.A. Boretti, Transient operation of internal combustion engines with

Rankine waste heat recovery systems, Appl. Therm. Eng. 48 (2012) 18–23. doi:10.1016/j.applthermaleng.2012.04.043.

[131] V. Grelet, T. Reiche, V. Lemort, M. Nadri, P. Dufour, Transient performance evaluation of waste heat recovery rankine cycle based system for heavy duty trucks, Appl. Energy. 165 (2016) 878–892. doi:10.1016/j.apenergy.2015.11.004.

[132] S. Kim, B. Won, S. Rhi, S. Kim, J. Yoo, J. Jang, Thermoelectric Power Generation System for Future Hybrid Vehicles Using Hot Exhaust Gas, J. Electron. Mater. 40 (2011) 778–783. doi:10.1007/s11664-011-1569-1.

[133] Z.H. Dughaish, Lead telluride as a thermoelectric material for thermoelectric power generation, Phys. B Condens. Matter. 322 (2002) 205–223. doi:10.1016/S0921-4526(02)01187-0.

[134] S. LeBlanc, Thermoelectric generators: Linking material properties and systems engineering for waste heat recovery applications, Sustain. Mater. Technol. 1–2 (2014) 26–35. doi:10.1016/j.susmat.2014.11.002.

[135] K. Salzgeber, P. Prenninger, A. Grytsiv, P. Rogl, E. Bauer, Skutterudites: Thermoelectric Materials for Automotive Applications?, J. Electron. Mater. 39 (2009) 2074–2078. doi:10.1007/s11664-009-1005-y.

[136] D. Champier, Thermoelectric generators: A review of applications, Energy Convers. Manag. 140 (2017) 167–181. doi:10.1016/j.enconman.2017.02.070.

[137] W. He, S. Wang, C. Lu, X. Zhang, Y. Li, Influence of different cooling methods on thermoelectric performance of an engine exhaust gas waste heat recovery system, Appl. Energy. 162 (2016) 1251–1258. doi:10.1016/j.apenergy.2015.03.036.

[138] V. Pandiyarajan, M. Chinna Pandian, E. Malan, R. Velraj, R.V. Seeniraj, Experimental investigation on heat recovery from diesel engine exhaust using finned shell and tube heat exchanger and thermal storage system, Appl. Energy. 88 (2011) 77–87. doi:10.1016/j.apenergy.2010.07.023.

[139] E. Feru, B. de Jager, F. Willems, M. Steinbuch, Two-phase plate-fin heat exchanger modeling for waste heat recovery systems in diesel engines, Appl. Energy. 133 (2014) 183–196. doi:10.1016/j.apenergy.2014.07.073.

[140] Z. Niu, H. Diao, S. Yu, K. Jiao, Q. Du, G. Shu, Investigation and design optimization of exhaust-based thermoelectric generator system for internal combustion engine, Energy Convers. Manag. 85 (2014) 85–101. doi:10.1016/j.enconman.2014.05.061.

[141] W. He, S. Wang, Y. Li, Y. Zhao, Structural size optimization on an exhaust exchanger based on the fluid heat transfer and flow resistance characteristics applied to an automotive thermoelectric generator, Energy Convers. Manag. 129 (2016) 240–249. doi:10.1016/j.enconman.2016.10.032.

[142] W. He, S. Wang, L. Yue, High net power output analysis with changes in exhaust temperature in a thermoelectric generator system, Appl. Energy. 196 (2017) 259–267. doi:10.1016/j.apenergy.2016.12.078.

[143] A. Patyk, Thermoelectric generators for efficiency improvement of power generation by motor generators - Environmental and economic perspectives, Appl. Energy. 102 (2013) 1448–1457. doi:10.1016/j.apenergy.2012.09.007.

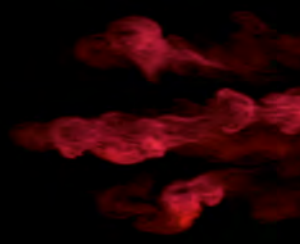

UdG